Charge Transport Dynamics in Electrochemistry

Edmund Dickinson

St John's College
University of Oxford

A thesis submitted for the degree of D.Phil.
in Physical and Theoretical Chemistry.

Trinity Term 2011

Charge Transport Dynamics in Electrochemistry

Edmund Dickinson

St John's College, University of Oxford

A thesis submitted for the degree of D.Phil. in Physical and Theoretical Chemistry.

Trinity Term 2011

Abstract

Electrolytic solutions contain mobile ions that can pass current, and are essential components of any solution-phase electrochemical system. The Nernst–Planck–Poisson equations describe the electrodynamics and transport dynamics of electrolytic solutions.

This thesis applies modern numerical and mathematical techniques in order to solve these equations, and hence determine the behaviour of electrochemical systems involving charge transport. The following systems are studied: a liquid junction where a concentration gradient causes charge transport; an ideally polarisable electrode where an applied potential difference causes charge transport; and an electrochemical cell where electrolysis causes charge transport.

The nanometre Debye length and nanosecond Debye time scales are shown to control charge separation in electrolytic solutions. At equilibrium, charge separation is confined to within a Debye length scale of a charged electrode surface. Non-equilibrium charge separation is compensated in solution on a Debye time scale following a perturbation, whereafter electroneutrality dictates charge transport. The mechanism for the recovery of electroneutrality involves both migration and diffusion, and is non-linear for larger electrical potentials.

Charge separation is an extremely important consideration on length scales comparable to the Debye length. The predicted features of capacitive charging and electrolysis at nanoelectrodes are shown to differ qualitatively from the behaviour of larger electrodes. Nanoscale charge separation can influence the behaviour of a larger system if it limits the overall rate of mass transport or electron transfer.

This thesis advocates the use of numerical methods to solve the Nernst–Planck–Poisson equations, in order to avoid the simplifying approximations required by traditional analytical methods. As this thesis demonstrates, this methodology can reveal the behaviour of increasingly elaborate electrochemical systems, while illustrating the self-consistency and generality of fundamental theories concerning charge transport.

Acknowledgements

This thesis would have not have been possible without the tireless assistance of my supervisor, Professor Richard Compton. I would like to thank him in equal measure for both the instructive and detailed advice he provided throughout, and the considerable academic freedom he allowed me in the direction of my research.

Everyone in the Compton group made the three years of my doctorate highly entertaining, by virtue of their diversity, talent, enthusiasm and sense of good fun. Regular visits to the Lamb and Flag assisted considerably in the preparation of the work in this thesis.

I am extremely grateful to St John's College, which in seven years has provided me with a home, good food, a bar, a great number of my friends, and an undergraduate degree. What is more, its generosity in awarding me a graduate scholarship enabled my doctoral work in Oxford.

Further acknowledgements are due as follows:

- I would like to thank Leon Freitag for his hard work in setting up the numerical simulations reported in Chapter 4, as well as Pembroke College, Oxford, and Friedrich-Schiller-Universität Jena for enabling his work in Oxford.

- I am very grateful to Dr Juan Limon-Petersen and Dr Neil Rees for providing the experimental voltammetry discussed in Chapter 9. Also, Dr Thomas Doneux (Université Libre de Bruxelles) is thanked for many fruitful multilingual discussions on the theories discussed in Chapter 10.

- The following people are thanked for assistance in the provision and translation of foreign language papers: Helena and Patrick Dickinson, Alex Kabakaev (Tomsk Polytechnic University), Benjamin Oestringer and Yvann Stephens.

- I frequently depended upon the websites Wikipedia, Wolfram Alpha, Wolfram Mathworld and EqWorld for rapid revision and corroboration of mathematical results.

I am indebted to my parents for their love and encouragement, which were invaluable throughout my efforts to become the third Dr Dickinson in the family.

Contents

Introduction

In this thesis, numerical and mathematical methods are employed to solve the Nernst–Planck–Poisson equation set, in order to describe charge transport dynamics in certain representative electrochemical systems.

Chapters 1–3 are introductory. In Chapter 1, the fundamental theories of thermodynamics, electrodynamics and mass transport dynamics for electrolytic solutions are introduced, in order to derive the Nernst–Planck–Poisson equation set. Chapter 2 discusses the mathematical methods required for this thesis, while Chapter 3 discusses the corresponding numerical methods.

Chapter 4 presents research into a dynamic theory of liquid junction potentials, in which a concentration gradient drives charge separation. The subsequent charge transport leads to a constant potential difference which indicates a non-equilibrium condition.

Chapters 5–6 describe research on charge transport at an ideally polarisable electrode. In Chapter 5, the equilibrium properties of the diffuse double layer at such an electrode are described, including the qualitatively altered double layer at a nanoelectrode. This is extended in Chapter 6 to the theory of capacitive charging, the process by which this equilibrium is attained following a perturbation, with particular reference to non-linear charge transport dynamics.

Chapters 7–10 consider charge transport due to electrolysis at an electrode. Chapter 7 is introductory and concerns existing theories of electrode thermodynamics, electrode kinetics and cyclic voltammetry under diffusion-only conditions. Chapter 8 critiques the electroneutrality approximation in order to assess its usefulness for both equilib-

rium and dynamic problems. The alternative zero-field approximation is introduced in Chapter 9, again with a critical discussion, followed by a detailed description of macroelectrode cyclic voltammetry subject to this approximation. The latter is also corroborated by experiment. Chapter 10 then describes diffuse double layer effects on steady-state voltammetry, with predictions for non-classical nanoelectrode voltammetry.

The work reported in this thesis has contributed to seven published papers. Material originally published in these works is reproduced within by the kind permission of the copyright holders ACS (*Journal of Physical Chemistry*), Elsevier (*Chemical Physics Letters* and *Journal of Electroanalytical Chemistry*) and Springer (*Journal of Solid State Electrochemistry*). References and direct links to the online articles are given here:

E. J. F. Dickinson, J. G. Limon-Petersen, N. V. Rees and R. G. Compton, *J. Phys. Chem. C*, 2009, **113**, 11157–11171. http://pubs.acs.org/doi/abs/10.1021/jp901628h.

E. J. F. Dickinson and R. G. Compton, *J. Phys. Chem. C*, 2009, **113**, 17585–17589. http://pubs.acs.org/doi/abs/10.1021/jp906404h.

E. J. F. Dickinson, L. Freitag and R. G. Compton, *J. Phys. Chem. B*, 2010, **114**, 187–197. http://pubs.acs.org/doi/abs/10.1021/jp908024s.

E. J. F. Dickinson and R. G. Compton, *Chem. Phys. Lett.*, 2010, **497**, 178–183. http://dx.doi.org/10.1016/j.cplett.2010.08.011.

E. J. F. Dickinson and R. G. Compton, *J. Electroanal. Chem.*, 2011, **655**, 23–31. http://dx.doi.org/10.1016/j.jelechem.2011.02.016.

E. J. F. Dickinson, J. G. Limon-Petersen and R. G. Compton, *J. Solid State Electrochem.*, 2011, **15**, 1335–1345. http://dx.doi.org/10.1007/s10008-011-1323-x

E. J. F. Dickinson and R. G. Compton, *J. Electroanal. Chem.*, 2011, **661**, 198–212. http://dx.doi.org/10.1016/j.jelechem.2011.08.002.

The relation of these published works with the content of each chapter will be addressed in the chapter introductions, and the contributions of co-authors will be acknowledged where appropriate.

Chapter 1

Properties of electrolytic solutions

This chapter will introduce the fundamental theories concerning electrolytic solutions, which form the foundation for the work in this thesis.

1.1 Electrical properties

In his doctoral research, Svante Arrhenius observed that whereas pure water or solid salts are electrical insulators, a solution of salt in water is electrically conducting.[1] To explain this, he hypothesised that when salts dissolve in a polar solvent, such as water, they dissociate into charged particles – ions – which are independently solvated. These dissolved ions are called *electrolyte* and such a solution is termed *electrolytic*.

The mobility of dissolved ions allows charge to be passed through an electrolytic solution, thereby conducting electricity. Equally, by applying an electric field, cations (positive ions) and anions (negative ions) can be separated due to their respective attraction or repulsion, and so charge can accumulate in an electrolytic solution.

Therefore, we can identify some general properties of electrolytic solutions:

- They conduct electricity, because they contain freely dissociated ions which can move through the solution.
- They are *resistive*, because the solution contains only a finite number of ions, and these move with only a finite velocity.
- They are *capacitive*, because the free motion of cations and anions allows charge to be separated by an electric field.

Here, we have drawn analogies with an electrical circuit, in which "resistance" means the applied voltage required to drive a given current, and "capacitance" means the charge separated per applied voltage.

Having made this analogy, it is tempting to assume that an electrolytic solution will behave exactly like a corresponding circuit element with a defined resistance in ohms and a defined capacitance in farads. While this may be true in certain specific or simplified cases, it is not sufficient for most situations, because the local resistivity and capacitance of a solution depend on its local ionic constitution, which may be perturbed in a complex manner by various stimuli: for instance, chemical reaction or diffusion. It is therefore necessary to consider the thermodynamics and electrodynamics of electrolytic solutions in order to successfully describe charge transport.

1.2 Thermodynamics

The modern science of thermodynamics was developed in the 19th century, based principally upon observations in the gas phase. The key determinations are encompassed in three axiomatic laws. The first states that heat and work are interchangeable forms

of energy and that their sum is conserved in a closed system; the second states that the entropy (statistical disorder) of a closed system tends to increase for any spontaneous change; and the third states that at the absolute zero of temperature, all molecular motion ceases.[2]

For an ideal gas, these considerations, together with a mathematical definition of entropy, lead to a law relating pressure to the other state functions of the system:

$$p = \frac{nRT}{V} \tag{1.1}$$

where p is pressure, n is the number of moles of gas, R is the gas constant, T is temperature and V is volume.

The most useful state function for normal chemical purposes is the Gibbs energy, denoted G, which describes the amount of work extractable from a chemical system at constant pressure. From definition, G is given:

$$G = H - TS \tag{1.2}$$

where H denotes enthalpy and S denotes entropy. It follows from the first and second laws of thermodynamics that:

$$dG = V\,dp - S\,dT \tag{1.3}$$

Then, for an ideal gas at a given temperature, the Gibbs energy at a non-standard pressure is given with respect to the Gibbs energy at the standard pressure $p^{\ominus}$ as follows:

$$\int_{p'=p^{\ominus}}^{p'=p} dG = nRT \int_{p^{\ominus}}^{p} \frac{dp'}{p'} \tag{1.4}$$

so

$$G(T) = G^{\ominus}(T) + nRT \ln\left(\frac{p}{p^{\ominus}}\right) \tag{1.5}$$

Defining the chemical potential μ as the first partial derivative of Gibbs energy with respect to molar amount, we find:

$$\mu = \left.\frac{\partial G}{\partial n}\right|_{p,T} = \mu^{\ominus} + RT \ln \frac{p}{p^{\ominus}} \tag{1.6}$$

In 1885, van 't Hoff proposed and verified experimentally that the osmotic pressure of a dilute solution with respect to pure solvent is identical to the pressure of the solute in the gas phase, under the same conditions, if the solvent were imagined to be absent.[3] That is, for dissolved i:

$$\Pi = \frac{n_i RT}{V} = C_i RT \tag{1.7}$$

where Π is the osmotic pressure of a solution of i with concentration C_i. If the ideal gas law is equally valid for relating osmotic pressures:

$$\mu_i = \mu_i^{\ominus} + RT \ln\left(\frac{C_i}{C_i^{\ominus}}\right) \tag{1.8}$$

The standard concentration $C_i^{\ominus}$ is conventionally incorporated into the quantity $\mu_i^{\ominus}$ which is then dependent upon the units chosen.

Equation 1.8 is justified by the requirement of equilibrium of the solute between the solution and gas phases. It is exact in the limit of infinite dilution, but because of inter-molecular interactions by the solute in both phases, this equilibrium may not give a partial pressure that obeys the ideal gas law for all concentrations.[2] In this case, it is conventional to express the chemical potential of the dissolved species in terms of

an activity a_i:

$$\mu_i = \mu_i^{\ominus} + RT \ln a_i \tag{1.9}$$
$$= \mu_i^{\ominus} + RT \ln \gamma_i + RT \ln C_i$$

where γ_i is an activity coefficient which depends on the concentration of i as well as on any extrinsic variables. This is the fundamental relationship governing the thermodynamics of a solution containing uncharged species.

1.3 Electrodynamics

1.3.1 Fundamental electrodynamical equations

Although a general thermodynamic relationship has been developed above, no consideration has yet been made of the influence of electromagnetic interactions on the dynamics of ions in an electrolytic solution. The fundamental classical relations governing the interrelation of charge, electric field and electromagnetic force are Maxwell's equations and the Lorentz force law.[4,5] Strictly, these equations also incorporate the effects of the magnetic field generated by a moving charge, but this can generally be neglected in the study of electrolytic solutions, because ions move sufficiently slowly in solution that their corresponding magnetic fields are negligible with respect to other contributing forces.*

Ignoring the magnetic field, the relevant equations are respectively Gauss's law and

*In the specific case of this thesis, magnetic fields may also be excluded because all of the problems considered are in high symmetry environments where the electric field has zero curl, such that no magnetic field exists according to Faraday's law of induction.

the Lorentz force law:

$$\nabla \cdot \mathbf{E} = \frac{\rho}{\epsilon_s \epsilon_0} \tag{1.10}$$

$$\mathbf{F} = q\mathbf{E} \tag{1.11}$$

Here, $\mathbf{E}$ is the electric field vector, ρ is the charge density, ϵ_0 is the permittivity of free space, ϵ_s is the relative permittivity (or dielectric constant) of the medium, and $\mathbf{F}$ is the force vector acting on a test charge with magnitude q. $\nabla\cdot$ denotes the divergence operator (see also Section 2.1). These equations imply Coulomb's inverse square law for the force between two point charges q_1 and q_2 as a function of their separation r_{12}:

$$\mathbf{F} = \frac{q_1 q_2}{4\pi\epsilon_s \epsilon_0 r_{12}^2} \tag{1.12}$$

However, Coulomb's law only holds for static charges, whereas Gauss's law and the Lorentz force law are equally valid for moving charges.[5]

1.3.2 Electrical potential and Gauss's law

It is convenient to reframe the above equations in terms of an electrical potential ϕ. The electric field is the negative gradient of ϕ:

$$\mathbf{E} = -\nabla\phi \tag{1.13}$$

where ∇ is the gradient operator and the minus sign is included to ensure that positive charges are attracted down the potential gradient. The electromagnetic force perceived by a charge is then governed by the electric field between two points with different electrical potential.

The electrical potential may be understood as an additional electrical potential energy applying to charged particles, measured with respect to their charge. We must

incorporate the additional potential energy associated with the electromagnetic interaction of the ion into the above expression for the chemical potential of an ideal solution (Equation 1.8). On the basis of the electrical potential as an energy per unit charge, we determine the additional potential energy as the product of charge and potential:

$$\begin{aligned}\mu_i(\phi) &= \mu_i(\phi = 0) + z_i e N_\mathrm{A} \phi \\ &= \mu_i^\ominus + RT \ln a_i + z_i F \phi\end{aligned} \tag{1.14}$$

where N_A is the Avogadro constant, e is the charge on an electron, z_i is the charge number of the ion i and F is the Faraday constant (the charge of one mole of electrons, $= N_\mathrm{A} e \approx 96485$ C).

In the potential formulation, Gauss's law becomes:

$$\nabla^2 \phi + \frac{\rho}{\epsilon_\mathrm{s} \epsilon_0} = 0 \tag{1.15}$$

where ∇^2 is the Laplacian operator, which is the divergence of a gradient (see also Section 2.1).

This equation has useful integrated forms in highly symmetric environments which relate the electric field to the enclosed charge within a surface. Specifically, in a linearly symmetric space with coordinate x (see also Section 2.1.2 below), the enclosed charge q_enc in the "Gaussian box" defined by the domain inside a surface at $x = a$ with area A is given:

$$\frac{q_\mathrm{enc}}{A} = -\epsilon_\mathrm{s} \epsilon_0 \left.\frac{\partial \phi}{\partial x}\right|_{x=a} \tag{1.16}$$

In a hemispherically symmetric space with radial coordinate r, the enclosed charge within a hemispherical Gaussian surface defined by the shell $r = a$ is given:

$$\frac{q_\mathrm{enc}}{2\pi a^2} = -\epsilon_\mathrm{s} \epsilon_0 \left.\frac{\partial \phi}{\partial r}\right|_{r=a} \tag{1.17}$$

1.3.3 Derivation of the Poisson equation

For an electrolytic solution, the only charge carriers are dissociated ions. There are no free electrons in the solution. Hence, the charge density may be expressed as:

$$\rho = e \sum_i z_i \frac{n_i}{V} \tag{1.18}$$

This assumes that the concentration of ions is sufficiently large that it can be represented statistically by a continuous variable.

Converting to molar quantities:

$$\rho = N_\mathrm{A} e \sum_i z_i C_i = F \sum_i z_i C_i \tag{1.19}$$

and substituting into Gauss's Law (Equation 1.15):

$$\nabla^2 \phi + \frac{F}{\epsilon_\mathrm{s} \epsilon_0} \sum_i z_i C_i = 0 \tag{1.20}$$

This is commonly called the Poisson equation[†] and is the fundamental relation between electric field and charge separation for an electrolytic solution.

Dimensional analysis of the Poisson equation can lead us to certain conclusions. Normalising molar energy by RT and molar charge by F, and normalising to a reference electrolyte concentration C^*, we achieve:

$$\nabla^2 \theta + \frac{F^2 C^*}{RT \epsilon_\mathrm{s} \epsilon_0} \sum_i z_i c_i = 0 \tag{1.21}$$

and multiplying through by the collection of constants:

$$2 x_\mathrm{D}^2 \nabla^2 \theta + \sum_i z_i c_i = 0 \tag{1.22}$$

where θ and c_i are normalised potential and concentration respectively, and x_D is a

[†]Strictly it is *a* Poisson equation since Poisson derived it in terms of general charge density [*Bull. Soc. Phil.* 1813], but this is not the common electrochemical usage.

characteristic parameter with units of length, commonly referred to as the *Debye length*:

$$x_{\mathrm{D}} = \sqrt{\frac{RT\epsilon_s\epsilon_0}{2F^2C^*}} \tag{1.23}$$

The factor of two is retained here since it simplifies many equations developed from the Poisson equation.

The Debye length indicates the length over which separated charge, and hence electric fields, are screened in an electrolytic solution. For the region around a certain quantity of charge in an electrolytic solution, the range over which the electric field can vary is limited by the Debye length. This length scale is encountered very frequently in the study of charge transport in electrolytic solutions and so will be referred to throughout this thesis.

For water at 298 K and infinite dilution,[6] the dielectric constant $\epsilon_{\mathrm{s}} \approx 78.5$. Then, for 1 mM electrolyte, $x_{\mathrm{D}} \approx 9.6$ nm; for 1 M electrolyte, $x_{\mathrm{D}} \approx 0.3$ nm. The presence of electrolyte influences the solvent permittivity, but not to a considerable extent. These values indicate that electric fields are screened over very short distances in aqueous electrolytic solutions. Hence the approximation $x_{\mathrm{D}} = 0$ is often applied, to yield from Equation 1.22 the expression that:

$$\sum_i z_i c_i = 0 \tag{1.24}$$

which states that charge separation in electrolytic solution is zero. Equation 1.24 is therefore called the *electroneutrality* condition. The utility and deficiencies of this natural approximation in various contexts will also be considered throughout this thesis.

1.4 Mass transport: the Nernst–Planck equation

The required connection between thermodynamics and dynamic, non-equilibrium mass transport was made by Nernst.[7] He argued that the force acting on a dissolved ion or molecule could be expressed as the local gradient of its chemical potential. Hence, all species in solution have a tendency to migrate towards a minimum of chemical potential. On this basis, for the dissociated ion i:

$$\begin{aligned} \mathbf{F}_i &= -\nabla \mu_i \\ &= -RT\,\nabla \ln C_i - z_i F\,\nabla \phi \end{aligned} \tag{1.25}$$

so long as activity effects due to $\gamma_i \neq 1$ can be ignored. Now we assume that ions moving in solution attain a limiting velocity due to friction from solvent molecules, which is proportional to the applied force.

$$\mathbf{v}_i \propto \mathbf{F}_i \tag{1.26}$$

This proportionality can be quantified using the definition of mobility, u_i, as the ratio of limiting velocity to applied field:

$$u_i = \left| \frac{\mathbf{v}_i}{z_i \nabla \phi} \right| \tag{1.27}$$

so

$$\mathbf{v}_i = -u_i \left(\frac{RT}{F} \nabla \ln C_i + z_i \nabla \phi \right) \tag{1.28}$$

Having established that the velocity of the ions is given by the above expression, the flux of ions through a given area may be expressed:

$$\begin{aligned} \mathbf{J}_i &= C_i \, \mathbf{v}_i \\ &= -u_i \left(\frac{RT}{F} C_i \, \nabla \ln C_i + z_i C_i \, \nabla \phi \right) \end{aligned} \tag{1.29}$$

Now, simplifying $C_i \, \nabla \ln C_i$ to ∇C_i and introducing the Einstein relation to define a diffusion coefficient D_i:

$$D_i = \frac{RT}{F} \, u_i \tag{1.30}$$

we derive the Nernst–Planck equation for the flux of an ionic species.

$$\mathbf{J}_i = -D_i \left(\nabla C_i + \frac{z_i F}{RT} \, C_i \, \nabla \phi \right) \tag{1.31}$$

Planck is credited additionally due to his early development of the differential form of this equation,[8] and due to his framing of the equation in terms of concentration rather than osmotic pressure.[9]

In the above equation, the flux of an ion is the sum of two terms, each representing a different mode of mass transport. The first depends on the concentration gradient and therefore quantifies diffusion. Diffusion is a statistical process arising because the thermal motion of ions tends to equalise their concentrations, minimising chemical potential (Equation 1.8) by maximising entropy, in agreement with the 2nd Law of Thermodynamics. Note that where the electric field is zero ($\nabla \phi = 0$), the Nernst–Planck equation reduces to Fick's 1st Law of Diffusion:[10]

$$\mathbf{J}_i = -D_i \, \nabla C_i \tag{1.32}$$

A neutral molecule with $z_\mathrm{A} = 0$ has only diffusional mass transport and so also obeys

Fick's 1st Law of Diffusion.

The second term in the Nernst–Planck equation describes organised motion of ions with or against electric fields according to their charge. This motion derives from the Coulombic attraction or repulsion of ions by an electric field, and is termed *migration*. It is also sometimes described as electrostatic migration, although since migration by definition describes moving charge, this terminology is not strictly accurate.

The Nernst–Planck equation as reported here does not include a convection term, although solvent convection certainly influences the mass transport of dissolved species in real systems. Convection will be ignored in this thesis since the systems under consideration involve sufficiently short length and time scales for the effect of thermal motion of bulk solvent to be considered negligible.

In the absence of an overall flux ($\mathbf{J}_i = 0$), the Nernst–Planck equation can be integrated to the thermodynamic Boltzmann equation, in which the difference in concentrations due to a potential difference away from a reference potential ϕ_0 is given:

$$\frac{C_i}{C_{i,0}} = \exp\Big(- \frac{z_i F}{RT}(\phi - \phi_0)\Big) \tag{1.33}$$

This equation can equally well be derived from consideration of the chemical potential at unit activity, since it is a statement of equilibrium.

1.5 Time-dependent mass transport

Time dependence in mass transport can be incorporated by the continuity equation, which expresses the principle of conservation of mass:

$$\frac{\partial C_i}{\partial t} = -\nabla \cdot \mathbf{J}_i \tag{1.34}$$

where t is the time coordinate. This equation assumes that no chemical reactions exist which might augment or reduce C_i independently from mass transport. Then, the change of concentration at a point must equal the sum of sources and sinks at that point, i.e. the divergence of the local flux vector. Hence:

$$\frac{\partial C_i}{\partial t} = D_i \left(\nabla^2 C_i + \frac{z_i F}{RT} \nabla \cdot (C_i \nabla \phi) \right) \tag{1.35}$$

which is the time-dependent Nernst–Planck equation. Again, if $\nabla \phi = 0$, we recover Fick's 2nd Law of Diffusion:[10]

$$\frac{\partial C_i}{\partial t} = D_i \nabla^2 C_i \tag{1.36}$$

This diffusion equation can equally well be derived by statistical consideration of the random thermal motion of molecules, as should be expected if the statistical and thermodynamical descriptions of entropy are self-consistent. Accordingly, the root mean square displacement of a diffusing molecule in some time t is given, after Einstein,[11] by:

$$\sqrt{\langle x^2 \rangle} = \sqrt{2Dt} \tag{1.37}$$

A diffusion layer therefore expands at a rate proportional to the square root of time. This proportionality dictates the spatial extent of a perturbation due to diffusion, and is crucial to electrolytic solution dynamics whenever a concentration gradient is present.

1.6 Determining electrolytic solution properties

The Nernst–Planck equation relates the motion of ions to the electric field and hence, indirectly, to the potential difference between two points. It is then possible to consider the magnitude of the conductivity of the solution containing k different ionic species.

The total ionic current i through an area A is then given:

$$\begin{aligned} i &= \sum_k z_k F A \mathbf{J}_k \\ &= -FA\left(\sum_k z_k D_k \nabla C_k + \sum_k z_k^2 D_k \frac{F}{RT} C_k \nabla\phi\right) \\ &\approx -FAD\left(\nabla\left(\sum_k z_k C_k\right) + \frac{F}{RT}\nabla\phi \sum_k z_k^2 C_k\right) \\ &\approx -\frac{DF^2}{RT} A \nabla\phi \sum_k z_k^2 C_k \end{aligned} \tag{1.38}$$

where it has been assumed that all $D_k \approx D$ and that the electroneutrality condition holds. Under these conditions we have obtained a simple relation between ionic current and potential difference. By analogy to Ohm's law:[5]

$$i = \frac{-\Delta\phi}{R_\mathrm{s}} \approx \frac{-\nabla\phi\Delta x}{R_\mathrm{s}} = -\sigma A \nabla\phi \tag{1.39}$$

where R_s denotes resistance and σ denotes the conductivity of the medium. Hence:

$$\sigma \approx \frac{DF^2}{RT} \sum_k z_k^2 C_k \tag{1.40}$$

Defining the ionic strength I as:

$$I = \frac{1}{2} \sum_k z_k^2 C_k \tag{1.41}$$

a simplified expression is obtained

$$\sigma \approx D \frac{2F^2 I}{RT} = D \frac{\epsilon_\mathrm{s}\epsilon_0}{x_\mathrm{D}^2} \tag{1.42}$$

In this way, the conductivity of an electrolytic solution can be estimated. The conductivity increases in direct proportion to the ionic strength, as first determined experimentally by Arrhenius. Without the simplifying approximations made here, however, relations from conventional electrodynamics, such as Ohm's law, do not yield unambiguous expressions for properties such as solution conductivity.

The most significant relations introduced in this chapter are the Nernst–Planck equation, the continuity equation and the Poisson equation (Equations 1.31, 1.34 and 1.20 respectively), which collectively will be described as the Nernst–Planck–Poisson (NPP) equation set. These equations provide the theoretical framework employed in this thesis to determine the behaviour of model electrolytic solution systems and hence draw conclusions about their chemistry. The derivations presented above demonstrate that these equations incorporate fundamental thermodynamic and electrodynamic relations, and so are completely consistent with established chemical and physical laws. Since the solution of one or more of these equations is non-trivial for problems of interest in charge transport, however, it is necessary to develop an arsenal of mathematical and numerical approaches, which are detailed in the following two chapters.

Bibliography

[1] S. Arrhenius, *Z. Physik. Chem.*, 1887, **1**, 631–648.

[2] E. B. Smith, *Basic Chemical Thermodynamics*, Imperial College Press, London, 5th edn., 2004.

[3] J. H. van 't Hoff, *Z. Physik. Chem.*, 1887, **1**, 481–508.

[4] J. Clerk Maxwell, *Phil. Trans. Royal Soc. London*, 1865, **155**, 459–512.

[5] J. D. Jackson, *Classical Electrodynamics*, John Wiley & Sons, New York, 2nd edn., 1975.

[6] D. G. Archer and P. Wang, *J. Phys. Chem. Ref. Data*, 1990, **19**, 371–411.

[7] W. Nernst, *Z. Physik. Chem.*, 1889, **4**, 129–181.

[8] M. Planck, *Wied. Ann.*, 1890, **39**, 161–186.

[9] M. Planck, *Wied. Ann.*, 1890, **40**, 561–576.

[10] A. Fick, *Pogg. Ann.*, 1855, **94**, 59–86.

[11] A. Einstein, *Ann. Phys.*, 1905, **17**, 549–560.

Chapter 2

Mathematical methods

This chapter introduces the mathematical methods employed in the solution of the Nernst–Planck–Poisson equation set in this thesis.[1,2]

2.1 Geometry

The equations introduced in Chapter 1 were given in the generic language of vector calculus, using the operators ∇, $\nabla\cdot$ and ∇^2 to denote gradient, divergence and the Laplacian respectively. These operators take different forms depending upon the coordinate system employed.

This thesis will consider linear and hemispherical coordinate systems in 'real' space. Both of these are one-dimensional coordinate systems which imply a high degree of symmetry in the system. In addition, transforms of these coordinates will be employed to facilitate theoretical work.

2.1.1 Three-dimensional space

Three-dimensional space is conventionally parameterised by three orthogonal Cartesian coordinates x, y and z. A scalar function in this space has a single value depending on each of these coordinates and is written as $f(x, y, z)$. A vector function in this space has a component in each of the coordinate directions and is written:

$$\mathbf{f}(x, y, z) = f_x(x, y, z)\,\hat{\mathbf{i}} + f_y(x, y, z)\,\hat{\mathbf{j}} + f_z(x, y, z)\,\hat{\mathbf{k}} \tag{2.1}$$

where $\hat{\mathbf{i}}$, $\hat{\mathbf{j}}$ and $\hat{\mathbf{k}}$ are vectors of unit length in the x, y and z directions respectively. Therefore, a three-dimensional vector function is defined by three scalar functions.

The gradient operator gives the magnitude and direction of the gradient of a scalar function, in three dimensions:

$$\nabla f = \frac{\partial f}{\partial x}\,\hat{\mathbf{i}} + \frac{\partial f}{\partial y}\,\hat{\mathbf{j}} + \frac{\partial f}{\partial z}\,\hat{\mathbf{k}} \tag{2.2}$$

The divergence operator gives the magnitude of the source or sink of a vector function:

$$\nabla \cdot \mathbf{f} = \frac{\partial f_x}{\partial x} + \frac{\partial f_y}{\partial y} + \frac{\partial f_z}{\partial z} \tag{2.3}$$

The Laplacian operator is the divergence of the gradient of a scalar function:

$$\nabla^2 f = \frac{\partial^2 f}{\partial x^2} + \frac{\partial^2 f}{\partial y^2} + \frac{\partial^2 f}{\partial z^2} \tag{2.4}$$

2.1.2 Linear coordinates

The linear coordinate system describes position using a single coordinate x. The yz-plane for a given x is then assumed to be homogeneous, so $f(x, y, z) = f(x)$. Then:

$$\begin{aligned} \nabla f &= \frac{\partial f}{\partial x}\,\hat{\mathbf{i}} \\ \nabla \cdot \mathbf{f} &= \frac{\partial f}{\partial x} \\ \nabla^2 f &= \frac{\partial^2 f}{\partial x^2} \end{aligned} \tag{2.5}$$

2.1.3 Hemispherical coordinates

The hemispherical coordinate system assumes that for positive z, position can be described using a single coordinate r which is the radial distance from the origin:

$$r = \sqrt{x^2 + y^2 + z^2} \tag{2.6}$$

Then, the hemispherical shell for a given r is assumed to be homogeneous, so all functions have complete angular symmetry and $f(x, y, z) = f(r)$. The operators are:

$$\begin{aligned} \nabla f &= \frac{\partial f}{\partial r}\,\hat{\mathbf{r}} \\ \nabla \cdot \mathbf{f} &= \frac{1}{r^2}\frac{\partial (r^2 f)}{\partial r} \\ \nabla^2 f &= \frac{1}{r^2}\frac{\partial}{\partial r}\left(r^2 \frac{\partial f}{\partial r}\right) \end{aligned} \tag{2.7}$$

where $\hat{\mathbf{r}}$ is a vector of unit length in the r direction. The additional complexity of these operators accounts for the altered symmetry properties of the coordinate system: in particular, the area of the homogeneous hemispherical shell for a given r increases with r^2, whereas the area of the homogeneous planes in a linear coordinate system is constant irrespective of the value of x.

2.1.4 Coordinate transformation

Equations can often be simplified by a coordinate transformation. If we transform from x into a coordinate $q = g(x)$, the operators above are altered according to the chain rule:

$$\frac{\partial}{\partial x} = \frac{\partial}{\partial q}\frac{\partial q}{\partial x} = \frac{dg}{dx}\frac{\partial}{\partial q} \tag{2.8}$$

Substitution into the above expressions then allows transformation of the operators into the appropriate forms in the coordinate q.

2.2 Normalisation

The equations presented in Chapter 1 were all dimensional: that is, the constants and the dependent and independent variables of the equations have dimensions, and so their values depend on the units chosen. These equations can be generalised by a process of normalisation, where the constants and variables are made dimensionless such that they do not depend on the choice of units. This process also permits dimensional analysis to reveal characteristic length and time scales and characteristic dimensionless parameters which dictate the behaviour of a system.

To accomplish the normalisation of a system, standard dimensional quantities are selected for a set of base units, and the equations are normalised with respect to these quantities. The base units are respectively length, time, concentration, potential (voltage) and current.

Hence, denoting a standard quantity with a superscript *, dimensionless length,

radial length, time, concentration, potential and current are defined respectively as:

$$\begin{aligned} X &= \frac{x}{x^*} \\ R &= \frac{r}{x^*} \\ \tau &= \frac{t}{t^*} \\ c &= \frac{C}{C^*} \\ \theta &= \frac{\phi}{\phi^*} \\ j &= \frac{i}{i^*} \end{aligned} \tag{2.9}$$

Throughout, concentration is normalised by

$$C^* = C_q^* \tag{2.10}$$

where C_q^* is the bulk concentration of the reference species q, and potential is normalised by

$$\phi^* = \frac{RT}{F} = \frac{kT}{e} \tag{2.11}$$

which is a suitable normalisation considering the definition of electrical potential as energy per unit charge.

The time-dependent Nernst–Planck equation is then:

$$\frac{\partial c_i}{\partial \tau} = D_i \, \frac{t^*}{x^{*2}} \left(\nabla^2 c_i + z_i \, \nabla \cdot (c_i \, \nabla \theta) \right) \tag{2.12}$$

where the gradient, divergence and Laplacian operators are now with respect to the normalised X or R coordinate. This suggests an appropriate relation between the normalisation of time and the normalisation of space:

$$t^* = \frac{x^{*2}}{D_q} \tag{2.13}$$

where D_q is the diffusion coefficient of the reference species q. This ensures an ideally dimensionless time-dependent Nernst–Planck equation containing no extraneous constants except for the normalised diffusion coefficient:

$$\frac{\partial c_i}{\partial \tau} = D_i' \left(\nabla^2 c_i + z_i \, \nabla \cdot (c_i \, \nabla \theta) \right) \tag{2.14}$$

where

$$D_i' = \frac{D_i}{D_q} \tag{2.15}$$

The choice of x^* will vary depending on the particular problem under consideration. Note that having defined these standard quantities, the appropriate normalisations for a variable or constant with any other units may be derived by a combination of the five base units. For instance, a constant with units of velocity should be normalised to a standard quantity $v^* = x^*/t^* = D_q/x^*$ since velocity is length per time.

Based on the above, the individual Nernst–Planck, continuity and Poisson equations have been normalised to the following:

$$\mathbf{J'}_i = -D_i' \, (\nabla c_i + z_i c_i \, \nabla \theta) \tag{2.16}$$

$$\frac{\partial c_i}{\partial \tau} = -\nabla \cdot \mathbf{J'}_i \tag{2.17}$$

$$\nabla^2 \theta + \frac{1}{2} \left(\frac{x^*}{x_\mathrm{D}} \right)^2 \sum_i z_i c_i = 0 \tag{2.18}$$

Note that the normalised flux is given as

$$\mathbf{J'}_i = \mathbf{J}_i \frac{x^*}{C_q^* D_q} \tag{2.19}$$

which has been derived from the base unit normalisations. This expression for flux

further implies a suitable choice of normalisation for current:

$$i^* = FA\,J^* = \frac{FAC_q^* D_q}{x^*} \tag{2.20}$$

where A is the area through which the current passes.

2.3 Differential equations

For a system containing n species, the Nernst–Planck–Poisson equation set comprises n time-dependent Nernst–Planck equations, as well as the Poisson equation, for a total of $n+1$ equations. Equally, the n concentrations c_i and the potential θ comprise $n+1$ unknown functions, such that since the problem contains as many independent equations as there are unknowns, we might hope to solve the simultaneous equations to determine the unknowns uniquely. However, these equations are not algebraic equations, but differential equations: that is, they involve at least one derivative of an unknown. In general, the solution of differential equations is more demanding than normal algebraic equations, since the derivatives must be integrated to find the unknown function. Here, some relevant definitions and techniques will be introduced.

If the unknowns of a differential equation are functions of only one variable, the derivatives are ordinary and so the equation is an ordinary differential equation (ODE). By comparison, if the unknowns are functions of more than one variable, the derivatives must be partial, and so the equation is a partial differential equation (PDE). The time-dependent Nernst–Planck–Poisson equation set is therefore a set of partial differential equations. If the equation set is taken at steady state where all $\partial c_i/\partial\tau = 0$, the unknowns c_i and θ are functions of the space coordinate only. In this case, the Nernst–Planck–Poisson equation set is a set of ordinary differential equations. In general,

ordinary differential equations are simpler to solve.

The order of a differential equation is defined as the degree of the highest derivative in the equation. Both the Nernst–Planck and Poisson equations are second order differential equations. Any second order ODE can be decomposed into two first order ODEs since:

$$\frac{d^2 f}{dx^2} + q(x) = 0 \tag{2.21}$$

can be written as

$$\begin{aligned} \frac{dg}{dx} + q &= 0 \\ g &= \frac{df}{dx} \end{aligned} \tag{2.22}$$

2.4 Boundary conditions

The general solution of an nth order ODE typically contains at least n undetermined coefficients. These coefficients may only be assigned by consideration of boundary conditions which constrain the unknown function $f(x)$ and/or its derivative $f'(x)$ at certain boundaries in the space x. Boundary conditions are classified into various types:

- A Dirichlet boundary is one where a function is constrained to take a constant value at a boundary, such as a fixed potential:

  $$f(x = x_k) = \lambda \tag{2.23}$$

  with λ a constant.

- A Neumann boundary is one where the first derivative of a function is constrained to take a constant value at a boundary, such as a fixed potential gradient (electric

field):

$$f'(x = x_k) = \lambda \tag{2.24}$$

- A Robin boundary is one where a linear combination of a function and its first derivative is constrained to take a constant value at a boundary:

$$f'(x = x_k) + \lambda_1 f(x = x_k) = \lambda_2 \tag{2.25}$$

- A Cauchy boundary is one where both a Dirichlet and Neumann boundary condition are required to apply at a single boundary.

All of the above will be encountered in this thesis. Other more complex boundary conditions also exist. As a general rule, each boundary condition can be used to determine one of the coefficients in the general solution of a differential equation, such that a unique solution exists for a differential equation together with a complete set of n boundary conditions. For a partial differential equation, boundary conditions are typically required in all variables.

2.5 Laplace transformation

2.5.1 Solution of linear ODEs

Linear ODEs with constant coefficients can generally be solved by a method known as Laplace transformation. The Laplace transform is defined as:

$$\bar{f}(s) = \mathcal{L}_{x\to s}\left\{f(x)\right\} = \int_0^\infty f(x)\,\mathrm{e}^{-sx}\,dx \tag{2.26}$$

The function $f(x)$ is transformed to a function $\bar{f}(s)$ in the s-domain (Laplace space). The function is therefore resolved into exponential components with differing rates of

decay. Laplace transformation may be suitably applied to any continuous function with a semi-infinite domain $0 \leq x < \infty$, and is useful for ordinary differential equations in such a function with a boundary condition at $x = 0$.

The utility of a Laplace transform is that it converts differential expressions into algebraic expressions, as shown by evaluating the Laplace transform of a derivative using integration by parts:

$$\begin{aligned} \mathcal{L}_{x\to s}\left\{\frac{df}{dx}\right\} &= \int_0^\infty \frac{df}{dx}\,\mathrm{e}^{-sx}\,dx \\ &= \left[f(x)\,\mathrm{e}^{-sx}\right]_0^\infty + s\int_0^\infty f(x)\,\mathrm{e}^{-sx}\,dx \\ &= s\bar{f}(s) - f(0) \end{aligned} \tag{2.27}$$

The derivative in the real x-domain has been transformed into an algebraic expression in the Laplace s-domain. The algebraic equation associated with an ODE can then be solved in Laplace space, and the result is transformed back. The major difficulty with this technique tends to be the inverse transformation, since the formal definition of the inverse transform is a complex integral:

$$f(x) = \mathcal{L}^{-1}_{s\to x}\left\{\bar{f}(s)\right\} = \int_{a-i\cdot\infty}^{a+i\cdot\infty} \bar{f}(s)\,\mathrm{e}^{+sx}\,ds \tag{2.28}$$

where a is a real number chosen such that singularities in $\bar{f}(s)$ are confined to $\mathrm{Re}(s) < a$. Typically the evaluation of this integral is achieved either by contour integration, or the inverse transform is assessed by consulting standard results for the forward transform. Numerical techniques also exist to evaluate $\mathcal{L}^{-1}$ approximately.[3]

2.5.2 Solution of linear PDEs

Given that a Laplace transform is able to transform an ODE into an algebraic equation, the method can also be used to transform a PDE into an ODE, which can then be solved more easily. This follows since for a function $f(x,t)$:

$$\begin{aligned}\mathcal{L}_{t\to s}\left\{\frac{\partial f}{\partial t}\right\} &= \int_0^\infty \frac{\partial f}{\partial t}\,\mathrm{e}^{-st}\,dt \\ &= \left[f(x,t)\,\mathrm{e}^{-st}\right]_0^\infty + s\int_0^\infty f(x,t)\,\mathrm{e}^{-st}\,dt \\ &= s\bar{f}(x,s) - f(x,t=0)\end{aligned} \tag{2.29}$$

whereas

$$\begin{aligned}\mathcal{L}_{t\to s}\left\{\frac{\partial f}{\partial x}\right\} &= \int_0^\infty \frac{\partial f}{\partial x}\,\mathrm{e}^{-st}\,dt \\ &= \int_0^\infty \frac{\partial}{\partial x}\left(f(x,t)\,\mathrm{e}^{-st}\right)\,dt \\ &= \frac{\partial}{\partial x}\int_0^\infty f(x,t)\,\mathrm{e}^{-st}\,dt \\ &= \frac{\partial \bar{f}}{\partial x}\end{aligned} \tag{2.30}$$

Hence a Laplace transform in the variable t will reduce partial derivatives in t to algebraic expressions, without affecting partial derivatives in any other variable. A partial differential equation in x and t is then reduced to an ordinary differential equation in x alone, which can be solved for $\bar{f}(x,s)$; then, inversion of the transform recovers $f(x,t)$. The variable x is treated as a constant with respect to Laplace transformation and its inverse, since the domain of integration is independent of x.

2.5.3 Laplace convolution

A useful theorem involving Laplace transformation is the convolution theorem, which states that:

$$\mathcal{L}^{-1}_{s\to t}\left\{\bar{f}(s)\cdot\bar{g}(s)\right\} = f(t) * g(t) \tag{2.31}$$

where the convolution operator $*$ is defined

$$f(t) * g(t) = \int_0^t f(t)g(\tau - t)\,d\tau = \int_0^t g(t)f(\tau - t)\,d\tau \tag{2.32}$$

The convolution of two signals in time is therefore understood as the product of their Laplace transforms.

The Dirac delta function $\delta(t)$ is an identity function under the convolution operator. That is:

$$x(t) * \delta(t) = x(t) \tag{2.33}$$

This relation is useful to describe a class of problems termed *linear time-invariant*,[4] examples of which will be encountered in this thesis. If an output function is related linearly to an input function, i.e. by expressing an arbitrary input function $x(t)$ as a linear combination of delta function inputs:

$$x(t) = \int_{-\infty}^{\infty} x(\tau)\,\delta(t - \tau)\,d\tau \tag{2.34}$$

then the output is a linear combination of a transfer function $h(t)$ which is the output response of the system to a delta function input:

$$y(t) = \int_{-\infty}^{\infty} x(\tau)h(\tau - t)\,d\tau = x(t) * h(t) \tag{2.35}$$

Therefore

$$\bar{y}(s) = \bar{x}(s)\,\bar{h}(s) \tag{2.36}$$

and so the transfer function in Laplace space is the ratio of the Laplace space output to input. This property allows the response to *any* input can be derived if the output to a single input is known.

2.6 Conclusion

Unfortunately, even with the above mathematical techniques for approaching differential equations, the Nernst–Planck–Poisson equation set is frequently unsolvable by conventional mathematical methods. This is largely because it is non-linear and so the above integration and transform methods cannot be applied directly. The Nernst–Planck–Poisson equations can be linearised, but only subject to certain approximations, as will be discussed for various problems in this thesis. In more complex cases, the equation set must be solved by numerical methods using a computer, as will be discussed in the following chapter.

Bibliography

[1] G. Stephenson, *Mathematical Methods for Science Students*, Longmans, London, 1961.

[2] D. G. Duffy, *Transform Methods for Solving Partial Differential Equations*, Chapman & Hall/CRC, Boca Raton, Florida, 2004.

[3] W. T. Weeks, *J. ACM*, 1966, **13**, 419–429.

[4] M. Schetzen, *Linear Time-Invariant Systems*, IEEE Press, Piscataway, New Jersey, 2003.

Chapter 3

Numerical methods

This chapter will set out the required methods for solving differential equations numerically. The bulk of the results presented in this thesis are determined using the methods discussed here.

3.1 The method of finite differences

Since a digital computer is unable to treat a continuous function exactly, numerical methods depend on approximating differential equations to large sets of algebraic equations, which can be solved by the conventional computational methods described below. The discretisation of a derivative by pointwise approximation to an associated algebraic expression is termed the finite difference method.

Consider the Taylor series of a function close to some point $x = x_0$:

$$f(x_0 + \Delta x) = f(x_0) + f'(x_0)\,\Delta x + f''(x_0)\,\frac{(\Delta x)^2}{2} + ... \tag{3.1}$$

in which f' and f'' represent the first and second derivatives of $f(x)$ with respect to x.

Rearranging:

$$f'(x_0) = \frac{f(x_0 + \Delta x) - f(x_0)}{\Delta x} + f''(x_0)\frac{\Delta x}{2} + ... \tag{3.2}$$

Therefore, the approximation

$$f'(x_0) \approx \frac{f(x_0 + \Delta x) - f(x_0)}{\Delta x} \tag{3.3}$$

has an error proportional to Δx to leading order, which is termed an $O(\Delta x)$ error*. As $\Delta x \to 0$, the approximation becomes exact. Therefore, a derivative may be accurately approximated by the linear combination of function values at two points, so long as the separation of the points is small. As $\Delta x \to 0$, the result obtained from the approximate method is said to *converge* towards the exact result.

The approximation above is described as *forward differencing*, since the derivative a point is evaluated with respect to the function value at that point and the next point. A related approximation is *backward differencing*, which has the same error:

$$f'(x_0) = \frac{f(x_0) - f(x_0 - \Delta x)}{\Delta x} + O(\Delta x) \tag{3.4}$$

A more accurate approximation can be achieved by *central differencing*:

$$f'(x_0) = \frac{f(x_0 + \Delta x) - f(x_0 - \Delta x)}{2\Delta x} + O\Big((\Delta x)^2\Big) \tag{3.5}$$

in which the two Δx errors from the forward and backward components cancel. However, this approximation may be numerically awkward because the approximate expression for the derivative at x_0 becomes independent of the function value at the same point x_0.

*In algorithm analysis, the 'big-oh' $O(f(N))$ notation means "to leading order". That is, as the size of a problem $N \to \infty$, the number of steps tends to a constant multiplied by the function $f(N)$. The same notation as used here means that as $\Delta x \to 0$, the error becomes exactly proportional to Δx, since terms in higher powers of Δx will decrease more rapidly.

A second derivative can be approximated by considering Taylor series at two neighbouring points:

$$f(x_0 + \Delta x) = f(x_0) + f'(x_0)\,\Delta x + f''(x_0)\,\frac{(\Delta x)^2}{2} + ... \tag{3.6}$$

$$f(x_0 - \Delta x) = f(x_0) - f'(x_0)\,\Delta x + f''(x_0)\,\frac{(\Delta x)^2}{2} - ... \tag{3.7}$$

Adding these together and re-arranging, and noting that all the terms in odd-order derivatives cancel:

$$f''(x_0) = \frac{f(x_0 + \Delta x) - 2f(x_0) + f(x_0 - \Delta x)}{(\Delta x)^2} + O((\Delta x)^2) \tag{3.8}$$

Having established that continuous derivatives can be approximated to a certain tolerance by finite linear combinations of function values, the numerical method for solving ordinary differential equations for an unknown $f(x)$ on a finite domain requires a grid of n points x_i, where $x_{i+1} = x_i + \Delta x$. At each point x_i, the differential equation is approximated by finite differencing to an algebraic equation. At the boundaries, the boundary conditions are also discretised where necessary. This yields a total of n simultaneous algebraic equations which can be solved computationally for the n unknowns $f(x_i)$, thus approximately determining the unknown function $f(x)$.

Other techniques exist for solving ordinary differential equations numerically, such as finite element methods or Runge-Kutta integration.[1] However, the finite difference method is best suited for solving complex equations in simple geometries, exactly as required for the Nernst–Planck–Poisson equation set in the one-dimensional geometries discussed in Chapter 2. Hence, the finite difference method is applied for the vast majority of the work in this thesis.

3.2 Expanding grid

In fact, the gridding points x_i do not need to be equally spaced. To ensure convergence of the approximations for the derivatives, a high density of points is required where $f(x)$ is non-linear, i.e. where its higher derivatives are non-zero and so higher order terms contribute to the Taylor series. The total number of points n can be reduced by introducing an expanding grid with high grid density for the domain of x where $f(x)$ is non-linear, but sparse grid density for the domain where $f(x)$ is approximately linear. This accelerates the numerical solution by decreasing the size of the algebraic equation set arising from finite differencing.

The modified expressions for the finite difference approximations for an expanding grid are:[2]

$$f'(x_i) \approx \frac{f_{i+1} - f_{i-1}}{\Delta x_+ + \Delta x_-} \tag{3.9}$$

$$f''(x_i) \approx \frac{\frac{f_{i+1}-f_i}{\Delta x_+} - \frac{f_i - f_{i-1}}{\Delta x_-}}{\frac{1}{2}(\Delta x_+ + \Delta x_-)} \tag{3.10}$$

where

$$\Delta x_+ = x_{i+1} - x_i \tag{3.11}$$

$$\Delta x_- = x_i - x_{i-1} \tag{3.12}$$

These approximations are, in general, accurate to $O(\Delta x)$, which is sufficient to allow for convergence of the numerical solution by decreasing grid spacing. The reduced order of accuracy is more than overcome by the efficient minimisation of Δx in regions where the error magnitudes from $f''(x)$ and higher derivatives are particularly large, while still allowing Δx to become large in regions where these higher derivatives tend

to zero. Hence, the overall error terms are made negligible across the whole simulation space, without requiring an excess of grid points.

The most easily customised expanding grid was found to combine constant grid point spacing close to a boundary $X = X_0$ where $f''(X)$ is large with linearly expanding grid point spacing outside of a point $X = X_0 + X_s$. The grid is defined:

$$X_0 \leq X \leq X_s \qquad X_{i+1} = X_i + \gamma_X X_s \tag{3.13}$$

$$X > X_s \qquad X_{i+1} = X_i + \gamma_X X_i$$

where γ_X is a tuneable scaling parameter. In radial space, a similar grid was applied with parameters γ_R and R_s.

The definition of the linear spacing in the domain $X \leq X_s$ ensures that grid spacing does not change abruptly either side of X_s. This has the consequence that reducing the value of either of the parameters γ_X and X_s will increase the grid density and hence improve convergence by increasing the accuracy of the finite difference approximation. However, decreasing γ_X increases grid density consistently across the whole space, whereas decreasing X_s increases grid point density close to the boundary $X = X_0$ without affecting grid point density distant from this boundary.

For all studies, a convergence study was performed for both parameters, to ensure that an appropriate compromise was reached between simulation accuracy and simulation runtime. In general, the required solution tolerance was $< 0.1\%$ error compared to the exact solution as $\gamma_X \to 0$ and $X_s \to 0$, as assessed from key output parameters. In this way, optimal maximum values of γ_X and X_s were determined, such that simulation runtime could be minimised without impairing accuracy.

3.3 Partial differential equations

In solving the time-dependent NPP equation set, it is necessary to discretise the time derivative as well as the space derivatives. The time domain $\tau > 0$ is then discretised using a certain number of time steps, with the initial conditions being applied at the first time step. Denoting $\mathbf{f}_k$ as the vector of the variable f across all n space points at the time step k, then a forward finite difference in time gives:

$$\frac{\mathbf{f}_{k+1} - \mathbf{f}_k}{\Delta\tau} = g(\mathbf{f}_k) \tag{3.14}$$

so

$$\mathbf{f}_{k+1} = \mathbf{f}_k + \Delta\tau \cdot g(\mathbf{f}_k) \tag{3.15}$$

in which case, since $\mathbf{f}_0$ is known from the initial conditions specified for the problem, $\mathbf{f}_{k+1}$ can be calculated directly for all subsequent timesteps by iteration of the equation above, since $\mathbf{f}_k$ is known at each time step. This is termed the explicit method. The explicit method is extremely rapid since determining the evolution of $\mathbf{f}$ at each time step only requires the evaluation of the function $g(\mathbf{f}_k)$. However, the explicit method is also numerically unstable, meaning that errors propagate and the time-dependent behaviour of $\mathbf{f}$ becomes oscillatory unless the time step $\Delta\tau$ is extremely short.[1,2]

An alternative approach assumes backward differencing with respect to the time step $k + 1$:

$$\frac{\mathbf{f}_{k+1} - \mathbf{f}_k}{\Delta\tau} = g(\mathbf{f}_{k+1}) \tag{3.16}$$

so

$$\mathbf{f}_{k+1} = \mathbf{f}_k + \Delta\tau \cdot g(\mathbf{f}_{k+1}) \tag{3.17}$$

The right-hand side of this equation is now unknown and so this represents a set of simultaneous equations which must be solved for the variables at the subsequent time step. This is termed the implicit method: it is numerically stable, but much slower because $\mathbf{f}_{k+1}$ cannot be calculated by function evaluation but rather must be determined by solving a full equation set.[1,2] Nonetheless, the implicit method allows much larger $\Delta\tau$ values to be chosen as a consequence of its superior stability, so it is preferred. Implicit methods have been standard for numerical solutions of the Nernst–Planck–Poisson equation set since the pioneering work of Brumleve and Buck,[3] and the implicit method is used for all time-dependent numerical simulation in this thesis.

As with space discretisation, $\Delta\tau$ must be minimised to ensure that the finite differencing approximation in time is converged. However, shorter time steps also increases simulation runtime, so an irregular time grid provides an advantageous compromise for some problems. Typically, these are problems where the derivatives in time are very large immediately following $\tau = 0$, such that the rate of change of the variables is especially fast at short time. Then, a linearly expanding time grid is used, parameterised by an expansion rate γ_τ and an expansion onset time τ_s:

$$\begin{aligned} 0 \leq \tau \leq \tau_\mathrm{s} \qquad & \tau_{i+1} = \tau_i + \gamma_\tau \, \tau_\mathrm{s} \\ \tau > \tau_\mathrm{s} \qquad & \tau_{i+1} = \tau_i + \gamma_\tau \, \tau_i \end{aligned} \tag{3.18}$$

For other problems, where there is negligible perturbation of the initial conditions at short time, a regularly spaced time grid is used.

Having established that both time-independent and time-dependent finite difference problems generate large sets of algebraic simultaneous equations to be solved, methods for solving these equations will now be discussed.

3.4 Solving linear simultaneous equations

Each equation in a set of n linear simultaneous equations in n variables has the form:

$$\sum_{j=0}^{n-1} a_{ij}\, x_j = z_i \tag{3.19}$$

with all a_{ij} and z_i constant, and x_j variable. The entire set can be expressed in matrix form as:

$$\mathbf{A}\,\mathbf{x} = \mathbf{z} \tag{3.20}$$

where $\mathbf{x}$ is the vector of n unknowns $\{x_0, x_1, ..., x_{n-1}\}$, $\mathbf{z}$ is a vector of n known constants $\{z_0, z_1, ..., z_{n-1}\}$, and the matrix $\mathbf{A}$ consists of n^2 matrix elements a_{ij}, where a_{ij} is the coefficient of the unknown x_j in the ith linear equation.

Such a matrix equation can be solved by an arithmetical process known as Gaussian elimination.[1] This algorithm requires $O(n^3)$ operations, and so it is generally slow for large n and heavily penalises runtime for an increased number of space steps. However, a more efficient alternative is available, which takes advantage of the distribution of zeroes in the matrix $\mathbf{A}$. Since the equation arising from finite differencing of an ODE for one particular space point has non-zero coefficients only with respect to variables at the same space point or neighbouring space points, the matrix is *diagonal*: that is, $a_{ij} = 0$ for $|i - j| > q$, in which q is a constant depending on the number of unknown functions. The number of non-zero diagonals is $m = 2q + 1$. A diagonal matrix is indicated at Figure 3.1.

As a first example, consider a three-diagonal matrix equation, where $a_{ij} = 0$ for $|i - j| > 1$. Here, each of the i linear equations has only three non-zero terms: this is the case for the finite differencing of a linear ordinary differential equation in a

$$\begin{pmatrix} a_{q,0} & \cdots & a_{m-1,0} & 0 & 0 & 0 & \cdots \\ a_{q-1,1} & a_{q,1} & \cdots & a_{m-1,1} & 0 & 0 & \cdots \\ \vdots & \vdots & \vdots & \vdots & \vdots & \vdots & \vdots \\ \cdots & 0 & a_{0,j} & \cdots & a_{m-1,j} & 0 & \cdots \\ \vdots & \vdots & \vdots & \vdots & \vdots & \vdots & \vdots \\ \cdots & 0 & 0 & a_{0,n-2} & \cdots & a_{q,n-2} & a_{q+1,n-2} \\ \cdots & 0 & 0 & 0 & a_{0,n-1} & \cdots & a_{q,n-1} \end{pmatrix}$$

Figure 3.1: A diagonal matrix, showing the regular distribution of zeroes.

single variable, such as Fick's 2nd Law of Diffusion (Equation 1.36). An efficient $O(n)$ solution procedure for this particular case is given by the Thomas algorithm.[1] The Thomas algorithm is $O(n^2)$ times faster than Gaussian elimination, thus hugely improving the rate and scalability of the numerical solution.

The Thomas algorithm works by LU decomposition of the matrix $\mathbf{A}$ into lower and upper triangular matrices $\mathbf{L}$ and $\mathbf{U}$, where these matrices have entirely zero entries above and below the main diagonal, respectively. The triangular matrices give the following relations:

$$\mathbf{A}\,\mathbf{x} = \mathbf{L}\,\mathbf{U}\,\mathbf{x} = \mathbf{L}\,\mathbf{y} = \mathbf{z} \tag{3.21}$$

where

$$\mathbf{U}\,\mathbf{x} = \mathbf{y} \tag{3.22}$$

The algorithm is fast because the LU decomposition of an m-diagonal matrix can be achieved in $O(m^2 n)$ time. The solution for the unknown vectors $\mathbf{y}$ and $\mathbf{x}$ is trivial and requires $O(mn)$ time due to the special distribution of zeroes in the triangular matrices. So, if $m \ll n$, the overall process of solving the equations becomes $O(n)$. Even if the diagonality of $\mathbf{A}$ is increased because the problem has multiple continuous

differential equation variables, as in the Nernst–Planck–Poisson equation set, $m \leq 25$ for the systems considered in this thesis, whereas typically $10^3 < n < 10^6$.

A generic algorithm for the solution by LU decomposition of a matrix equation of size n and diagonality m was developed by the author and is reported in Appendix A. This algorithm was used for all matrix equations solved in the work making up this thesis.

3.5 Solving non-linear simultaneous equations

Although we have developed a method for solving linear simultaneous equations, the Nernst–Planck–Poisson equation set of interest in this thesis is non-linear. The simultaneous equations resulting from application of the finite difference method will then also be non-linear: that is, the equations cannot be written as linear combinations of the unknown variables. Therefore, the method in Section 3.4 for solving a set of linear simultaneous equations cannot be applied directly.

The standard method for solving a set of non-linear simultaneous equations is the iterative Newton–Raphson method.[1] This is a multidimensional elaboration of the Newton–Raphson method for solving a single non-linear equation, in which the equation is written in the form $f(x) = 0$, and the method finds the value of x for which this equation holds, i.e. the *root* of the equation.

Consider the Taylor series of $f(x)$ close to an initial guess x_0 for the root:

$$f(x) \approx f(x_0) + (x - x_0)f'(x_0) = 0 \tag{3.23}$$

Then

$$x \approx x_0 - \frac{f(x_0)}{f'(x_0)} \tag{3.24}$$

If the initial guess is suitable, a sequence of iterations of this type will converge to the root where $f(x) = 0$ exactly. Denoting each iteration of guess for the root as x_z, the algorithm is repeated iterations of:

$$x_{z+1} = x_z - \frac{f(x_z)}{f'(x_z)} \tag{3.25}$$

The convergence of these iterations to a root is dependent upon the smoothness and monotonicity of the function and the quality of the initial guess. If the initial guess is poor, it is possible that the Newton–Raphson method will not converge to a root and so the technique will fail. The success of the technique therefore often requires a suitably chosen function and an informed initial guess.

For a function of n variables x_0, x_1, ... x_{n-1}, written as a vector $\mathbf{x}$, the Newton–Raphson method can be applied using the partial derivative with respect to each variable:

$$f(\mathbf{x}) \approx f(\mathbf{x}_0) + \sum_n (x_n - x_{n,0}) \frac{\partial f(\mathbf{x}_0)}{\partial x_n} \tag{3.26}$$

so, defining $u_n = x_n - x_{n,0}$:

$$\sum_n u_n \frac{\partial f(\mathbf{x}_0)}{\partial x_n} = -f(\mathbf{x}_0) \tag{3.27}$$

Where there are n simultaneous equations associated with the n variables, this may be extended, such that for each function m:

$$\sum_n u_n \frac{\partial f_m(\mathbf{x}_0)}{\partial x_n} = -f_m(\mathbf{x}_0) \tag{3.28}$$

which may be expressed for the vectors $\mathbf{u}$ and $\mathbf{f}$ in the matrix form:

$$\mathbf{J}(\mathbf{x}_0)\,\mathbf{u} = -\mathbf{f}(\mathbf{x}_0) \tag{3.29}$$

where $\mathbf{J}$ is the $n \times n$ square matrix for which the element J_{mn} in the m-th row and n-th column is defined:

$$J_{mn} = \frac{\partial f_m}{\partial x_n} \tag{3.30}$$

and is termed the Jacobian matrix. For finite difference problems, the Jacobian will be diagonal since each algebraic equation only depends on the values of unknowns at a single grid point or its nearest neighbours, and so $J_{mn} = 0$ for $|m - n| > q$.

Then, to solve a set of non-linear equations, the set of linear equations represented by Equation 3.29 is solved by evaluating $\mathbf{J}$ and $\mathbf{f}$ for the current trial solution $\mathbf{x}$ to calculate $\mathbf{u}$. Then $\mathbf{x}$ is augmented by $\mathbf{u}$ and the process is repeated, until either all values u_i are less than a characteristic parameter ϵ, or all values u_i/f_i are less than ϵ. When these conditions are satisfied, $\mathbf{x}$ is converged to the required root to a given tolerance. The numerical work in this thesis used $\epsilon = 10^{-5}$.

The ability of the iterative Newton–Raphson method to converge to a solution is critically dependent on the quality of the initial guess, much more so than is true for the single variable Newton–Raphson method. In particular, due to the increased dimensionality of the problem, there may be a 'trade-off' between the convergence of the different constituting equations to their own closest root, causing the iteration to 'miss' the point in the n-dimensional function space where all functions simultaneously have roots.[1]

In the time-dependent case, this problem is easily mitigated because as $\Delta\tau \rightarrow 0$, the known values for the variables at one time step more closely resemble their

unknown values at the next time step. If $\Delta\tau$ is sufficiently small, convergence of the Newton–Raphson method is guaranteed by the negligible change of the system variables in the time $\Delta\tau$. By contrast, for a time-independent problem, an informed initial guess is required. The analytical and related methods used to determine a consistently convergent initial guess will be discussed on a case-by-case basis for the time-independent problems reported in this thesis.

3.6 Computational details

The application of these numerical methods was achieved by simulation programs written by the author, in the programming language C++ using the open source Bloodshed Dev-C++ software (v4, http://www.bloodshed.net/devcpp.html) as a development environment with an incorporated Windows compiler (mingw). An object-oriented design was adopted for the various programs to facilitate debugging and to allow for extensive code re-use when the supporting mathematical model or numerical method was changed, as well as providing generic input and output procedures.[4] Simulations were run on a Dell Precision T3400 desktop computer with an Intel Core2 Quad Q9550 2.83 GHz processor and 3.2 GB of RAM, under Windows XP Professional SP3. No simulations were parallelised and therefore runtimes reported in this thesis are for only one processor core.

3.7 Conclusion

The numerical solution of the Nernst–Planck–Poisson equation set in this thesis is achieved by successive simplifying approximations. First, finite differencing in space

and time converts the partial differential equations into the solution of a set of non-linear simultaneous algebraic equations for each timestep, according to the implicit method. The simultaneous equation set is solved by approximating the functional gradients around an initial guess as linear. The solution to the linear equation set is achieved by elimination and applied iteratively until convergence to the solution of the non-linear set is attained. Having established this solution method for the fundamental equations describing charge transport in electrolytic solutions, particular examples relevant to the dynamics of electrochemical systems may now be considered.

Bibliography

[1] W. H. Press, S. A. Teukolsky, W. T. Vetterling and B. P. Flannery, *Numerical Recipes. The Art of Scientific Computing.*, Cambridge University Press, Cambridge, 3rd edn., 2007.

[2] D. Britz, *Digital Simulation in Electrochemistry*, Springer-Verlag, Berlin, 3rd edn., 2005.

[3] T. R. Brumleve and R. P. Buck, *J. Electroanal. Chem.*, 1978, **90**, 1–31.

[4] N. A. Solter and S. J. Kleper, *Professional C++*, Wiley Publishing, Inc., Hoboken, New Jersey, 2005.

Chapter 4

Liquid junction potentials

A liquid junction is a boundary between two solutions where at least one ion is present in different concentrations either side of the boundary. The equilibration of a liquid junction involves charge transport which can be described by the Nernst–Planck–Poisson equation set, and a potential difference is observed across the junction, for which a new dynamic theory is developed in this chapter. This work has been published by the Journal of Physical Chemistry B,[1] and the critique of the electroneutrality approximation in this context has been published by the Journal of Solid State Electrochemistry.[2] Leon Freitag, a visiting undergraduate student to Pembroke College, Oxford, from Friedrich-Schiller-Universität Jena (Germany), performed the majority of the numerical simulation programming and data collection for this work.

4.1 Introduction

4.1.1 What is a liquid junction potential?

When a phase boundary is formed between two solutions with unequal concentrations of one species of ion – that is, when a liquid junction is formed – a concentration gradient is established across the boundary such that diffusion of that ion will occur. Except for certain special cases, such as where a cation and anion share a common concentration gradient and have equal diffusion coefficients, ionic diffusion leads to charge separation since different ions diffuse at different rates. This charge separation can be expressed as an electric field according to the Poisson equation (Equation 1.20), and hence from the Nernst–Planck equations, migration will also occur. The electric field can be measured as a potential difference (voltage) across the solution, which is termed the *liquid junction potential*.

Because opposite charges attract, the induced migration tends to oppose the initial relative rate of diffusion. An initially more rapidly diffusing cation is decelerated by its attraction to the excess of anions it has left behind, and *vice versa*. Therefore, initially faster ions are decelerated, and initially slower ions are accelerated.

Liquid junctions were classified into three types by Lingane:[3] Type 1 is a junction of two solutions with a common composition but different concentration; Type 2 is a junction of two solutions of different composition but common concentration; and Type 3 is all other liquid junctions. To avoid undue complexity, Type 3 junctions are not considered in this thesis, although the methodology set out in this chapter has been applied to the study of some Type 3 junctions since this work was published.[4] Figure 4.1 displays liquid junctions of Types 1 and 2.

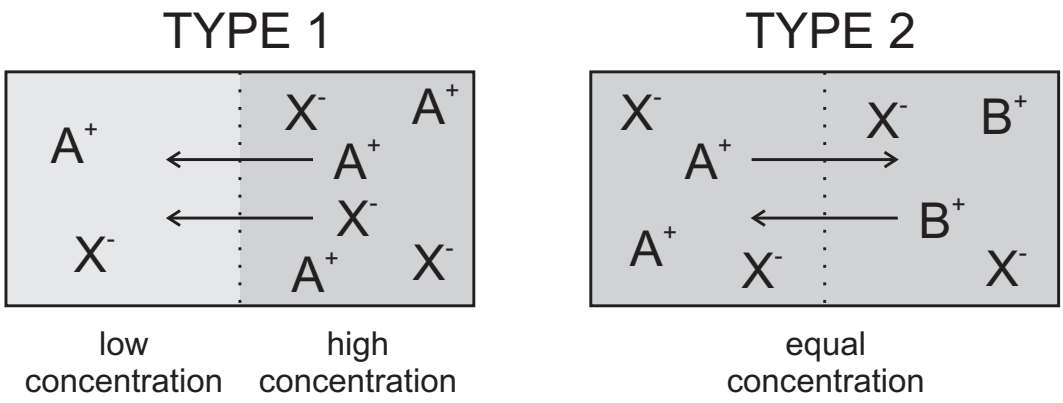

Figure 4.1: Lingane's Type 1 and Type 2 liquid junctions.

An exemplar Type 1 liquid junction is the boundary between two HCl (aq) solutions of different pH; an exemplar Type 2 liquid junction is the boundary between equimolar NaCl (aq) and KCl (aq) solutions.

4.1.2 Traditional theories of liquid junctions

In the traditional concept of a liquid junction, as developed more than one hundred years ago by Nernst and Planck,[5–7] the electric field will develop in time until the fluxes of the two species are equal; then, the discrepancy in their rates of diffusion, arising from unequal diffusion coefficients, is precisely balanced by their opposite migrational attraction. When transport of both ions is equally rapid, there is no net ionic current and so no further charge separation occurs across the junction. Under this condition, the potential difference across the space is constant.

Both Nernst and Planck employed the electroneutrality condition (Equation 1.24) in determining their results. For an electroneutral solution of the ions A^+ and X^-, such that $c_A = c_X = c$, which is also free of ionic current such that $J_A = J_X$:

$$D'_A \, (\nabla c + c \, \nabla \theta) = D'_X \, (\nabla c - c \, \nabla \theta) \tag{4.1}$$

Note that a linearly symmetric electroneutral solution must have constant ionic current

in order to remain electroneutral. On rearranging:

$$-\nabla\theta = \frac{D'_{\mathrm{A}} - D'_{\mathrm{X}}}{D'_{\mathrm{A}} + D'_{\mathrm{X}}} \nabla \ln c \tag{4.2}$$

which can be integrated for a hypothetical Type 1 liquid junction across an electroneutral solution (Equation 4.4, below) as was reported by both Nernst and Planck.[5,6]

Planck generalised his arguments in a subsequent paper by introducing the concept of a finite boundary layer, in which the fluxes of the constituent ions were assumed to rapidly attain a constant value, i.e. the ionic concentrations are at steady state.[7] This can only be true if the ionic concentrations are linear within the boundary layer, and so constant (bulk) concentrations must be assumed at the edges of the boundary layer. These arguments allow the derivation of a general transcendental equation for the liquid junction potential for any composition.

The culmination of the Planck model, in which activity effects are ignored and an electroneutral steady state within a confined boundary layer is assumed, was the Henderson equation[8] for the liquid junction potential, which in the dimensionless notation used in this thesis is written:

$$\Delta\theta_{\mathrm{LJP}} = \frac{\sum_i \mathrm{sgn}(z_i) D'_i \left(c^*_{i,\mathrm{R}} - c^*_{i,\mathrm{L}}\right)}{\sum_i |z_i| D'_i \left(c^*_{i,\mathrm{R}} - c^*_{i,\mathrm{L}}\right)} \ln\left(\frac{\sum_i |z_i| D'_i c^*_{i,\mathrm{L}}}{\sum_i |z_i| D'_i c^*_{i,\mathrm{R}}}\right) \tag{4.3}$$

where $\mathrm{sgn}(x)$ is the sign function and is $+1$ for positive numbers and -1 for negative numbers. The subscripts L and R denote the bulk conditions in the two phases left and right of the junction respectively.

For a Type 1 liquid junction with a monovalent electrolyte $\mathrm{A^+X^-}$ in unequal concentration either side of the junction, the Henderson equation reduces to:

$$\Delta\theta_{\mathrm{LJP}} = \frac{D'_{\mathrm{A}} - D'_{\mathrm{X}}}{D'_{\mathrm{A}} + D'_{\mathrm{X}}} \ln\left(\frac{c^*_{\mathrm{L}}}{c^*_{\mathrm{R}}}\right) \tag{4.4}$$

For a Type 2 liquid junction with equimolar monovalent electrolytes A^+X^- left of the junction and B^+X^- right of the junction, the Henderson equation reduces to:

$$\Delta\theta_{\mathrm{LJP}} = \ln\left(\frac{D'_{\mathrm{A}} + D'_{\mathrm{X}}}{D'_{\mathrm{B}} + D'_{\mathrm{X}}}\right) \tag{4.5}$$

Although these special cases were reported identically by Nernst and Planck,[5,6] the simple formula for the general case is due to Henderson.[8]

Although successful in yielding an expression for the liquid junction potential, the concepts of steady state, a confined boundary layer and the imposition of electroneutrality all immediately introduce difficulties to the discussion of the system, which will be critically assessed here.

4.2 Deficiencies of classical liquid junction models

4.2.1 The inherent paradox of electroneutrality

Internal inconsistencies due to the imposition of electroneutrality have been recognised historically. The first use of the electroneutrality approximation was by Nernst in 1889,[5] in his study of electromotive forces in electrolyte solutions. He introduced it without justification, stating:

> "In that within the solutions no free electricity [*sic*]* can persist (at least not in any quantity such that its total amount would be remotely comparable to the fixed + and – electricity on the ions), so the condition
>
> $$p'_1 + p'_2 + ... = p''_1 + p''_2 + ...$$
>
> must be fulfilled."

*The [*sic*] is used to indicate antiquated terminology while maintaining a faithful translation. "Free electricity" is taken to mean "free charge density" in a modern translation, but in the originals the word(s) "(freie) Elektrizität" are used consistently in place of "Ladung" or "Ladungsdichte".

- Walther Nernst, May 1889[†]

Planck then employed the electroneutrality approximation in order to find the steady-state potential difference across a liquid junction in which two solutions of different concentrations are left to freely diffuse into one another.[6] In the course of this work he highlighted its dangers:

> "The action of electrostatic forces was accounted for by Nernst, via the assumption that absolutely no free electricity [*sic*] may arise within the solution; hence these forces may indeed be ascertained. This assumption admittedly corresponds to the laws of electrostatics to a good approximation, and also suffices for the objective pursued by Nernst; but it would only be exactly accurate if the charges of the ions, as measured electrostatically, were infinitely large. As the ions indeed have very large, but nevertheless finite, electrostatic charges, it follows that before electrical forces can come into action, as a rule a finite and determinable amount of free electricity [*sic*] must have been established in the solution.
>
> - Max Planck, December 1889[‡]

On the grounds of the vanishing value of ϵ_0, however, Planck persuaded himself that the "free electricity" – that is, charge separation – is equally vanishing, or at least is dispersed on an experimentally negligible timescale, and hence electroneutrality is an acceptable approximation, which may be advocated for its utility in finding mathematical solutions to problems in the theory of electrolytic solutions. Planck was sufficiently confident in the approximation that he introduced it in his more general work on liquid junction potentials without any further caveat, merely stating it as fact established by his previous work.[7]

Planck was strictly correct in his criticism, however: despite its widespread use, the electroneutrality approximation suffers from a fundamental inherent paradox which

[†]Author's own translation from the original, pp. 133–134. The p_i' refer to osmotic pressures of cations and the p_i'' refer to osmotic pressures of anions, ignoring the solvent according to the van 't Hoff theory.[9] By "fixed electricity", Nernst presumably means that $\sum_i z_i c_i \ll \sum_i |z_i| c_i$.

[‡]Author's own translation from the original, p. 163.

is rarely acknowledged. In solving the Nernst–Planck equations, we are trying to determine the effect of the electric field, which describes Coulombic forces and hence only exists in the presence of a net charge separation. But to determine the electric field, we have made the approximation of zero charge separation – what, then, is the cause of the electric field? In effect, the electric field may take any value it pleases in order that electroneutrality is maintained. Coulombic attractions are hence arbitrarily strong, such that any charge separation is damped instantly by an arbitrary migration of opposite charge. The electric field is not constrained in any way to satisfy Maxwell's equations.

The implied inconsistency with Maxwell's equations and the associated paradox of electric fields in the absence of charge separation have been criticised as disadvantageous to the correct understanding of liquid junction potentials,[2,10] even though the electroneutrality approximation can be justified by dimensional analysis and yields a closed form expression for the liquid junction potential.

4.2.2 Fixed Dirichlet boundary

The Planck model arbitrarily applies constant concentration (Dirichlet) conditions at the two edges of the boundary layer. The concentration gradient is then discontinuous at these boundaries and therefore the Nernst–Planck equation does not hold: inside the boundary layer, both ions flow down a potential gradient, whereas outside the boundary layer, concentrations are constant and the electric field is zero, so there is no net ionic flux. In the recent study of Perram et al.,[10] the replenishment of material to constant concentration at a finitely positioned boundary was denounced as unphysical, since it is not consistent with the laws of conservation of mass, unless a convectional

Nernst layer is arbitrarily invoked. In free solution, a convection layer is not expected at a short timescale.

In fact, doubt has long been cast on the meaning of Planck's results: in 1930, Guggenheim wrote "The physical conditions corresponding to the Planck formula have not generally been understood".[11] He defined the Planck model as a 'constrained' liquid junction, as diffusion is limited by the finite boundaries, and he recognised the 'free' liquid junction, in which the diffuse layer may expand to infinity, as more physically realisable for a simple liquid-liquid contact in a cell. Consideration of Planck's original work would suggest that the finite boundary layer was invoked for reasons of mathematical necessity rather than physical insight[§].

The mathematical tools for dealing with free liquid junctions were developed by Hickman,[12] who argued that electroneutrality is the long time asymptote to a complete description of the behaviour, but the implications of his results for the dynamics of liquid junctions were not discussed in an electrochemical context. This work was followed up by Jackson who clearly described the long time behaviour and critically assessed the use of electroneutrality.[13] The theories of Hickman and Jackson will be discussed below in the context of simulation results.

[§]Planck (author's translation) – "[The integrable Nernst–Planck equation] is, however, clearly only applicable for a constant variation of the concentrations in space, and so at first sight will fail if it is applied to determine the potential difference between two different homogeneous solutions, since the condition that the derivatives in x are everywhere 0 fails at the contact surface. Nevertheless we can substitute another case instead, wherein the concentrations are constant, if instead of the boundary surface, we adopt a boundary layer of extremely small but nonetheless finite thickness..."[7]

4.3 Computational literature

4.3.1 Review of past work

Despite the feasibility of solving the Nernst–Planck–Poisson equation set, without approximation, using numerical methods, very few computational studies of the liquid junction have deviated from Planck's boundary layer description. Except for the discussion of some special cases where a tangible boundary does indeed limit diffusion, there is scant evidence in the literature that understanding has improved since Guggenheim's writing in 1930 – since the 1960s, the simulation of liquid junction potential formation has been studied extensively, but almost always with the imposition of finitely positioned boundary conditions. Numerical simulation work to 2009 is summarised in Table 4.1: the studies most distinct from the Planck model are those by Hafemann[14] and Bagg,[15–17] in which the computed grid of points was allowed to grow to avoid constrained diffusion, but in neither case were the results analysed in their physical context.

As discussed above, Perram et al. criticised electroneutrality and constant concentration boundary conditions as unphysical, but the alternative in their numerical simulation work invoked Neumann boundary conditions at finite boundaries, thus maintaining conservation of mass, but confining the study to a 'constrained' junction.[10] This study noted that a pseudo-steady state potential difference is maintained so long as bulk solution remains available, and that the characteristic and constant potential arising from the charge separation achieved at this pseudo-steady state is equivalent to that predicted by classical theory. Since the simulated liquid junction was constrained, however, all liquid junction potentials observed were necessarily transient and collapsed

Author	Year	Method	Boundary	E/N	Activity	Comments
Nernst[5]	1889	An. NP	Finite Dir.	Yes	No	
Planck[6,7]	1890	An. NP	Finite Dir.	Yes	No	
Henderson[8,18]	1907-08	An. Thermo.	Finite Dir.	Yes	No	
Goldman[19]	1943	An. NP	Finite Dir.	Yes	No	Finite membrane.
Hafemann[14]	1965	Exp. NPP	Expg. Dir.	No	Yes	
Hickman[12]	1970	An. NPP	Inf. Dir.	No	No	$t \to \infty$
Goldberg et al.[20]	1972	Exp. NPP	Finite Dir.	No	Yes	Onsager equations.
Jackson[13]	1974	An. NPP	Inf. Dir.	No	No	$t \to \infty$
Morf[21]	1977	An. NP	Finite Dir.	Yes	No	Mean mobilities.
Brumleve et al.[22,23]	1978-81	Imp. NPP	Finite Dir.	No	No	
Mafé et al.[24]	1986	Imp. NPP	Finite Dir.	No	No	
Bagg[15–17]	1990-92	NI	Expg. Dir.	No	Yes	
Horno et al.[25]	1992	Network NP	Finite Neu.	No	No	
Martuzans et al.[26]	1998	Imp. NPP	Finite Neu.	No	No	
Skryl[27]	2000	Imp. NPP	Finite Neu.	No	No	Hyperbolic diffusion.
Sokalski et al.[28,29]	2001-03	Imp. NPP	Finite Dir.	No	No	Membrane potentials.
Josserand et al.[30]	2003	2D FEM NP	Finite Neu.	Yes	No	Microchannel flow.
Park et al.[31]	2006	LB NPP	Finite Neu.	No	No	Microchannel flow.
Perram et al.[10]	2006	Imp. NPP	Finite Neu.	No	No	
Filipek et al.[32]	2009	Imp. NPP	Finite Neu.	No	No	Membrane potentials.
this work	2009	Imp. NPP	Quasi-inf. Dir.	No	No	

Table 4.1: Review of work concerned with analysis and simulation of liquid junction potentials. Abbreviations: E/N: electroneutrality approximation; An.: analytical; Exp.: explicit finite difference; Imp.: implicit finite difference; NI: numerical integration; FEM: finite element method; LB: lattice Boltzmann method; NP: Nernst-Planck; NPP: Nernst-Planck-Poisson; Thermo.: thermodynamic; Dir.: Dirichlet; Neu.: Neumann; Expg.: expanding; Inf.: infinite.

as the diffusion layer around the junction encountered the impermeable boundaries. In this case the system equilibrium of electroneutrality, constant c_i and $\theta = 0$ across all space could be attained in finite time, which is not true if the supply of bulk solution is unconstrained.

4.3.2 Scope of this work

The bulk solution either side of an experimental liquid junction in an electrochemical cell is typically extensive, but the dynamics of 'free' liquid junction formation, independent of the cell size and neglecting convection, are not yet well established. Here,

the dynamics of liquid junctions are determined, as a function of diffusion coefficients, bulk concentrations and other pertinent system variables. Neither a constrained system with finite boundaries nor electroneutrality shall be required as *a priori* simplifications. Where relevant, the Hickman–Jackson method is used for mathematical analysis.[12,13]

The principal aim of this work will be to demonstrate that the liquid junction potential is best understood as resulting from a *dynamic* junction of varying charge and size. Planck's assumption of a static boundary layer, made in order to invoke an integrable steady state expression for concentration, is superfluous: a time-independent liquid junction potential arises even for a continuously diffusing, non-steady-state system. In fact, the potential difference is shown to be a necessarily non-equilibrium property of the system.

4.4 Theoretical model

4.4.1 Geometry and variables

The theoretical model follows the general prescription of Chapters 2 and 3, but certain details particular to the liquid junction system must be introduced.

We consider a homogeneous solution either side of a planar junction, such that mass transport can be modelled in the linear coordinate X (Section 2.1.2). For a Type 1 liquid junction, only two monovalent ions A^+ and X^- are present, whereas for a Type 2 liquid junction, three monovalent ions A^+, B^+ and X^- are present. At the start of the simulation at $\tau = 0$, some imagined barrier at the junction is removed, allowing the ions to diffuse freely.

The space normalisation is set to the Debye length on the right-hand side of the

junction ($x^* = x_{\mathrm{D,R}}$), to simplify the Poisson equation (Equation 2.18) as much as possible. Concentration is normalised to the concentration of X^- on the right-hand side of the junction ($C^*_{\mathrm{X,R}}$) and time is normalised to a reference diffusion coefficient D_{X}, since the species X^- is present at non-zero concentration for all solutions in all liquid junction types. Then, for i = A, B or X, the Nernst–Planck–Poisson equation set is:

$$\frac{\partial^2 c_i}{\partial X^2} + z_i \frac{\partial}{\partial X}\left(c_i \frac{\partial \theta}{\partial X}\right) - \frac{1}{D'_i}\frac{\partial c_i}{\partial \tau} = 0 \tag{4.6}$$

$$\frac{\partial^2 \theta}{\partial X^2} + \frac{1}{2}\sum_i z_i c_i = 0 \tag{4.7}$$

where D'_i is equally normalised to D_{X}.

4.4.2 Boundary conditions

The space coordinate is centred at the initial junction position of $X = 0$ and expands to a pseudo-infinite boundary. The outer boundaries are positioned such that they will vastly exceed the outer edge of the diffusion layer throughout the simulation time. The maximum value of $|X|$ used in the simulation, $X_{\max}$, is therefore defined as $6\sqrt{D'_{\max} \cdot \tau_{\max}}$, where $D'_{\max}$ is the largest normalised diffusion coefficent of any species, and $\tau_{\max}$ is the maximum τ value for the simulation, given as an input parameter.

Since from normalisation of Equation 1.37 the mean extent of the diffusion layer in normalised variables is $\sqrt{2D'_{\max}\tau}$, it can be shown that the relative perturbation of concentration by diffusion at a distance $6\sqrt{D'_{\max}\tau}$ from the initial position of a concentration gradient is less than 10^{-6}. Therefore, the problem of a free liquid junction with effectively limitless bulk solution can be considered using only a finite simulation space, without a transformation of the space coordinate, as whatever $\tau_{\max}$ is chosen,

the simulation space is sufficiently large to ensure that no flux or electric field will arise outside the boundaries of the space. If sufficiently large, the exact boundary position does not affect the evolution of the system.

At the outer boundaries, the concentrations of the ions at the boundaries are set to be constant and equal to their bulk values (Dirichlet conditions), i.e. for all $\tau > 0$:

$$X = +X_{\max} \qquad c_i = c_{i,\mathrm{R}}^* \tag{4.8}$$

$$X = -X_{\max} \qquad c_i = c_{i,\mathrm{L}}^*$$

As there is never exchange of material at the boundaries, and the system is initially electroneutral, the simulation space contains zero enclosed charge at all times. Therefore, the electric field is zero at the outer boundaries according to Gauss's Law (Equation 1.16), so that for all $\tau > 0$:

$$X = \pm X_{\max} \qquad \frac{\partial \theta}{\partial X} = 0 \tag{4.9}$$

It follows that the liquid junction potential can be calculated as

$$\Delta\theta_{\mathrm{LJP}} = \theta(+X_{\max}) - \theta(-X_{\max}) \tag{4.10}$$

At $\tau = 0$, the concentration profile of each ion is defined by a step function:

$$X > 0 \qquad c_i = c_{i,\mathrm{R}}^* \tag{4.11}$$

$$X = 0 \qquad c_i = \frac{c_{i,\mathrm{R}}^* + c_{i,\mathrm{L}}^*}{2}$$

$$X < 0 \qquad c_i = c_{i,\mathrm{L}}^*$$

The particular values of $c_{i,\mathrm{L/R}}^*$ depend on the liquid junction type and are given in Table 4.2, in which c_{L}^* is set as an input parameter.

Species	$c^*_{i,\mathrm{L}}$	$c^*_{i,\mathrm{R}}$
A	c^*_{L}	1
B	0	0
X	c^*_{L}	1

(a) Type 1.

Species	$c^*_{i,\mathrm{L}}$	$c^*_{i,\mathrm{R}}$
A	1	0
B	0	1
X	1	1

(b) Type 2.

Table 4.2: Boundary concentrations for liquid junctions of: a) Type 1; b) Type 2.

4.4.3 Gridding and computation

The simulation space is divided into $2n + 1$ points, with the grid expanding outwards in both directions from $X = 0$ according to the definitions in Section 3.2. The grid is symmetric about the junction centre, with dense regular grid spacing close to the junction, where concentration gradients will initially be extremely large, and sparse grid spacing for efficiency close to the bulk boundaries, where the solution remains unperturbed throughout the simulation. Since the initial conditions are not equilibrated, the system is rapidly perturbed at $\tau > 0$. Therefore the time grid is initially dense, and expands according to the definitions in Section 3.3.

A convergence study was performed, using $\Delta\theta_{\mathrm{LJP}}$ as a diagnostic variable, across several orders of magnitude in τ. The optimal parameters, giving $< 0.2\%$ error with respect to a fully converged parameter set, were: $5 \times 10^{-4} \leq \gamma_{\mathrm{X}} \leq 10^{-3}$, $X_{\mathrm{s}} = 10^{-6}$, $\gamma_\tau = 10^{-4}$ and $\tau_{\mathrm{s}} = 10^{-2}$.

The first and second derivatives are centrally differenced and the time derivative is differenced according to the implicit method. The iterative Newton–Raphson method is then applied at each timestep as normal; with the above gridding parameters, this was found to converge unconditionally, within the range of liquid junction systems simulated. With three variables (Type 1), the Jacobian matrix is 9-diagonal; with

four variables (Type 2), the Jacobian matrix is 13-diagonal. The Type 2 simulations are therefore almost three times slower due to the increased diagonality as well as the increased number of variables.

Typical runtimes were 3–5 h for a Type 1 liquid junction simulation to $\tau_{\max} = 10^3$, due to the high convergence demands of the system.

4.5 Type 1 liquid junction potentials: results

4.5.1 Simulated limiting potentials

Simulated liquid junction potentials for a Type 1 system were achieved by running a dynamic simulation until some τ where the potential is approximately constant, as assessed by some time where:

$$\frac{\Delta\theta_{\mathrm{LJP}}(\tau/2)}{\Delta\theta_{\mathrm{LJP}}(\tau)} \geq 0.998 \tag{4.12}$$

i.e. the potential difference between the two phases has reached an approximately constant value. Type 1 liquid junctions were simulated for $D'_{\mathrm{A}} = 0.4$, 0.6, 0.8, 0.9, as well as the special case of HCl|KCl, where $D'_{\mathrm{A}} \approx 4.582$ (at infinite dilution in water, 298 K).[33] The following concentration ratios were considered: $\log_{10} c^*_{\mathrm{L}} = -0.1$, -0.5, -1, -1.5 and -2.

These simulated potentials were compared with the classical Henderson equation, and strong agreement ($< 0.25\%$) was observed in all cases (Figure 4.2).

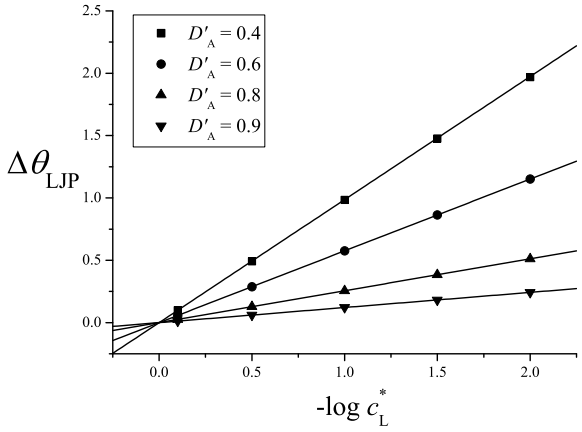

Figure 4.2: Comparison of simulated liquid junction potentials (symbols) at pseudo-steady state and the theoretical values given by the Henderson equation (lines), for a Type 1 system with varying D'_A and c^*_L.

4.5.2 Observed dynamics of liquid junction evolution

The dynamics of liquid junction formation were investigated in detail for the junction between two solutions of HCl with respective concentrations of 1 mM and 10 mM ($c^*_L = 0.1$).

The potential difference, $\Delta\theta_{LJP}$, is plotted as a function of τ on a logarithmic scale to illustrate its evolution (Figure 4.3). The maximum electric field is also plotted, as assessed from the greatest magnitude of $\partial\theta/\partial X$ in the system. The maximum electric field is plotted in place of the electric field at $X = 0$, since the position where the maximum field occurs is not fixed to $X = 0$, but rather is found to move. The maximum electric field quantifies the degree of charge separation in the junction, according to Gauss's Law (Equation 1.16), and therefore is crucial to the discussion of the potential difference across the junction, as is discussed in more detail in Section 4.5.3 below.

Figure 4.3 demonstrates that immediately after $\tau = 0$, the potential difference increases proportionally to τ, and the maximum electric field increases proportionally to $\tau^{\frac{1}{2}}$. The electric field resulting from faster transport of H^+ than Cl^- achieves a

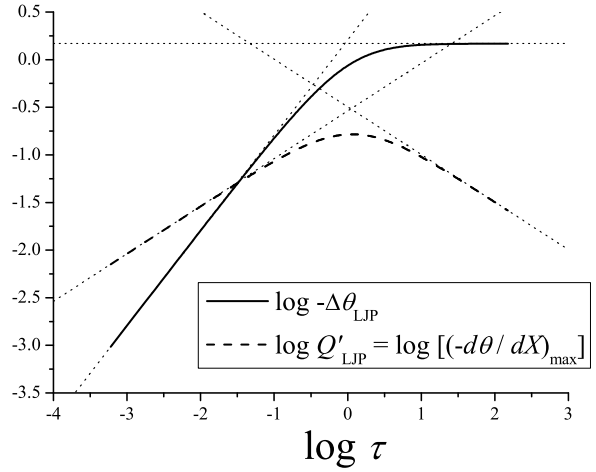

Figure 4.3: Dynamic evolution of the liquid junction potential ($\Delta\theta_{\mathrm{LJP}}$) and charge separation ($Q_{\mathrm{LJP}} = (-\partial\theta/\partial X)_{\mathrm{max}}$) for the Type 1 junction of 1 mM and 10 mM HCl (aq), plotted on a logarithmic scale in time. Asymptotic limits derived using a zero-feedback approach ($\tau \to 0$), and Boltzmann transform asymptotic analysis ($\tau \to \infty$) are plotted against the simulation data.

maximum at $\tau \approx 1$; in dimensional units, the maximum field is ≈ 1.3 MV m^{-1} at ≈ 5 ns after contact between the solutions. After the electric field reaches its critical limiting value, the potential difference approaches the Henderson limiting value at long time, but the electric field does *not* become constant, but rather decays in magnitude as $\tau^{-\frac{1}{2}}$.

Defining τ_{trs} as the characteristic transition time where the maximum field at the junction occurs, concentration and electric field profiles were recorded at a logarithmic range of times from $\tau = 10^{-2}\,\tau_{\mathrm{trs}}$ to $\tau = 10^{2}\,\tau_{\mathrm{trs}}$. These are shown at Figures 4.4–4.6. The evolution of the associated dimensionless electric field, $\xi \equiv \partial\theta/\partial X$, is also shown at Figure 4.7. It is evident that at longer times, the position of maximum field in the system is mobile and moves away from the initial position of the junction; additionally, the concentration profiles become increasingly asymmetric in this range.

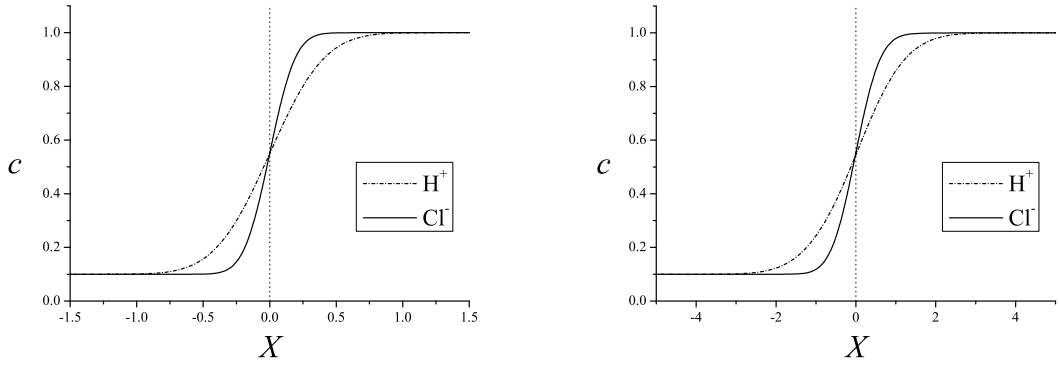

Figure 4.4: Concentration profiles for the HCl (aq) system at times (a) $\tau = 0.01\,\tau_{\mathrm{trs}}$ and (b) $\tau = 0.1\,\tau_{\mathrm{trs}}$ following junction formation. In the former, the junction is predominantly symmetric and resembles the independent diffusion-only case; in the latter, the point of isoconcentration has begun to move away from $X = 0$, although symmetry still dominates.

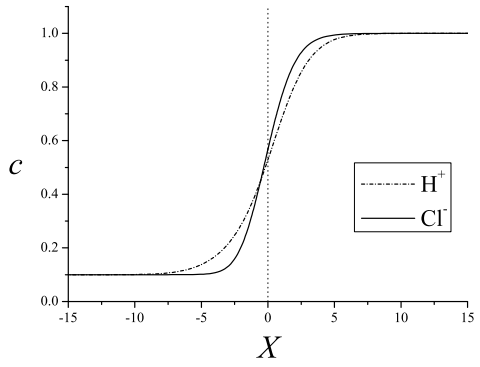

Figure 4.5: Concentration profiles for the HCl (aq) system at a time $\tau = \tau_{\mathrm{trs}}$ following junction formation. Here the field is maximal; the profiles show substantial asymmetry and the point of isoconcentration has moved perceptibly away from $X = 0$.

4.5.3 Capacitive analogy to describe the dynamics

The point of maximum electric field, X_{MaxField}, occurs where $\partial^2\theta/\partial X^2 = 0$, and hence, from Equation 4.7, where $c_{\mathrm{A}} = c_{\mathrm{X}}$. The integrated form of Gauss's Law states that the electric field at the surface of a charged volume is proportional to the charge within it (Equation 1.16), such that in normalised coordinates we can define:

$$\frac{\partial\theta}{\partial X} = -Q' \tag{4.13}$$

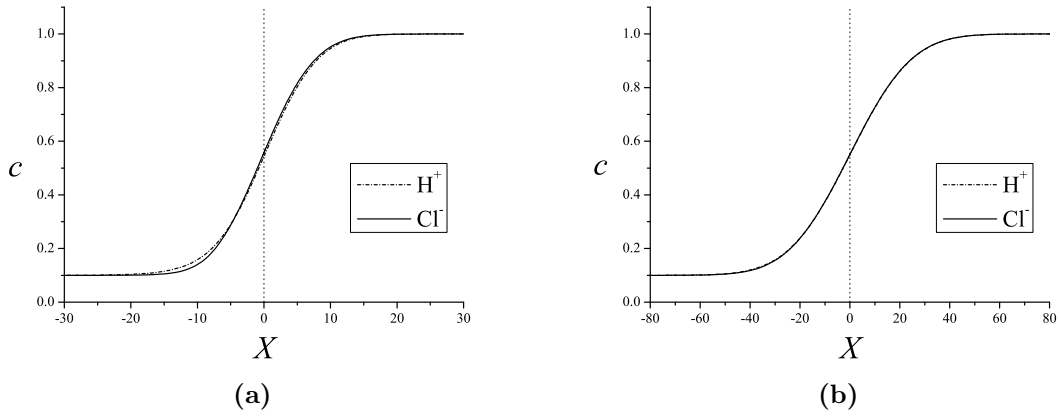

Figure 4.6: Concentration profile for the HCl (aq) system at times (a) $\tau = 10\,\tau_{\mathrm{trs}}$ and (b) $\tau = 100\,\tau_{\mathrm{trs}}$ following junction formation. In the former, electroneutrality is increasing in the system and symmetry is slowly being recovered, although the point of isoconcentration continues to recede from $X = 0$. In the latter, the overall profile appears electroneutral, but in fact a finite charge separation still exists which is maintaining a steady potential difference as the junction grows; close examination shows the point of isoconcentration to be diffusing towards negative X.

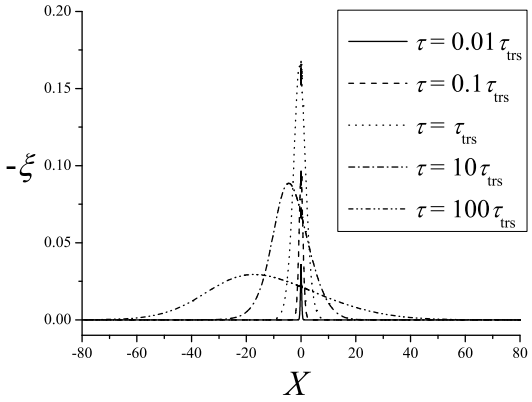

Figure 4.7: Evolution of the electric field profile for the HCl (aq) system at times $\tau = 0.01\,\tau_{\mathrm{trs}}$ to $\tau = 100\,\tau_{\mathrm{trs}}$ following junction formation. Increased asymmetry and the movement of X_{LJP}, the position of maximum field, away from the initial junction position are both evident. $\xi \equiv \partial\theta/\partial X$.

where

$$Q' = \frac{q'}{(2RT\epsilon_s\epsilon_0 C^*)^{\frac{1}{2}}} \tag{4.14}$$

and where q' is the enclosed charge per unit area.

The significance of the position of maximum field in the system may be recognised as follows. Considering that the overall domain $-X_{\max} < X < +X_{\max}$ is uncharged, the charge contained within $-X_{\max} < X < X_{\text{MaxField}}$ must be opposite to that in $X_{\text{MaxField}} < X < +X_{\max}$. Therefore, as shown in Figure 4.8, X_{MaxField} represents a plane of maximum overall charge separation, as the solution charge on one side of this point is equal in magnitude but opposite in sign to the solution charge on the other side.

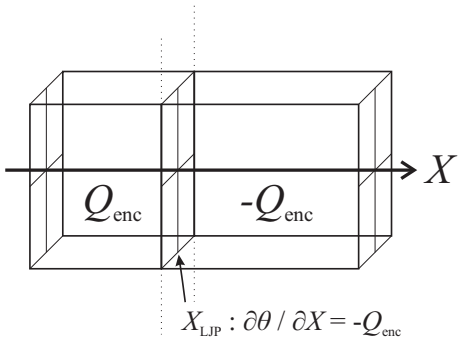

Figure 4.8: Representation of the liquid junction as two adjoining Gaussian boxes with equal and opposite charge.

X_{MaxField} may therefore be termed the *liquid junction position* and denoted X_{LJP}. In this case, the total degree of charge separation in the liquid junction is given:

$$Q'_{\text{LJP}} = -\left.\frac{\partial\theta}{\partial X}\right|_{\max} \tag{4.15}$$

The liquid junction may now be discussed by analogy to a parallel plate capacitor, where the 'plates' are represented by the volumes of solution either side of X_{LJP}, which have dimensionless charges $\pm(\partial\theta/\partial X)_{X=X_{\text{LJP}}}$. This 'capacitor' charges and discharges

spontaneously in time, with an associated potential difference from which the 'capacitance' of the system may be inferred. From Figure 4.3, it is clear that the 'capacitor' discharges to zero charge separation at infinite time without any alteration of its potential difference. At $\tau < \tau_{\text{trs}}$, the flux of H^+ across the junction is greater than the flux of Cl^- (charging), but at $\tau > \tau_{\text{trs}}$, these fluxes are *not* equal as supposed in the Planck model, but rather the flux of Cl^- is now greater than that of H^+ (discharging).

The simulated motion of this junction position, X_{LJP} is plotted logarithmically against time at Figure 4.9, which shows that in the short time limit, it moves from its initial position as $\tau^{\frac{3}{2}}$, and at long time as $\tau^{\frac{1}{2}}$.

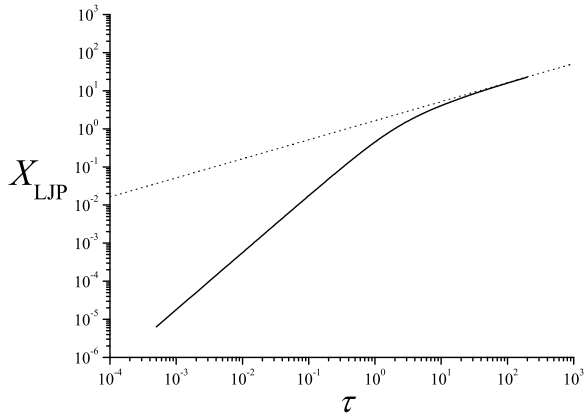

Figure 4.9: Evolution of the position of the liquid junction, X_{LJP}, for the HCl system, together with the long time behaviour predicted by asymptotic analysis.

4.5.4 The liquid junction spatial extent

The overall spatial extent of the liquid junction was also evaluated from the simulation data. The junction spatial extent, ΔX_θ, is defined as:

$$\Delta X_\theta = X\left(\theta = \frac{99}{100}\Delta\theta_{\text{LJP}}\right) - X\left(\theta = \frac{1}{100}\Delta\theta_{\text{LJP}}\right) \tag{4.16}$$

This is an effective measure of the range of non-zero electric field, and so of the range over which there is charge separation and the electroneutrality condition is not obeyed. ΔX_θ is plotted on a logarithmic scale against τ at Figure 4.10, which shows that the junction initially grows as $\tau^{\frac{1}{2}}$; its growth is then slightly perturbed around the time when the field is maximum, before again approaching a $\tau^{\frac{1}{2}}$ asymptote as $\tau \to \infty$.

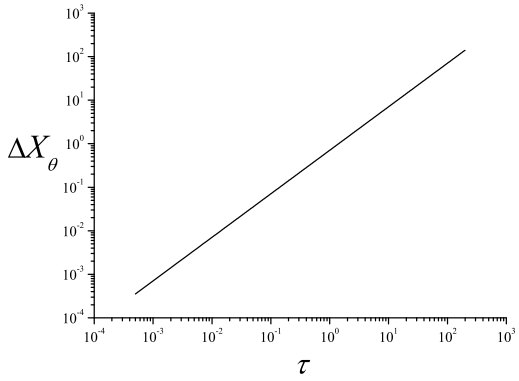

Figure 4.10: The junction spatial extent ΔX_θ as a function of τ on a logarithmic scale, for the HCl system. The junction expands as $\tau^{\frac{1}{2}}$ at both short and long times.

4.5.5 Asymptotic analysis at $\tau \to 0$

The $\tau \to 0$ limiting behaviour of the Type 1 liquid junction may be quantified by means of asymptotic analysis. Because charge separation is negligible at short time, $\tau \to 0$ behaviour is dominated by diffusion. The migrational flux can be approximated to zero and the electric field is then treated as arising directly from diffusion-only mass transport, ignoring migrational feedback.

The solution of the diffusion equation from the initial condition of a step function concentration profile is easily obtained by either Laplace transformation or Boltzmann analysis, and is well known.[34] If the initial condition at $\tau = 0$ is:

$$c_i(X, 0) = \alpha + \beta \operatorname{sgn}(X) \tag{4.17}$$

then solving Fick's 2nd Law yields for $\tau > 0$:

$$c_i(X,\tau) = \alpha + \beta \operatorname{erf}\left(\frac{X}{2\sqrt{D'_i\tau}}\right) \tag{4.18}$$

where $\operatorname{erf}(x)$ is the error function. For consistency with our generic Type 1 junction, the constants α and β are:

$$\begin{aligned}\alpha &= \frac{1+c^*_{\mathrm{L}}}{2} \\ \beta &= \frac{1-c^*_{\mathrm{L}}}{2}\end{aligned} \tag{4.19}$$

Substitution into the Poisson equation yields:

$$\begin{aligned}\frac{\partial^2\theta}{\partial X^2} &= \frac{1}{2}\left(c_{\mathrm{X}} - c_{\mathrm{A}}\right) \\ &= \frac{\beta}{2}\left(\operatorname{erf}\left(\frac{X}{2\sqrt{D'_{\mathrm{X}}\tau}}\right) - \operatorname{erf}\left(\frac{X}{2\sqrt{D'_{\mathrm{A}}\tau}}\right)\right)\end{aligned} \tag{4.20}$$

Integrating from the zero-field boundary at $X = -\infty$ into solution yields:

$$\begin{aligned}\frac{\partial\theta}{\partial X} &= \frac{\beta}{2}\int_{-\infty}^{X}\left(\operatorname{erf}\left(\frac{X'}{2\sqrt{D'_{\mathrm{X}}\tau}}\right) - \operatorname{erf}\left(\frac{X'}{2\sqrt{D'_{\mathrm{A}}\tau}}\right)\right)dX' \\ &= \frac{\beta}{2}\left(X\left(\operatorname{erf}\left(\frac{X}{p}\right) - \operatorname{erf}\left(\frac{X}{q}\right)\right) + \frac{1}{\sqrt{\pi}}\left(p\,\mathrm{e}^{-\frac{X^2}{p^2}} - q\,\mathrm{e}^{-\frac{X^2}{q^2}}\right)\right)\end{aligned} \tag{4.21}$$

where $p = 2\sqrt{D'_{\mathrm{X}}\tau}$ and $q = 2\sqrt{D'_{\mathrm{A}}\tau}$. The integration is accomplished quite easily but care must be taken with limits: mathematical details were reported in the Supporting Information to reference [1].

The liquid junction potential is recovered by the further integration of the field between the two zero-field boundaries:

$$\begin{aligned}\Delta\theta_{\mathrm{LJP}} &= \frac{\beta}{2}\int_{-\infty}^{\infty}\left(X\left(\operatorname{erf}\left(\frac{X}{p}\right) - \operatorname{erf}\left(\frac{X}{q}\right)\right) + \frac{1}{\sqrt{\pi}}\left(p\,\mathrm{e}^{-\frac{X^2}{p^2}} - q\,\mathrm{e}^{-\frac{X^2}{q^2}}\right)\right)\mathrm{d}X \\ &= \frac{\beta}{2}\left((p^2-q^2) + \int_{-\infty}^{\infty} X\left(\operatorname{erf}\left(\frac{X}{p}\right) - \operatorname{erf}\left(\frac{X}{q}\right)\right)\mathrm{d}X\right) \\ &= \frac{\beta}{4}\left(p^2-q^2\right)\end{aligned} \tag{4.22}$$

which on substitution for β, p and q gives:

$$\Delta\theta_{\mathrm{LJP}} = \frac{1 - c_{\mathrm{L}}^*}{2} \left(D'_{\mathrm{X}} - D'_{\mathrm{A}}\right) \cdot \tau \tag{4.23}$$

The point of maximum field occurs where $c_{\mathrm{A}} = c_{\mathrm{X}}$, as discussed in Section 4.5.3, which from Equation 4.18 is necessarily at $X = 0$ for $\tau > 0$. Now, substitution of $X = 0$ into Equation 4.21 yields:

$$\left.\frac{\partial\theta}{\partial X}\right|_{\mathrm{max}} = \frac{1 - c_{\mathrm{L}}^*}{2} \frac{\sqrt{D'_{\mathrm{X}}} - \sqrt{D'_{\mathrm{A}}}}{\sqrt{\pi}} \cdot \sqrt{\tau} \tag{4.24}$$

These short time results for liquid junction potential and electric field are plotted as the $\tau \to 0$ asymptotes in Figure 4.3, with evident agreement with simulation for both observables in this limit.

4.5.6 Asymptotic analysis as $\tau \to \infty$

Hickman[12] introduced $\tau \to \infty$ asymptotic analysis as a means of deriving the Henderson equation without recourse to electroneutrality; the $(\partial\theta/\partial X)_{\mathrm{max}} \propto \tau^{-\frac{1}{2}}$ relaxation of the junction was correctly identified in following work by Jackson,[13] where the observation of a constant potential was rationalised in terms of the expansion of the junction.

Hickman used the Boltzmann transformation[35] to facilitate the $\tau \to \infty$ asymptotic analysis. This transformation was first introduced to assist in the solution of the diffusion equation when $D(x)$ is not constant and consists of substituting $z = x/\sqrt{t}$ into the diffusion equation to find solutions as functions of z.

The Boltzmann transformation for long time may be written as a transformation

$(X, \tau) \to (z, u)$ where:

$$z = \frac{X}{\sqrt{\tau}} \tag{4.25}$$

$$u = \frac{1}{\tau} \tag{4.26}$$

and so

$$\frac{\partial}{\partial X} = u^{\frac{1}{2}} \frac{\partial}{\partial z} \tag{4.27}$$

$$\frac{\partial}{\partial \tau} = -\frac{uz}{2} \frac{\partial}{\partial z} - u^2 \frac{\partial}{\partial u} \tag{4.28}$$

Therefore the transformed Nernst–Planck–Poisson equations in a linear geometry are:

$$\frac{\partial^2 c_i}{\partial z^2} + z_i \frac{1}{u} \frac{\partial}{\partial z}(c_i \eta) + \frac{1}{D_i'} \left(\frac{z}{2} \frac{\partial c_i}{\partial z} + u \frac{\partial c_i}{\partial u} \right) = 0 \tag{4.29}$$

$$\frac{\partial \eta}{\partial z} + \frac{1}{2} \sum_i z_i c_i = 0 \tag{4.30}$$

where η is the dimensionless electric field:

$$\eta = \frac{\frac{\partial \theta}{\partial X}}{\sqrt{\tau}} \tag{4.31}$$

At this point is helpful to provide a brief summary of work by Hickman[12] and Jackson[13] on $\tau \to \infty$ asymptotic analysis of the Type 1 liquid junction, after which their results can be extended to consider junction motion and comparison with the numerical simulation results presented above.

The Boltzmann transformed forms of the NPP equations for a Type 1 system are:

$$\frac{\partial^2 c_\mathrm{A}}{\partial z^2} + \frac{1}{u} \frac{\partial}{\partial z}(c_\mathrm{A} \eta) + \frac{1}{D_\mathrm{A}'} \left(\frac{z}{2} \frac{\partial c_\mathrm{A}}{\partial z} + u \frac{\partial c_\mathrm{A}}{\partial u} \right) = 0 \tag{4.32}$$

$$\frac{\partial^2 c_\mathrm{X}}{\partial z^2} - \frac{1}{u} \frac{\partial}{\partial z}(c_\mathrm{X} \eta) + \frac{1}{D_\mathrm{X}'} \left(\frac{z}{2} \frac{\partial c_\mathrm{X}}{\partial z} + u \frac{\partial c_\mathrm{X}}{\partial u} \right) = 0 \tag{4.33}$$

$$\frac{\partial \eta}{\partial z} + \frac{c_\mathrm{A} - c_\mathrm{X}}{2} = 0 \tag{4.34}$$

These may be reformulated to new equations (4.32)+(4.33) and (4.32)−(4.33) in terms of a local ionic strength $\sigma = c_\mathrm{A} + c_\mathrm{X}$ and a local charge density $\rho = c_\mathrm{A} - c_\mathrm{X}$:

$$\frac{\partial^2\sigma}{\partial z^2} + \frac{1}{u}\frac{\partial}{\partial z}(\rho\eta) + \delta_1\left(\frac{z}{2}\frac{\partial\sigma}{\partial z} + u\frac{\partial\sigma}{\partial u}\right) + \delta_2\left(\frac{z}{2}\frac{\partial\rho}{\partial z} + u\frac{\partial\rho}{\partial u}\right) = 0 \tag{4.35}$$

$$\frac{\partial^2\rho}{\partial z^2} + \frac{1}{u}\frac{\partial}{\partial z}(\sigma\eta) + \delta_2\left(\frac{z}{2}\frac{\partial\sigma}{\partial z} + u\frac{\partial\sigma}{\partial u}\right) + \delta_1\left(\frac{z}{2}\frac{\partial\rho}{\partial z} + u\frac{\partial\rho}{\partial u}\right) = 0 \tag{4.36}$$

$$\frac{\partial\eta}{\partial z} + \frac{\rho}{2} = 0 \tag{4.37}$$

where:

$$\delta_1 = \frac{D'_\mathrm{X} + D'_\mathrm{A}}{2D'_\mathrm{A}D'_\mathrm{X}} \tag{4.38}$$

$$\delta_2 = \frac{D'_\mathrm{X} - D'_\mathrm{A}}{2D'_\mathrm{A}D'_\mathrm{X}} \tag{4.39}$$

An asymptotic expansion is then assumed for the three variables $\sigma(z,u)$, $\rho(z,u)$, and $\eta(z,u)$:

$$f(z,u) = \sum_{i=0}^{\infty} f_i(z)\,u^i \tag{4.40}$$

so that as $\tau \to \infty$ and hence $u \to 0$, the asymptotic solution consists exclusively of the leading non-zero terms as the higher order terms will vanish.

Substituting into the Nernst–Planck–Poisson equations generates a power series in u for each equation, which is equal to zero for *all* u. Hence, the coefficients of each power of u must also equal zero. The terms of the Nernst–Planck equations in u^{-1} and of the Poisson equation in u^0 require:

$$\frac{d(\rho_0\eta_0)}{dz} = 0 \tag{4.41}$$

$$\frac{d(\sigma_0\eta_0)}{dz} = 0 \tag{4.42}$$

$$\frac{d\eta_0}{dz} + \frac{\rho_0}{2} = 0 \tag{4.43}$$

If $\eta_0(z)$ is non-zero, $\partial\theta/\partial X = \eta_0(z)\sqrt{\tau} \to \infty$ across all space as $\tau \to \infty$, which is inconsistent with the Poisson equation, as the charge density ρ is confined to zero at the boundaries $X = \pm\infty$. Hence $\eta_0(z) = 0$, and the above can be summarised by:

$$\rho_0 = \eta_0 = 0 \tag{4.44}$$

i.e. electroneutrality at long time, to leading order. This result was implied by the outer asymptotic analysis performed for a related membrane potential problem by MacGillivray[36] and is consistent with the dissipation of charge by Coulombic attraction as a system tends to a electroneutral equilibrium.

Now, from the terms of the Nernst–Planck equations in u^0:

$$\frac{d^2\sigma_0}{dz^2} + \delta_1 \frac{z}{2}\frac{d\sigma_0}{dz} = 0 \tag{4.45}$$

$$\frac{d}{dz}(\sigma_0\eta_1) + \delta_2 \frac{z}{2}\frac{d\sigma_0}{dz} = 0 \tag{4.46}$$

Equation 4.45 is a straightforward ordinary differential equation in one function, which can be integrated to:

$$\frac{d\sigma_0}{dz} = \lambda \exp\left(-\frac{z^2\delta_1}{4}\right) \tag{4.47}$$

where λ is a constant. Integrating from the boundary at $z = -\infty$ inwards, where $\sigma_0 = 2c_{\mathrm{L}}^*$ from the boundary conditions:

$$\sigma_0 = 2c_{\mathrm{L}}^* + \lambda\sqrt{\frac{\pi}{\delta_1}}\left(1 + \operatorname{erf}\left(\frac{z\sqrt{\delta_1}}{2}\right)\right) \tag{4.48}$$

and evaluating at $z = +\infty$:

$$\begin{aligned}\sigma_0(\infty) &= 2 \\ &= 2\left(c_{\mathrm{L}}^* + \lambda\sqrt{\frac{\pi}{\delta_1}}\right)\end{aligned} \tag{4.49}$$

such that

$$\lambda = (1 - c_{\mathrm{L}}^{*})\sqrt{\frac{\delta_1}{\pi}} \tag{4.50}$$

Therefore, with some rearrangement and substituting in the expressions for α and β introduced above (Equation 4.19):

$$\sigma_0 = 2\left(\alpha + \beta \operatorname{erf}\left(\frac{z\sqrt{\delta_1}}{2}\right)\right) \tag{4.51}$$

$$\frac{d\sigma_0}{dz} = 2\beta\sqrt{\frac{\delta_1}{\pi}}\,\exp\left(-\frac{z^2\delta_1}{4}\right) \tag{4.52}$$

Substituting into Equation 4.46:

$$\frac{d}{dz}(\sigma_0\eta_1) = -\delta_2\beta z\sqrt{\frac{\delta_1}{\pi}}\,\exp\left(-\frac{z^2\delta_1}{4}\right) \tag{4.53}$$

and as $\eta_1(-\infty) = 0$, this can be integrated to

$$\sigma_0\eta_1 = 2\beta\frac{\delta_2}{\delta_1}\sqrt{\frac{\delta_1}{\pi}}\,\exp\left(-\frac{z^2\delta_1}{4}\right) \tag{4.54}$$

Therefore

$$\begin{aligned}\eta_1 &= \frac{\beta\,\delta_2}{\sqrt{\delta_1\pi}} \cdot \frac{\exp\left(-\frac{z^2\delta_1}{4}\right)}{\alpha + \beta \operatorname{erf}\left(\frac{z\sqrt{\delta_1}}{2}\right)} \\ &= \frac{\delta_2}{\delta_1} \cdot \frac{\frac{d\sigma_0}{dz}}{\sigma_0}\end{aligned} \tag{4.55}$$

The $\tau \to \infty$ behaviour of the system of the electric field is then:

$$\frac{\partial\theta}{\partial X} \approx \eta_1(z) \cdot u \cdot \sqrt{\tau} = \frac{\eta_1}{\sqrt{\tau}} \tag{4.56}$$

to leading order. This predicted field profile was compared with simulation in a long time case, with excellent agreement (Figure 4.11).

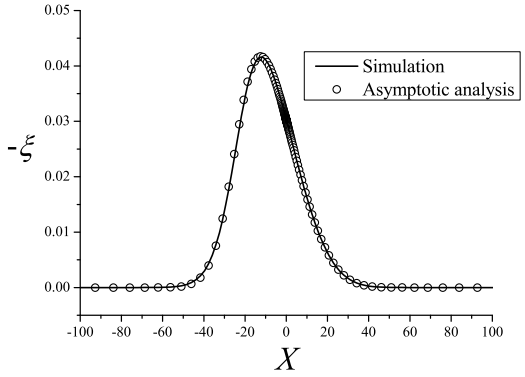

Figure 4.11: Comparison of the simulated electric field for the model HCl system at long time ($\tau = 100\tau_{\text{trs}}$) with the leading non-zero term in the asymptotic analysis introduced by Hickman and Jackson. $\xi \equiv \partial\theta/\partial X$.

The liquid junction potential may now be determined by the integration of η_1:

$$\begin{aligned}\Delta\theta_{\text{LJP}} &= \int_{-\infty}^{\infty} \eta_1(z)\, dz \\ &= \frac{\delta_2}{\delta_1} \int_{-\infty}^{\infty} \frac{\frac{d\sigma_0}{dz}}{\sigma_0}\, dz \\ &= \frac{\delta_2}{\delta_1} \ln\left|\frac{\sigma(\infty)}{\sigma(-\infty)}\right| \\ &= \frac{\delta_2}{\delta_1} \ln\left|\frac{\alpha+\beta}{\alpha-\beta}\right|\end{aligned} \tag{4.57}$$

On substitution for α, β, δ_1 and δ_2, this recovers the Type 1 Henderson equation (Equation 4.4) precisely, without the *a priori* assumption of either electroneutrality or a constrained boundary layer with linear concentration profiles.

This concludes a summary of work on the Type 1 case in Hickman[12] and Jackson,[13] but the interesting observation of a moving junction position in the simulation results suggests further development. To the first order of approximation, the field is maximum where $d\eta_1/dz = 0$, neglecting the trivial cases $z = \pm\infty$. Differentiation of the simplified expression in Equation 4.55 gives:

$$\frac{\mathrm{d}\eta_1}{\mathrm{d}z} = \frac{\delta_2}{\delta_1} \frac{\sigma_0 \frac{\mathrm{d}^2\sigma_0}{\mathrm{d}z^2} - \left(\frac{\mathrm{d}\sigma_0}{\mathrm{d}z}\right)^2}{\sigma_0^2} \tag{4.58}$$

As σ_0 is finite for all z, this evaluates to zero where:

$$\sigma_0 \frac{\mathrm{d}^2\sigma_0}{\mathrm{d}z^2} - \left(\frac{\mathrm{d}\sigma_0}{\mathrm{d}z}\right)^2 = 0 \tag{4.59}$$

which can be written with the substitutions $s = z\sqrt{\delta_1}/2$ and $\gamma = \alpha/\beta$ as:

$$\gamma + \mathrm{erf}(s) + \frac{\mathrm{e}^{-s^2}}{s \cdot \sqrt{\pi}} = 0 \tag{4.60}$$

γ relates systematically to c_{L}^* as $c_{\mathrm{L}}^* = (\gamma - 1)/(\gamma + 1)$. This equation is apparently not invertable. It is single-valued and finite, however, for all $\gamma > 1$, and so a root $s(\gamma)$ may be evaluated numerically. It follows that

$$X_{\mathrm{LJP}} = \frac{2s(\gamma)}{\delta_1} \cdot \sqrt{\tau} \tag{4.61}$$

which is plotted as the $\tau \to \infty$ asymptote in Figure 4.9. Note that $s(\gamma) < 0$ because diffusion of both species is to the left, and so drives the junction position to the left of the junction.

From the substitution of Equation 4.61 back into Equation 4.55, the long time charge separation is determined as

$$Q'_{\mathrm{LJP}} = -\left.\frac{\partial\theta}{\partial X}\right|_{X=X_{\mathrm{LJP}}} \approx \frac{\delta_2 \cdot s(\gamma)}{\sqrt{\delta_1}} \frac{1}{\sqrt{\tau}} \tag{4.62}$$

which is plotted as the $\tau \to \infty$ asymptote in Figure 4.3. This demonstrates that as $\tau \to \infty$, the Type 1 liquid junction approaches a state of continuous loss of charge, at an asymptotic rate proportional to $\tau^{-\frac{1}{2}}$.

4.6 Discussion of Type 1 dynamics

4.6.1 General trends

A dynamic theory of liquid junction potentials must therefore account for junction charging and expansion proportional to $\tau^{\frac{1}{2}}$ at short time, and for the following observations at long time:

- The potential approaches a limiting value but the electric field decreases proportionally to $\tau^{\frac{1}{2}}$.
- The concentration profiles become asymmetric.
- The liquid junction position moves away from its initial position.
- The spatial extent of charge separation continues to grow as $\tau^{\frac{1}{2}}$.

These observations are inconsistent with the concept of a static, confined liquid junction at steady state within a boundary layer, as proposed by Planck.[7]

4.6.2 Short time behaviour

At very short time, insufficient charge separation has developed for the electric field in solution to significantly influence the mass transport of the ions. Their migrational flux is hence negligible, and so the concentration profiles approximately obey the diffusion equation. The charge separation arising from unequal diffusion develops proportionally to the rate of diffusion through the junction, i.e. as $\tau^{\frac{1}{2}}$ according to the Einstein relation. Equivalently, the size of the diffusion layer either side of $X = 0$ is also expanding as $\tau^{\frac{1}{2}}$, as shown by the trends in ΔX_θ.

Based on the understanding of a potential difference as representing the energy, per unit charge, associated with the Coulombic force opposing a charge separation, it is clear that the potential difference must be proportional both to the density of charge separated and to the distance of separation. This follows from Gauss's Law in the linear space:

$$\frac{\partial \theta}{\partial X} = Q' \tag{4.63}$$

and therefore for two parallel planes of charge Q' and $-Q'$ separated by a distance X, the potential difference is given:

$$\theta = Q'X \tag{4.64}$$

Assuming that the mean distance of charge separation is proportional to the spatial extent of the liquid junction, i.e. to $\tau^{\frac{1}{2}}$, taking the product of both contributions to the potential difference predicts a linear increase in time, exactly as observed. That is, at short times, diffusion causes a linear growth in junction potential because a charge of magnitude $\propto \tau^{\frac{1}{2}}$ is being separated by an increasing distance $\propto \tau^{\frac{1}{2}}$, where the proportionality is expected from the Einstein expression for the spatial extent of a diffusion layer (Equation 1.37).

4.6.3 Transitional behaviour

The increasing electric field must, however, impact upon the mass transport of A^+ and X^- by inducing migration. The observed motion of $X_{\mathrm{LJP}} \propto \tau^{\frac{3}{2}}$, which is not accounted for by an asymptotic analysis that ignores migration, proves that there are tangible migration effects on the junction at all times $\tau > 0$.

As the electric field increases, transport of the initially faster leading ion is decel-

erated and that of the initially slower species is accelerated. The electric field is not uniform through the junction, however, but is maximal at the junction centre and falls away to zero at either side. Therefore, the discrepancy in migrational flux between A^+ and X^-, and hence the extent of compensation for their differing rates of diffusion, is greater at the junction centre than in either the region of lower concentration to the left *or* the region of higher concentration to the right. This causes a 'bunching' of the junction: the leading species profile is squashed to the right and stretched to the left, and *vice versa* for the following species, such that the junction position itself moves with the concentration gradient away from its initial position, and the electric field becomes asymmetric. This is best exhibited by the concentration profiles recorded at the point of maximum field (Figure 4.5).

The junction continues to charge as long as the flux of the initially faster ion exceeds that of the initially slower ion, but since this charging increases the electric field which opposes the charging process, the rate of charging must gradually slow. The rate of charging falls to zero, i.e. equal fluxes of both species at the junction, at a characteristic time τ_{trs}. This time can be identified with the Debye time, $t_{\mathrm{D}} = x_{\mathrm{D}}^2/D$, which is the time required for an ion to diffuse across one Debye length. As the diffusion layer exceeds the extent of the Debye length, the requirement to screen electric fields and achieve overall electroneutrality begins to dominate the diffusional gradient. For typical concentrations and diffusion coefficients, t_{D} is of the order of 5–50 ns.

Under a condition of equal fluxes, Planck argued that the potential difference across the junction is constant,[7] but as the junction charge is constant, this can then only be true if the mean distance of charge separation in the junction is also constant; where the diffusion layers for A^+ and X^- can continue to expand without constraint, this

is not true. Therefore, as the region of maximum field 'diffuses' to a region of lower diffusive flux, the flux of the initially slower ion will overtake that of the initially faster ion. So, the net ionic current across the electroneutral point X_{LJP} changes sign, and and the junction begins to discharge. All behaviour of the liquid junction following this transition tends towards compensation for the charge separation already generated as a consequence of unequal diffusive fluxes on a nanosecond timescale.

4.6.4 Long time behaviour

Note that the system is tending towards an equilibrium with equal concentrations everywhere, and hence no concentration or charge gradients. If there has been a net transfer of charge across the junction at short time, there must be some transfer of charge in the opposite direction at long time, before an electroneutral equilibrium can be recovered. Although the system will be electroneutral at equilibrium, if an infinite supply of bulk solution is available on either side of the junction, this equilibrium cannot be attained in finite time.

The concentration profiles following the Debye time (Figure 4.6) show that the continued relaxation of the field permits the approximate recovery of electroneutrality around the initial junction position; the overall position of the junction, about which charge is separated, continues to move with the concentration gradient. As the $\tau \rightarrow \infty$ asymptote is attained, the junction discharges as $\tau^{\frac{1}{2}}$, i.e. proportionally to the continuing diffusion. However, the junction is also growing proportionally to $\tau^{\frac{1}{2}}$.

The limiting constant potential difference across the liquid junction is therefore justified in terms of unconstrained diffusion forcing both an increase in the mean distance of charge separation $\propto \tau^{\frac{1}{2}}$ and a decrease in the magnitude of that charge $\propto \tau^{\frac{1}{2}}$. In

the limit $\tau \to \infty$ these proportionalities cancel precisely and cause a constant liquid junction potential. The system remains dynamic ($\partial c_i/\partial \tau \neq 0$), however; both species are continuously diffusing at a rate approaching the mean of their diffusion coefficients (Equation 4.51), and the Nernst-Planck equations are *not* at steady state.

The liquid junction potential is only constant so long as diffusion continues unconstrained and so is only constant as long as the diffuse layer does not encounter some boundary where bulk solution is depleted, as is demonstrated by the collapse of the corresponding potentials in the numerical study of constrained liquid junctions by Perram et al.[10] The system is also not locally electroneutral – it merely tends to electroneutrality in the infinite time limit. The potential difference is therefore associated with a finite charge separation which originates in the discrepancy in diffusive flux occurring at short times and under low electric field conditions, when the junction size is less than the Debye length, and is never fully compensated.

The agreement of simulation with asymptotic theory in both limits, as well as the provision, by simulation, of data concerning the dynamic transition between these two conditions, has afforded a comprehensive and consistent understanding of the Type 1 liquid junction potential. Of fundamental importance is that the constant limiting liquid junction potential for a free junction *only exists as a dynamic property* of the system, given that charge separation is entirely due to the initial conditions. It cannot be recovered from a static ($\partial c_i/\partial \tau = 0$) treatment, as in the classical solution, without the use of physically meaningless approximations or boundary conditions. Indeed, since the equilibrium of the system is electroneutral, a potential difference is by definition indicative of a non-equilibrium, dynamic condition.

The distinction between the Planck model and the model discussed in this chapter

is highlighted in the schematic at Figure 4.12.

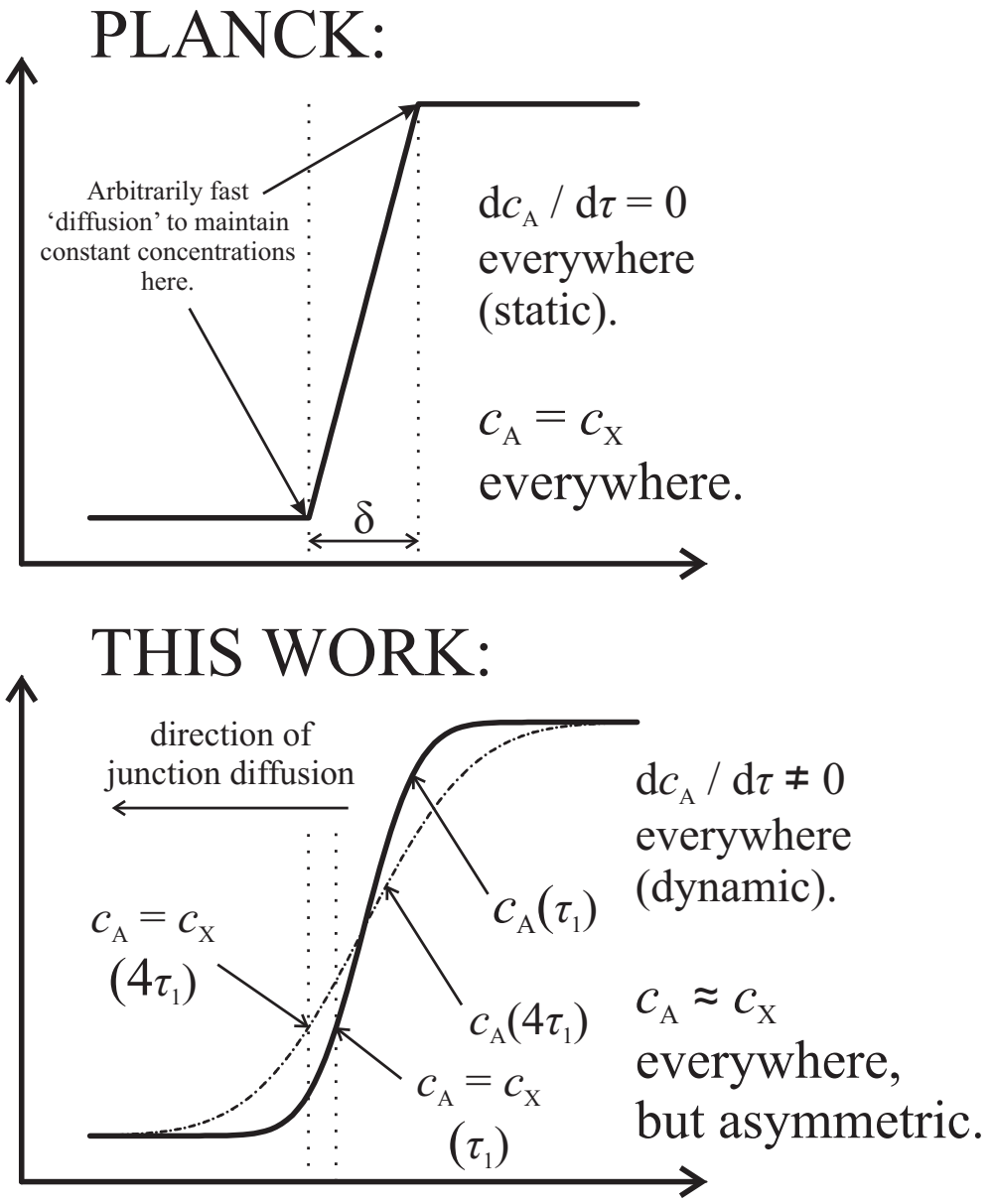

Figure 4.12: Schematic demonstrating the fundamentally different physical pictures entailed by Planck's static liquid junction and the dynamic model proposed in this work.

4.7 Type 2 liquid junctions

4.7.1 Simulated limiting potentials

The limiting liquid junction potentials for a set of Type 2 liquid junctions were simulated for D'_{A} and $D'_{\mathrm{B}} = 0.5$, 0.75, 1, 1.5 and 2, as well as the special cases of equimolar aqueous HCl|KCl and NaCl|KCl ($D'_{\mathrm{H^+}} = 4.582$, $D'_{\mathrm{Na^+}} = 0.6564$, $D'_{\mathrm{K^+}} = 0.9631$, at infinite dilution, 298 K).[33] The simulations used the same steady-state condition as for the Type 1 liquid junction (Equation 4.12). Simulation agreed with the Henderson equation to a tolerance of $\leq 0.8\%$ (Figure 4.13). The work of Hickman[12] showed that the Henderson equation is *not* exact for Type 2 and so exact agreement is not necessarily expected between the Henderson equation and a simulation based on the Nernst–Planck–Poisson equations without approximation.

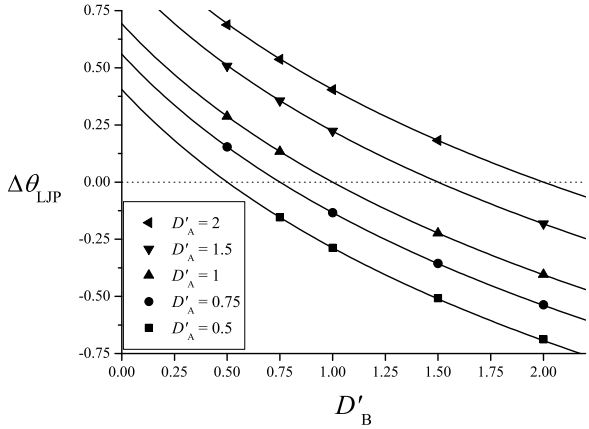

Figure 4.13: Comparison of simulated liquid junction potentials (symbols) at pseudo-steady state, and the theoretical values given by the Henderson equation (lines), for a Type 2 system with varying D'_{A} and D'_{B}. The dotted line indicates $D'_{\mathrm{A}} = D'_{\mathrm{B}}$, where the liquid junction potential is zero according to the Henderson equation.

4.7.2 Observed dynamics of liquid junction evolution

The detailed dynamical theory was extended to Type 2 junctions by investigation of the junction between equally concentrated aqueous solutions of NaCl and KCl.

The essential trends in liquid junction potential and maximum electric field, as a function of time, are the same as for the Type 1 case: a logarithmic plot is shown at Figure 4.14. We may therefore expect a similar physical rationalisation of the constant potential across the liquid junction as in the Type 1 case. Again, the transition time between charging and discharging occurs at $\tau_{\mathrm{trs}} \approx 1$; for 10 mM solutions this corresponds to $t_{\mathrm{trs}} \approx 7$ ns in this case, at which time the maximum electric field is ≈ 0.3 MV m^{-1}.

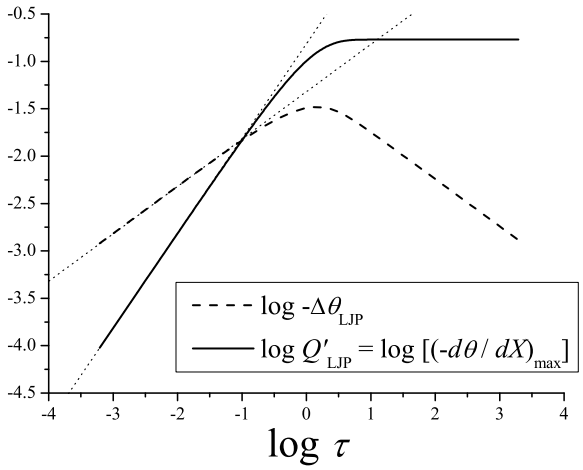

Figure 4.14: Dynamic evolution of liquid junction potential ($\Delta\theta_{\mathrm{LJP}}$) and charge separation ($Q_{\mathrm{LJP}} = -(\partial\theta/\partial X)_{\mathrm{max}}$) for the Type 2 junction of equimolar NaCl (aq) and KCl (aq), plotted on a logarithmic scale in time. Asymptotic limits as $\tau \to 0$ derived using a zero-feedback approach are plotted against the simulation data.

Some exemplar concentration profiles, across a similar logarithmic range either side of τ_{trs} as in the Type 1 case, are shown at Figures 4.15–4.17. As in Type 1 we observe approximately diffusional behaviour at short time; longer times give greater asymmetry of the concentration profiles as the field extends. Interestingly, the point where $c_{\mathrm{A}} = c_{\mathrm{B}}$

deviates from $X = 0$, but not extensively.

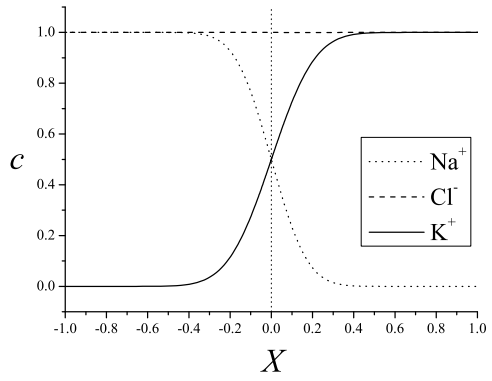

Figure 4.15: Concentration profile for the NaCl|KCl (aq) system at a time $\tau = 0.01\,\tau_{\text{trs}}$ following junction formation. As at short time for Type 1, the concentration profiles are symmetric and resemble the diffusion-only case; the diffuse layer associated with K^+ is more extensive than that of Na^+ due to differences in diffusion coefficient.

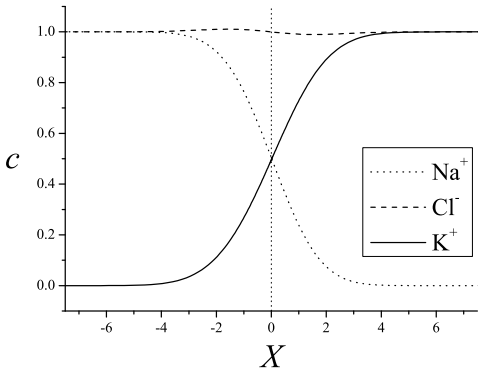

Figure 4.16: Concentration profile for the NaCl|KCl (aq) system at a time $\tau = \tau_{\text{trs}}$ following junction formation. The concentration profile of X has become increasingly asymmetric under the influence of the electric field, and the point where $c_{\text{Na}^+} = c_{\text{K}^+}$ is now at $X < 0$.

The corresponding evolution of the electric field profile is shown at Figure 4.18. A deviation of X_{LJP} away from $X = 0$ is not evident until $\tau > \tau_{\text{trs}}$ and even then at lower magnitudes than in the Type 1 example, where the variation in diffusion coefficients was much greater.

The trend of a general expansion of the liquid junction extent also resembles that for the Type 1 case (Figure 4.19), with a correlation to the size of the diffusion layer which expands proportionally to $\tau^{\frac{1}{2}}$.

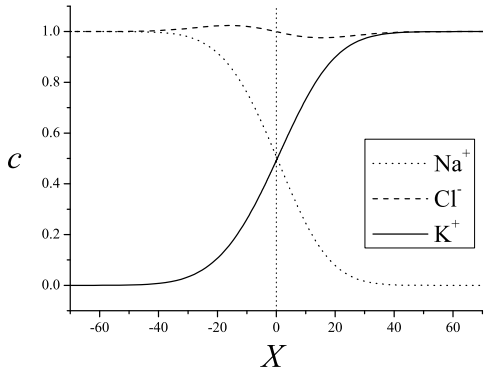

Figure 4.17: Concentration profile for the NaCl|KCl (aq) system at a time $\tau = 100\,\tau_{\mathrm{trs}}$ following junction formation. The asymmetry is further increased here and the point where $c_{\mathrm{Na^+}} = c_{\mathrm{K^+}}$ has shifted again to $X > 0$.

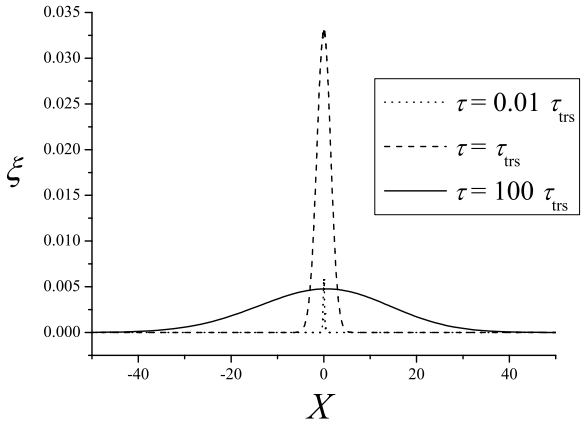

Figure 4.18: Evolution of the electric field profile for the NaCl|KCl (aq) system at times $\tau = 0.01\,\tau_{\mathrm{trs}}$ to $\tau = 100\,\tau_{\mathrm{trs}}$ following junction formation. Increased asymmetry of the initial junction position is evident; close analysis shows that the liquid junction position, X_{LJP}, varies with time.

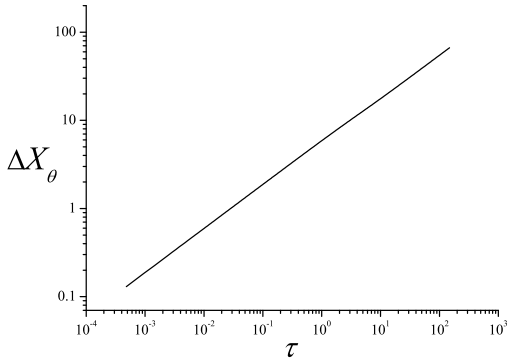

Figure 4.19: ΔX_θ as a function of τ on a logarithmic scale, for the model Type 2 NaCl|KCl liquid junction.

4.7.3 Asymptotic analysis at $\tau \to 0$

The $\tau \to 0$ limiting behaviours of the Type 2 liquid junction may be approached by the zero-feedback approximation as for Type 1 (Section 4.5.5). The mathematics are in fact simplified as the equimolar concentrations give $\alpha_{\mathrm{A}} = \alpha_{\mathrm{B}} = \frac{1}{2}$ and $\beta_{\mathrm{B}} = -\beta_{\mathrm{A}} = \frac{1}{2}$. The species X may be ignored as it is uniformly concentrated at $\tau = 0$ and hence its diffusive flux is zero.

Substitution into the Poisson equation then yields in this case:

$$\frac{\partial^2 \theta}{\partial X^2} = \frac{1}{4}\left(\operatorname{erf}\left(\frac{X}{2\sqrt{D'_{\mathrm{A}}\tau}}\right) - \operatorname{erf}\left(\frac{X}{2\sqrt{D'_{\mathrm{B}}\tau}}\right)\right) \tag{4.65}$$

which is the same problem as the Type 1 case but with:

$$\beta = \frac{1}{2} \quad ; \quad p = 2\sqrt{D'_{\mathrm{A}}\tau} \quad ; \quad q = 2\sqrt{D'_{\mathrm{B}}\tau} \tag{4.66}$$

and so the same solutions (in β, p, q) apply.

$$\left.\frac{\partial \theta}{\partial X}\right|_{\max} \approx \frac{1}{2\sqrt{\pi}}\left(\sqrt{D'_{\mathrm{A}}} - \sqrt{D'_{\mathrm{B}}}\right) \cdot \sqrt{\tau} \tag{4.67}$$

and

$$\Delta\theta_{\mathrm{LJP}} \approx \frac{D'_{\mathrm{A}} - D'_{\mathrm{B}}}{2} \cdot \tau \tag{4.68}$$

These are plotted as the $\tau \to 0$ asymptotes in Figure 4.14, and again show excellent agreement with simulation in this limit.

4.7.4 Asymptotic analysis as $\tau \to \infty$

Unfortunately, the simple long-time asymptotic analysis in the Type 1 case is not possible in the Type 2 case. Hickman used a further perturbation involving the diffusion coefficients to achieve approximate results.[12]

To the first approximation, he reported the electric field as:

$$\frac{\partial\theta}{\partial X} \approx -\sqrt{\frac{2}{\pi}}\,\frac{\mathrm{e}^{-z^2}}{\gamma+\mathrm{erf}(z)}\,\frac{1}{\tau} \tag{4.69}$$

where z is defined as above for Type 1 and

$$\gamma = \frac{D'_{\mathrm{B}} + D'_{\mathrm{A}} + 2D'_{\mathrm{X}}}{D'_{\mathrm{B}} - D'_{\mathrm{A}}} \tag{4.70}$$

This expression can be integrated to yield the Type 2 Henderson equation (Equation 4.5); however, given that a second asymptotic expansion is required, the Henderson equation is not exact for Type 2, even as $\tau \to \infty$.

A comparison of the electric field predicted by the Hickman theory with dynamic simulation is presented here for the first time.

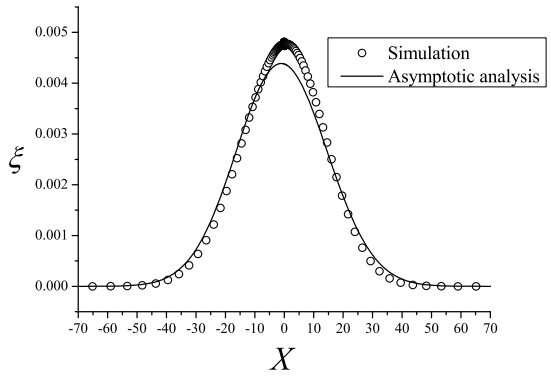

Figure 4.20: Comparison of the simulated electric field for the model NaCl|KCl (aq) system, $-\xi$, at long time ($\tau = 100\tau_{\mathrm{trs}}$) with the leading non-zero term in the asymptotic analysis introduced by Hickman.

The comparison at Figure 4.20 shows that the expression at Equation 4.69 is in fact not an effective description of the electric field in the system at $\tau = 100\,\tau_{\mathrm{trs}}$. The position of the maximum field is poorly predicted, and the general shape of the simulated field is not consistent with the leading term arising from the Hickman theory.

As above, the electric field can be differentiated to find the temporal evolution of X_{LJP}. Again, however, comparison with simulation shows that the analysis of X_{LJP} is

very poor indeed; even the predicted direction of the motion of X_{LJP} is incorrect, as simulation shows that the junction moves in the positive X direction at long times, whereas the opposite is predicted by numerical analysis.

In the Type 2 case, it is assumed that although the accuracy of the Henderson equation compared to simulation implies that the *integral* of the higher terms in Hickman's approximation is negligible, these terms may be significant in the region of high field at the centre of the junction, and so inherent asymmetries occurring in these higher terms will alter the dynamic trends in the electric field and junction position.

4.7.5 Conclusion on Type 2 dynamics

Although the asymptotic analysis performed for the Type 1 liquid junction is not tractable for the Type 2 case, numerical simulation has demonstrated that the dynamic trends in potential difference and charge separation associated with a Type 2 liquid junction are the same as those for Type 1.

A short time limit where the electric field may be neglected exists, and a straightforward diffusional analysis gives results that agree closely with the $\tau \to 0$ trends observed from numerical simulation. The unequal rates of diffusion of Na^+ and K^+, in opposing directions, causes a charge separation and hence a potential difference that develops as τ, because diffusion drives both junction charging and junction expansion as $\tau^{\frac{1}{2}}$ (Equation 1.37). As the electric field develops, it decelerates the mass transport of the initially faster species and accelerates the mass transport of the initially slower species. The electric field at the junction position achieves a maximum approximately at the Debye time, which is when the junction extends one Debye length and so restoration of electroneutrality becomes the dominant driving force in the system.

As in Type 1, the non-uniformity of the electric field causes dynamic asymmetry in the concentration profiles. In particular, the concentration profile of the common ion species X^- ceases to be uniform. These asymmetries cause the position of the liquid junction to move, and in the Type 2 case this motion is not well accounted for by asymptotic theory. Empirical evidence from simulation shows a long time $\tau^{\frac{1}{2}}$ diffusion of the junction position. Although asymptotic theory correctly predicts the Henderson equation, its leading term is clearly inadequate as a general description of the electric field in this case.

Again, the constant liquid junction potential can be rationalised on the basis of the expansion of the junction in time occurring at a rate proportional to $\tau^{\frac{1}{2}}$, which balances a loss of charge in the junction also proportional to $\tau^{\frac{1}{2}}$, such that a constant potential difference arises as an exclusively dynamic property of the system.

4.8 Liquid junction timescales

Type 1 liquid junctions approach a long time asymptote of constant potential difference across the junction, which is caused by the increased mean distance of charge separation in the junction exactly balancing the decrease in magnitude of separated charge. The time required to attain this asymptotic limit is an unknown variable, however, and so was studied by simulation.

An appropriate timescale for the attainment of asymptotic behaviour is that to required for the system to achieve 99% of the potential difference predicted by the Henderson equation, defined as τ_{ss}:

$$\tau_{\text{ss}} = \tau(\Delta\phi_{\text{LJP}} = 0.99\Delta\phi_{\text{Henderson}}) \tag{4.71}$$

The simulation results are indicated in Figure 4.21.

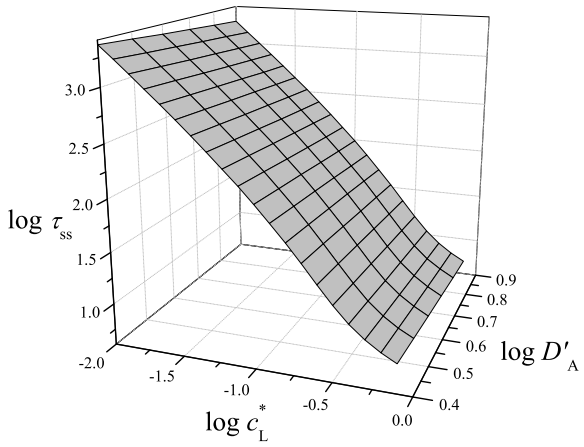

Figure 4.21: Comparison of τ_{ss}, on a logarithmic scale, required to achieve asymptotic behaviour for a Type 1 system with varying D'_A and c^*_L.

In general, as the ratio c^*_L becomes more extreme, a longer timescale is noted before asymptotic behaviour is attained, which is consistent with a lengthening of the Debye time in the more weakly conductive solution left of the junction. The dependence on D'_A is comparatively weak. Note that the dimensional time required for a liquid junction to attain its limiting potential is directly proportional to ϵ_s and is inversely proportional to D_X and C^*_R. A solution of higher conductivity therefore achieves its limiting potential more rapidly, but in a solution of higher permittivity, the greater screening of electric fields allows the liquid junction diffusion layer to extend further before reaching the Debye length and approaching an electroneutral condition. Therefore, for a common ionic mobility, the formation of a liquid junction potential requires a longer timescale in a solution of increased permittivity.

τ_{ss} was also investigated for Type 2 junctions according to the definition above (Equation 4.71). As expected, it was found that greater absolute diffusion coefficients accelerate all mass transport processes and hence accelerate the rate of attainment of asymptotic behaviour. The effects of ionic strength and permittivity apply just as in

the Type 1 case (Section 4.8).

4.9 Conclusions

In this chapter, two liquid junction systems (Figure 4.1) have been analysed using the Nernst-Planck-Poisson equation set, without the *a priori* assumption of electroneutrality, and employing quasi-infinite boundary conditions that imply free bulk solution and avoid the physical inconsistencies identified in the traditional Planck–Henderson liquid junction model.[10]

The dynamic theory introduced here arises as a synthesis of novel computational and mathematical study with the asymptotic analysis performed by Hickman[12] and Jackson[13] in the early 1970s – work which has not been considered in computational studies of the liquid junction dating from the modern era[10,27–29] when accurate simulation of the NPP equations, an extremely computationally demanding procedure, has become viable.

A constant liquid junction potential results from charge separation engendered by unequal rates of diffusion. This charge separation causes an electric field that modulates the unequal transport of species, within the Debye time of a few tens of nanoseconds. As the diffusion layer expands to exceed the Debye screening length of the solution a transition occurs where the charge separation achieves its maximum, and the liquid junction to begin to discharge towards its *equilibrium* state of electroneutrality throughout the system. At times longer than the Debye time, the drive for system electroneutrality dictates the charge transport across the junction (see for example Figure 4.6), as expected given the strength of the electroneutrality approximation over

distances greater than a few Debye lengths.

As long as the diffuse layer encounters no finite boundaries, however, the electroneutral equilibrium is not attained in finite time: rather, continuing diffusion causes the junction to grow at a rate proportional to $\sqrt{t}$, which is equal to its rate of discharge as $\sqrt{t}$, such that a constant potential difference arises, because less charge is separated across a greater distance. This potential difference arises at timescales of 10–1000 ns after junction formation for typical aqueous systems, by which time the diffuse layer is approximately 10–1000 nm in extent.

In contrast to Planck's assumption,[7] the only steady state of the free liquid junction system, i.e. a state where the time derivatives of all species concentrations everywhere in space is zero, is the unattainable equilibrium where concentrations are constant across all space. Electroneutrality is never attained exactly, and so a finite potential difference across the junction is physically acceptable. By using simulation techniques in order to incorporate the Poisson equation in full, rather than relying on the electroneutrality approximation, the potential difference is clearly attributable to the quantity and distribution of separated charge, however negligible or widespread this charge may be, avoiding inherent confusions or paradoxes due to the use of electroneutrality to describe dynamic charge transport (Section 4.2.1).

In conclusion, constant free liquid junction potentials arise as *dynamic* properties of the system and are indicative of a non-equilibrium condition. In a confined system where equilibrium can be attained, the liquid junction potential collapses.[10] Any attempt, as is common in the traditional conception of a liquid junction potential, to derive the unconstrained liquid junction potential on the basis of a *static* system, where the Nernst–Planck equations may be taken at such a steady state and hence

integrated, must necessarily contain some inconsistency with known laws of physics such as conservation of mass or charge. The static model, unlike the dynamic model, does not represent a valid physical picture of the liquid junction potential.

By considering charge transport due only to a concentration gradient, considerations common to all charge transport systems in electrolytic solution have been revealed. These include the relative freedom of charge separation over distances of a few Debye lengths, and the correspondingly strong drive for restoration of electroneutrality over times longer than the Debye time following a perturbation at a fixed point in solution. In the following two chapters, these concepts and the general methodology are extended to charge transport caused by an applied potential in an electrochemical cell, rather than as a consequence of diffusion.

Bibliography

[1] E. J. F. Dickinson, L. Freitag and R. G. Compton, *J. Phys. Chem. B*, 2010, **114**, 187–197.

[2] E. J. F. Dickinson, J. G. Limon-Petersen and R. G. Compton, *J. Solid State Electrochem.*, 2011, **15**, 1335–1345.

[3] J. J. Lingane, *Electroanalytical Chemistry*, Wiley, New York, 2nd edn., 1958.

[4] K. R. Ward, E. J. F. Dickinson and R. G. Compton, *J. Phys. Chem. B*, 2010, **114**, 4521–4528.

[5] W. Nernst, *Z. Physik. Chem.*, 1889, **4**, 129–181.

[6] M. Planck, *Wied. Ann.*, 1890, **39**, 161–186.

[7] M. Planck, *Wied. Ann.*, 1890, **40**, 561–576.

[8] P. Henderson, *Z. Physik. Chem.*, 1907, **59**, 118–127.

[9] J. H. van 't Hoff, *Z. Physik. Chem.*, 1887, **1**, 481–508.

[10] J. W. Perram and P. J. Stiles, *Phys. Chem. Chem. Phys.*, 2006, **8**, 4200–4213.

[11] E. A. Guggenheim, *J. Am. Chem. Soc.*, 1930, **52**, 1315–1337.

[12] H. J. Hickman, *Chem. Eng. Sci.*, 1970, **25**, 381–398.

[13] J. L. Jackson, *J. Phys. Chem.*, 1974, **78**, 2060–2064.

[14] D. R. Hafemann, *J. Phys. Chem.*, 1965, **69**, 4226–4231.

[15] J. Bagg, *Electrochim. Acta*, 1990, **35**, 361–365.

[16] J. Bagg, *Electrochim. Acta*, 1990, **35**, 367–370.

[17] J. Bagg, *Electrochim. Acta*, 1992, **37**, 719–723.

[18] P. Henderson, *Z. Physik. Chem.*, 1908, **63**, 325–345.

[19] D. E. Goldman, *J. Gen. Physiol.*, 1943, **27**, 37–60.

[20] R. N. Goldberg and H. S. Frank, *J. Phys. Chem.*, 1972, **76**, 1758–1762.

[21] W. E. Morf, *Anal. Chem.*, 1977, **49**, 810–813.

[22] T. R. Brumleve and R. P. Buck, *J. Electroanal. Chem.*, 1978, **90**, 1–31.

[23] T. R. Brumleve and R. P. Buck, *J. Electroanal. Chem.*, 1981, **126**, 55–71.

[24] S. Mafé, J. Pellicer and V. M. Aguilella, *J. Phys. Chem.*, 1986, **90**, 6045–6050.

[25] J. Horno, J. Castilla and C. F. Gonzalez-Fernandez, *J. Phys. Chem.*, 1992, **96**, 854–858.

[26] B. Martuzans and Y. Skryl, *J. Chem. Soc., Faraday Trans.*, 1998, **94**, 2411–2416.

[27] Y. Skryl, *Phys. Chem. Chem. Phys.*, 2000, **2**, 2969–2976.

[28] T. Sokalski and A. Lewenstam, *Electrochem. Commun.*, 2001, **3**, 107–112.

[29] T. Sokalski, P. Lingenfelter and A. Lewenstam, *J. Phys. Chem. B*, 2003, **107**, 2443–2452.

[30] J. Josserand, G. Lagger, H. Jensen, R. Ferrigno and H. H. Girault, *J. Electroanal. Chem.*, 2003, **546**, 1–13.

[31] J. Park, K. Y. Huh and X. Li, *J. Electroanal. Chem.*, 2006, **591**, 141–148.

[32] R. Filipek, K. Szyskiewicz-Warzecha, B. Bożek, M. Danielewski and A. Lewenstam, *Defect and Diffusion Forum*, 2009, **283-286**, 487–493.

[33] A. J. Bard and L. R. Faulkner, *Electrochemical Methods: Fundamentals and Applications*, John Wiley & Sons, New York, 2nd edn., 2001.

[34] H. S. Carslaw and J. C. Jaeger, *Conduction of Heat in Solids*, Oxford University Press, 2nd edn., 1986.

[35] L. Boltzmann, *Wied. Ann.*, 1894, **53**, 959–964.

[36] A. D. MacGillivray, *J. Chem. Phys.*, 1968, **48**, 2903–2907.

Chapter 5

Diffuse double layer: equilibrium

In the previous chapter, significant dynamic features of non-equilibrium charge transport driven by a concentration gradient were discussed. This chapter introduces the electrochemical cell, and presents analysis of the equilibrium of the diffuse double layer at the surface of a working electrode, with particular reference to non-classical behaviour at nanoelectrodes. These concepts provide a framework for the study of dynamic charge transport in an electrochemical cell. This work has been published by the Journal of Physical Chemistry C,[1] and this chapter also draws on discussions published by the Journal of Electroanalytical Chemistry.[2,3]

5.1 The electrochemical cell

When two electrically conducting electrodes are connected by a wire and then immersed in an electrolytic solution, a closed electrical circuit is formed, because the electrolytic solution is also conducting. If no reaction in solution can occur by electron transfer to or from an immersed electrode, the electrode is described as *ideally polarisable*.[4]

Then, when the potential difference between the two electrodes is altered, any current drawn is due to ionic transport rather than due to electron transfer associated with a heterogeneous reaction at the electrode-solution interface. This chapter and Chapter 6 discuss ionic transport; in Chapters 7–10, current due to heterogeneous reactions (so-called "Faradaic current") will be considered.

One electrode is typically a standard reference electrode, meaning an electrode with a rest potential that is well established on a standard scale. By international convention, the potential scale for electrochemical cells is calibrated to the standard hydrogen electrode, in which an aqueous solution with unit activity of protons (pH 0) is in equilibrium with 1 bar hydrogen gas at a platinum electrode. A more practical reference electrode in aqueous solution is the saturated calomel electrode, in which a saturated aqueous solution of chloride ions is in equilibrium with solid mercurous chloride in contact with a liquid mercury electrode.[4]

Having established a reference potential, such that the potential difference between the two electrodes can be measured consistently, current drawn by the system is measured at the other electrode, which is described as the working electrode. The reference electrode is termed 'ideal' if a potentiostat can be used to apply a potential difference between the working and reference electrodes in which the potential at the reference electrode is unchanged, such that only conditions at the working electrode are perturbed. This standard setup, with an ideally polarisable working electrode, is indicated at Figure 5.1.

For the purposes of discussing non-Faradaic current due to ionic transport, it will be assumed that the potential of the reference electrode is negligibly perturbed by acting as a counter electrode in passing the current through the circuit. This issue will

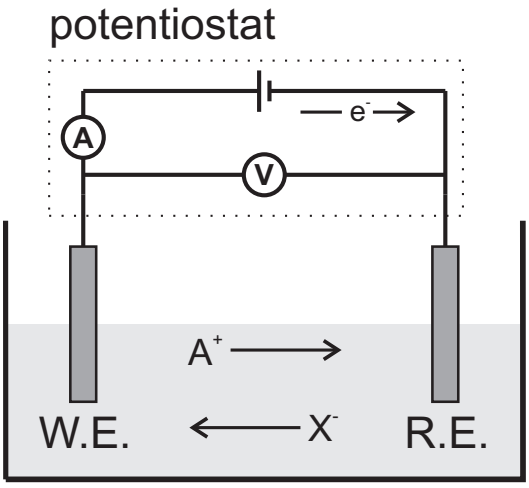

Figure 5.1: Schematic of an idealised electrochemical cell illustrating a simplified potentiostatic circuit. W.E.: working electrode; R.E.: reference electrode. The current carried through the circuit is carried by electrons in the wire and by ions in the solution, with concomitant accumulation or depletion of ions at the electrode interfaces as the electrode charge alters.

be considered more practically in Chapter 7.

Each electrode will have a certain excess charge due to the population of electrons in its conduction bands, which is described as a Fermi level and corresponds to the electron energy, or electrical potential. An electrode may be either positively or negatively charged, and this is quantified by the surface potential of the electrode. Considering the relation of the different potentials in the system, let us define the dimensional potential between the working and reference electrodes as E:

$$E \equiv (\phi_{\mathrm{w}} - \phi_{\mathrm{s}}) - (\phi_{\mathrm{ref}} - \phi_{\mathrm{s}}) \tag{5.1}$$

where ϕ_{w} is the potential of the working electrode, ϕ_{s} is the potential of bulk solution, and ϕ_{ref} is the potential of the reference electrode. All of these potentials are absolute. Further, let us set ϕ_{s} as the reference potential for the entire system, so on this absolute scale, $\phi_{\mathrm{s}} \equiv 0$ and:

$$E = \phi_{\mathrm{w}} - \phi_{\mathrm{ref}} \tag{5.2}$$

Now, we introduce a *potential of zero charge*, E_{pzc}, which is the applied potential difference such that the working electrode is uncharged, i.e. the value of E for which $\phi_{\mathrm{w}} = \phi_{\mathrm{s}} = 0$, such that the working electrode has zero excess charge with respect to bulk solution. Therefore:

$$E_{\mathrm{pzc}} = -\phi_{\mathrm{ref}} \tag{5.3}$$

and

$$\phi_{\mathrm{w}} = E - E_{\mathrm{pzc}} \tag{5.4}$$

Therefore, the potential difference between the working electrode and bulk solution may be determined from the difference between the two measurable parameters E and E_{pzc}. In normalised units this will be termed an *overpotential* and is written:

$$\theta_0 = \frac{F}{RT}\left(\phi_{\mathrm{w}} - \phi_{\mathrm{s}}\right) = \frac{F}{RT}(E - E_{\mathrm{pzc}}) \tag{5.5}$$

in which both E and E_{pzc} are measured with respect to a common reference electrode.

5.2 The double layer

5.2.1 Definition

The *double layer* is the region of an electrolytic solution close to the surface of an electrode where an electric field exists due to the excess charge on the electrode. The offset of the Fermi level from the bulk solution potential corresponds to either accumulation or depletion of electrons at the electrode surface, and hence a Coulombic force acts on ions in solution. At equilibrium, the excess electrode charge is balanced by an opposite excess charge in the adjacent solution, which screens the electric field due to

the electrode.

5.2.2 Derivation of Gouy–Chapman theory

The first theoretical treatment of the double layer was by Helmholtz and pre-dated the understanding of ionic dissociation in solution, such that he treated the double layer as an ideal capacitor.[5] Gouy and Chapman independently developed a theory for a diffuse double layer in which the electrolytic solution theories in Chapter 1 are applied at equilibrium.[6,7]

For a monovalent binary electrolyte A^+X^-, the Gouy–Chapman theory is developed as follows. We take the working electrode surface to be held at a constant potential θ_0 with respect to bulk solution. Each ion is at equilibrium in the electric field, so the Boltzmann equation holds for each ion:

$$c_i = \exp(-z_i\theta) \tag{5.6}$$

where the concentration is normalised to the concentration of AX in bulk solution (C^*) where $\theta = 0$, such that this is a normalised simplification of Equation 1.33.

The electrode is assumed to be very large with respect to the double layer, and so the double layer geometry is approximated as linear. We will normalise the linear space to the Debye length, as in the previous chapter. In this geometry, the Poisson equation is then:

$$\frac{d^2\theta}{dX^2} + \frac{\mathrm{e}^{-\theta} - \mathrm{e}^{+\theta}}{2} = 0 \tag{5.7}$$

or

$$\frac{d^2\theta}{dX^2} - \sinh\,\theta = 0 \tag{5.8}$$

subject to $\theta = \theta_0$ at $X = 0$ and $\theta \to 0$ as $X \to \infty$. Since this equation is a function of the variable θ only, by incorporation of the equilibrium Boltzmann equation, it is termed the *Poisson–Boltzmann equation*.

Although non-linear, this equation can be solved using the identity:

$$\frac{d^2}{dX^2} = \frac{1}{2}\frac{d}{d\theta}\left(\frac{d\theta}{dX}\right)^2 \tag{5.9}$$

so that integrating from bulk solution inwards

$$\begin{aligned}\left(\frac{d\theta}{dX}\right)^2 - \left(\frac{d\theta}{dX}\bigg|_{X\to\infty}\right)^2 &= 2\int_0^\theta \sinh\theta'\, d\theta' \\ &= 2\left(\cosh\,\theta - 1\right) \\ &= 4\,\sinh^2\left(\frac{\theta}{2}\right)\end{aligned} \tag{5.10}$$

The condition of constant $\theta = 0$ as $X \to \infty$ constrains that the electric field tends to zero in the same limit, so:

$$\begin{aligned}\left(\frac{d\theta}{dX}\right)^2 &= 4\,\sinh^2\left(\frac{\theta}{2}\right) \\ \frac{d\theta}{dX} &= \pm 2\,\sinh\left(\frac{\theta}{2}\right)\end{aligned} \tag{5.11}$$

Since if $\theta > 0$, $d\theta/dX < 0$ to satisfy $\theta \to 0$ as $X \to \infty$, and so the sign must be negative. A further integration, this time from the electrode into solution, gives:

$$\int_{\theta_0}^{\theta} \frac{d\theta'}{2\sinh\left(\frac{\theta}{2}\right)} = -\int_0^X dX' = -X \tag{5.12}$$

The integral on the left is evaluated as follows:

$$\begin{aligned}\int_{\theta_0}^{\theta} \frac{d\theta'}{2\sinh\left(\frac{\theta'}{2}\right)} &= \int_{\theta_0}^{\theta} \frac{d\theta'}{4\sinh\left(\frac{\theta'}{4}\right)\cosh\left(\frac{\theta'}{4}\right)} \\ &= \int_{\theta_0}^{\theta} \frac{d\left(\tanh\left(\frac{\theta'}{4}\right)\right)}{\tanh\left(\frac{\theta'}{4}\right)} \\ &= \ln\left|\frac{\tanh\left(\frac{\theta}{4}\right)}{\tanh\left(\frac{\theta_0}{4}\right)}\right|\end{aligned} \tag{5.13}$$

Therefore:

$$\mathrm{e}^{-X} = \frac{\tanh\left(\frac{\theta}{4}\right)}{\tanh\left(\frac{\theta_0}{4}\right)} \tag{5.14}$$

which is the Gouy–Chapman expression for the potential distribution of a double layer consisting only of a monovalent binary salt. This type of double layer is described as a *diffuse double layer* because the charge in the double layer is due to a diffuse excess of one charge of ions in the dissociated electrolyte.

Note that the Gouy–Chapman equation may be re-arranged to:[3,8]

$$\theta = \mathrm{sgn}(\theta_0)\ \ln\left|\coth^2\left(\frac{X + X_0}{2}\right)\right| \tag{5.15}$$

where

$$X_0 = 2\,\mathrm{arccoth}\left(\exp\left(\frac{|\theta_0|}{2}\right)\right) \tag{5.16}$$

5.2.3 Properties of the Gouy–Chapman diffuse double layer

The Taylor series of $\tanh x$ about $x = 0$ is:

$$\tanh x = x + ... \tag{5.17}$$

such that if $|\theta_0| \ll 1$, then because $|\theta| \leq |\theta_0|$, the Gouy–Chapman expression tends to:

$$\theta \approx \theta_0\,\mathrm{e}^{-X} \tag{5.18}$$

Therefore, for an overpotential significantly less than RT/F, the potential profile is predicted to decay exponentially on the scale of the Debye length. This confirms the understanding of the Debye length as the distance over which electric fields are screened in an electrolytic solution, as was introduced by the dimensional analysis in Section 1.3. In this case, the positive and negative surface excesses of oppositely and similarly charged ions, respectively, screen the electric field due to excess charge on the electrode over a distance of a few Debye lengths.

The charge contained in the double layer can be calculated by integration of the Poisson equation, defining a normalised charge (per unit area) Q':

$$Q'(X) \equiv \frac{d\theta}{dX} = \frac{1}{2}\int_X^\infty \left(\sum_i z_i c_i\right) dX \tag{5.19}$$

such that from the normalisation definitions in Chapter 2:

$$Q' = \frac{q'}{2FC^* x_\mathrm{D}} = \frac{q'}{(2RT\epsilon_\mathrm{s}\epsilon_0 C^*)^{\frac{1}{2}}} \tag{5.20}$$

where q' is the dimensional charge per area.

Accordingly, the normalised separated charge on both the electrode and the double layer, at equilibrium is given by $|Q'(0)|$, which is:

$$Q'_\mathrm{DL} = 2\sinh\left(\frac{|\theta_0|}{2}\right) \tag{5.21}$$

from Equation 5.11. The excess charge on the electrode is exactly opposite to the charge on the double layer, from the requirement of overall electroneutrality at equilibrium. In the linear regime at low overpotential, a first order Taylor series approximation gives:

$$Q'_\mathrm{DL} \approx |\theta_0| \tag{5.22}$$

i.e. a linear relationship between applied potential and double layer charge.

The differential capacitance of the double layer is defined as the partial derivative of electrode charge with respect to applied potential. Hence, defining the normalised differential capacitance (per area) as K'_{d}:

$$K'_{\mathrm{d}} = \frac{\partial Q'_{\mathrm{DL}}}{\partial \theta_0} = \cosh\left(\frac{|\theta_0|}{2}\right) \tag{5.23}$$

Again, from the normalisation definitions, this can be related to the dimensional differential capacitance per unit area (C'_{d}) as:

$$K'_{\mathrm{d}} = \frac{C'_{\mathrm{d}}}{C'^{*}_{\mathrm{d}}} = C'_{\mathrm{d}} \frac{x_{\mathrm{D}}}{\epsilon_{\mathrm{s}}\epsilon_0} \tag{5.24}$$

At low overpotential where $K'_{\mathrm{d}} \approx 1$, $C'_{\mathrm{d}} \approx \epsilon_{\mathrm{s}}\epsilon_0/x_{\mathrm{D}}$, which implies typical dimensional values of C'_{d} in the range 5–200 μF cm^{-2}.

5.3 Extension to a hemispherical space

The Gouy–Chapman description of the diffuse double layer assumes that the electrode is much larger than the double layer. For a nanoelectrode, where the dimensions of the electrode approach the Debye length of a typical electrolytic solution, this is no longer true. Experimental nanoelectrode systems have become increasingly common for practical applications in the last decade, together with novel fabrication and characterisation techniques, as illustrated by some examples from the literature.[9–13] The theory associated with nanoscale double layers remains relatively undeveloped, however. A study of the equilibrium condition of the double layer is therefore a necessary stage before the dynamics of nanoscale double layers can be considered.

The theory of the diffuse double layer will be extended here to consider a nanoscale double layer, by solving the Poisson–Boltzmann equation in a hemispherical space sur-

rounding an electrode with a given radius $r = r_e$. Some previous literature exists concerning such a solution. Debye and Hückel solved the spherical Poisson–Boltzmann equation subject to the approximation of linearised potential ($\theta \ll 1$), in their determination of the time-averaged charge distribution surrounding an ion.[14] In addition, a variety of analytical and numerical solutions of the Poisson–Boltzmann equation, involving varying degrees of approximation, have been presented for planar, cylindrical and spherical geometries.[15–22] However, the practical electrochemical interpretation of size or ionic strength effects on the double layer, in the spherical case, has been neglected by all past workers, to the best of the author's knowledge.

5.4 Limitations of the Gouy–Chapman model

The Gouy–Chapman model takes no account of the finite size of ions. Stern modified the Gouy–Chapman theory by including an 'outer Helmholtz plane', which is the plane of closest approach of solvated ions to the electrode surface.[23] A compact layer of adsorbed solvent molecules inside this plane also contributes to the screening of the electric field, which falls off according to Coulomb's law through this electroneutral layer. Grahame clarified the modern mathematical form of the Gouy–Chapman–Stern theory, and also considered the influence of specific adsorption of ionic species on the electrode.[24] This latter effect is very commonly encountered in practice, which greatly complicates the experimental verification of theories concerning the behaviour of the 'free' electrolytic solution close to the electrode.

In employing the Poisson–Boltzmann equation to describe the diffuse double layer at a nanoelectrode, we implicitly accept certain assumptions. In effect, we are confined

to consider nanoelectrodes with sufficient excess charge for classical theory to remain applicable. As such, this theory does not consider quantised charging or Coulomb staircase effects.[25–27] Equally, the effects of finite ion volume and finite ion number, as well as maximum ionic concentrations in the close packing limit are ignored, and the permittivity of the medium is assumed to be uniform: however, given the finite size of ions there is a maximum ionic concentration that can feasibly be present in the diffuse double layer. As early as 1947, Grahame wrote that "the neglect of [ionic] crowding is likely to prove to be the most serious defect of the kinetic theories of the diffuse double layer now in vogue".[24] Some attempts to account for this by modification of the Poisson–Boltzmann equation have been presented.[28]

The intention of this work is to develop classical theory to include the hemispherical geometry, such that physical effects attributable to the increased curvature of the diffuse double layer can be recognised. It is not intended to provide a comprehensive, detailed model of an experimentally realisable diffuse double layer. Since the original publication of this work, some of the effects ignored here have recently been discussed by Wang et al.[29]

5.5 Theoretical model

5.5.1 Geometry and normalisation

For a study in the hemispherical space surrounding an electrode, we choose to normalise the space to the electrode radius ($x^* = r_e$), such that the space domain is $1 \leq R < \infty$ where $R = 1$ is the electrode surface. Then, the Poisson–Boltzmann equation in

hemispherical space, for a monovalent binary electrolyte A^+X^-, is:

$$\frac{1}{R^2}\frac{d}{dR}\left(R^2\frac{d\theta}{dR}\right) - R_e^2 \sinh\theta = 0 \tag{5.25}$$

where

$$R_e = \frac{r_e}{x_D} \tag{5.26}$$

The appropriate boundary conditions are $\theta = \theta_0$ at $R = 1$ and $\theta \to 0$ as $R \to \infty$.

The normalised charge (per area) can be constructed in this geometry as follows:

$$Q'(R) = \frac{1}{R_e}\frac{d\theta}{dR} = \frac{R_e}{2}\int_R^\infty \left(\sum_i z_i c_i\right) R^2\, dR \tag{5.27}$$

hence

$$Q'_{DL} = -\frac{1}{R_e}\left.\frac{d\theta}{dR}\right|_{R=1} \tag{5.28}$$

where the division by R_e ensures that Q' and K'_d are identically normalised in the hemispherical space. Note that Q'_{DL} represents a separated charge; the sign of the charge is in fact opposite in the solution. The corresponding Gouy–Chapman expressions (Equations 5.21 and 5.23) can be referred to as the planar double layer limit.

5.5.2 Gridding and computation

For the numerical work, an expanding R grid was used, according to the definitions in Section 3.2. For computational convenience, the outer boundary condition is applied at a finite distance $R = R_{max}$, which is set to a large number, typically $R = 10^5$. It was verified that altering R_{max} to a larger number had no effect on the simulation results. Converged parameters for the expanding space grid were established by a detailed convergence study at varying R_e and θ_0, using Q' as a diagnostic observable; the optimal parameters were $\gamma_R = 10^{-4}$ and $R_s = 10^{-6}$.

The second derivative is centrally differenced, and the iterative Newton–Raphson method is applied to solve the ODE with an initial guess of $\theta = 0$ over all space, which was unconditionally convergent for $|\theta_0| < 15$ with the above gridding parameters. The Jacobian matrix is three-diagonal since there is only one variable. A concentration and potential profile could typically be generated for a given parameter set in less than one second.

5.6 Analytical theory

5.6.1 Low overpotential

The hemispherical Poisson–Boltzmann equation cannot be solved analytically in full, but it can be solved in the low potential (Debye–Hückel) limit. The Debye–Hückel approximation takes $\theta \ll 1$, and so $\sinh(\theta) \approx \theta$, thus linearising the equation to:[14]

$$\frac{1}{R^2}\frac{d}{dR}\left(R^2\frac{d\theta}{dR}\right) - R_\mathrm{e}^2\,\theta = 0 \tag{5.29}$$

Linear problems in spherical symmetry of this type are often solved by a substitution of the form $\chi = R \cdot \theta$, which yields:

$$\frac{\partial^2\chi}{\partial R^2} - R_\mathrm{e}^2\,\chi = 0 \tag{5.30}$$

subject to

$$\begin{aligned} R = 1 \qquad & \chi = \theta_0 \\ R \to \infty \qquad & \frac{\chi}{R} \to 0 \end{aligned} \tag{5.31}$$

The equation can be rewritten as:

$$\frac{1}{2}\frac{\partial}{\partial\chi}\left(\frac{\partial\chi}{\partial R}\right)^2 = R_\mathrm{e}^2\,\chi \tag{5.32}$$

Since

$$\frac{\partial\theta}{\partial R} = \frac{1}{R}\left(\frac{\partial\chi}{\partial R} - \frac{\chi}{R}\right) \tag{5.33}$$

we can conclude that $\partial\chi/\partial R \to 0$ as $R \to \infty$, and so from integration:

$$\begin{aligned}\left(\frac{\partial\chi}{\partial R}\right)^2 &= -2R_\mathrm{e}^2\int_0^\chi \chi'\,d\chi' \\ &= -R_\mathrm{e}^2\,\chi^2\end{aligned} \tag{5.34}$$

and

$$\frac{\partial\chi}{\partial R} = -R_\mathrm{e}\,\chi \tag{5.35}$$

From Gauss's Law for a spherical space, we can relate the potential gradient at the electrode surface to its enclosed charge. Normalisation of Equation 1.17 gives:

$$\begin{aligned}Q'_\mathrm{DL} &= -\frac{1}{R_\mathrm{e}}\left.\frac{\partial\theta}{\partial R}\right|_{R=1} \\ &= -\frac{1}{R_\mathrm{e}}\left(\left.\frac{\partial\chi}{\partial R}\right|_{R=1} - \chi_0\right) \\ &= -\frac{1}{R_\mathrm{e}}\left(-R_\mathrm{e}\,\theta_0 - \theta_0\right) \\ &= \theta_0\left(1 + \frac{1}{R_\mathrm{e}}\right)\end{aligned} \tag{5.36}$$

and hence

$$K'_\mathrm{d} = 1 + \frac{1}{R_\mathrm{e}} \tag{5.37}$$

For a large electrode, as $R_\mathrm{e} \to \infty$, the hemispherical result agrees with the Gouy–Chapman prediction that $K'_\mathrm{d} \approx 1$ for low overpotential (Equation 5.23). However, the second term in the hemispherical equation suggests an additional 'excess' double layer

capacitance due to the hemispherical nature of the diffuse double layer, which becomes significant as $R_e \to 1$, i.e. where $r_e \to x_D$. This is the case for nanoelectrodes, where an augmented capacitance is expected due to the curvature of the double layer.

5.6.2 Solution at a point charge

Although the situation $r_e \ll x_D$ is not practically realisable because it implies an electrode of atomic scale, it is an instructive limiting case to consider theoretically. In this limit, $R_e \to 0$, and therefore from the Poisson equation:

$$\nabla^2\theta = \frac{1}{R^2}\frac{d}{dR}\left(R^2\frac{d\theta}{dR}\right) \to 0 \tag{5.38}$$

This is equivalent to the equation for the electric field due to a point charge in vacuum, and the solution has the familiar Coulombic form:

$$\frac{d\theta}{dR} = -\frac{\theta_0}{R^2} \tag{5.39}$$

In this limit

$$Q'_{DL} = \frac{\theta_0}{R_e} \tag{5.40}$$

and

$$K'_d = \frac{1}{R_e} \tag{5.41}$$

i.e. the capacitance per unit area becomes independent of the applied potential, but also becomes dependent on the electrode radius, as suggested by the low potential analysis above. Irrespective of the applied potential, no classical double layer is predicted in this limit because the electric field becomes negligible across a distance considerably less than the Debye length. In effect, the charge separation no longer contributes to screening the electric field.

Clearly a real nanoelectrode will not display the same behaviour as for a point charge, where r_e is required to be much smaller than atomic scale, but as $r_e \to x_D$, we can expect nanoelectrode behaviour to more closely resemble the Coulomb solution with an ideal inverse square dependence for the electric field. Therefore, the nanoelectrode regime where $r_e \approx x_D$ is expected to be intermediate between a potential-dependent diffuse double layer of the Gouy–Chapman type, and a potential-independent spherical layer of charge of the Coulomb type.

5.7 Numerical results and discussion

5.7.1 Diffuse double layer at high overpotential

The conclusions developed above by the analysis of the point charge and low overpotential limiting cases can now be developed by simulation, as numerical methods allow the Poisson–Boltzmann equation to be solved in hemispherical space for any values of θ_0 and R_e.

An initial study was performed for a potential step to $\theta_0 = 5$, which in dimensional units is a potential step to $E - E_{pzc} \approx 130$ mV. Figure 5.2 shows simulated results for normalised surface charge density, Q'_{DL}, as a function of R_e (and hence r_e).

A size-dependent transition is indeed observed between the Coulomb and Gouy–Chapman limits as the double layer becomes relatively spherical for small electrode sizes and relatively planar for large electrode sizes, even at high overpotential where the analysis in Section 5.6.1 does not apply. In the limit $R_e \to 0$ and $R_e \to \infty$, the expected asymptotic behaviours are attained. The region of transition is detailed at Figure 5.3.

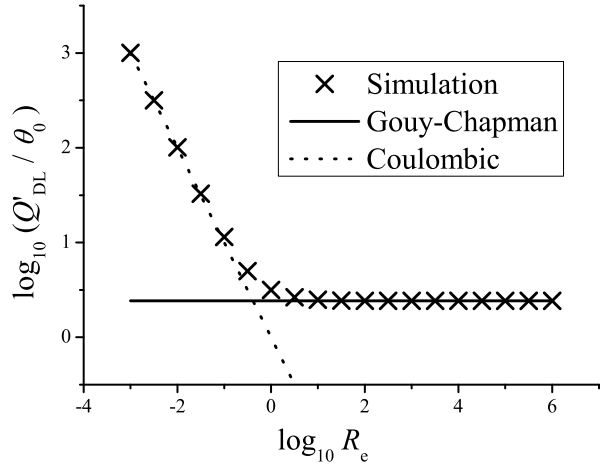

Figure 5.2: Comparison of the equilibrium charge on the double layer, Q'_{DL}, to the Coulombic and Gouy–Chapman limiting cases as a function of R_{e}.

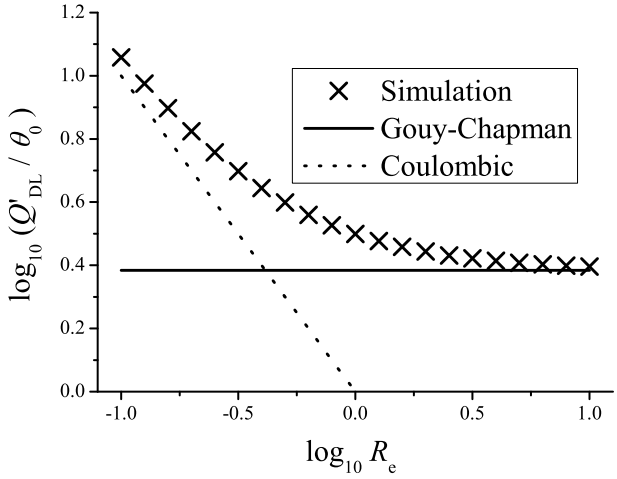

Figure 5.3: Equilibrium charge on the double layer, Q'_{DL}, in the transition region of R_{e} between the Coulombic and Gouy–Chapman limiting cases.

5.7.2 Effect of electrode radius

Having established trends in the system parameters R_{e}, a real system can be modelled by setting $T = 298$ K and $\epsilon_{\mathrm{s}} = 78.54$. Bulk concentrations of 1 mM and 100 mM were considered, and a charging potential of $\theta_0 = 5$ was assumed. The results are presented at Figure 5.4.

At $r_{\mathrm{e}} > 50$ nm, a constant excess charge per unit area is observed in the diffuse

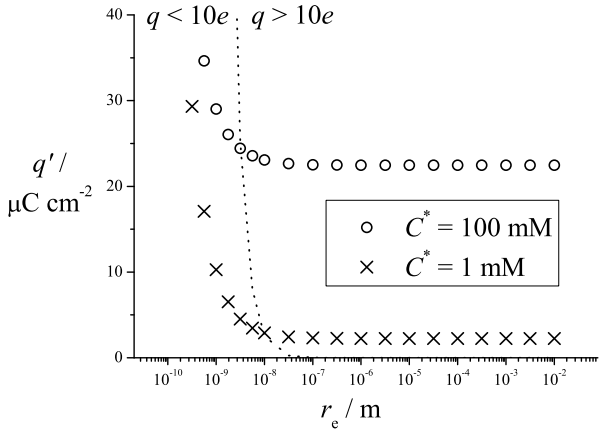

Figure 5.4: Simulated q' as a function of r_e, for aqueous solutions at room temperature.

double layer, irrespective of electrode size, exactly as predicted by the Gouy-Chapman model. By comparison, substantial excess charge density is predicted for nanoelectrodes. At a lower ionic strength, the Debye length is longer, and so the effect of double layer curvature is observed at larger electrode sizes. Note that in the case C^* = 1 mM, the charge density increases more rapidly as r_e is reduced than is the case for C^* = 100 mM, since the Debye length is longer in the former case.

Left of the division marked in Figure 5.4, the charge on the electrode is less than 10 electron charges, such that quantum and single-ion effects may be expected to dominate and hence our theory is not appropriate. For both concentrations, however, double layer curvature induces deviations of several per cent from the classical planar Gouy-Chapman theory at electrode radii larger than those where quantised charging is expected.

5.7.3 Analysis in terms of differential capacitance

For an ideal Coulombic point charge, the differential capacitance is (Equations 5.24 and 5.41):

$$C'_{\mathrm{d}} = \frac{\epsilon_s \epsilon_0}{r_{\mathrm{e}}} \tag{5.42}$$

i.e. not a function of potential.

Equivalently, for the Gouy-Chapman model for a planar electrode, the differential capacitance is (Equations 5.23 and 5.24):

$$C'_{\mathrm{d}} = \frac{\epsilon_s \epsilon_0}{x_{\mathrm{D}}} \cosh\left(\frac{F}{2RT}(E - E_{\mathrm{pzc}})\right) \tag{5.43}$$

i.e. an approximately exponential function of potential, at large overpotential.

Theoretical differential capacitance curves were produced by simulating q' at various values of $(E - E_{\mathrm{pzc}})$ and differentiating the resulting curves numerically. The simulated results for $C^* = 1$ mM and varying electrode size are shown at Figure 5.5, again demonstrating a transition in the behaviour of the diffuse double layer for electrode radii in the nanoscale region.

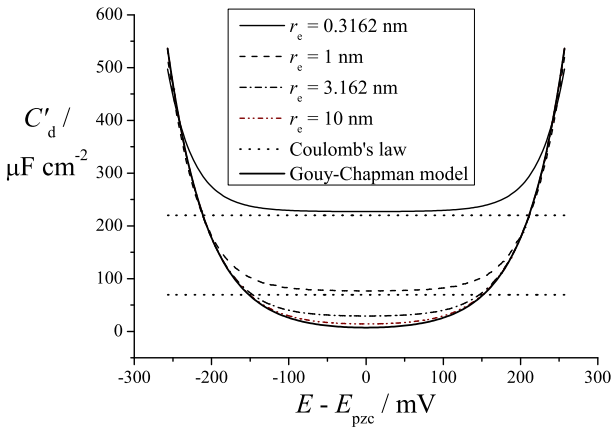

Figure 5.5: Simulated differential capacitance curves for electrodes of varying sizes, shown with the theoretical predictions of Coulomb's law (for the two smallest radii cases) and the planar Gouy–Chapman model. $r_{\mathrm{e}} = 0.3162$, 1, 3.162 and 10 nm; aqueous solution at room temperature is assumed.

For reduced electrode radius, Coulombic behaviour, where capacitance is not a function of potential, is observed across an increased potential window either side of E_{pzc}. The smallest electrodes here are presented for continuity of theory rather than to represent any real behaviour for hypothetical sub-nanoscale electrodes. Nonetheless, the attainment of Coulombic behaviour is general to $R_{\mathrm{e}} \to 0$ and it is therefore projected that at micromolar concentrations where the Debye length is several tens of nanometres, Coulombic behaviour should be observable for nanoscale electrodes where the absolute charge of the double layer is sufficiently large to neglect single-ion effects.

5.8 Conclusions

A rational approach to analysis of numerical solutions of the Poisson–Boltzmann equation in a hemispherical space demonstrates that the diffuse double layer at a charged nanoelectrode must differ significantly from the predictions of classical planar Gouy–Chapman theory. Marked curvature of the double layer, which arises when the electrode radius is of similar size to the Debye length, causes qualitatively altered diffuse double layer properties for nanoelectrodes with $r_{\mathrm{e}} < 50$ nm, for typical concentrations of electrolyte. As the ionic strength is reduced, deviations from classical theory are expected to occur for larger electrodes.

These curvature effects include excess double layer charge and constant, Coulombic differential capacitance across an increased potential window. For small overpotentials, double layer curvature causes electric fields to tend towards the ideal situation of a Coulombic point charge, and a Gouy–Chapman diffuse double layer with an exponentially decaying electric field is no longer observed. For smaller electrodes or lower ionic

strengths, the capacitive properties of the diffuse double layer will obey Coulomb's law, rather than the Gouy–Chapman equation, over a wider potential window.

The comprehensive analysis of the equilibrium of a diffuse double layer for a hemispherical ideally polarisable electrode provides a framework for dynamic charge transport problems in this system. In the next chapter, the time-dependent Nernst–Planck–Poisson equation set is employed in order to consider how equilibrium is recovered following perturbation of this system, with particular reference to capacitive charging of the diffuse double layer following a potential step.

Bibliography

[1] E. J. F. Dickinson and R. G. Compton, *J. Phys. Chem. C*, 2009, **113**, 17585–17589.

[2] E. J. F. Dickinson and R. G. Compton, *J. Electroanal. Chem.*, 2011, **655**, 23–31.

[3] E. J. F. Dickinson and R. G. Compton, *J. Electroanal. Chem.*, 2011, **661**, 198–212.

[4] A. J. Bard and L. R. Faulkner, *Electrochemical Methods: Fundamentals and Applications*, John Wiley & Sons, New York, 2nd edn., 2001.

[5] H. Helmholtz, *Wied. Ann.*, 1879, **7**, 337–382.

[6] L. G. Gouy, *C. R. Hebd. Séances Acad. Sci.*, 1909, **149**, 654–657.

[7] D. L. Chapman, *Philos. Mag.*, 1913, **25**, 475–481.

[8] V. Levich, *Dokl. Akad. Nauk SSSR*, 1949, **67**, 309–312.

[9] R. W. Murray, *Chem. Rev.*, 2008, **108**, 2688–2720.

[10] D. Krapf, M.-Y. Wu, R. M. M. Smeets, H. W. Zandbergen, C. Dekker and S. G. Lemay, *Nano Lett.*, 2006, **6**, 105–109.

[11] P. Hugelmann, M. Hugelmann and W. Schindler, *J. Electroanal. Chem.*, 2008, **612**, 131–139.

[12] H. Li and N. Wu, *Nanotechnology*, 2008, **19**, 275301.

[13] Y. Liu, Y. Zhu, Y. Zeng and F. Xu, *Nanoscale Res. Lett.*, 2009, **4**, 210–215.

[14] P. Debye and E. Hückel, *Physik. Z.*, 1923, **24**, 185–206.

[15] F. H. Stillinger, Jr., *J. Chem. Phys.*, 1961, **35**, 1584–1589.

[16] A. J. Loeb, J. Overbeek and P. Wiesema, *The Electrical Double Layer Around a Spherical Colloid Particle*, MIT Press, Cambridge, Mass., 1961.

[17] J. R. Delmastro and G. L. Booman, *J. Electroanal. Chem.*, 1971, **32**, 157–163.

[18] A. N. Stokes, *J. Chem. Phys.*, 1976, **65**, 261–264.

[19] J. Frahm and S. Diekmann, *J. Colloid Interface Sci.*, 1979, **70**, 440–447.

[20] B. Tenchov and I. Brankov, *J. Colloid Interface Sci.*, 1986, **109**, 172–180.

[21] Z.-W. Wang, G.-Z. Li, X.-Z. Yi, D.-R. Guan and A.-J. Lou, *J. Dispersion Sci. Technol.*, 2001, **22**, 349–354.

[22] R. Tuinier, *J. Colloid Interface Sci.*, 2003, **258**, 45–49.

[23] O. Stern, *Z. Elektrochem.*, 1924, **30**, 508–516.

[24] D. C. Grahame, *Chem. Rev.*, 1947, **41**, 441–501.

[25] J. R. Reimers and N. S. Hush, *J. Phys. Chem. B*, 2001, **105**, 8979–8988.

[26] S. Chen and R. W. Murray, *J. Phys. Chem. B*, 1999, **103**, 9996–10000.

[27] R. S. Ingram, M. J. Hostetler, R. W. Murray, T. G. Schaaff, J. Khoury, R. L. Whetten, T. P. Bigioni, D. K. Guthrie and P. N. First, *J. Am. Chem. Soc.*, 1997, **119**, 9279–9280.

[28] C. W. Outhwaite, *Condens. Matter Phys.*, 2004, **7**, 719–733.

[29] H. Wang and L. Pilon, *J. Phys. Chem. C*, 2011, **115**, Article ASAP, doi: 10.1021/jp204498e.

Chapter 6

Diffuse double layer: capacitive charging

In this chapter, the dynamics of the hemispherical diffuse double layer at an ideally polarisable electrode are considered for different capacitive charging experiments. In particular, the non-equilibrium charge transport predicted using the Nernst–Planck–Poisson model is compared with results from the common model of an equivalent electrical circuit with a resistor and capacitor in series. The latter is found to be deficient under many conditions. This work has been published by the Journal of Electroanalytical Chemistry.[1]

6.1 Introduction

6.1.1 Capacitive charging

Chapter 5 discussed the equilibrium condition of the diffuse double layer at a charged working electrode, subject to a series of assumptions. If the potential at the working electrode is changed dynamically, however, the diffuse double layer cannot attain its new equilibrium condition instantaneously because charge transport occurs at a

finite rate. The dynamic processes by which the double layer accumulates or disperses charge are collectively termed *capacitive charging*. Measurable currents due to the ionic transport involved in charging or discharging the double layer are a common feature of experimental voltammetry.[2]

Rather than employing the complicated Nernst–Planck–Poisson equation set, capacitive charging is commonly analysed using the RC equivalent circuit (Figure 6.1), in which an ideal resistor and capacitor are considered in series with a voltage source.* The solution is therefore considered to have an ideal, constant and homogeneous resistance, R_s, and the double layer is considered to have an ideal, constant and homogeneous capacitance, C_d.

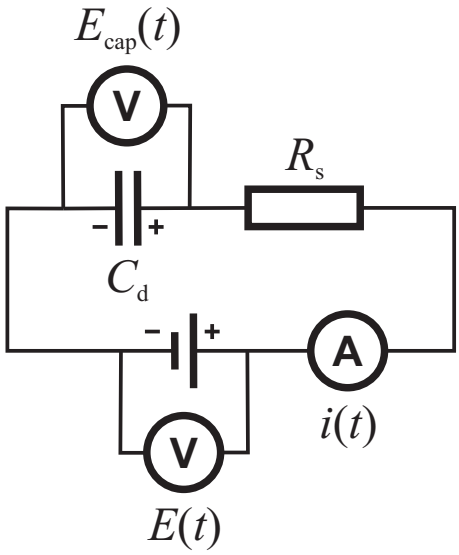

Figure 6.1: Schematic of the RC equivalent circuit.

In Chapter 1, the implausibility of describing electrolytic solution dynamics with constant, homogeneous electrical circuit parameters was highlighted. The strict de-

*Note that while the capacitance C describes the ratio of charge on the capacitor to voltage across it ($E_{\mathrm{cap}}(t)$), the applied potential $E(t)$ is the potential difference associated with the voltage source. These are equivalent only when the current is zero. In the discussion hereafter, capacitance will be understood to refer to the circuit (and the physical system it represents) as a whole, and so E refers to the applied voltage. As shall be demonstrated, this circuit capacitance equals C at zero current.

pendence of the local resistivity or capacitance of an electrolytic solution upon its dynamically varying ionic composition implies that results from the RC circuit model must be treated with caution. In this chapter, a more refined dynamic theory of capacitive charging is established using the time-dependent Nernst-Planck-Poisson equation set. In this way, it is possible to identify the conditions, if any, under which the RC circuit may be considered physically meaningful for describing charge transport in the diffuse double layer. As in the previous chapter, both mathematical and numerical methods are employed as required.

Note that as in the previous chapter, neither the compact layer nor finite ion size effects will be considered, and therefore there is ample opportunity to further refine this theory to describe a more realistic system; nonetheless, a rational study using the Nernst–Planck–Poisson equation set can identify common features of capacitive charging attributable to size effects or non-linear potential regimes, without these being shrouded in the complication of a detailed and extensively parameterised description of the compact double layer. Also, the arguments here will concern ideally smooth electrodes, and so do not incorporate deviations from ideal RC behaviour associated with "constant phase angles" due to electrode surface roughness.[3–5] The aim of this chapter, then, is to reveal the charging behaviour of the diffuse double layer at the interface between an electrolytic solution and an electrode, and to determine regimes where that behaviour differs from that predicted by an ideal RC circuit.

6.1.2 Experimental methods

Two experimental approaches are considered by which the diffuse double layer can be perturbed. The first is a potential step away from the potential of zero charge, such

that an excess charge is rapidly applied to the working electrode by the potentiostat. Double layer charge is then accumulated dynamically under the influence of the electric field until that field is completely screened, i.e. equilibrium is attained. The ionic current passed through the solution is measured such that a plot of current against time (a chronoamperogram) contains information about the capacitive charging dynamics. This current is initially substantial but decays to zero after a certain charging time.

The other experimental approach to be considered is impedance spectroscopy. Here, a sinusoidal voltage waveform away from the potential of zero charge is applied to the working electrode at a given frequency. The ionic current will display a time lag with respect to the input, and therefore by considering the phase shift of different components of the output current with respect to the input frequency, an apparent impedance (complex resistance) can be measured.

The real component of the impedance is the resistance of the system, which is the ratio of current drawn to potential applied with no phase shift; the imaginary component of the impedance is associated with the capacitance of the system, in which a component of the current drawn is phase shifted from the input voltage due to the accumulation and depletion of charge. These results are conventionally presented in a Nyquist plot, in which the real and imaginary impedances are plotted with respect to each other for different input frequencies.[2,6]

6.1.3 Results from the RC equivalent circuit

For the RC circuit (Figure 6.1), we may use Kirchhoff's voltage law to take the sum of voltages across the various components as zero.[7] Defining the applied overpotential

(voltage) as E, the charge on the capacitor as q, and the current as i:

$$E - iR_{\mathrm{s}} - \frac{q}{C_{\mathrm{d}}} = 0 \tag{6.1}$$

Noting that $i = dq/dt$, and rearranging:

$$\frac{dq}{dt} + \frac{q}{R_{\mathrm{s}}C_{\mathrm{d}}} = \frac{E}{R_{\mathrm{s}}} \tag{6.2}$$

such that if a potential step is applied rapidly from initial conditions where $q = 0$, perturbing the system away from equilibrium:

$$q = EC_{\mathrm{d}}\left(1 - \exp\left(\frac{-t}{R_{\mathrm{s}}C_{\mathrm{d}}}\right)\right) \tag{6.3}$$

and

$$i = \frac{\mathrm{d}q}{\mathrm{d}t} = \frac{E}{R_{\mathrm{s}}}\exp\left(\frac{-t}{R_{\mathrm{s}}C_{\mathrm{d}}}\right) \tag{6.4}$$

From the above results, it is clear that $q \to EC_{\mathrm{d}}$ as $t \to \infty$, confirming that the capacitor is ideal. In approaching this equilibrium condition, the capacitive charging current decays exponentially according to a characteristic time constant $R_{\mathrm{s}}C_{\mathrm{d}}$, such that more resistive or more capacitive interfaces will charge more slowly. This is logical since it will take longer to accumulate charge if either less charge can be driven by a voltage in a given time, or more total charge must be accumulated.

In impedance spectroscopy, the impedance spectrum $Z(j\omega) = Z'(\omega) - jZ''(\omega)$ may be inferred from Ohm's law for the linear system by Laplace transformation to a Laplace coordinate $j\omega$ (that is, a one-sided Fourier transform in a coordinate ω):

$$Z(j\omega) = \frac{\bar{V}(j\omega)}{\bar{I}(j\omega)} \tag{6.5}$$

where $\bar{V}$ and $\bar{I}$ are the Laplace transforms of the input potential and the output current respectively; j is the imaginary unit and ω is the spectroscopic frequency. This

approach is valid because the RC circuit system belongs to a class of problems termed linear time-invariant, in which the output is a linear function of the input.[7,8] It follows that:

$$\bar{V} = \frac{E}{j\omega} \tag{6.6}$$

and

$$\bar{I} = \frac{EC_\mathrm{d}}{1 + jR_\mathrm{s}C_\mathrm{d}\omega} \tag{6.7}$$

so

$$Z = \frac{E}{j\omega}\frac{1 + jR_\mathrm{s}C_\mathrm{d}\omega}{EC_\mathrm{d}} = R_\mathrm{s} + \frac{1}{C_\mathrm{d}}\frac{1}{j\omega} = R_\mathrm{s} - j\frac{1}{C_\mathrm{d}\omega} \tag{6.8}$$

Therefore $Z' = R_\mathrm{s}$ and $Z'' = 1/C_\mathrm{d}\omega$, such that the resistive and capacitive components of charging are separated into the real and imaginary components of the impedance, respectively.[6]

The problems above, and others, have been reviewed in the textbook of Bard and Faulkner.[2] In all of the above $q = 0$ has been taken to be zero when $t = 0$, i.e. the step or impedance wave begins exactly at the potential of zero charge of the system. This can rarely be guaranteed in practice.

RC circuit analysis can only be meaningful where the parameters R_s and C_d are constant and independent of the experiment for a given system. Values for these parameters are revealed by the analysis below using the Nernst–Planck–Poisson model, together with the range in which they may be considered physically meaningful.

6.2 Theoretical model

6.2.1 Determination of the appropriate geometry

A great deal of theoretical work has already been performed on the charging dynamics of diffuse double layers, including the effects of applied voltage and solution composition. This work has been reviewed by Bazant et al.[9] and a further recent study by Beunis et al.[10] introduced a variety of limiting cases. The former work also extended the range of known analytical solutions, providing an exact Laplace transform for the transient capacitive current for low applied voltages, where the Nernst–Planck equation can be linearised, as well as applying asymptotic analysis to non-linear cases.

The adoption of a linear geometry is common to almost all of these studies, however. The reason for adopting this geometry is that since the size of the electrode greatly exceeds the typical extent of the double layer, the effect of double layer curvature is assumed to only arise for very small electrodes, as discussed in the previous chapter. The double layer is indeed physically planar to an excellent approximation for electrodes larger than nanoscale, but this argument applies exclusively *at equilibrium*. Immediately following a potential step, the electric field due to the charge on the electrode will extend into the solution in all directions, and so has spherical symmetry, assuming that the cell itself is large with respect to the electrode. Unless the solution is confined to a capillary leading directly to the reference electrode, very little is linear about the geometry of the system, and consideration of a simple model problem underlines this.

Let us suppose that the cell is being held potentiostatically at its potential of zero charge, E_{pzc}, such that solution is electroneutral in the vicinity of the working electrode. Then the cell potential is rapidly stepped to a new potential $E - E_{\mathrm{pzc}}$. If

we assume that reorientation of the polar solvent is much faster than the motion of solvated ions, an electric field is established across solution instantaneously, with the solution remaining roughly electroneutral. The instantaneous potential distribution following the potential step is given by the electroneutral Poisson equation, which is the Laplace equation:

$$\nabla^2\phi = 0 \tag{6.9}$$

with boundary conditions of $\phi = E - E_{\text{pzc}}$ at the electrode, and $\phi \to 0$ in bulk solution. If the geometry is linear and bulk solution is treated as the boundary $x \to \infty$, we immediately encounter a problem since there exists no solution consistent with these boundary conditions.

Of course, we can introduce an arbitrary cell length L such that at $x = L$, the bulk solution boundary $\phi = 0$ holds. Then, the Laplace equation solves to a constant electric field, $\phi = (E - E_{\text{pzc}})(1 - \frac{x}{L})$. However, in this case, we must assume that L is a strong function of the displacement of the reference and working electrodes. We then expect the initial capacitive current to depend strongly on this displacement, even when it is very large, which is a rather nonsensical situation and completely ignores bulk solution which is equally distant from both electrodes, in which range electroneutrality is also retained.

In a hemispherical space, however, the Coulombic solution $\phi = (E - E_{\text{pzc}})(\frac{r_{\text{e}}}{r})$ arises straightforwardly, giving a simple dependence on electrode radius, r_{e}, and no dependence at all on the exact position of the reference electrode, provided it is sufficiently distant and bulk solution is plentifully available. This conforms to expected behaviour and has the added advantage that all length scales are quantified easily and in a manner

that is not arbitrary. Therefore, for the charging problem, it is appropriate to consider mass transport in a hemispherical geometry. In the limit $r_e \gg x_D$, where x_D is the Debye length, the planar Gouy–Chapman equilibrium condition should be recovered in the limit of long time.

6.2.2 Choice of transformed coordinates for analysis

The work of Bazant et al.[9] clarified the importance of a mixed timescale in charging problems, in which both the diffusional timescale and Debye timescale are important. In the hemispherical geometry, these scales are:

$$\tau_{\text{diff}} = \frac{Dt}{r_e^2} \tag{6.10}$$

$$\tau_D = \frac{Dt}{x_D^2} \tag{6.11}$$

corresponding to the time normalisation t^* associated with a space scaled to the electrode ($x^* = r_e$) and a space scaled to the Debye length ($x^* = x_D$), respectively. The influence of the Debye scale was noted in the linear problem of liquid junctions in Chapter 4, and the influence of both scales is evident in the equilibrium condition discussed in Chapter 5.

As in Section 4.4.1, a space normalisation by x_D will render the Poisson equation ideally dimensionless, i.e. without extraneous coefficients. However, a space normalisation by r_e is standard for diffusional processes. Also it is convenient because the electrode boundary is set at $R = 1$, and this normalisation renders the Coulombic field ideally dimensionless (as in Equation 5.39).

Following Bazant et al.,[9] a compromise is achieved by normalising the coordinates

according to a geometric mean of the two scales:

$$x^* = \sqrt{r_\mathrm{e} x_\mathrm{D}} \tag{6.12}$$

and hence

$$t^* = \frac{r_\mathrm{e} x_\mathrm{D}}{D_q} \tag{6.13}$$

where q is the chosen normal species. The hemispherical domain is then $\kappa_\mathrm{e} \leq R < \infty$, where the electrode surface is at $R = \kappa_\mathrm{e}$. From definition:

$$\kappa_\mathrm{e} = \sqrt{\frac{r_\mathrm{e}}{x_\mathrm{D}}} = \sqrt{R_\mathrm{e}} \tag{6.14}$$

In hemispherical space, the time-dependent Nernst–Planck–Poisson equation set is then:

$$\frac{1}{R^2}\frac{\partial}{\partial R}\left(R^2\left(\frac{\partial c_i}{\partial R} + z_i c_i \frac{\partial \theta}{\partial R}\right)\right) - \frac{1}{D_i'}\frac{\partial c_i}{\partial \tau} = 0 \tag{6.15}$$

$$\frac{1}{R^2}\frac{\partial}{\partial R}\left(R^2 \frac{\partial \theta}{\partial R}\right) + \frac{1}{2}\kappa_\mathrm{e}^2 \sum_i z_i c_i = 0 \tag{6.16}$$

Except for nanoelectrodes, the electrode radius is much greater than the Debye length and so $R_\mathrm{e} \gg 1$: in this case $\kappa_\mathrm{e} \gg 1$ will also hold.

6.2.3 Gridding and computation

For the numerical work in this chapter, the time-dependent Nernst–Planck-Poisson equation set was solved using the implicit method, with central differencing of the space derivatives. Both the independent and dependent variables were transformed.

The space R is transformed into a space $-1 \leq y \leq 1$, such that the boundary $R \to \infty$ could be treated exactly within a finite simulation space; the transformation is also chosen in order to achieve smooth concentration profiles both at short time

(Coulomb length scale) and long time (Debye length scale):

$$y = 1 - \left(\frac{\kappa_\mathrm{e}^2}{\kappa_\mathrm{e}^2 + \gamma_1 \, \kappa_\mathrm{e} \, (R - \kappa_\mathrm{e})} + \frac{1}{1 + \gamma_2 \, \kappa_\mathrm{e} \, (R - \kappa_\mathrm{e})} \right) \tag{6.17}$$

The success of subsequent work using a simpler radial transformation, as reported in Chapter 10, tends to suggest that this complicated transformation might be superfluous, if correct gridding parameters for the radial transformation were evaluated.

The space grid expands towards $y = 0$ from both $y = -1$ and $y = 1$, according to the definitions in Section 3.2. An expanding time grid is also optimal, since the potential step causes a strong perturbation of the system following $\tau = 0$; the definitions in Section 3.3 were followed. A convergence study was performed using the capacitive current j_cap at several of orders of τ as the diagnostic variable, and the converged gridding parameters in the transformed space were: $\gamma_1 = 10$, $\gamma_2 = 0.1$, $\gamma_\mathrm{R} = 10^{-3}$, $R_\mathrm{s} = 0.02$, $5 \times 10^{-4} \leq \gamma_\tau \leq 10^{-3}$, and $\tau_\mathrm{s} = 0.1$.

A logarithmic transformation of the dependent variables c_A and c_X is employed, since this was found to greatly improve the convergence properties of the numerical solution:

$$u_i = \ln c_i \tag{6.18}$$

Since all $c_i > 0$, this transformation is mathematically sound. The Nernst–Planck equation is then:

$$D'_i \, (\nabla u_i + z_i \, \nabla \theta) + \mathbf{J}'_i \, \exp(-u_i) = 0 \tag{6.19}$$

such that as flux tends to zero, the equation tends to become linear in this choice of

variable. The time-dependent Nernst–Planck equation is:

$$\begin{aligned}\frac{\partial u_i}{\partial \tau} &= -\frac{1}{c_i}\,\nabla\cdot\mathbf{J'}_i \\ &= \nabla\cdot\left(\frac{\mathbf{J'}_i}{c_i}\right) - \nabla\left(\frac{1}{c_i}\right)\cdot\mathbf{J'}_i \\ &= D'_i\left(\nabla^2 u_i + z_i\nabla^2\theta + \nabla u_i\,\left(\nabla u_i + z_i\,\nabla\theta\right)\right)\end{aligned} \tag{6.20}$$

As a compromise to the enhanced linearity of this equation as equilibrium is approached, the Poisson equation must adopt an exponential dependency:

$$\nabla^2\theta + \frac{1}{2}\,\kappa_{\mathrm{e}}^2\,\left(\mathrm{e}^{u_{\mathrm{A}}} - \mathrm{e}^{u_{\mathrm{X}}}\right) = 0 \tag{6.21}$$

The logic of the transformation is that as equilibrium is approached, the logarithmic variables tend to the simple relations $u_{\mathrm{A}} = -\theta$ and $u_{\mathrm{X}} = +\theta$ according to the Boltzmann equation. By incorporating this natural exponential dependency into the variables used in the iterative Newton–Raphson method, the linearity of the equation set is enhanced and contributions to numerical instability are minimised. One possible example of such an instability would be rounding errors of very large numbers arising from exponential relations: in the transformed variable, we are guaranteed that $|u_i| \leq |\theta_0|$ across all time and space.

6.3 The Debye–Falkenhagen equation

Debye and Falkenhagen analysed the dynamics of double layer charging at low overpotential by applying the Debye–Hückel approximation (Section 5.6.1) to the time-dependent Nernst–Planck–Poisson equation set[11] .

In the course of a charging experiment, it is reasonable to suppose that the largest deviation of any concentration from bulk will be the surface excess, at equilibrium, of

the ion which has the opposite charge as the electrode; that is, in charging the double layer, no ion accumulates transiently in solution to a concentration greater than is achieved in the equilibrium double layer. The normalised surface concentration of the ion of opposite charge is $\exp(|\theta_0|)$ according to the Boltzmann equation. So, if $|\theta_0| \ll 1$ according to the Debye–Hückel approximation, then:

$$c_{i,0} = \mathrm{e}^{-z_i\theta_0} \approx 1 - z_i\theta_0 \tag{6.22}$$

If the concentration over all space is expressed as

$$c_i = 1 + \delta c_i \tag{6.23}$$

then the perturbation term δc_i obeys $|\delta c_i| \leq |\theta_0| \ll 1$ over all space, and so:

$$z_i c_i \frac{\partial\theta}{\partial R} \approx z_i \frac{\partial\theta}{\partial R} \tag{6.24}$$

thus linearising the Nernst–Planck equation.

For the case of an inert binary monovalent electrolyte $\mathrm{A^+X^-}$, if we initially assume $D_\mathrm{A} = D_\mathrm{X}$, then the Nernst–Planck equation for X may be subtracted from that for A, such that defining the dimensionless charge separation as $\rho = c_\mathrm{A} - c_\mathrm{X}$:

$$\begin{aligned}\frac{\partial\rho}{\partial\tau} &= \frac{\partial c_\mathrm{A}}{\partial\tau} - \frac{\partial c_\mathrm{X}}{\partial\tau} \\ &= \Big(\nabla^2 c_\mathrm{A} + \nabla\cdot(c_\mathrm{A}\,\nabla\theta)\Big) - \Big(\nabla^2 c_\mathrm{X} - \nabla\cdot(c_\mathrm{X}\,\nabla\theta)\Big) \\ &= \nabla^2\rho + \nabla\cdot\Big((c_\mathrm{A} + c_\mathrm{X})\,\nabla\theta\Big) \\ &\approx \nabla^2\rho + 2\,\nabla^2\theta\end{aligned} \tag{6.25}$$

From the Poisson equation:

$$\nabla^2\theta = -\frac{1}{2}\,\kappa_\mathrm{e}^2\,\rho \tag{6.26}$$

so, substituting for $\nabla^2\theta$:

$$\frac{\partial\rho}{\partial\tau} = \nabla^2\rho - \kappa_{\mathrm{e}}^2\,\rho \tag{6.27}$$

which is the Debye–Falkenhagen equation. This is a linear equation describing dynamic mass transport of charged species at low potential and hence low deviation from electroneutrality.

The properties of the Debye-Falkenhagen equation following a potential step were discussed in detail for linear space by Bazant et al.[9] In the spherical case, the increased complexity of ∇^2 makes direct solution more challenging. The spherical equation, however, has the estimable advantage of involving no arbitrary length scales. In particular the equation in this geometry is independent of the reference electrode position, so long as it is sufficiently distant from the working electrode. The technique for solution is the removal of radial dependence by introducing a variable $u = R \cdot \rho$, such that the resulting equation is amenable to Laplace transformation by analogy to the linear case. The Poisson equation may be transformed similarly, using $\chi = R \cdot \theta$, as in the equilibrium analysis in Section 5.6.1. The solution of the Debye–Falkenhagen equation in hemispherical space has not been attempted before and is set out below.

6.4 Theory with equal diffusion coefficients

6.4.1 Solving the spherical Debye–Falkenhagen equation

It can be demonstrated that the theory of linear time-invariant systems is applicable to the low potential capacitive charging of a solution with equal diffusion coefficients.

On introducing the substitutions $u = R \cdot \rho$ and $\chi = R \cdot \theta$ to the Debye–Falkenhagen

equation and the Poisson equation:

$$\frac{\partial u}{\partial \tau} = \frac{\partial^2 u}{\partial R^2} - \kappa_e^2 u \tag{6.28}$$

$$\frac{\partial^2 \chi}{\partial R^2} + \frac{1}{2}\kappa_e^2 u = 0 \tag{6.29}$$

An arbitrary input voltage is assumed, in which the surface overpotential θ_0 is a known function $\theta_0(\tau)$.

In the dynamic case, we begin from an initially electroneutral condition at $\tau = 0$:

$$u(0, R) = 0 \tag{6.30}$$

$$\chi(0, R) = \kappa_e \, \theta_0(\tau = 0) \tag{6.31}$$

i.e. a Coulombic potential distribution (Equation 5.39) associated with a given potential difference to bulk solution across an electroneutral space. At $\tau > 0$, the following boundary conditions apply as $R \to \infty$:

$$\frac{u}{R} \to 0 \tag{6.32}$$

$$\frac{\chi}{R} \to 0 \tag{6.33}$$

because bulk solution has a reference potential of zero and is electroneutral. At the electrode ($R = \kappa_e$), both species A and X are inert, and so they have zero flux into or out of the electrode, and the potential is fixed by the input voltage. Hence, at this boundary:

$$\frac{\partial u}{\partial R} - \frac{u}{R} + 2\left(\frac{\partial \chi}{\partial R} - \frac{\chi}{R}\right) = 0 \tag{6.34}$$

$$\frac{\chi}{R} = \theta_0(\tau) \tag{6.35}$$

Using the standard Laplace transformations of partial derivatives in Section 2.5.2, the

Laplace transformation of Equation 6.28, from the time coordinate τ to a Laplace coordinate s, is:

$$\mathcal{L}_{\tau\to s}(6.28) \Rightarrow s\bar{u} = \frac{\partial^2 \bar{u}}{\partial R^2} - \kappa_e^2 \bar{u} \tag{6.36}$$

so that introducing a variable $k = \sqrt{s + \kappa_e^2}$:

$$\frac{\partial^2 \bar{u}}{\partial R^2} - k^2 \bar{u} = 0 \tag{6.37}$$

and solving this ordinary differential equation in R:

$$\bar{u} = A(s)\,\exp(kR) + B(s)\,\exp(-kR) \tag{6.38}$$

where A and B are arbitrary functions of s but not R. Condition (6.32) requires $A(s) = 0$.

Laplace transformation of Equation 6.29 gives, on substituting for $\bar{u}$:

$$\mathcal{L}_{\tau\to s}(6.29) \Rightarrow \frac{\partial^2 \bar{\chi}}{\partial R^2} = -\frac{\kappa_e^2}{2} \cdot B(s) \cdot \exp(-kR) \tag{6.39}$$

Integrating:

$$\int_R^\infty \frac{\partial^2 \bar{\chi}}{\partial R'^2}\, dR' = \frac{-\kappa_e^2}{2} B(s) \int_R^\infty \exp(-kR')\, dR' \tag{6.40}$$

$$\frac{\partial \bar{\chi}}{\partial R} = \frac{\kappa_e^2}{2k}\, B(s) \exp(-kR) \tag{6.41}$$

where the requirement that both $\partial\theta/\partial R$ and θ tend to zero as $R \to \infty$ is sufficient to confine $\partial\chi/\partial R$ as zero in the same limit.

Substitution of this result together with boundary condition (6.35) into boundary condition (6.34) followed by a few lines of algebraic manipulation achieves:

$$B(s) = \frac{-2\bar{\theta}_0(s)}{k + \frac{1}{\kappa_e} - \frac{\kappa_e^2}{k}}\, \exp(k\kappa_e) \tag{6.42}$$

and so

$$\frac{\partial\bar{\chi}}{\partial R} = -\bar{\theta}_0(s)\frac{\kappa_\mathrm{e}^2}{k^2+\frac{k}{\kappa_\mathrm{e}}-\kappa_\mathrm{e}^2}\cdot\exp(k(\kappa_\mathrm{e}-R)) \tag{6.43}$$
$$= -\bar{\theta}_0(s)\frac{\kappa_\mathrm{e}^2}{s+\frac{k}{\kappa_\mathrm{e}}}\cdot\exp(k(\kappa_\mathrm{e}-R))$$

from which the capacitive transient may be derived.

The capacitive (charging) current can be related to the rate of change of the electric field at the electrode-solution interface, according to Gauss's Law (Equation 1.17):

$$i_\mathrm{cap} = \frac{\partial q}{\partial t} = \frac{\partial}{\partial t}\left(-2\pi r_\mathrm{e}^2\,\epsilon_\mathrm{s}\epsilon_0\,\frac{\partial\phi}{\partial r}\right) \tag{6.44}$$

so that applying the required normalisation conditions, the dimensionless capacitive current can be defined as[†]:

$$j_\mathrm{cap} = \frac{i_\mathrm{cap}}{2\pi FC^*Dr_\mathrm{e}} = \frac{-2}{\kappa_\mathrm{e}}\,\frac{\partial^2\theta}{\partial\tau\partial R}\bigg|_{R=\kappa_\mathrm{e}} \tag{6.45}$$

Note that j_cap has been normalised to the electrode space ($x^* = r_\mathrm{e}$), to give a common normalisation to that for the Faradaic current in an equivalent hemispherical system (as in Chapters 7–10).

Now

$$\frac{\partial^2\theta}{\partial\tau\partial R}\bigg|_{R=\kappa_\mathrm{e}} = \frac{1}{\kappa_\mathrm{e}}\,\frac{\partial^2\chi}{\partial\tau\partial R}\bigg|_{R=\kappa_\mathrm{e}} - \frac{1}{\kappa_\mathrm{e}^2}\,\frac{\partial\chi}{\partial\tau}\bigg|_{R=\kappa_\mathrm{e}} \tag{6.46}$$
$$= \frac{1}{\kappa_\mathrm{e}}\left(\frac{\partial^2\chi}{\partial\tau\partial R}\bigg|_{R=\kappa_\mathrm{e}} - \frac{\partial\theta_0}{\partial\tau}\right)$$

[†]The use of j for dimensionless current is standard in the literature on voltammetry, and is used here to emphasise the correlation between the capacitive currents in this chapter and the Faradaic currents in subsequent chapters, since the same normalisation is used for both. To mitigate possible confusion with the imaginary unit j in other parts of the chapter, "cap" is used consistently as a subscript when current is being discussed.

and

$$\mathcal{L}\left(\left.\frac{\partial^2\chi}{\partial\tau\partial R}\right|_{R=\kappa_e} - \frac{\partial\theta_0}{\partial\tau}\right) = \left(s\cdot\left.\frac{\partial\bar{\chi}}{\partial R}\right|_{R=\kappa_e}\right) - \left(s\cdot\bar{\theta}_0(s) - \theta_0(0)\right) \tag{6.47}$$

Hence the Laplace transformation of the current is

$$\bar{i}(s) = \mathcal{L}_{\tau\to s}\Big(j_{\text{cap}}(\tau)\Big) = \left(2s\cdot\bar{\theta}_0(s)\cdot\left(\frac{1}{s+\frac{k}{\kappa_e}} + \frac{1}{\kappa_e^2}\right)\right) - \frac{2\theta_0(0)}{\kappa_e^2} \tag{6.48}$$

So, there exists a linear relationship between the current and voltage functions in Laplace space, and hence the system is linear overall. The step function response can then be used to determine the response for any input (Section 2.5.3). Particularly, the impedance spectrum can be determined by substituting $j\omega$ for s in the Laplace space solution to a step function input, as will be developed below.

6.4.2 Transient charging current following a potential step

For the potential step problem, $s\cdot\bar{\theta}_0 = \theta(0) = \theta_0$ which simplifies the above to a single term:

$$j_{\text{cap}}(\tau) = \mathcal{L}^{-1}_{s\to\tau}\left(\frac{2\theta_0}{s+\frac{k}{\kappa_e}}\right) = \mathcal{L}^{-1}_{s\to\tau}\left(\frac{2\theta_0}{s+\sqrt{1+\frac{s}{\kappa_e^2}}}\right) \tag{6.49}$$

Let us approximate $\sqrt{1+\frac{s}{\kappa_e^2}}$ by its Taylor series. From numerical examination of the function, the nth order Taylor series approximation is accurate to 1% when $\frac{s}{\kappa_e^2} < \frac{1}{a_n}$, where $a_0 \approx 50$ and $a_1 \approx 3$. Noting that the Laplace coordinate s corresponds roughly to $\tau^{-\frac{1}{2}}$, we can take the nth order Taylor series to be an accurate approximation where:

$$\frac{1}{\sqrt{\tau}} < \frac{\kappa_e^2}{a_n} \tag{6.50}$$

and hence

$$\tau > \left(\frac{a_n^2}{\kappa_e^4}\right) \tag{6.51}$$

Substituting back into dimensional coordinates, this gives a range of accuracy of

$$\frac{t}{t_{\mathrm{D}}} > \left(a_n^2 \times \frac{x_{\mathrm{D}}}{r_{\mathrm{e}}} \right) \tag{6.52}$$

where t_{D} is the characteristic Debye time and is defined x_{D}^2/D. For typical electrolyte concentrations and diffusion coefficients, the Debye time is at most 1 μs and more typically is tens of nanoseconds. It is clear, then, that the requirement of 'long time' is in fact not at all stringent from an experimental point of view; since R_{e} is of the order 1 – 10^6 for most real systems, the available t range is large even for a low order Taylor series.

Considering the zeroth order Taylor series, we take $\sqrt{1+\frac{s}{\kappa_{\mathrm{e}}^2}} \to 1$, so:

$$\frac{1}{s+\sqrt{1+\frac{s}{\kappa_{\mathrm{e}}^2}}} \approx \frac{1}{1+s} \tag{6.53}$$

and

$$\mathcal{L}_{s\to\tau}^{-1}\left(\frac{1}{1+s}\right) = \exp(-\tau) \tag{6.54}$$

i.e. strictly at *long time and low voltage*, and with equal diffusion coefficients, an exponential decay analogous to the RC circuit is predicted, with a decay constant exactly equal to 1 in our choice of a mixed time coordinate. This approximation is accurate to 1% for $(t/t_{\mathrm{D}}) > (2500 \times (x_{\mathrm{D}}/r_{\mathrm{e}}))$. This inequality is satisfied for any experimentally measurable timescale, except when the electrode is nanoscale and so $r_{\mathrm{e}} \to x_{\mathrm{D}}$.

Less stringently, the second term of the Taylor series may be included to give a first order approximation, which is 1% accurate for $s < (3 \times \kappa_{\mathrm{e}}^2)$, which is equivalent to $(t/t_{\mathrm{D}}) > (9 \times (x_{\mathrm{D}}/r_{\mathrm{e}}))$. Further terms of this Taylor series may reasonably be neglected: we are excluding the contribution of large values of s as corresponding to (vanishingly)

small values of τ. So:

$$\frac{1}{s+\sqrt{1+\frac{s}{\kappa_e^2}}} \approx \frac{1}{s+1+\frac{s}{2\kappa_e^2}} = \frac{1}{\left(1+\frac{1}{2\kappa_e^2}\right)s+1} \tag{6.55}$$

and rearranging, we find that to this next order of approximation

$$j_{cap}(\tau) \approx 2\theta_0 \left(\frac{2\kappa_e^2}{2\kappa_e^2+1}\right) \exp\left(-\left(\frac{2\kappa_e^2}{2\kappa_e^2+1}\right)\tau\right) \tag{6.56}$$

Again we recover an exponential decay at long time, with a slightly altered decay constant; for large κ_e (large electrodes) this further term rapidly tends to unity and so the first order correction is unnecessary. It should be noted here that since the additional term in the decay constant also appears as a multiplying factor to the current as a whole, by comparison with Equation 6.4 it can be identified with a change in the resistance, R_s, and not of the capacitance.

Converting back into real units, we note that for the charging problem at low potential, to zeroth order:

$$R_{s,0} = \frac{RT}{F}\frac{1}{4\pi FDC^* r_e} = \frac{1}{2\pi\epsilon_s\epsilon_0}\frac{x_D^2}{r_e D} \tag{6.57}$$

$$C'_{d,0} = \frac{\epsilon_s\epsilon_0}{x_D} \tag{6.58}$$

Therefore, the capacitance associated with the charging process is the same as that given for differential capacitance by the Gouy–Chapman theory (Equation 5.43). This strongly suggests that this capacitance is physically meaningful, and in the limit of a large electrode and low applied potential, charging is well described by an RC circuit. To first order, the capacitance is unchanged, but:

$$R_{s,1} = \left(1+\frac{x_D}{2r_e}\right) R_{s,0} \tag{6.59}$$

i.e. a slightly elevated resistance over that predicted by Gouy-Chapman theory is seen

as $r_e \to x_D$.

At first sight this determination is entirely contradictory with the predictions made for the equilibrium condition in the previous chapter. By including the influence of size by solving the Nernst–Planck–Poisson equation set in a hemispherical geometry, a correction was predicted to the differential capacitance at equilibrium (Equation 5.37). For the dynamic capacitive charging problem, by contrast, the electrode size does not alter the capacitance, but does introduce a correction to the resistance. In both cases the correction is only relevant when r_e is a few Debye lengths or less.

The resolution of this problem lies in appreciating that although the initial electroneutral condition for the dynamic solution requires that the solution charge, q_{soln}, is zero at $\tau = 0$, it does not constrain that the electrode charge, $q_e = 0$. Indeed, since the applied potential is well defined, the enclosed charge on the electrode immediately following the potential step, before any ionic migration, is easily calculated, since this follows simply from Coulomb's law:

$$q_e = 2\pi\epsilon_s\epsilon_0 r_e \, \phi_0 \tag{6.60}$$

and therefore the charge density is

$$q_e' = \frac{\epsilon_s\epsilon_0}{r_e} \, \phi_0 \tag{6.61}$$

which is precisely the correction term noted at equilibrium in the previous chapter (Equation 5.37).

Therefore, the correction to the steady-state differential capacitance is associated with the "Coulomb charge" on the electrode, i.e. the charge on the electrode when it is held at a potential difference with respect to a reference electrode separated by an electroneutral solution. This charge density becomes increasingly significant for

nanoelectrodes, whereas the Gouy–Chapman diffuse double layer charge density is independent of electrode size. Since no ionic motion is required to achieve this electrode charge, it occurs at $\tau = 0$ in tandem with the potential step. The Coulomb charge is not measured by the charging transient, since this transient measures the change of electrode charge *after* $\tau = 0$; therefore this size effect does not alter the apparent capacitance associated with the decay constant for this process.

Therefore, for a nanoelectrode, the total accumulation of charge in solution during the charging transient is not exactly opposite to the total accumulation of charge on the electrode. This disparity marginally lengthens the time required to form the double layer and arises in the RC expression as an excess resistance. The capacitance predicted at steady state does not, however, dictate the perceived charging capacitance for a nanoelectrode and so there is no single 'system capacitance' as is normally understood. Equally, the 'solution' resistance, R_s, is a strong function of r_e and so is as much a property of the electrode as it is of the solution. Therefore, especially for nanoelectrodes, these parameters in the RC circuit model lack a clear physical definition.

6.4.3 Impedance for low applied potential

An exact result has been developed for the Laplace space solution for the hemispherical system under the low potential limit, and so the impedance spectrum follows directly[12] by substituting $j\omega$ for s, and taking $Z(j\omega) = \bar{\theta}_0(j\omega)/\bar{i}(j\omega)$.

In the case of impedance spectroscopy, $\theta(0) = 0$ at the beginning of the applied voltage wave, and so:

$$Z(j\omega) = \frac{1}{2j\omega} \frac{1}{\left(\frac{1}{j\omega + \frac{k}{\kappa_\mathrm{e}}} + \frac{1}{\kappa_\mathrm{e}^2} \right)} \tag{6.62}$$

where the first term in the denominator is the normal Gouy–Chapman diffuse double layer impedance and the second is associated with the "Coulomb charge" which is placed on a nanoelectrode by applying a potential. Assuming that this term is negligible, the expression simplifies to:

$$Z(j\omega) = \frac{1}{2} - j\frac{\sqrt{j\omega + \kappa_e^2}}{2\kappa_e \omega} \tag{6.63}$$

If $r_e \gg x_D$, i.e. the electrode is not nanoscale, and $\omega \ll \kappa_e^2$:

$$Z(j\omega) = \frac{1}{2} - j\frac{1}{2\omega} \tag{6.64}$$

which corresponds to the ideal (zeroth order) resistance as real impedance and the Gouy-Chapman capacitance as imaginary impedance respectively, in complete agreement with the predictions of RC circuit analysis.

The condition $\omega \ll \kappa_e^2$ applied above requires frequencies less than the Debye frequency D/x_D^2. The Debye frequency is in the range 1 MHz – 1 GHz for typical electrolytic solutions, which is not an experimentally achievable range with normal electrochemical impedance spectroscopy equipment. Note that the Debye frequency is also not a function of electrode size. Hence even when κ_e is small we can accurately assume that $\omega \ll \kappa_e^2$.

If the Coulomb charging term is not negligible, then approximating $k \approx \kappa_e$:

$$Z(j\omega) = \frac{\kappa_e^2}{2}\frac{1}{\kappa_e^2 + 1 + j\omega} - j\frac{\kappa_e^2}{2\omega}\frac{1}{\kappa_e^2 + 1 + j\omega} \tag{6.65}$$

and so clearly

$$Z(j\omega) \approx Z(j\omega)_{GC} \cdot \left(\frac{\kappa_e^2}{\kappa_e^2 + 1 + j\omega}\right) \tag{6.66}$$

which is similar to the first order correction noted for the transient resistance. It must be noted, however, that in this case the resistance is slightly reduced. Therefore the

nanoscale correction to the complex impedance is opposite to the correction to the transient resistance, underlining that properties due to an "electrical circuit analogy" cease to be meaningful at the nanoscale.

6.5 The case of unequal diffusion coefficients

When $D_\mathrm{A} \neq D_\mathrm{X}$, the above analysis may not apply. If one ion is more mobile than the other, it will react more quickly to a step in potential and so the capacitive properties of the double layer are altered. The problem can be approached analytically by choosing to normalise time more generally by the mean of the diffusion coefficients:

$$t^* = \frac{2r_\mathrm{e}x_\mathrm{D}}{D_\mathrm{A}+D_\mathrm{X}} = \frac{r_\mathrm{e}x_\mathrm{D}}{D_\mathrm{mean}} \tag{6.67}$$

The solution of the NPP equations for unequal diffusion coefficients is feasible in the Laplace space under the Debye–Falkenhagen approximation and is reported in Appendix B. The effect of unequal diffusion coefficients can be parameterised by a constant $\delta = (D_\mathrm{A} - D_\mathrm{X})/(D_\mathrm{A} + D_\mathrm{X})$ which for less than infinite disparity in rates of diffusion takes values $|\delta| < 1$. For the case of equal diffusion coefficients above, $\delta = 0$.

Unfortunately, both the analysis and the expression for the resulting transient in Laplace space are extremely cumbersome for unequal diffusion coefficients. Under the approximation that $s^2 \ll R_\mathrm{e}^4(1-\delta^2)^2/4\delta^2$, long time values for R_s and C'_d can be derived: in this limit, the charging transient again displays an exponential decay as predicted by the RC circuit model. For a large electrode at low overpotential:

$$R_\mathrm{s} = \frac{1}{\pi\epsilon_\mathrm{s}\epsilon_0(D_\mathrm{A}+D_\mathrm{X})}\frac{r_\mathrm{e}}{x_\mathrm{D}^2} = \frac{2D_\mathrm{A}}{D_\mathrm{A}+D_\mathrm{X}}R_{\mathrm{s},0} \tag{6.68}$$

$$C'_\mathrm{d} = C'_{\mathrm{d,GC}} \tag{6.69}$$

These results suggest that elevating either diffusion coefficient will decrease the resistance of the solution, which is consistent with the expectation that the solution is more conductive if the electrolyte is more mobile. Altering the diffusion coefficients does not affecting the capacitance, which remains equivalent to its value as inferred from the system equilibrium, which cannot depend on dynamic properties such as species diffusion coefficients. Therefore, RC circuit analysis is still relevant at low potential even in the case of unequal diffusion coefficients; the resistance is altered such that the rate of charging is proportional to the arithmetic mean of the diffusion coefficients of the ions involved. In effect, the equivalent circuit resistance behaves as two resistors in series, one associated with each ion.

6.6 Simulation Results

As in the previous chapter, numerical simulation was employed to extend the scope of the discussion to outside the low potential regime where the Debye–Hückel approximation can be used to obtain analytical results.

6.6.1 The effect of size

The predictions of Section 6.4.2 are confirmed by numerical simulation of two representative capacitive transients, for electrode sizes of $R_e = 10$ and one for $R_e = 10^3$, which are typical nano- and microelectrode situations respectively. A very small applied potential of $\theta_0 = 0.01$ is assumed, with an initially uncharged electrode. According to the first order theory developed above, the correction from the classical resistance is 5% in the first case and 0.05% in the second. The transients are shown at Figures 6.2

and 6.3.

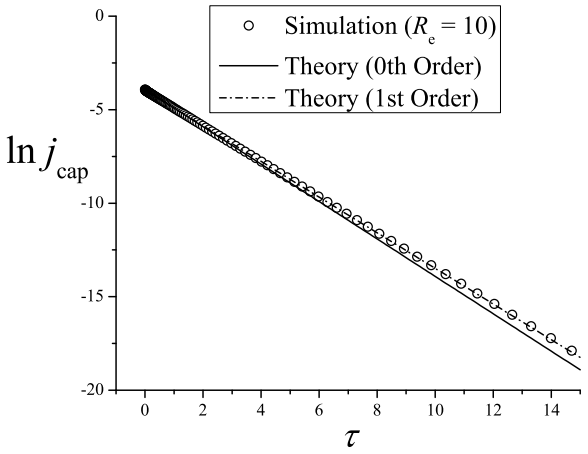

Figure 6.2: Simulated capacitance transient for a step from the PZC to $\theta_0 = 0.01$, with $R_e = 10$. Zeroth and first order analytical treatments are shown for comparison. The zeroth order transient is an accurate approximation of the case $R_e = 1000$, normalised appropriately, so a comparison of micro- and nanoelectrode transients may also be seen.

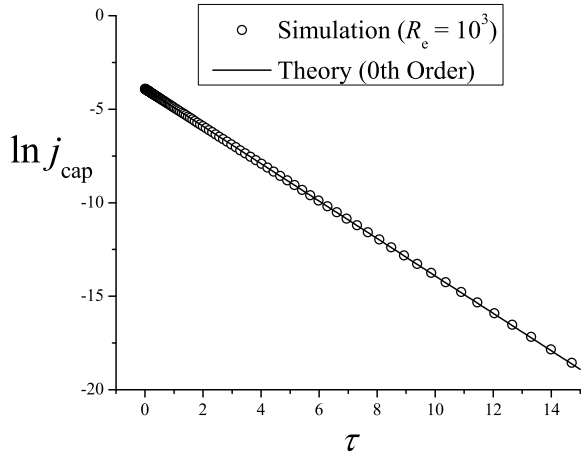

Figure 6.3: Simulated capacitance transient for a step from the PZC to $\theta_0 = 0.01$, with $R_e = 1000$. The zeroth order analytical treatment is shown for comparison.

In the simulated capacitive transient for a nanoelectrode, only the first order theory taking into account the size effect is accurate, whereas for the microelectrode, where the Debye length is negligible on the electrode scale, the zeroth order theory is entirely adequate. Figure 6.2 also displays a normalised comparison of the nanoelectrode and

microelectrode cases, since the latter is given accurately by the zeroth order treatment; a size-dependent alteration of the decay constant of charging is evident.

Simulation therefore confirms the analytical prediction that at low applied potential, the RC description, using Gouy–Chapman theory to describe capacitance and a classical resistance as shown above, is an excellent description of the diffuse double layer for a microelectrode. This 'solution' resistance is, however, a property of the electrode as well as of the solution. For the nanoelectrode, the curve can still be described in terms of R_s and C'_d values, since both the charging transient and impedance spectrum take the same functional form as predicted by the RC circuit model. As demonstrated above, however, the values of these parameters are dependent on the experiment in question and so cannot be directly associated with those inferred from impedance spectroscopy or differential capacitance, thus undermining the physical validity of the RC model for nanoelectrode charging.

6.6.2 The effect of large overpotential

None of the analysis above applies to overpotentials similar to or greater than RT/F. Although the low potential range is typical for impedance studies where small overpotentials are preferred, it is not typical in chronoamperometry or cyclic voltammetry experiments where ranges of many units RT/F are explored in order to access different thermodynamic regimes of an electrode reaction, as will be explored through Chapters 7–10.

The Gouy–Chapman theory, which is applicable at equilibrium for electrodes significantly larger than the Debye length, gives the form of the diffuse double layer charge

density per area as:

$$Q'_{\mathrm{DL}} = 2 \sinh\left(\frac{\theta_0}{2}\right) \tag{6.70}$$

from Equation 5.21, which is approximately linear only in the limit of small θ_0. For higher overpotentials, the diffuse double layer charge is predicted to vary exponentially with applied potential. Since proportionally more charge has to be assembled on the double layer, more migration of material is required, and so capacitive charging is expected to take longer. In particular, the significance of non-linear terms in the high overpotential limit implies deviation from an ideal exponential behaviour.

The prediction of slower, non-exponential charging is confirmed by simulation, as indicated by comparing simulated charging transients $\theta = 0.05$ and $\theta = 5$ for a micro-electrode where $R_{\mathrm{e}} = 1000$. The low and high potentials are displayed on linear and logarithmic current scales in Figure 6.4.

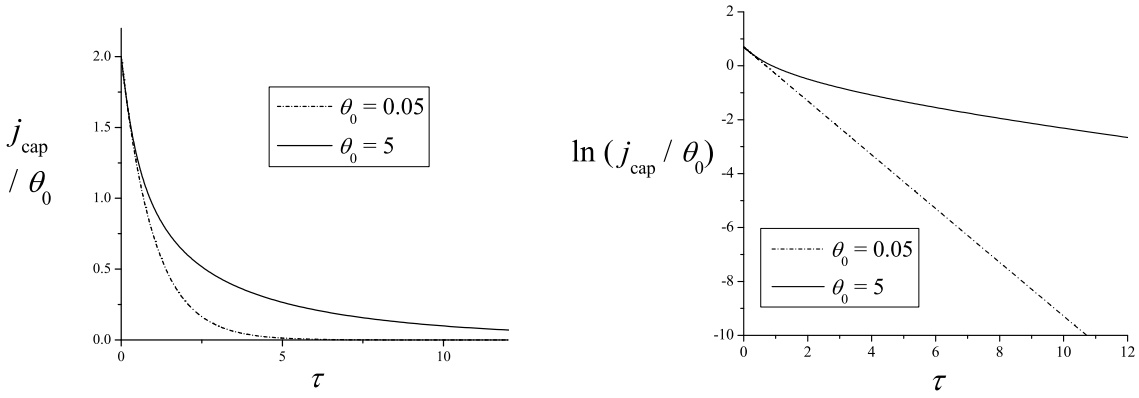

Figure 6.4: Simulated capacitive charging transient for a step to $\theta_0 = 0.05$ and to $\theta_0 = 5$, with $R_{\mathrm{e}} = 10^3$, comparing the low and high potential limits. Current on: (a) a linear scale; and (b) a logarithmic scale in which exponential decay is a straight line.

The distinct feature of the non-linear diffuse double layer charging transient is the much longer non-exponential 'tail', corresponding to the assembly of excess charge at the double layer. More specifically, in the positive potential case a greater accumulation

of anion is required than depletion of cation, and so the formation of the double layer requires the establishment of a significant ionic strength gradient in addition to the separation of charge. This process clearly requires more protracted charge transport than the ideal charging of a low potential (linear) diffuse double layer in which the variation in surface excess is roughly equivalent for both ions.

The extent of deviation from exponential decay (RC behaviour) as a function of electrode overpotential may be explored by considering the "apparent" exponential decay constant of a charging transient. Since an ideal exponential transient has $\partial \ln j_{\text{cap}}/\partial\tau = -k$ where k is the decay constant, we can plot $k_{\text{app}} \equiv -\partial \ln j_{\text{cap}}/\partial\tau$ as a τ-dependent apparent decay constants. In regions where k_{app} is constant, the RC circuit is a good description, but not where it is variable. The numerical simulation results are shown in Figure 6.5 for a series of applied θ_0 values, at different times τ and for both a nano- and microelectrode. The predicted constant k from the spherical Debye–Falkenhagen equation is also plotted for clarity. It is clear that while the RC description is excellent at all times for $\theta_0 \ll 1$, it becomes increasingly inaccurate at longer times for $\theta_0 \approx 1$ and is wholly inaccurate for $\theta_0 > 1$.

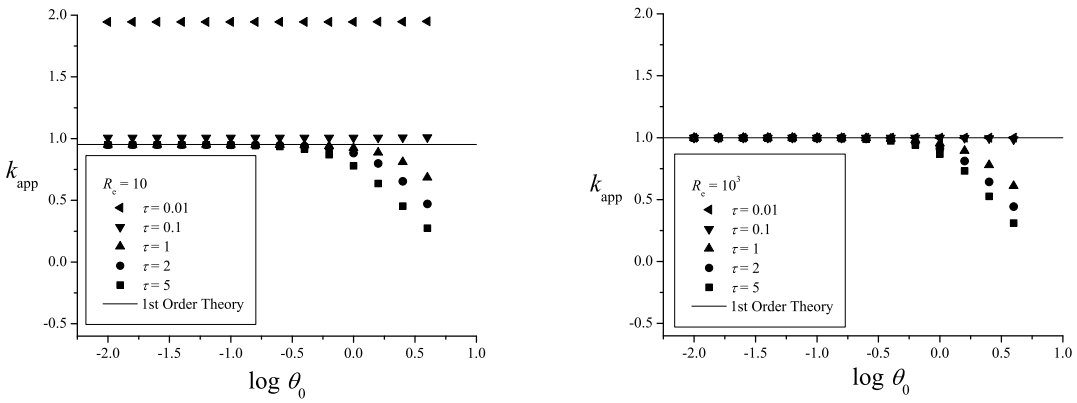

Figure 6.5: $k_{\text{app}} \equiv -\partial \ln j_{\text{cap}}/\partial\tau$, for various values τ in a capacitance transient and at various applied θ_0 from $\theta_0 = 0.01$ to $\theta_0 \approx 4$, for $R_{\text{e}} = 10$ and 10^3.

For nanoelectrodes at very short times, all transients deviate from exponential behaviour, since the asymptotic requirement developed in the analytical theory that $\tau \ll R_e^{-2}$ is no longer so well obeyed (Section 6.4.2). It is relevant to note that all transients show similar behaviour, exponential or otherwise, at short times – only once the charging process has developed to a sufficient extent that the surface excesses of the two ions are no longer symmetric does the rate of capacitive charging exhibit potential dependence. Of course, a higher applied overpotential increases the initial electric field acting on the electrolyte and so induces a potential-dependent situation more rapidly.

Capacitive charging is a non-linear process for high overpotential. Consequently, the low potential analysis does not apply in this regime, and since the form of the transient is not exponential, RC circuit analysis is also inappropriate as the charging 'constant' $R_s C_d$ is a strong function of time! Therefore RC circuit analysis is a poor description of the diffuse double layer for techniques in which applied potential varies by much more than RT/F, such as, for instance, conventional Faradaic chronoamperometry or cyclic voltammetry.

6.6.3 The effect of unequal diffusion coefficients

A range of numerical simulations were conducted to consider the effect of unequal diffusion coefficients on capacitive charging. The low-potential analysis above suggests that the characteristic decay time should be reduced according to the arithmetic mean of the diffusion coefficients. Additionally, some deviation from pure exponential behaviour may be expected for unequal diffusion coefficients, particularly the observation of a reduced decay constant at very long time.

Three normalised transients at low overpotential are shown at Figure 6.6 on a

constant time scale ($\tau_A \equiv D_A t / r_e x_D$), for a modest but realistic range of inequality in the diffusion coefficients; D_X and D_A are in the ratios 2:3, 1:1 and 3:2, respectively.

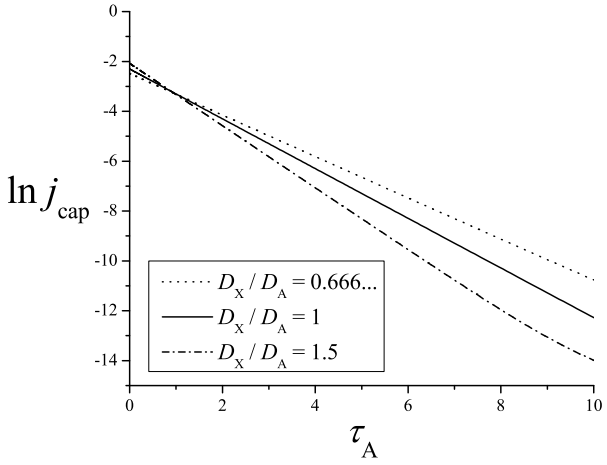

Figure 6.6: Simulated normalised capacitance transients for a step from the PZC to $\theta_0 = 0.05$, with $R_e = 10^4$ and $D_X/D_A = 0.666...$, 1, and 1.5. In this scale, an exponential decay is a straight line.

From this it is clear that the decay constant is inversely proportional to the mean diffusion coefficient and that deviations from exponential behaviour due to diffusion coefficient disparity are negligible. The interpretation of the RC circuit model as applying for large electrodes in the low potential regime is confirmed, with an apparent resistance given by the series combination of a resistance for each ion.

A more complete study at Figure 6.7 shows the variation of k_{app}, as defined above, in time and with varying diffusion coefficient ratio, for low overpotential. It is clear that for increasingly disparate diffusion coefficients, a greater acceleration of charging at short time is balanced by a greater deceleration at long time.

This can be understood because the equilibrium diffuse double layer at low overpotential has approximately symmetric accumulation and depletion of the two ions. Therefore, after rapid charge transport due to one ion, the system must "wait" for the slower ion to migrate in order to attain overall equilibrium. Clearly, since the

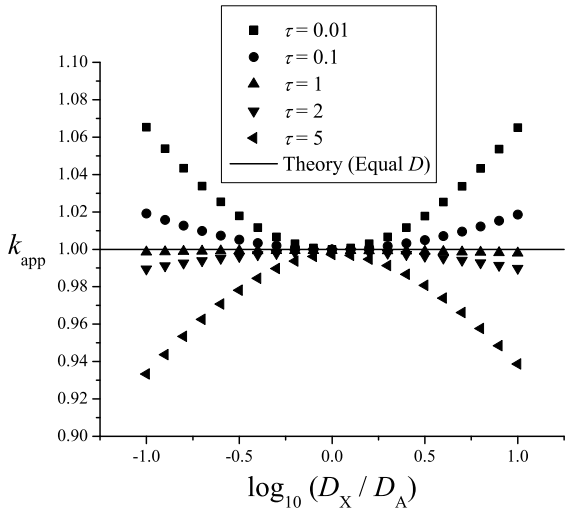

Figure 6.7: The effect of the diffusion coefficient ratio D_X/D_A on $k_{app} \equiv -\partial \ln j_{cap}/\partial\tau$, at different times during a capacitance transient with $\theta_0 = 0.05$ and $R_e = 10^4$.

diffusion coefficients do not affect the overall charge accumulated on the equilibrated diffuse double layer, the integral of the capacitive charging transient must be constant; hence, faster charging than for the case of equal diffusion coefficients at some time will correspond to slower charging at some other time.

In general, however, the observation of k_{app} very close to unity in a timescale normalised to the mean of the diffusion coefficients confirms that the two ions behave as two component resistances in series. This suggests that the effect of the charge interaction between the ions on their migration is to rapidly balance the rates of migration to a mean transport rate. The rate of double layer formation is hence the average of the contributions of each individual ion.

Note that very similar averaged behaviour may be observed in the long time limit of the liquid junction problem (Section 4.5.6), even though the liquid junction transients tend to an electroneutral equilibrium whereas the capacitive charging transient tends to a non-electroneutral equilibrium. As such, this may be viewed as a general limiting behaviour of the charge transport of symmetric binary electrolyte under the influence

of an external impetus for either diffusion or migration. Charge transport at a mean diffusion coefficient allows a smooth decay of charge separation from the charged surface to electroneutral bulk solution is established on the Debye time scale, and prevents local regions of charge separation from developing at long time.

6.7 Conclusions

In the arguments and results presented above, charge transport in a diffuse double layer on perturbation away from equilibrium has been analysed in a self-consistent manner without the traditional use of arbitrary length scales. Simulations and mathematical analysis were used in a complementary manner and with strong mutual agreement. A thorough analysis using the Nernst–Planck–Poisson equation set, which takes into account the particular interrelation of conductivity to ionic transport for an electrolytic solution, demonstrates that charge transport in this system can be described using an RC equivalent circuit only subject to stringent conditions. These conditions are:

- An electrode larger than nanoscale.
- An applied potential away from the potential of zero charge not larger than RT/F (≈ 25 mV).
- Moderately similar diffusion coefficients.

Where these conditions are violated, either ideal RC behaviour breaks down altogether, as is the case for the non-exponential capacitive charging transients observed at high applied potential, or, as for a nanoelectrode system, the physical meaning of the 'constants' R_s and C_d collapses since they depend on the experiment under consideration.

The condition of low applied potential, common in electrochemical impedance spectroscopy, is strictly necessary for equivalent circuit analysis to be meaningful to describe a diffuse double layer. Common experimental techniques in Faradaic analysis, such as chronoamperometry or cyclic voltammetry, regularly probe much larger potential ranges, and so such simple, linear models for the diffuse double layer are inapplicable in these situations. Consequently, values of R_s and C_d inferred from impedance spectroscopy must be treated with caution, since they are not representative universal properties of the system, and do not helpfully parameterise charge transport outside a linear potential regime. When the electrode length scale is comparable to the Debye length, these parameters also become ambiguous.

Chapters 4–6 have applied the Nernst–Planck–Poisson equation set to reveal the influence of the Debye scale and of both linear and non-linear perturbations upon charge transport in electrolytic solution. The following four chapters will discuss the interrelation of these fundamental concepts of electrolytic solution dynamics to the description of the electrode-solution interface when Faradaic current is passed, and therefore the ionic composition of the solution is dynamically varying.

Bibliography

[1] E. J. F. Dickinson and R. G. Compton, *J. Electroanal. Chem.*, 2011, **655**, 23–31.

[2] A. J. Bard and L. R. Faulkner, *Electrochemical Methods: Fundamentals and Applications*, John Wiley & Sons, New York, 2nd edn., 2001.

[3] W. Scheider, *J. Phys. Chem.*, 1975, **79**, 127–136.

[4] R. D. Armstrong and R. A. Burnham, *J. Electroanal. Chem.*, 1976, **72**, 257–266.

[5] T. C. Halsey and M. Leibig, *Ann. Phys. (San Diego)*, 1992, **219**, 109–147.

[6] *Impedance Spectroscopy: Theory, Experiment, and Applications*, ed. E. Barsoukov and J. R. Macdonald, John Wiley & Sons, New York, 2005.

[7] R. J. Smith and R. C. Dorf, *Circuits, Devices and Systems*, John Wiley & Sons, New York, 5th edn., 1992.

[8] M. Schetzen, *Linear Time-Invariant Systems*, IEEE Press, Piscataway, New Jersey, 2003.

[9] M. Z. Bazant, K. Thornton and A. Ajdari, *Phys. Rev. E*, 2004, **70**, 021506.

[10] F. Beunis, F. Strubbe, M. Marescaux, J. Beeckman, K. Neyts and A. R. M. Verschueren, *Phys. Rev. E*, 2008, **78**, 011502.

[11] P. Debye and H. Falkenhagen, *Physik. Z.*, 1928, **29**, 121–132.

[12] A. Bezegh and J. Janata, *J. Electroanal. Chem.*, 1986, **215**, 139–149.

Chapter 7

Cyclic voltammetry: introduction

This chapter will review the fundamental theories concerning the thermodynamics and kinetics of electron transfer at the electrode-solution interface. The common experimental technique of cyclic voltammetry is then introduced. The effects of electrode size, voltammetric scan rate and other system parameters are discussed, in order to provide a framework for the detailed study of charge transport in the context of cyclic voltammetry.

7.1 Electrolysis

The ideally polarisable electrode introduced in Chapter 5 is in fact atypical in nature and difficult to construct reliably. Much more commonly, chemical changes in the solution adjacent to a charged working electrode will occur by electron transfer to or from the electrode. A chemical reaction induced by heterogeneous electron transfer is termed *electrolysis*.

A simple electrochemical reaction between ions in solution can be written:

$$\mathrm{A}^{z_\mathrm{A}}\,(\mathrm{soln}) \rightleftarrows \mathrm{B}^{z_\mathrm{B}}\,(\mathrm{soln}) + n\mathrm{e}^-\,(\mathrm{m}) \tag{7.1}$$

with z_i the charge on each species. Conservation of charge requires that $z_\mathrm{B} = z_\mathrm{A} + n$.

The current drawn can be related to the rate of the associated reaction by Faraday's laws of electrolysis,[1,2] which incorporate the laws of conservation of charge and mass. Current drawn at a working electrode due to electrolysis is consequently termed *Faradaic current*. In a modern notation, Faraday's laws are summarised by the statement that the Faradaic current is proportional to the incident mass transport of the reactant molecule A in the following manner:

$$i = \frac{\partial q}{\partial t} = nFAJ_\mathrm{A} \tag{7.2}$$

with n representing the number of electrons transferred to the electrode per molecule of reactant*, F is the Faraday constant (Section 1.3.2), A is the area of the electrode and J_A is the flux of reactant *into* the electrode.†

From conservation of mass:

$$J_\mathrm{A} + J_\mathrm{B} = 0 \tag{7.3}$$

i.e. the flux of A consumed at the electrode-solution interface must equal the flux of B generated at the electrode-solution interface.

*The sign of n has been defined such that current is positive for oxidation, as is conventional.

†This assumes that transport to the electrode is regular across its surface; although this often not the case in practice, such as for microelectrode voltammetry at a disc, it will be assumed for the simplified geometries described in this thesis.

7.2 Electrode thermodynamics

The thermodynamics of electrolysis may be determined from consideration of the fundamental theories set out in Section 1.2. If the electrode reaction (Equation 7.1) is at equilibrium, then the chemical potentials of the reactants and products must be equal:

$$\mu_{\mathrm{A}} = \mu_{\mathrm{B}} + n\mu_{\mathrm{e}} \tag{7.4}$$

The chemical potential of an ionic species is given as (Equation 1.14):

$$\mu_i = \mu_i^{\ominus} + RT \ln a_i + z_i F\phi \tag{7.5}$$

and so at equilibrium

$$\mu_{\mathrm{A}}^{\ominus} + RT \ln a_{\mathrm{A}} + z_{\mathrm{A}} F\phi_{\mathrm{s}} = \mu_{\mathrm{B}}^{\ominus} + RT \ln a_{\mathrm{B}} + z_{\mathrm{B}} F\phi_{\mathrm{s}} + n\mu_{\mathrm{e}}^{\ominus} - nF\phi_{\mathrm{m}} \tag{7.6}$$

where ϕ_{s} is the potential of the solution adjacent to the electrode, and ϕ_{m} is the potential of the electrode itself – that is, the Fermi level of the electrons in the electrode. Rearranging

$$\Delta\mu^{\ominus} + RT \ln\left(\frac{a_{\mathrm{B}}}{a_{\mathrm{A}}}\right) + (z_{\mathrm{B}} - z_{\mathrm{A}})\, F\phi_{\mathrm{s}} - nF\phi_{\mathrm{m}} = 0 \tag{7.7}$$

and recognising that $(z_{\mathrm{B}} - z_{\mathrm{A}}) = n$:

$$\Delta\phi = \frac{\Delta\mu^{\ominus}}{nF} + \frac{RT}{nF} \ln\left(\frac{a_{\mathrm{B}}}{a_{\mathrm{A}}}\right) \tag{7.8}$$

where $\Delta\phi = \phi_{\mathrm{m}} - \phi_{\mathrm{s}}$, the potential difference between the electrode and the solution. The activities of the product and reactant ions are equal when the electrode-solution potential difference takes a certain value, denoted $\Delta\phi^{\ominus}$:

$$\Delta\phi^{\ominus} = \frac{\Delta\mu^{\ominus}}{nF} = \frac{\Delta G^{\ominus}}{nF} \tag{7.9}$$

where $\Delta G^{\ominus}$ is the molar Gibbs free energy change of reaction. This relation is logical considering the definition of potential as an energy per unit charge.

The potential difference across the electrode-solution interface cannot be measured directly. However, it can be measured with respect to a reference electrode potential:

$$E \equiv \Delta\phi - \Delta\phi_{\text{ref}} \tag{7.10}$$

and therefore

$$E^{\ominus} = \Delta\phi^{\ominus} - \Delta\phi_{\text{ref}} \tag{7.11}$$

Hence

$$E = E^{\ominus} + \frac{RT}{nF} \ln\left(\frac{a_{\text{B}}}{a_{\text{A}}}\right) \tag{7.12}$$

such that the *standard reduction potential* of the A/B redox couple is the potential difference $E^{\ominus}$. By convention, $E^{\ominus}$ is recorded with respect to the standard hydrogen reference electrode, which has a defined reference potential of 0 V (Section 5.1).

Expanding the activity as the product of an activity coefficient and a concentration, it follows that:

$$E = E^{\ominus} + \frac{RT}{nF} \ln\left(\frac{\gamma_{\text{B}}}{\gamma_{\text{A}}}\right) + \frac{RT}{nF} \ln\left(\frac{C_{\text{B}}}{C_{\text{A}}}\right) \tag{7.13}$$

Defining the *formal reduction potential* $E_{\text{f}}^{\ominus}$ as the standard potential measured for equal concentrations of reactant and product:

$$E_{\text{f}}^{\ominus} = E^{\ominus} + \frac{RT}{nF} \ln\left(\frac{\gamma_{\text{B}}}{\gamma_{\text{A}}}\right) \tag{7.14}$$

and so

$$E = E_{\text{f}}^{\ominus} + \frac{RT}{nF} \ln\left(\frac{C_{\text{B}}}{C_{\text{A}}}\right) \tag{7.15}$$

This equation is named the Nernst equation after its formulator.[3]

In normalised units, a normalised overpotential η can be introduced:

$$\eta \equiv \frac{nF}{RT}\,(E - E_{\mathrm{f}}^{\ominus}) \tag{7.16}$$

such that the Nernst equation is

$$\eta = \ln\left(\frac{c_{\mathrm{B}}}{c_{\mathrm{A}}}\right) \tag{7.17}$$

or alternatively

$$c_{\mathrm{A}} - c_{\mathrm{B}}\,\mathrm{e}^{-\eta} = 0 \tag{7.18}$$

The direction of electron transfer n has been incorporated into the normalised overpotential such that a positive η always represents a drive for the reaction of A to B, even for a reduction where this formally represents a negative overpotential.

7.3 Electrode kinetics

The above thermodynamic arguments make clear the position of equilibrium of a chemical reaction that is mediated by electron transfer to or from an electrode. An applied overpotential provides a driving force for electron transfer between the electrode and solution, and hence shifts the equilibrium concentrations of the species A and B. However, the rate at which electrons are transferred, and hence at which equilibrium is attained, has not yet been discussed. The standard theory of electrode kinetics is the Butler–Volmer theory, which was initially proposed for slow reactions by Erdey-Grúz and Volmer.[4] Butler determined that this theory was general to electrode reactions, since it is consistent with the thermodynamic Nernst equation, and so can also apply to fast reactions.[5]

The Butler–Volmer model assumes that the flux of the reactant A – that is, the

rate of reaction at the surface, from Faraday's laws – can be expressed as the sum of forward and reverse reactions which are first-order with respect to the concentration of reactant and product respectively:

$$J_{\mathrm{A}} = k_{\mathrm{A}}\, C_{\mathrm{A}} - k_{\mathrm{B}}\, C_{\mathrm{B}} \tag{7.19}$$

in which k_{A} and k_{B} are the rate constants for electron transfer between the electrode and the solution species A and B respectively, and have units of velocity.

According to the transition state theory, these rate constants are related to molar activation energies with respect to a transition state ‡:

$$k_i \propto \exp\left(-\frac{\Delta G_i^{\ddagger}}{RT}\right) \tag{7.20}$$

$$\Delta G_{\mathrm{A}}^{\ddagger} = \mu_{\ddagger} - \mu_{\mathrm{A}} \tag{7.21}$$

$$\Delta G_{\mathrm{B}}^{\ddagger} = \mu_{\ddagger} - (\mu_{\mathrm{B}} + n\mu_{\mathrm{e}}) = \Delta G_{\mathrm{A}}^{\ddagger} - \Delta G^{\ominus} \tag{7.22}$$

The approximation is then made that the dependence of the transition state energy upon electrical potential is intermediate between that of the reactants and products:

$$\mu_{\ddagger} \approx \mu_{\ddagger}^{\ominus} + z_{\mathrm{A}} F\, \phi_{\mathrm{s}} + n\alpha' F\, \phi_{\mathrm{s}} - n\alpha' F\, \phi_{\mathrm{m}} \tag{7.23}$$

where $0 \leq \alpha' \leq 1$ and represents the potential dependence of the transition state as a linear combination of reactants and products. Therefore:

$$\begin{aligned} \Delta G_{\mathrm{A}}^{\ddagger} &\approx \Delta G_{\mathrm{A}}^{\ddagger,\ominus} - n\alpha'\, F\Delta\phi \\ &= \lambda_{\mathrm{A}} - n\alpha' F\,(E - E_{\mathrm{f}}^{\ominus}) \end{aligned} \tag{7.24}$$

where λ_{A} is a constant. Hence

$$k_{\mathrm{A}} = k_{\mathrm{A}}^{0}\, \exp\left(+\frac{\alpha' nF}{RT}\,(E - E_{\mathrm{f}}^{\ominus})\right) \tag{7.25}$$

with k^0_{A} an empirical constant.

Equally:

$$\begin{aligned}\Delta G^{\ddagger}_{\mathrm{B}} &= \Delta G^{\ddagger}_{\mathrm{A}} - \Delta G^{\ominus} \\ &= \lambda_{\mathrm{B}} + nF(1-\alpha')\left(E - E^{\ominus}_{\mathrm{f}}\right)\end{aligned} \tag{7.26}$$

Hence

$$k_{\mathrm{B}} = k^0_{\mathrm{B}} \exp\left(\frac{(\alpha'-1)nF}{RT}(E - E^{\ominus}_{\mathrm{f}})\right) \tag{7.27}$$

Therefore:

$$J_{\mathrm{A}} = k^0_{\mathrm{A}} \exp\left(+\frac{\alpha' nF}{RT}\left(E - E^{\ominus}_{\mathrm{f}}\right)\right) c_{\mathrm{A}} - k^0_{\mathrm{B}} \exp\left(\frac{(\alpha'-1)nF}{RT}(E - E^{\ominus}_{\mathrm{f}})\right) c_{\mathrm{B}} \tag{7.28}$$

At equilibrium, the current is zero and the Nernst equation holds. Hence:

$$k^0_{\mathrm{A}} \exp\left(+\frac{\alpha' nF}{RT}\left(E - E^{\ominus}_{\mathrm{f}}\right)\right) c_{\mathrm{A}} - k^0_{\mathrm{B}} \exp\left(\frac{(\alpha'-1)nF}{RT}(E - E^{\ominus}_{\mathrm{f}})\right) c_{\mathrm{B}} = 0 \tag{7.29}$$

Multiplying through by $\exp\left(\frac{-n\alpha' F}{RT}(E - E^{\ominus}_{\mathrm{f}})\right)$

$$c_{\mathrm{A}} - \frac{k^0_{\mathrm{B}}}{k^0_{\mathrm{A}}} \exp\left(-\frac{nF}{RT}(E - E^{\ominus}_{\mathrm{f}})\right) c_{\mathrm{B}} = 0 \tag{7.30}$$

Therefore, to satisfy the Nernst equation:

$$k^0_{\mathrm{A}} = k^0_{\mathrm{B}} \equiv k^0 \tag{7.31}$$

where k^0 is termed the Butler–Volmer heterogeneous rate constant.

By convention, α' is expressed as a Butler–Volmer transfer coefficient α which is defined in the reductive direction to take values $0 \leq \alpha \leq |n|$. The relation of α to α' is summarised for one-electron transfers in Table 7.1.

In summary:

$$J_{\mathrm{A}} = k^0 \left(\exp\left(\frac{+\alpha' nF}{RT}(E - E^{\ominus}_{\mathrm{f}})\right) c_{\mathrm{A}} - \exp\left(\frac{(\alpha'-1)nF}{RT}(E - E^{\ominus}_{\mathrm{f}})\right) c_{\mathrm{B}}\right) \tag{7.32}$$

n	α
$+1$	$1-\alpha'$
-1	α'

Table 7.1: Different systems for defining the transfer coefficient for the potential dependence of the transition state energy for a heterogeneous electron transfer.

or in normalised units

$$J'_{\mathrm{A}} = K^0 \left(\mathrm{e}^{\alpha' \eta}\, c_{\mathrm{A}} - \mathrm{e}^{(\alpha'-1)\eta}\, c_{\mathrm{B}} \right) \tag{7.33}$$

where

$$K^0 = k^0 \frac{x^*}{t^*} = \frac{k^0 x^*}{D} \tag{7.34}$$

according to Section 2.2.

The normalised Butler–Volmer equation can be rearranged to a homogeneous form:

$$c_{\mathrm{A}} - c_{\mathrm{B}}\, \mathrm{e}^{-\eta} - \frac{J'_{\mathrm{A}}}{K^0}\, \mathrm{e}^{-\alpha' \eta} = 0 \tag{7.35}$$

Here it is quite clear that the Butler–Volmer equation reduces to the Nernst equation either at zero current, or where the reaction is very fast, i.e. as $K^0 \to \infty$.

Both k^0 and α are empirical parameters. Quantitative calculation of these parameters from fundamental chemical considerations has in general eluded theoretical investigation. The most successful theory to date is the Marcus theory, in which $\Delta G^{\ddagger}$ is related to the required reorganisation in order to achieve adiabatic electron transfer in the transition state, in accordance with the Franck–Condon principle.[6] This thesis will not consider the reasons behind particular values of k^0 and α, but rather will treat them as freely variable parameters that influence the observed electrode kinetics.

7.4 The cyclic voltammetry experiment

Cyclic voltammetry is a ubiquitous electrochemical technique with diverse applications to sensing, mechanistic analysis, and the analysis of surfaces and interfaces.[2,7] A voltammogram is recorded by scanning the potential difference applied to a working electrode linearly in time, and recording the current as a function of potential, as indicated in Figure 7.1.

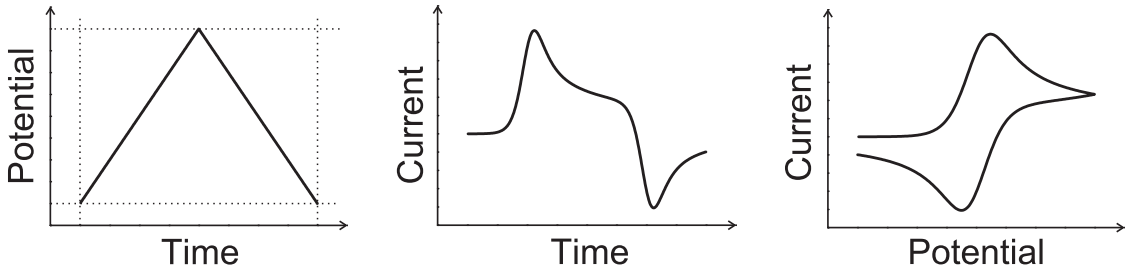

(a) Applied potential. **(b)** Recorded current. **(c)** Voltammogram.

Figure 7.1: Schematic for the cyclic voltammetry experiment. (a) indicates the *applied* voltage waveform; (b) and (c) indicate the *recorded* current waveform with respect to two choices of abscissa.

The rate of the linear scan is termed the *scan rate* and is denoted v:

$$v = \left| \frac{\partial E}{\partial t} \right| \tag{7.36}$$

In normalised units, the scan rate is denoted σ:

$$\sigma = \left| \frac{\partial \eta}{\partial \tau} \right| = v \, \frac{t^*}{\phi^*} = \frac{F}{RT} \, \frac{x^{*2}}{D_\mathrm{A}} \, v \tag{7.37}$$

The current-potential waveform is highly sensitive to the concentration and diffusion coefficient of the reactant, as well as to the electrode kinetics and thermodynamics of the electrolysis reaction. Therefore, cyclic voltammetry allows the simultaneous determination of numerous physical parameters. This is facilitated by recording voltammetry at a range of scan rates, such that increased dynamic information is available.

In performing a cyclic voltammetry experiment, it is necessary to consider the prac-

ticalities of passing significant current through an electrochemical cell. In particular, it is inadvisable to pass significant current at the reference electrode, as any associated chemical changes of the reference electrode will alter its reference potential. To avoid this problem, a three-electrode setup is often used, in which the current passed at the working electrode is delivered through a counter electrode with high surface area, such that it does not limit the passage of current. Since the counter electrode is separated in solution from the reference electrode, it does not perturb the reference potential. The three-electrode system is indicated at Figure 7.2.

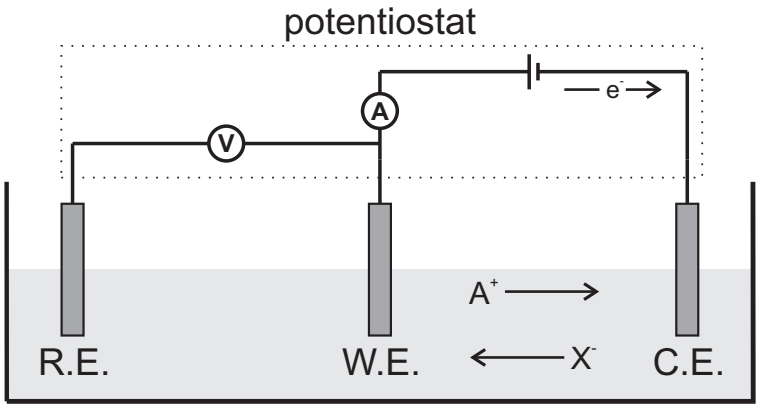

Figure 7.2: Schematic of an idealised three-electrode electrochemical cell for a cyclic voltammetry experiment. W.E.: working electrode; R.E.: reference electrode; C.E: counter electrode.

In the work in this thesis, it will be assumed that the reference electrode and counter electrode behave ideally, such that a potential difference $\Delta\phi$ can be set precisely between the working electrode and bulk solution. Under these conditions, the theoretical model only needs to consider mass transport and electrodynamics at the working electrode.

7.5 General theoretical model for voltammetry

It is conventional in analytical voltammetry to add a large excess of inert electrolyte to the solution, termed *supporting electrolyte*, in order to increase the solution conductivity. Typical supporting electrolytes include KCl in water and tetrabutylammonium perchlorate in acetonitrile. This supporting electrolyte is introduced to attain a condition of near-zero electric field; the extent to which this can be achieved will be developed below.

The same electrochemical cell geometry as in Chapters 5–6 will be considered, in which the working electrode is assumed to be hemispherical with a radius $r = r_\mathrm{e}$, surrounded by an infinite supply of bulk solution. This geometry uses a space normalisation $x^* = r_\mathrm{e}$, and the results agree with linear theory as $r_\mathrm{e} \to \infty$.

Four ionic (or neutral) species must be considered. The electroactive species are the reactant and product A and B which appear in the electrochemical equilibrium defined by Equation 7.1, and the charges of these species are defined by the variables z_A and n appearing in that equation. Concentration will be normalised against the bulk concentration of the reactant, C^*_A.

In addition to the reactant and product, an inert binary monovalent supporting electrolyte $\mathrm{M^+X^-}$ is assumed. These ions are present in bulk at a normalised concentration c_sup where:

$$c_\mathrm{sup} = \frac{C_\mathrm{sup}}{C^*_\mathrm{A}} \tag{7.38}$$

If the reactant A is charged, it must have a counter-ion to maintain electroneutrality in bulk solution. The counter-ion is assumed to be either $\mathrm{M^+}$ or $\mathrm{X^-}$ depending on the charge z_A. The bulk concentrations of the four ions (or neutral species, if A or B is

neutral) are summarised in Table 7.2.

	$z_\mathrm{A} < 0$	$z_\mathrm{A} \geq 0$
c_A^*	1	1
c_B^*	0	0
c_M^*	$c_\mathrm{sup} + \lvert z_\mathrm{A} \rvert$	c_sup
c_X^*	c_sup	$c_\mathrm{sup} + \lvert z_\mathrm{A} \rvert$

Table 7.2: Summary of bulk concentrations for the cyclic voltammetry model.

The initial conditions at $\tau = 0$ are $c_i = c_i^*$ and $\theta = 0$. The same conditions hold in bulk ($R \to \infty$) for $\tau > 0$, assuming limitless bulk solution is available on the experimental timescale.

The time coordinate is normalised to D_A, the diffusion coefficient of the reactant species. Then, the time-dependent Nernst–Planck equations are:

$$\frac{\partial c_\mathrm{A}}{\partial \tau} = \nabla^2 c_\mathrm{A} + \nabla \cdot (z_\mathrm{A} c_\mathrm{A} \nabla \theta) \tag{7.39}$$

$$\frac{\partial c_\mathrm{B}}{\partial \tau} = D'_\mathrm{B} \left(\nabla^2 c_\mathrm{B} + \nabla \cdot (z_\mathrm{B} c_\mathrm{B} \nabla \theta) \right) \tag{7.40}$$

$$\frac{\partial c_\mathrm{M}}{\partial \tau} = D'_\mathrm{M} \left(\nabla^2 c_\mathrm{M} + \nabla \cdot (c_\mathrm{M} \nabla \theta) \right) \tag{7.41}$$

$$\frac{\partial c_\mathrm{X}}{\partial \tau} = D'_\mathrm{X} \left(\nabla^2 c_\mathrm{X} - \nabla \cdot (c_\mathrm{X} \nabla \theta) \right) \tag{7.42}$$

A fifth equation is required to define the electrodynamics: various choices will be introduced in the following chapters.

The species M and X are inert and hence their incident flux is zero at the electrode surface:

$$\left. \frac{\partial c_\mathrm{M}}{\partial R} \right|_{R=1} + c_{\mathrm{M},0} \left. \frac{\partial \theta}{\partial R} \right|_{R=1} = 0 \tag{7.43}$$

$$\left.\frac{\partial c_{\mathrm{X}}}{\partial R}\right|_{R=1} - c_{\mathrm{X},0} \left.\frac{\partial \theta}{\partial R}\right|_{R=1} = 0 \tag{7.44}$$

Also, conservation of mass relates the fluxes of A and B at the electrode surface:

$$\left.\frac{\partial c_{\mathrm{A}}}{\partial R}\right|_{R=1} + z_{\mathrm{A}} c_{\mathrm{A},0} \left.\frac{\partial \theta}{\partial R}\right|_{R=1} + D'_{\mathrm{B}} \left(\left.\frac{\partial c_{\mathrm{B}}}{\partial R}\right|_{R=1} + z_{\mathrm{B}} c_{\mathrm{B},0} \left.\frac{\partial \theta}{\partial R}\right|_{R=1} \right) = 0 \tag{7.45}$$

The boundary condition for the potential at the surface will depend on the electrodynamical equation chosen in bulk solution.

A final boundary condition describes how the concentrations of the ions A and B at the electrode surface are related to the applied overpotential. This is typically either the Nernst or Butler–Volmer equation, depending on whether or not the electrode kinetics are sufficiently fast for the concentrations to be thermodynamically equilibrated, irrespective of the scan rate. Either of these equations can be expressed in the general form:

$$f(c_{\mathrm{A},0}, c_{\mathrm{B},0}, j_{\mathrm{A}}, \eta, \theta_0) = 0 \tag{7.46}$$

Note that the derivations of the Nernst and Butler–Volmer equations above assumed that the potential difference across the electrode-solution interface, $\phi_{\mathrm{w}} - \phi_{\mathrm{s},0}$, was equal to the potential difference from the electrode to bulk solution, $\phi_{\mathrm{w}} - \phi_{\mathrm{s}}$. In fact, if an electric field exists between the solution at the electrode surface and bulk, as may be expected if the solution has finite conductivity, these potential differences will differ. Specifically, the potential difference at the electrode-surface interface is reduced by a quantity $\Delta\phi_{\mathrm{OD}}$:

$$\phi_{\mathrm{w}} - \phi_{\mathrm{s},0} = (\phi_{\mathrm{w}} - \phi_{\mathrm{s}}) - (\phi_{\mathrm{s},0} - \phi_{\mathrm{s}}) \tag{7.47}$$

$$= \Delta\phi_{\mathrm{appl}} - \Delta\phi_{\mathrm{OD}} \tag{7.48}$$

Therefore the apparent overpotential η_{app} is given as:

$$\eta_{\text{app}} = \eta - n\theta_0 \tag{7.49}$$

where θ_0 is the value of the variable θ at $R = 1$. When $\theta_0 \neq 0$, the overpotential η must be replaced with $(\eta - n\theta_0)$ in Equations 7.18 and 7.35.

The potential drop across the solution, $\Delta\phi_{\text{OD}}$, is sometimes referred to as the *ohmic drop*, since it can be correlated with the resistance of the solution. The solution resistance does not obey Ohm's law in the sense of having a constant resistance, however, and so this terminology has been criticised as a misnomer.[8,9] In this thesis, the term ohmic drop will be used, since Ohm's law can be required to hold, but with the necessary caveat that the resistance inferred from Ohm's law is time- and space-dependent during an electrochemical experiment and so is not a universal property of the system.

The applied overpotential η for a linear sweep varies as:

$$\eta = \eta_{\text{i}} + \sigma\tau \tag{7.50}$$

where η_{i} is the initial overpotential, and on the reverse sweep as

$$\eta = \eta_{\text{f}} - \sigma(\tau - \tau_{\text{f}}) \tag{7.51}$$

where η_{f} is the switching potential and $\tau_{\text{f}} = (\eta_{\text{f}} - \eta_{\text{i}})/\sigma$.

In dimensional units, the current is given:

$$\begin{aligned} j &= \left.\frac{\partial c_{\text{A}}}{\partial R}\right|_{R=1} + z_{\text{A}} c_{\text{A}} \left.\frac{\partial \theta}{\partial R}\right|_{R=1} \\ &= nF(2\pi r_{\text{e}}^2) J'_{\text{A}} \\ &= 2\pi n F C^*_{\text{A}} D_{\text{A}} r_{\text{e}} \end{aligned} \tag{7.52}$$

in which, as for the overpotential, n has been incorporated into the normalisation such

that the normalised current j is positive, even for a reduction where the dimensional current is formally negative.

Since the boundary condition at the electrode surface depends upon η, the rate at which the surface concentrations are perturbed is proportional to the rate of change of η, i.e. proportional to σ. In the normalised system of choice:

$$\sigma = \frac{F}{RT}\frac{r_{\mathrm{e}}^2}{D_{\mathrm{A}}}v \tag{7.53}$$

Where $\sigma \to 0$, the perturbation of the electrode surface concentrations is slow with respect to the rate of diffusion as parameterised by the normalised time coordinate τ. By contrast, where $\sigma \to \infty$, the electrode surface concentrations are perturbed very rapidly with respect to diffusion.

7.6 Diffusion-only voltammetry

To consider the relative contribution of migration to mass transport of the electroactive species, let us multiply the Nernst–Planck equation for each species by z_i and then sum across all species in the system:

$$\frac{\partial(\sum_i z_i c_i)}{\partial \tau} = \nabla^2 \sum_i z_i D_i c_i + \nabla \cdot \left(\nabla\theta \sum_i z_i^2 D_i c_i \right) \tag{7.54}$$

If electroneutrality is obeyed and the diffusion coefficients are relatively similar:

$$\nabla \cdot \left(\nabla\theta \sum_i z_i^2 D_i c_i \right) \approx 0 \tag{7.55}$$

and so

$$\nabla\theta \propto \left(\sum_i z_i^2 D_i c_i \right)^{-1} \tag{7.56}$$

Therefore, as the normalised conductivity becomes large, electroneutral theory predicts that the electric field $\nabla\theta$ tends to zero. Since $\theta = 0$ by definition in bulk solution, $\theta \to 0$ everywhere, and the flux due to migration vanishes.

Since as the concentration of inert electrolyte becomes large, the range over which electric fields extend becomes infinitesimal, it is therefore common to assume that in the presence of a large quantity of supporting electrolyte, a "diffusion-only" theory of mass transport can be used. This is the most extreme simplifying assumption available concerning the electrodynamics of cyclic voltammetry; indeed, it amounts to ignoring the influence of the double layer and of electrodynamics in general. Under this assumption, Fick's diffusion equation (Equation 1.36) can be used to describe the mass transport of the species A and B, in place of the full Nernst–Planck equations:

$$\frac{\partial c_{\mathrm{A}}}{\partial \tau} = \nabla^2 c_{\mathrm{A}} \tag{7.57}$$

$$\frac{\partial c_{\mathrm{B}}}{\partial \tau} = D'_{\mathrm{B}} \nabla^2 c_{\mathrm{A}} \tag{7.58}$$

Note that since c_i has been normalised to the concentration of the electroactive species, a "large" quantity of supporting electrolyte means with respect to the concentration of the reactant, such that inert electrolyte must be added to attain diffusion-only voltammetry. It is not sufficient to increase the ionic strength of the reactant alone in order to achieve diffusion-only voltammetry, although this will nonetheless shorten the Debye length. This is discussed further in Chapter 9.

The observed voltammetry for a given diffusion-only system varies with the normalised scan rate σ. Since the real parameter that most strongly influences σ is not the dimensional scan rate v but rather the electrode radius r_{e}, it is clear that electrode size strongly influences observed voltammetry. In scanning the overpotential across one

unit RT/F, the elapsed time is RT/Fv, and so the thickness of the diffusion layer in the time required to perturb η by one normalised unit is given by the Einstein equation (Equation 1.37):

$$x_{\text{diff}} \approx \sqrt{2D_{\text{A}}t} \approx \sqrt{\frac{2D_{\text{A}}RT}{Fv}} = \frac{r_{\text{e}}\sqrt{2}}{\sqrt{\sigma}} \tag{7.59}$$

Therefore

$$\sigma = 2\left(\frac{r_{\text{e}}}{x_{\text{diff}}}\right)^2 \tag{7.60}$$

In the limit $\sigma \to \infty$, then, the electrode radius greatly exceeds the size of the diffusion layer on the experimental timescale, such that the diffusion layer remains predominantly planar throughout the voltammetric sweep. This behaviour is characteristic of voltammetry performed at macroelectrodes with $r_{\text{e}} \geq 1$ mm, and will be discussed in Section 7.7.

By contrast, in the limit $\sigma \to 0$, the size of the diffusion layer rapidly exceeds the size of the electrode radius. Therefore, the diffusion layer is hemispherical and diffusion from bulk solution to the electrode is fast with respect to the rate at which surface concentrations are perturbed. This behaviour is characteristic of voltammetry performed at microelectrodes with $r_{\text{e}} \leq 10$ μm, and will be discussed in Section 7.8.

7.7 Macroelectrode cyclic voltammetry

7.7.1 Infinite electrode kinetics

Under macroelectrode conditions where $\sigma \gg 1$, the diffusion layer is approximately planar and so the hemispherical coordinate can be approximated by a linear coordinate system, in which the diffusion equations can be approached by Laplace transformation,

although the exact solution can is still unattainable without numerical assistance. Assuming the Nernst equation holds, a characteristic reversible voltammogram for high σ is presented at Figure 7.3.

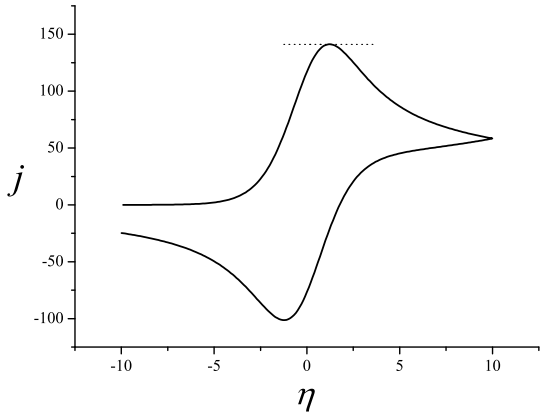

Figure 7.3: Reversible macroelectrode cyclic voltammetry. $D'_{\mathrm{B}} = 1$, $\sigma = 10^5$, $K^0 = 10^5$. The dotted line indicates the predicted peak current from the Randles–Ševčík equation for a linear diffusion layer.

The waveshape can be explained qualitatively by consideration of the interrelation between the electron transfer and diffusion processes. At the beginning of the voltammetric sweep, $\eta \ll 0$ and therefore the initial conditions are negligibly perturbed, and no significant current is drawn. As η is swept upwards, the increased thermodynamic drive for conversion of A to B causes current to be drawn: the current increases exponentially in proportion to the depletion of A at the electrode surface.

As η continues to increase, the conversion of A to B depletes the available concentration of A for reaction. The current then reaches a maximum, whereafter it decays under control of diffusion of the species A towards the electrode, where it reacts immediately since the reaction is strongly thermodynamically favoured. The diffusion-controlled current scales in proportion to $\tau^{-\frac{1}{2}}$, with some offset from the start of the scan: this proportionality is characteristic for diffusion in a planar system and was previously

encountered as a long time behaviour in the context of a liquid junction in Chapter 4.

On reversing the potential sweep, the same behaviour is observed: as the position of equilibrium begins to favour the reactant species A once more, an inverse current is drawn from reconversion of B to A. However, as the product species B is itself depleted at the electrode surface, the reconversion becomes diffusion-controlled. Therefore, a back peak is observed and the current decays back towards zero.

Some features of the reversible macroelectrode voltammogram can be quantified. Randles and Ševčík independently used graphical methods to solve the analytically intractable integral arising from Laplace analysis of the diffusion equation coupled with the Nernst equation.[10,11] The resulting Randles–Ševčík equation for the forward peak current for a single electron transfer ($|n| = 1$) at a macroelectrode, subject to the Nernst equation, is:

$$j_{\mathrm{pf}} = 0.446\,\sqrt{\sigma} \tag{7.61}$$

which is the limiting behaviour of a hemispherical system as the diffusion layer becomes planar, i.e. as $\sigma \to \infty$. The leading constant is reported to three significant figures.

The corresponding forward peak potential is:

$$\eta_{\mathrm{pf}} = 1.11 + \ln D'_{\mathrm{B}} \tag{7.62}$$

(three significant figures) such that

$$\Delta\eta_{\mathrm{pp}} = |\eta_{\mathrm{pf}} - \eta_{\mathrm{pb}}| = 2.22 \tag{7.63}$$

i.e. a dimensional ΔE_{pp} of about 57 mV. This variable is termed the *peak-to-peak separation*. This requires that the switching potential is sufficiently large not to affect the back peak potential. For practical potential windows, ΔE_{pp} is typically elevated

to 59–60 mV.

This ideal Randles–Ševčík behaviour is an important limiting case, but it is conditional on an electrode much larger than the size of the diffusion layer, and electrode kinetics much faster than the diffusional flux incident to the electrode.

7.7.2 Finite electrode kinetics

By Laplace analysis of the theoretical problem when the Butler–Volmer equation is obeyed, rather than the Nernst equation, Matsuda and Ayabe[12] demonstrated that macroelectrode voltammetry with finite electrode kinetics depends on a Matsuda–Ayabe parameter, Λ:

$$\Lambda = \frac{K^0}{\sqrt{\sigma}} \tag{7.64}$$

Where $\Lambda \gg 1$, the Nernstian response is observed, but as Λ becomes smaller, the voltammetry is altered due to the influence of the electrode kinetics. Because the current driven at a given overpotential is lower if the kinetics are finite, a greater overpotential is required to deplete the reactant species A at the electrode to the extent that a diffusion-limited current is observed. Therefore, the forward peak potential η_{pf} is increased. This applies to both the forward and reverse reactions, and so $\Delta\eta_{\mathrm{pp}} > 2.22$ for $\Lambda \to 0$.

Equally, the forward peak current is reduced because less current is being driven at the point where diffusion becomes rate-limiting. The corresponding Randles–Ševčík equation for a system with finite electrode kinetics is:

$$j_{\mathrm{pf}} = 0.496\sqrt{\alpha'\sigma} \tag{7.65}$$

The effect of decreased K^0 on macroelectrode cyclic voltammetry is shown in Figure

7.4.

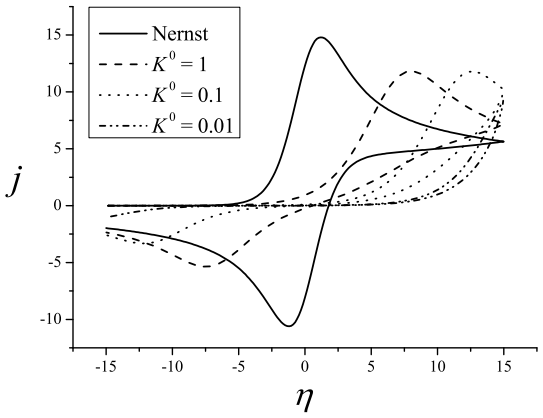

Figure 7.4: Quasi-reversible macroelectrode cyclic voltammetry. $D'_{\mathrm{B}} = 1$, $\sigma = 10^3$, $\alpha = 0.5$. Increasingly slow electrode kinetics increase the overpotential of the voltammetric peaks and reduce their current.

7.8 Microelectrode voltammetry

The macroelectrode (planar) description of cyclic voltammetry applies as $\sigma \to \infty$. Since the 1980s, however, micro- and nanoelectrodes have been employed with increasing frequency. In this case, the limit $\sigma \to 0$ applies, where the diffusion layer is approximately hemispherical: the radial mass transport to a microelectrode is considerably more efficient than linear diffusion, with concomitantly enhanced current density. This is particularly useful for electroanalysis since the signal-noise ratio is elevated by comparison to a macroelectrode.[13]

In addition, voltammetric theory can be simplified by the assumption of steady state, i.e. the concentrations at the electrode surface are equilibrated with bulk solution because mass transport across the diffusion layer is much faster than the rate at which the surface equilibrium is altered by the change in overpotential due to the voltammetric sweep. Under these conditions, $\partial c_i/\partial\tau \to 0$, and so the problem be-

comes time-independent: there is no hysteresis in the cyclic voltammogram because the current becomes dependent only on the potential, and is independent of the scan rate.

For diffusion-only steady-state voltammetry, the concentration profiles of A and B obey the hemispherical Laplace equation, and so to satisfy the bulk boundary conditions, the concentrations must take the exact forms:

$$c_{\mathrm{A}} = 1 - \frac{j_{\mathrm{A}}}{R} \tag{7.66}$$

$$c_{\mathrm{B}} = -\frac{j_{\mathrm{B}}}{D'_{\mathrm{B}} R} \tag{7.67}$$

where j_i are normalised fluxes; j_{A} is also the normalised current j, from Faraday's laws. Further, from conservation of mass at the electrode:

$$j_{\mathrm{A}} + j_{\mathrm{B}} = 0 \tag{7.68}$$

and so

$$c_{\mathrm{B},0} = \frac{1 - c_{\mathrm{A},0}}{D'_{\mathrm{B}}} \tag{7.69}$$

If $K^0 \to \infty$, the Nernst equation can be applied:

$$c_{\mathrm{A},0} - (1 - c_{\mathrm{A},0}) \frac{\mathrm{e}^{-\eta}}{D'_{\mathrm{B}}} = 0 \tag{7.70}$$

Hence

$$c_{\mathrm{A},0} = \frac{1}{1 + D'_{\mathrm{B}} \, \mathrm{e}^{+\eta}} \tag{7.71}$$

and

$$j_{\mathrm{A}} = \frac{1}{1 + \frac{\mathrm{e}^{-\eta}}{D'_{\mathrm{B}}}} \tag{7.72}$$

The steady-state voltammogram is characteristically sigmoidal, with the half-wave po-

tential at the formal reduction potential when the diffusion coefficients are equal. If D'_{B} is increased, the accelerated diffusion of B away from the electrode shifts the overall equilibrium in favour of B, such that the full voltammetric wave is shifted to lower overpotential. This is clarified by rewriting the equation in terms of an apparent overpotential η', where:

$$j_{\mathrm{A}} = \frac{1}{1 + \mathrm{e}^{-\eta'}} \tag{7.73}$$

where

$$\eta' = \eta + \ln D'_{\mathrm{B}} \tag{7.74}$$

The reversible steady-state voltammetry under diffusion-only conditions for a range of diffusion coefficient ratios is shown at Figure 7.5.

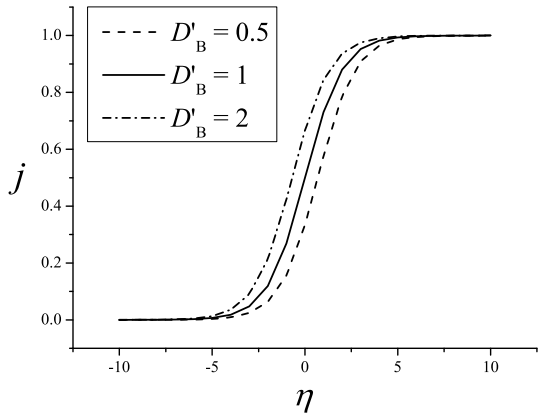

Figure 7.5: Steady-state (microelectrode) cyclic voltammetry for $D'_{\mathrm{B}} = 0.5$, 1, and 2, with thermodynamically reversible electrode kinetics.

If the electrode kinetics are finite, the current may be limited by the rate of electron transfer rather than the rate of diffusion, even under conditions of an equilibrated diffusion layer. Again, the current may be inferred by direct substitution for $c_{\mathrm{B},0}$ and

j_A as functions of $c_{\mathrm{A},0}$ into the normalised Butler–Volmer equation:

$$c_{\mathrm{A},0} - (1 - c_{\mathrm{A},0}) \left(\frac{\mathrm{e}^{-\eta}}{D'_\mathrm{B}} + \frac{\mathrm{e}^{-\alpha'\eta}}{K^0} \right) = 0 \tag{7.75}$$

hence

$$j_\mathrm{A} = \frac{1}{1 + \frac{\mathrm{e}^{-\alpha'\eta}}{K^0} + \frac{\mathrm{e}^{-\eta}}{D'_\mathrm{B}}} \tag{7.76}$$

As $K^0 \to 0$, the Butler–Volmer term tends to dominate such that $j_\mathrm{A} \to K^0 \, \mathrm{e}^{+\alpha'\eta}$ in accordance with the Tafel law for irreversible reactions.[2,14] Quasi-reversible steady-state voltammetry under diffusion-only conditions for a range of heterogeneous rate constants is shown at Figure 7.6.

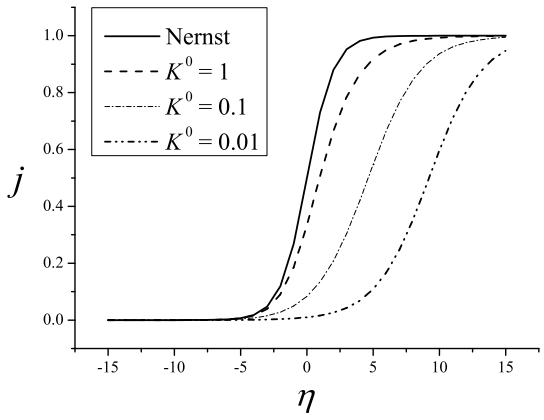

Figure 7.6: Steady-state (microelectrode) cyclic voltammetry with finite electrode kinetics. $D'_\mathrm{B} = 1$, $\alpha = 0.5$.

As $\eta \to \infty$, a limiting current of $j \to 1$ is attained irrespective of the electrode kinetics. This limiting current implies complete conversion of reactant to product at the electrode surface, at a diffusion-limited rate. In dimensional units:

$$i_\mathrm{lim} = 2\pi n F C^*_\mathrm{A} D_\mathrm{A} r_\mathrm{e} \tag{7.77}$$

and the limiting current density is

$$i'_\mathrm{lim} = \frac{n F C^* D_\mathrm{A}}{r_\mathrm{e}} \tag{7.78}$$

highlighting that the convergent hemispherical diffusion to smaller electrodes exhibit superior current density.

7.9 Conclusion

This chapter has introduced the cyclic voltammetry experiment and has described the dependence of voltammetric waveshape and quantitative observables, such as peak current and peak potential, on the relevant system parameters, subject to diffusion-only mass transport. In the next three chapters, the theory of cyclic voltammetry will be developed to conditions where charge transport is important. The theoretical model for diffusion-only voltammetry is an instructive limiting case for the theory of the more complex system, and will be required frequently.

Bibliography

[1] M. Faraday, *Phil. Trans. Royal Soc. London*, 1833, **123**, 23–54.

[2] A. J. Bard and L. R. Faulkner, *Electrochemical Methods: Fundamentals and Applications*, John Wiley & Sons, New York, 2nd edn., 2001.

[3] W. Nernst, *Ber. Kgl. Pr. Akad. Wiss.*, 1889, 83–95.

[4] T. Erdey-Grúz and M. Volmer, *Z. Physik. Chem.*, 1930, **150**, 203–213.

[5] J. A. V. Butler, *Trans. Faraday Soc.*, 1932, **28**, 379–382.

[6] R. A. Marcus, *J. Chem. Phys.*, 1956, **24**, 966–78.

[7] R. G. Compton and C. E. Banks, *Understanding Voltammetry*, Imperial College Press, London, 2nd edn., 2011.

[8] K. B. Oldham, *J. Electroanal. Chem.*, 1988, **250**, 1–21.

[9] J. G. Limon-Petersen, J. T. Han, N. V. Rees, E. J. F. Dickinson, I. Streeter and R. G. Compton, *J. Phys. Chem. C*, 2010, **114**, 2227–2236.

[10] J. E. B. Randles, *Trans. Faraday Soc.*, 1948, **44**, 327–338.

[11] A. Ševčík, *Collect. Czech. Chem. Commun.*, 1948, **13**, 349–377.

[12] H. Matsuda and Y. Ayabe, *Z. Elektrochem.*, 1955, **59**, 494–503.

[13] K. Aoki, *Electroanalysis*, 1993, **5**, 627–639.

[14] J. Tafel, *Z. Physik. Chem.*, 1905, **50**, 651–712.

Chapter 8

Cyclic voltammetry: the electroneutrality approximation

This chapter reviews the application of the electroneutrality approximation to charge transport problems in cyclic voltammetry. This review draws on a critical analysis of electroneutrality in electrochemistry which has been published by the Journal of Solid State Electrochemistry.[1] A novel, streamlined numerical solution method is presented for steady-state voltammetry subject to electroneutrality, as published by the Journal of Electroanalytical Chemistry.[2]

8.1 Origins of electroneutrality

In the hemispherical electrode geometry, the Poisson equation can be written as:

$$2\left(\frac{x_{\mathrm{D}}}{r_{\mathrm{e}}}\right)^{2}\nabla^{2}\theta+\sum_{i}z_{i}c_{i}=0 \tag{8.1}$$

If $x_{\mathrm{D}} \ll r_{\mathrm{e}}$, then $\sum_i z_i c_i \to 0$, except within a distance of a few x_{D} from a boundary condition where electroneutrality does not hold. This is the case at the electrode surface due to the uncompensated excess charge θ_0, as discussed in Chapters 5–6. This electric

field is screened by the double layer over a distance of a few Debye lengths: outside the double layer, electroneutrality holds.

The electroneutrality approximation amounts to the conclusion that insufficient Gibbs energy is available from diffusion or chemical reaction to separate charge in an electrolytic solution over a long distance or for a long time. On the basis of dimensional analysis, "long" means with respect to the Debye scale as parameterised by the Debye length (Equation 1.23) and Debye time. These are of the order of nanometres and nanoseconds respectively, and therefore charge separation rarely impacts on a macroscale experiment, and may be treated as absent to a good approximation.

Electroneutrality can be applied to a much wider set of situations than can the requirement of $\theta \to 0$ discussed in the previous chapter, since it does not require a high degree of inert support with respect to the reactant concentration. Cyclic voltammetry may be described by the Nernst–Planck equations together with the electroneutrality relation for any degree of electrolytic support, so long as:

- The Debye length is negligible compared to the size of the steady-state depletion layer, i.e. $x_{\mathrm{D}} \ll r_{\mathrm{e}}$.
- Capacitive currents due to double layer charging can be neglected.
- The Nernst or Butler–Volmer equation can be applied with reference to concentrations and potential *outside* the double layer.

The first condition holds for micro- and macroelectrodes, but not nanoelectrodes, for typical electrolyte concentrations in aqueous solution. The term "depletion layer" is used in place of diffusion layer, in consideration that the reactant may be transported by both diffusion and migration in the presence of an electric field. For the third

condition, if the flux that can be passed through the double layer is limited by any mechanism, it is not correct to use the electroneutrality relation. The assessment of whether or not this condition holds will be considered by modelling the diffuse double layer in full in Chapter 10.

Note that within the double layer, electroneutrality does not hold, by definition; the application of the electroneutrality condition to describe the electrodynamics of a system therefore implies that the double layer can be ignored.

8.2 Literature on electroneutral voltammetry

The properties of cyclic voltammetry subject to the electroneutrality approximation have been extensively studied in the last twenty-five years.

These studies have aimed to quantify the two principal effects which arise when voltammetry is performed in a weakly conducting electrolytic solution: ohmic drop and migration. Both effects result from the introduction of a net charge into the solution due to the passage of Faradaic current, which in the absence of sufficient supporting electrolyte cannot be rapidly screened on the timescale of the experiment. Since these effects occur entirely due to an uncompensated charge separation in a depletion layer, the explanation of either using electroneutrality is paradoxical, if nonetheless effective (as also addressed in Section 4.2.1).

Ohmic drop describes a shifting of voltammetric features to higher overpotentials due to the decreased conductivity of the solution and a consequent potential difference between the solution at the electrode surface and solution in bulk. This idea was introduced in Section 7.5 in which the apparent overpotential was identified as $(\eta -$

$n\theta_0$). Voltammetric features are therefore offset by a quantity θ_0, due to the excess overpotential required to overcome the resistance of the solution when Faradaic current is driven.

The contribution of migration to the incident flux of the electroactive species arises because the uncompensated electric field either augments or reduces the current under mass transport-limited conditions. Three cases can be identified: where $z_A n < 0$, the reaction of A produces a depletion layer of opposite charge and so A is attracted to the surface (higher flux); where $z_A n > 0$, the reaction produces a layer of like charge and so A is repelled from the surface (lower flux); and where $z_A = 0$, the flux of A is unaffected by the electric field, because A is neutral. In electroneutral theory, the charge that causes this migration implicitly resides in an infinitesimal layer adjacent to the electrode; the presence of a potential difference and an electric field in the absence of charge separation is an unavoidable contradiction of the electroneutrality approximation.

Author	Year	Type	Method	Comments
Bond et al.[3]	1984	SSV	Math.	$z_A = 0$ only.
Amatore et al.[4]	1987	SSV	Math.	Cylindrical; Nernstian; equal D.
Oldham[5]	1988	SSV	Math.	Nernstian.
Amatore et al.[6]	1988	SSV	Math.	Nernstian; equal D.
Cooper et al.[7,8]	1991–1992	SSV	Exp.	Comparison to Oldham theory.
Oldham et al.[9,10]	1992–1993	SSV	Math.	Nernstian; equal D.
Stojek et al.[11–13]	1995–1996	CA	Num.	Integration method for potential.
Stojek et al.[14–17]	1997–2005	CV/CA	Num.	
Bond et al.[18,19]	1998–2001	CV	Num.	Experimental comparisons; iR compensation.
Streeter et al.[20]	2008	CA	Num.	Comparison to other models.

Table 8.1: Literature concerning voltammetric theory subject to the electroneutrality approximation, to 2008. CA: Chronoamperometry; CV: cyclic voltammetry; Exp.: experimental; Math.: mathematical analysis; Num.: numerical simulation; SSV: steady-state voltammetry.

Confining our interest to voltammetry involving a single heterogeneous electron transfer, the literature on electroneutral theory and its direct comparison to experiment

is summarised in Table 8.1. Additionally, the field has been reviewed by Ciszkowska et al.[21] and by Bond.[22] In these works, it is standard to employ either the Nernst or Butler–Volmer equation to describe the electron transfer, which is assumed to take place at a plane in solution arbitrarily close to the outer edge of the double layer, where electroneutrality is maintained.

Two general themes can be noted in the literature. Up to the mid-1990s, work focused on developing predominantly analytical solutions to the problem of steady-state voltammetry subject to the electroneutrality approximation. The works of Oldham and Myland[9,10] provide the most general treatment of steady-state voltammetry, subject to the approximations of Nernstian (reversible) electrode kinetics and equal diffusion coefficients of all ions. Since the mid-1990s, numerical simulation has been employed to solve time-dependent problems subject to the electroneutrality approximation, such as macroelectrode cyclic voltammetry and chronoamperometry.

8.3 Steady-state voltammetry: numerical methods

8.3.1 Theoretical model

Existing work on steady-state voltammetry subject to electroneutrality makes a number of general determinations but, despite the extensive literature introduced in Table 8.1, does not offer a clear, rapid procedure for determining a voltammogram. For example, the work of Amatore et al. considers a cylindrical geometry in which steady-state is not attained.[4] The work of Oldham et al. draws a distinction between zero and negligible supporting electrolyte and convolutes the discussion of voltammetry by introducing "stress profiles" and other mathematical operations without a clear physical analogy.

Therefore, the following discussion has been developed by the author to synthesise existing results into a consistent numerical strategy for electroneutral theory, taking full advantage of known numerical techniques. No theoretical distinction is drawn between the condition of zero supporting electrolyte and that of a small quantity of supporting electrolyte, and the optimal numerical procedure for determining a voltammogram is clarified.

A radially transformed space y will be employed, where:

$$y = 1 - \frac{1}{R} \tag{8.2}$$

Therefore, $0 \leq y \leq 1$ where $y = 0$ is the electrode surface and $y = 1$ is bulk solution. At steady state, the flux of A, j_{A} is a constant in y-space equal to the normalised steady-state current (Equation 7.52).

The discussion will be confined to one-electron transfers where $n = \pm 1$. Let us define the supporting ion i as the inert ion with charge $+n$ and the supporting ion j as the inert ion with charge $-n$. Then, taking the general theoretical model for cyclic voltammetry at steady-state, the time-independent Nernst–Planck equations together with electroneutrality are:

$$\frac{dc_{\mathrm{A}}}{dy} + z_{\mathrm{A}} c_{\mathrm{A}} \frac{d\theta}{dy} - j_{\mathrm{A}} = 0 \tag{8.3}$$

$$\frac{dc_{\mathrm{B}}}{dy} + z_{\mathrm{B}} c_{\mathrm{B}} \frac{d\theta}{dy} + \frac{j_{\mathrm{A}}}{D'_{\mathrm{B}}} = 0 \tag{8.4}$$

$$\frac{dc_i}{dy} + n c_i \frac{d\theta}{dy} = 0 \tag{8.5}$$

$$\frac{dc_j}{dy} - n c_j \frac{d\theta}{dy} = 0 \tag{8.6}$$

$$z_{\mathrm{A}} c_{\mathrm{A}} + z_{\mathrm{B}} c_{\mathrm{B}} + n c_i - n c_j = 0 \tag{8.7}$$

subject to the conditions in Table 7.2 at $y = 1$.

At $y = 0$, the flux relations implied by the Nernst–Planck equations in B, i and j also hold, as does the electroneutrality condition. Note that at steady state, the fluxes of i and j are zero across all solution, since they are zero at the electrode surface where these species are inert. An additional relationship is required at $y = 0$ to describe the electrode kinetics.

8.3.2 Equal diffusion coefficients

As a first approximation, if $D'_{\mathrm{B}} = 1$, summing the four Nernst–Planck equations gives:

$$\frac{d\sum_k c_k}{dy} + \sum_k z_k c_k \frac{d\theta}{dy} = 0 \tag{8.8}$$

and so, since the second term is zero due to electroneutrality:

$$\sum_k c_k = \gamma \tag{8.9}$$

where γ is a constant equal to the sum of concentrations in bulk, as was first demonstrated by Amatore et al.[4]

Multiplying Equation 8.9 through by z_{B} and noting that $z_{\mathrm{B}} - z_{\mathrm{A}} = n$, by subtracting the electroneutrality condition (Equation 8.7) we achieve an expression for c_{A}. Equally, multiplying Equation 8.9 by z_{A} and subtracting the electroneutrality condition achieves an expression for c_{B}:

$$c_{\mathrm{A}} = \frac{1}{n}\Big(z_{\mathrm{B}}\gamma - (z_{\mathrm{B}} - n)c_i - (z_{\mathrm{B}} + n)c_j\Big) \tag{8.10}$$

$$c_{\mathrm{B}} = -\frac{1}{n}\Big(z_{\mathrm{A}}\gamma - (z_{\mathrm{A}} - n)c_i - (z_{\mathrm{A}} + n)c_j\Big) \tag{8.11}$$

Now

$$c_i = c_i^* \, \mathrm{e}^{-n\theta} \tag{8.12}$$

$$c_i = c_j^* \, \mathrm{e}^{+n\theta} \tag{8.13}$$

such that

$$c_\mathrm{A} = \frac{1}{n} \left(z_\mathrm{B}\gamma - (z_\mathrm{B} - n)c_i^* \mathrm{e}^{-n\theta} - (z_\mathrm{B} + n)c_j^* \mathrm{e}^{+n\theta} \right) \tag{8.14}$$

$$c_\mathrm{B} = -\frac{1}{n} \left(z_\mathrm{A}\gamma - (z_\mathrm{A} - n)c_i^* \mathrm{e}^{-n\theta} - (z_\mathrm{A} + n)c_j^* \mathrm{e}^{+n\theta} \right) \tag{8.15}$$

At this point the following shorthand notation is applied:

$$\lambda_i^k = (z_k - n)c_i^* \tag{8.16}$$

$$\lambda_j^k = (z_k + n)c_j^*$$

$$\lambda_\gamma^k = z_k\gamma$$

Differentiating Equation 8.14:

$$\frac{dc_\mathrm{A}}{dy} = \lambda_i^\mathrm{B} \mathrm{e}^{-n\theta} \frac{d\theta}{dy} - \lambda_j^\mathrm{B} \mathrm{e}^{+n\theta} \frac{d\theta}{dy} \tag{8.17}$$

Substituting into Equation 8.3:

$$\left(\lambda_i^\mathrm{B} \mathrm{e}^{-n\theta} - \lambda_j^\mathrm{B} \mathrm{e}^{+n\theta} + \frac{z_\mathrm{A}}{n} \left(\lambda_\gamma^\mathrm{B} - \lambda_i^\mathrm{B} \mathrm{e}^{-n\theta} - \lambda_j^\mathrm{B} \mathrm{e}^{+n\theta} \right) \right) \frac{d\theta}{dy} = j_\mathrm{A} \tag{8.18}$$

Integrating:

$$-\frac{1}{n} \int_0^{\theta_0} \left(- z_\mathrm{A}\lambda_\gamma^\mathrm{B} + (z_\mathrm{A} - n)\lambda_i^\mathrm{B} \mathrm{e}^{-n\theta} + (z_\mathrm{A} + n)\lambda_j^\mathrm{B} \mathrm{e}^{+n\theta} \right) d\theta = j_\mathrm{A} \int_1^0 dy \tag{8.19}$$

so

$$j_\mathrm{A} = \left((z_\mathrm{A} + n)\lambda_j^\mathrm{B} (\mathrm{e}^{+n\theta_0} - 1) \right) - \left((z_\mathrm{A} - n)\lambda_i^\mathrm{B} (\mathrm{e}^{-n\theta_0} - 1) \right) - n z_\mathrm{A} \lambda_\gamma^\mathrm{B} \theta_0 \tag{8.20}$$

where, for a one-electron transfer, $n^2 = 1$.

Let us define a variable

$$x_0 = \mathrm{e}^{-n\theta_0} \tag{8.21}$$

so $0 < x_0 \leq 1$, assuming positive ohmic drop for an oxidation and negative ohmic drop for a reduction.

Therefore:

$$j_\mathrm{A} = \left((z_\mathrm{A}+n)\lambda_j^\mathrm{B}\left(\frac{1-x_0}{x_0}\right)\right) - \Big((z_\mathrm{A}-n)\lambda_i^\mathrm{B}(x_0-1)\Big) + z_\mathrm{A}\lambda_\gamma^\mathrm{B}\ln(x_0) \tag{8.22}$$

This expression is general for $D_\mathrm{A} = D_\mathrm{B}$ irrespective of whether Nernstian or Butler–Volmer kinetics are applied.

8.3.3 Nernst equation with equal diffusion coefficients

According to the Nernst equation:

$$c_{\mathrm{A},0} = c_{\mathrm{B},0}\,\mathrm{e}^{-(\eta-n\theta_0)} = c_{\mathrm{B},0}\,\frac{\mathrm{e}^{-\eta}}{x_0} \tag{8.23}$$

Substituting the expressions above for c_A and c_B, introducing the λ_i^k shorthand, and multiplying through by n:

$$\lambda_\gamma^\mathrm{B} - \lambda_i^\mathrm{B}x_0 - \lambda_j^\mathrm{B}\frac{1}{x_0} = \left(-\lambda_\gamma^\mathrm{A} + \lambda_i^\mathrm{A}x_0 + \lambda_j^\mathrm{A}\frac{1}{x_0}\right)\frac{\mathrm{e}^{-\eta}}{x_0} \tag{8.24}$$

Now, multiplying through by $-x_0^2$ and collecting like terms:

$$\lambda_i^\mathrm{B}x_0^3 + \left(\lambda_i^\mathrm{A}\mathrm{e}^{-\eta} - \lambda_\gamma^\mathrm{B}\right)x_0^2 + \left(\lambda_j^\mathrm{B} - \lambda_\gamma^\mathrm{A}\mathrm{e}^{-\eta}\right)x_0 + \lambda_j^\mathrm{A}\mathrm{e}^{-\eta} = 0 \tag{8.25}$$

which is a cubic equation which from physical intuition has a real root in the domain $0 < x_0 \leq 1$.

Note that if $\lambda_i^\mathrm{B} = 0$ or $\lambda_j^\mathrm{A} = 0$, this reduces to a quadratic equation. This is the case if: $z_\mathrm{B} - n = 0$, when $z_\mathrm{A} = 0$; or $z_\mathrm{A} + n = 0$, when $z_\mathrm{B} = 0$. So if either A or B is a

neutral species, the equation is quadratic rather than cubic.

In either case, given that the root of a polynomial $P_n(x)$ is confined within a domain of x, it is trivial to solve for that root using the Newton–Raphson method (Equation 3.25), in which each iteration x^k is calculated according to:

$$x_0^k = x_0^{k-1} - \frac{P_n(x_0^{k-1})}{P_n'(x_0^{k-1})} \tag{8.26}$$

where

$$P_n' = \frac{dP_n}{dx} \tag{8.27}$$

A suitable initial guess is $x_0 = 1$, corresponding to zero ohmic drop, since the polynomial is smooth and monotonic close to $x_0 = 1$.

Having solved for x_0, it can be substituted into Equation 8.22 to find the flux j_A directly. Concentration profiles can be determined by taking the integral in Equation 8.19 to θ at y rather than to θ_0 at $y = 0$. This gives a closed expression for θ (and hence all four c_k) as a function of j_A and y. No numerical integration is required once j_A is known. Therefore, solving the cubic equation for θ_0 allows the concentration profiles of all species to be reconstructed in full.

Note that the numerical implementation is achieved straightforwardly and no 'iterative' procedures[10] are required to construct a cyclic voltammogram, beyond that implied within the Newton–Raphson method used to solve the cubic equation for the ohmic drop.

8.3.4 Butler–Volmer kinetics

The Butler–Volmer equation imposes finite kinetics upon the electrode reaction:

$$c_{\mathrm{A}} - c_{\mathrm{B}}\,\mathrm{e}^{-(\eta - n\theta_0)} - \frac{j_{\mathrm{A}}}{K^0}\,\mathrm{e}^{-\alpha'(\eta - n\theta_0)} = 0 \tag{8.28}$$

so

$$\begin{aligned} &\lambda_\gamma^{\mathrm{B}} - \lambda_i^{\mathrm{B}} x_0 - \lambda_j^{\mathrm{B}} \frac{1}{x_0} \\ &\quad + \left(\lambda_\gamma^{\mathrm{A}} - \lambda_i^{\mathrm{A}} x_0 - \lambda_j^{\mathrm{A}} \frac{1}{x_0}\right) \frac{\mathrm{e}^{-\eta}}{x_0} \\ &\quad - \frac{j_{\mathrm{A}}}{K^0}\,\mathrm{e}^{-\alpha'\eta} x_0^{\alpha'} = 0 \end{aligned} \tag{8.29}$$

As before this can be multiplied through by x_0 as many times as is required, to yield an overall equation of the form:

$$P_n(x_0) + x_0^{+\alpha'}\, Q_m(x_0) = 0 \tag{8.30}$$

where typically $m \neq n$. Given that we expect the root x_0 to arise in the domain $0 < x_0 \leq 1$ as before, this equation can also be solved straightforwardly by a Newton–Raphson method.

8.3.5 Unequal diffusion coefficients

If $D_{\mathrm{A}} \neq D_{\mathrm{B}}$, the analysis is more complicated. Summing the Nernst–Planck equations as above and defining the sum over all concentrations as a function $\gamma(y)$:

$$\frac{d\sum_k c_k}{dy} = \frac{d\sigma}{dy} = \delta\, j_{\mathrm{A}} \tag{8.31}$$

where

$$\delta = 1 - \frac{D_{\mathrm{A}}}{D_{\mathrm{B}}} \tag{8.32}$$

with $\delta = 0$ for the equal D case above.

Defining γ^* as the total concentration in bulk, and integrating:

$$\int_{\gamma}^{\gamma^*} d\gamma' = j_{\mathrm{A}}\delta \int_{y}^{1} dy' \tag{8.33}$$

$$\gamma = \gamma^* + j_{\mathrm{A}}\delta\,(y-1) \tag{8.34}$$

Also, defining $x = \mathrm{e}^{-n\theta}$ generally, the following expressions then apply for c_{A} and c_{B}:

$$c_{\mathrm{A}} = \frac{1}{n}\left(\lambda_{\gamma}^{\mathrm{B}} + z_{\mathrm{B}} j_{\mathrm{A}}\delta(y-1) - \lambda_{i}^{\mathrm{B}} x - \lambda_{j}^{\mathrm{B}}\frac{1}{x}\right) \tag{8.35}$$

$$c_{\mathrm{B}} = -\frac{1}{n}\left(\lambda_{\gamma}^{\mathrm{A}} + z_{\mathrm{A}} j_{\mathrm{A}}\delta(y-1) - \lambda_{i}^{\mathrm{A}} x - \lambda_{j}^{\mathrm{A}}\frac{1}{x}\right) \tag{8.36}$$

Noting that:

$$\frac{dc_{\mathrm{A}}}{dy} - \frac{z_{\mathrm{A}}}{nx}\frac{dx}{dy} = j_{\mathrm{A}} \tag{8.37}$$

the above expression for c_{A} can be differentiated to:

$$\frac{dc_{\mathrm{A}}}{dy} = n z_{\mathrm{B}} j_{\mathrm{A}}\delta - \lambda_{i}^{\mathrm{B}}\frac{dx}{dy} + \lambda_{j}^{\mathrm{B}}\frac{1}{x^2}\frac{dx}{dy} \tag{8.38}$$

so

$$\left(1 - n z_{\mathrm{B}}\delta\right) j_{\mathrm{A}} = \left(-\lambda_{i}^{\mathrm{B}} + \lambda_{j}^{\mathrm{B}}\frac{1}{x^2} + \frac{z_{\mathrm{A}}}{nx}\left(\lambda_{\gamma}^{\mathrm{B}} + z_{\mathrm{B}} j_{\mathrm{A}}\delta(y-1) - \lambda_{i}^{\mathrm{B}} x - \lambda_{j}^{\mathrm{B}}\frac{1}{x}\right)\right)\frac{dx}{dy} \tag{8.39}$$

This equation is no longer separable in x and y in such a manner that it can be integrated. The most efficient approach was found to be Newton–Raphson iteration of x_0 using a Runge–Kutta integration to 'shoot' from $y = 0$ to $y = 1$.[23] A finite difference approach would be equally plausible. In each case, once x_0 was determined, j_{A} was determined directly according to the Nernst equation or Butler–Volmer equation. Numerical integration could then be applied to determine the potential profile $\theta(y)$, and hence the concentration profiles of the four ionic species.

Even with unequal diffusion coefficients, a steady-state voltammogram with electroneutrality can be simulated in a fraction of a second using a normal desktop computer, complete with concentration profiles. This technique provides a useful and computationally inexpensive starting point as an initial guess for the functions c_{A}, c_{B} and θ in the presence of more complex boundary conditions, as will be discussed further in Chapters 9–10.

8.3.6 Exemplar voltammetry

To demonstrate some typical behaviour for steady-state voltammetry subject to the electroneutrality approximation, exemplar voltammetry is illustrated at Figures 8.1–8.3. The three cases $z_{\mathrm{A}}n < 0$, $z_{\mathrm{A}}n = 0$ and $z_{\mathrm{A}}n > 0$ are treated by considering one-electron oxidations ($n = +1$) of species A with $z_{\mathrm{A}} = -1$, 0, $+1$. A voltammogram is presented in each case for quantities of electrolytic support ranging from excess ($c_{\mathrm{sup}} = 10^3$) to negligible ($c_{\mathrm{sup}} = 0.1$). The voltammograms and associated concentration profiles were generated in less than 10 s using the algorithms set out above.

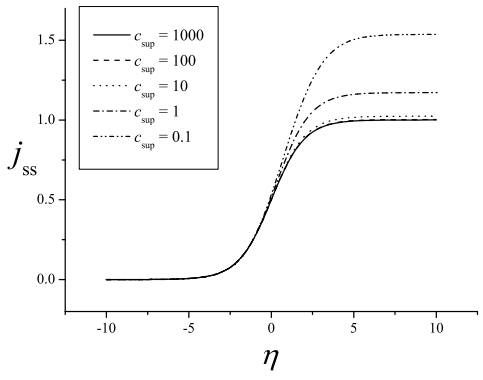

Figure 8.1: Simulated steady-state voltammetry for the one-electron oxidation of a species with $z_{\mathrm{A}} = -1$, at varying support. Note that reduced electrolytic support leads to attractive migration because $z_{\mathrm{A}}n < 0$.

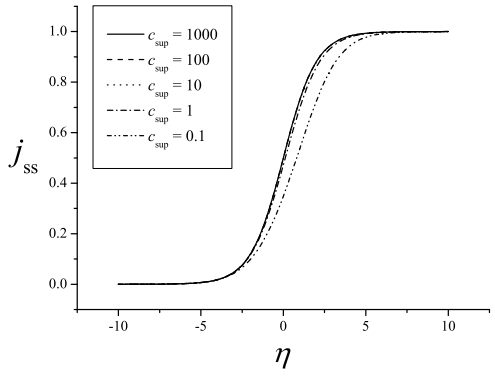

Figure 8.2: Simulated steady-state voltammetry for the one-electron oxidation of a species with $z_A = 0$, at varying support. Migration does not affect the mass transport of a neutral species, but ohmic drop does influence the position of the voltammetric wave.

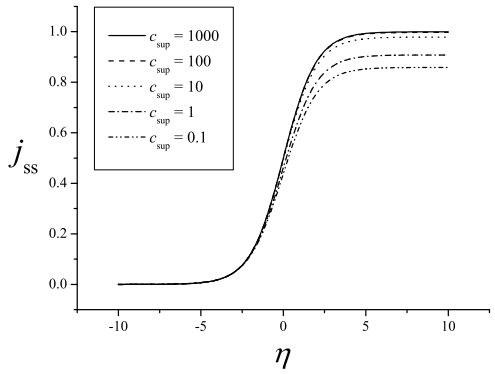

Figure 8.3: Simulated steady-state voltammetry for the one-electron oxidation of a species with $z_A = +1$, at varying support. Note that reduced electrolytic support leads to repulsive migration because $z_A n > 0$.

8.4 Alternatives to electroneutrality

Many more rigorous alternatives to electroneutrality have been considered for the description of weakly supported cyclic voltammetry. Oldham and Bond reviewed the suitability of the electroneutrality approximation for weakly supported steady-state voltammetry[24] by developing exact expressions for the steady states under two limiting cases. Their results confirmed that electroneutrality is accurate for electrodes larger than nanoscale. The limitations of electroneutrality for nanoelectrodes were discussed by Smith et al., specifically considering the inaccuracy of the approximation where the

depletion layer approaches the scale of the Debye length.[25]

Streeter et al.[20] reviewed the problem of weakly supported chronoamperometry and introduced a so-called 'zero-field' approximation, in which the detailed structure of the double layer is not considered and simply its infinitesimal size, compared to the depletion layer, is used to constrain a condition of zero enclosed charge within the plane of electron transfer. This approximation is critiqued in detail in the next chapter, and results based on zero-field are presented there.

The zero-field approximation has been successfully applied to model a range of voltammetric methods at micro- and macroelectrodes, performed in the Compton research group.[26–32] The timescales of these experiments tend to greatly exceed the Debye time, and the electrode is much larger than the Debye length, even with small concentrations of supporting electrolyte. The simulated results differ minimally from those that would result from an electroneutrality approximation, as would be expected for these conditions, although electroneutrality has not been assumed *a priori*. As such, the conclusions of electroneutral theory in terms of dynamic cyclic voltammetry have been corroborated by experiment, at least qualitatively, for electrodes of microscale and larger.[30]

Interestingly, electroneutrality is accurate even under 'extreme' conditions such as the stripping of pre-concentrated cadmium from a mercury drop in the total absence of supporting electrolyte, except for the cadmium salt solution.[31] The Faradaic stripping current causes charge to be injected very rapidly into solution, but the voltammetric currents are nonetheless, to a very strong approximation, controlled by the requirement of electroneutrality in the depletion layer, which exceeds the Debye length within nanoseconds. The voltammetry is depicted in Figure 8.4.

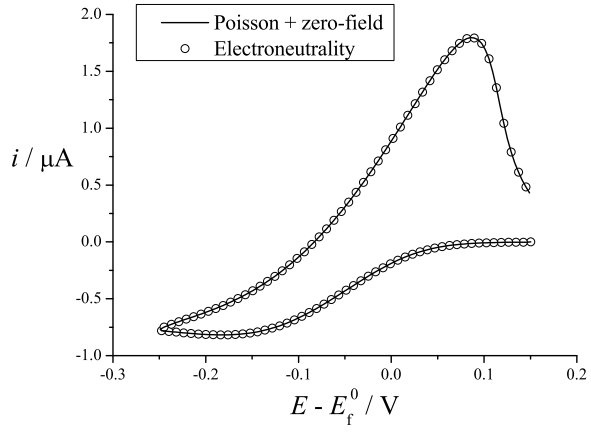

Figure 8.4: A comparison of simulated cyclic voltammograms for the formation of a thallium amalgam at a 45 μm mercury hemisphere by reduction of a 5 mM aqueous thallium nitrate solution, and the subsequent stripping of Tl(I), in the absence of additional supporting electrolyte and at a scan rate of 200 mV s^{-1}. The electroneutrality and zero-field approximations give equivalent results.

A major conclusion of this work was that stripping experiments, in which charge can be injected rapidly into solution, have much more stringent requirements for the quantity of inert support required for diffusion-only theory to be accurate than is the case for conventional solution-phase voltammetry with heterogeneous electron transfer to or from freely diffusing species.[31]

Another example of 'extreme' conditions is the electrolysis of a charged ion with zero added supporting electrolyte. In this case, electroneutrality can only be maintained by migration of the counter-ion of the electroactive species. This situation was discussed theoretically at steady state using the electroneutrality approximation, by Oldham.[9] Recently this problem has been approached dynamically, using chronoamperometry and cyclic voltammetry together with quantitative modelling using the Poisson equation and the zero-field approximation.[30,33] The results show very little discrepancy with Oldham's results (at steady state); those discrepancies that occur can be attributed to an exact steady state not in fact being achieved on the experimental timescale. Numer-

ical simulation indicates that except at very short time or distance, electroneutrality is obeyed.

As an example, a typical fit of an experimental cyclic voltammogram at trace support is presented at Figure 8.5, in which the presence of ionic impurities in the reactant required the modelling of a trace of inert electrolyte.

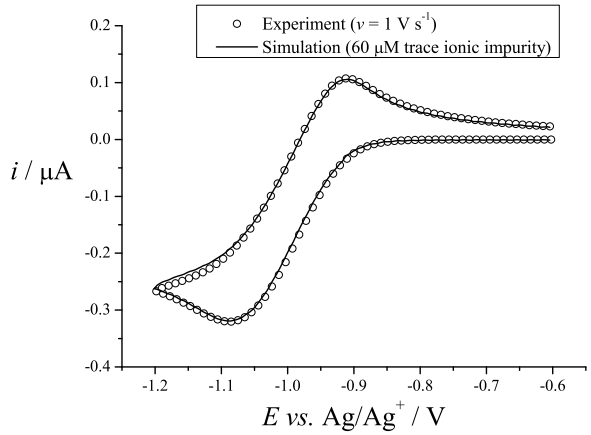

Figure 8.5: Experimental voltammetry for the reduction of unsupported 3 mM cobaltocenium hexafluorophosphate in acetonitrile on a 25 μm radius mercury hemisphere, compared to simulation using the Poisson equation and the zero-field approximation. Adapted from Limon-Petersen et al.,[33] figure 5, p. 140, with permission. Copyright Elsevier (2010).

Further, an example simulation using the Poisson equation with the zero-field approximation is shown for the case with a total absence of added supporting electrolyte at Figure 8.6, together with the equivalent result using the electroneutrality approximation.

It is clear that the voltammetry is effectively indistinguishable between the two approximations, because the electroneutral electric field, and hence the concentration profiles, is only inaccurate within a few Debye lengths of the electrode surface (Figure 8.7).

The use of numerical solution, however, permits the modelling of *dynamic* experiments across a range of scan rates and hence with a varied experimental timescale.

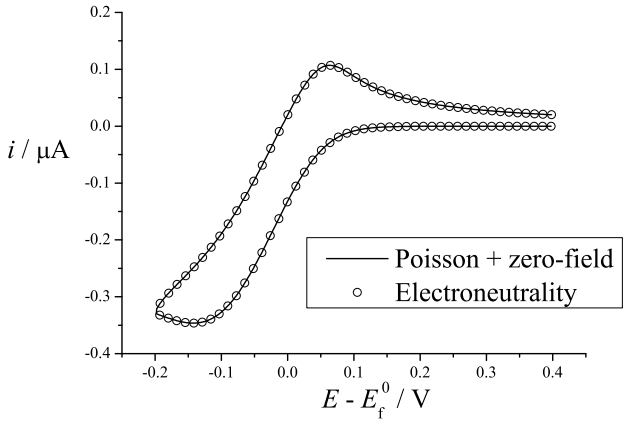

Figure 8.6: A comparison of simulated cyclic voltammograms for the reduction of unsupported 3 mM cobaltocenium hexafluorophosphate in acetonitrile on a 25 μm radius mercury hemisphere, showing that the electroneutrality and zero-field approximations give equivalent results.

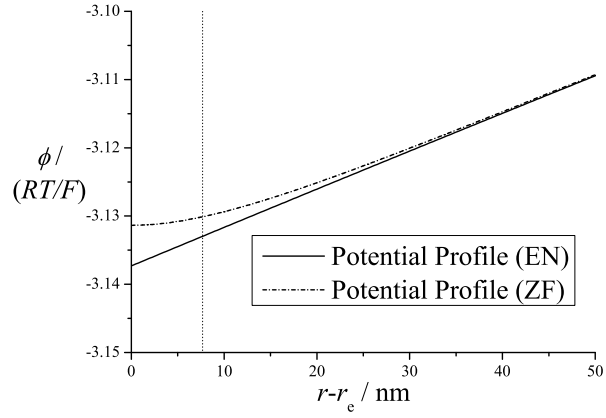

Figure 8.7: A comparison of simulated potential profiles at the forward peak current, for the reduction of unsupported 3 mM cobaltocenium hexafluorophosphate in acetonitrile on a 25 μm radius mercury hemisphere, showing the region in which the predicted potential profile differs between the electroneutrality and zero-field approximations. The vertical dotted line marks one unit Debye length from the electrode surface.

This allows better determination of experimental parameters such as diffusion coefficients and kinetic parameters, as well as improved mechanistic insight. For instance, numerical simulation of weakly supported dynamic experiments revealed that the comproportionation of anthraquinone with its dianion proceeds at a diffusionally-controlled rate in acetonitrile solution,[32] according to the principles set out at steady state by Norton et al.[34]

The investigation compared fully supported and weakly supported voltammetry. As the support ratio was reduced, the second reduction wave displayed a marked decrease in its transport-controlled current, corresponding to repulsive migration resisting the transport of an anion into a negatively-charged depletion layer. This shows that transport of the radical anion is rate-limiting, and therefore comproportionation occurs rapidly. The dependence of the current on the degree of electrolytic support cannot be explained by transport-controlled two-electron reduction of anthraquinone at the surface, since the neutral molecule is unaffected by the presence of an electric field.

Of course, steady-state investigation and analysis via electroneutrality – even of the dynamic data – could have attained the same conclusions. An excellent example of mechanistic analysis using electroneutral principles at steady state is the elucidation of the active comproportionation pathways in the reduction of fullerenes by Kowski et al.[35] However, the availability of numerical simulation for the analysis of dynamic voltammetry allows the use of different scan rates in order to investigate the relative rates of different chemical and diffusional processes.

8.5 Conclusions

The validity of the electroneutrality approximation when experimental time and space scales greatly exceed the Debye scale is borne out by detailed theoretical and experimental observation, both for liquid junction systems, as discussed in Chapter 4, and for voltammetry under weak electrolytic support, as demonstrated above. Charge transport at long times following a perturbation, or at long distances away from a point of perturbation, is predominantly controlled by the requirement of local electroneutrality.

The major advantage conferred by the electroneutrality approximation is that it greatly facilitates analytical solution of the Nernst–Planck equations: in this way, steady-state voltammetry and concentration profiles for cyclic voltammetry with any support ratio can be rapidly calculated by the method in Section 8.3. Analytical solutions of time-dependent charge transport problems are usually impossible, however, even with the electroneutrality approximation. Rather, experiments are typically analysed using numerical simulation. Since the implementation of the electroneutrality approximation does not make numerical simulation more straightforward or more stable, except in special cases such as equal diffusion coefficients,[4] it becomes unnecessary as an *a priori* assumption.

One major disadvantage of the electroneutrality approximation is the introduction of the paradox of a potential difference without any accompanying charge separation (Section 4.2.1). Simulations without electroneutrality allow more complete physical interpretations because electric fields are readily associated with charge separation. The electroneutrality approximation is useful and insightful for many charge transport problems and dictates voltammetric behaviour in a great variety of cases, but its use is perhaps superfluous once numerical simulation is adopted.

The next chapter will discuss the related zero-field approximation, and the properties of dynamic cyclic voltammetry under conditions where the quantity of electrolytic support is insufficient to apply diffusion-only theory. In Chapter 10, theories of voltammetry involving the diffuse double layer are considered. In both cases, it is convenient to eschew electroneutrality to approach charge transport problems without paradox and with greater subtlety, without concern over the appropriacy of treating Debye scales as negligible.

Bibliography

[1] E. J. F. Dickinson, J. G. Limon-Petersen and R. G. Compton, *J. Solid State Electrochem.*, 2011, **15**, 1335–1345.

[2] E. J. F. Dickinson and R. G. Compton, *J. Electroanal. Chem.*, 2011, **661**, 198–212.

[3] A. M. Bond, M. Fleischmann and J. Robinson, *J. Electroanal. Chem.*, 1984, **172**, 11–25.

[4] C. Amatore, M. R. Deakin and R. M. Wightman, *J. Electroanal. Chem.*, 1987, **225**, 49–63.

[5] K. B. Oldham, *J. Electroanal. Chem.*, 1988, **250**, 1–21.

[6] C. Amatore, B. Fosset, J. Bartelt, M. R. Deakin and R. M. Wightman, *J. Electroanal. Chem.*, 1988, **256**, 255–268.

[7] J. B. Cooper and A. M. Bond, *J. Electroanal. Chem.*, 1991, **315**, 143–160.

[8] J. B. Cooper, A. M. Bond and K. B. Oldham, *J. Electroanal. Chem.*, 1992, **331**, 877–895.

[9] K. B. Oldham, *J. Electroanal. Chem.*, 1992, **337**, 91–126.

[10] J. C. Myland and K. B. Oldham, *J. Electroanal. Chem.*, 1993, **347**, 49–91.

[11] A. Jaworski, M. Donten and Z. Stojek, *Anal. Chim. Acta*, 1995, **305**, 106–113.

[12] A. Jaworski, M. Donten and Z. Stojek, *J. Electroanal. Chem.*, 1996, **407**, 75–81.

[13] W. Hyk, M. Palys and Z. Stojek, *J. Electroanal. Chem.*, 1996, **415**, 13–22.

[14] W. Hyk and Z. Stojek, *J. Electroanal. Chem.*, 1997, **439**, 81–88.

[15] M. Ciszkowska, A. Jaworski and J. G. Osteryoung, *J. Electroanal. Chem.*, 1997, **423**, 95–101.

[16] W. Hyk and Z. Stojek, *Anal. Chem.*, 2002, **74**, 4805–4813.

[17] W. Hyk and Z. Stojek, *Anal. Chem.*, 2005, **77**, 6481–6486.

[18] A. M. Bond and S. W. Feldberg, *J. Phys. Chem. B*, 1998, **102**, 9966–9974.

[19] N. P. C. Stevens, M. B. Rooney, A. M. Bond and S. W. Feldberg, *J. Phys. Chem. A*, 2001, **105**, 9085–9093.

[20] I. Streeter and R. G. Compton, *J. Phys. Chem. C*, 2008, **112**, 13716–13728.

[21] M. Ciszkowska and Z. Stojek, *Anal. Chem.*, 2000, **72**, 754A–760A.

[22] A. M. Bond, in *Trends in Molecular Electrochemistry*, ed. A. J. L. Pombeiro and C. Amatore, Marcel Dekker, New York, 2004, ch. 14, pp. 445–502.

[23] W. H. Press, S. A. Teukolsky, W. T. Vetterling and B. P. Flannery, *Numerical Recipes. The Art of Scientific Computing.*, Cambridge University Press, Cambridge, 3rd edn., 2007.

[24] K. B. Oldham and A. M. Bond, *J. Electroanal. Chem.*, 2001, **508**, 28–40.

[25] C. P. Smith and H. S. White, *Anal. Chem.*, 1993, **65**, 3343–3353.

[26] J. G. Limon-Petersen, I. Streeter, N. V. Rees and R. G. Compton, *J. Phys. Chem. C*, 2008, **112**, 17175–17182.

[27] J. G. Limon-Petersen, I. Streeter, N. V. Rees and R. G. Compton, *J. Phys. Chem. C*, 2009, **113**, 333–337.

[28] E. J. F. Dickinson, J. G. Limon-Petersen, N. V. Rees and R. G. Compton, *J. Phys. Chem. C*, 2009, **113**, 11157–11171.

[29] J. G. Limon-Petersen, E. J. F. Dickinson, N. V. Rees and R. G. Compton, *J. Phys. Chem. C*, 2009, **113**, 15320–15325.

[30] J. G. Limon-Petersen, J. T. Han, N. V. Rees, E. J. F. Dickinson, I. Streeter and R. G. Compton, *J. Phys. Chem. C*, 2010, **114**, 2227–2236.

[31] J. G. Limon-Petersen, E. J. F. Dickinson, T. Doneux, N. V. Rees and R. G. Compton, *J. Phys. Chem. C*, 2010, **114**, 7120–7127.

[32] S. R. Belding, J. G. Limon-Petersen, E. J. F. Dickinson and R. G. Compton, *Angew. Chem., Int. Ed.*, 2010, **49**, 9242–9245.

[33] J. G. Limon-Petersen, E. J. F. Dickinson, S. R. Belding, N. V. Rees and R. G. Compton, *J. Electroanal. Chem.*, 2010, **650**, 135–142.

[34] J. D. Norton, W. W. Benson, H. S. White, B. D. Pendley and H. D. Abruña, *Anal. Chem.*, 1991, **63**, 1909–1914.

[35] M. Kowski, Z. Stojek and M. J. Palys, *Electrochem. Commun.*, 2009, **11**, 905–908.

Chapter 9

Cyclic voltammetry: the zero-field approximation

The zero-field approximation is a recent alternative to the electroneutrality approximation for describing the electrodynamics of voltammetry.[1] In this chapter, the zero-field approximation is analysed critically and the properties of cyclic voltammetry subject to the zero-field approximation are discussed. The approximation is then subjected to experimental corroboration. The critical analysis has been published by Chemical Physics Letters[2] and is augmented by further published by the Journal of Electroanalytical Chemistry.[3] The theory of cyclic voltammetry using the zero-field approximation has been published by the Journal of Physical Chemistry C,[4] together with the experimental work reported in this chapter. This experimental work was performed by Dr Juan Limon-Petersen and Dr Neil Rees as a collaboration within the Compton research group.

9.1 Introduction

The zero-field approximation was introduced by Streeter et al.[1] who found that it predicted the short-time current for weakly supported potential step chronoamperometry more accurately than the electroneutrality approximation discussed in the previous chapter, by comparison to a more complete double layer model. Whereas the electroneutrality approximation supposes that the charge density in solution is zero at all spaces and times, the zero-field approximation supposes only that the electrical double layer is negligible in extent compared to the electrode size. Consequently the zero-field approximation obeys Maxwell's equations throughout the diffusion layer, unlike electroneutrality, which may account for its superior performance for weakly supported systems at short times following a potential step.[1]

The approximation is illustrated in Figure 9.1.

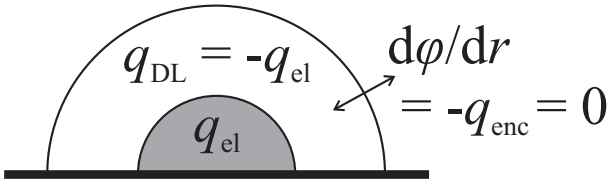

Figure 9.1: Schematic showing the logic of the zero-field approximation: the double layer (DL) has opposite charge to the electrode (el) and so $\partial\phi/\partial r \to 0$ outside the diffuse double layer.

If there exists a double layer which entirely compensates the charge on the electrode, the charge enclosed within the outer boundary of the double layer is zero, and therefore according to Gauss's Law (Equation 1.17), the electric field is zero at this outer boundary. The zero-field approximation sets $\nabla\phi = 0$ at $r = r_e$ exactly. In the normalised hemispherical space introduced in Chapter 7, this corresponds to:

$$\left.\frac{\partial\theta}{\partial R}\right|_{R=1} = 0 \tag{9.1}$$

as a boundary condition to the Poisson equation, with which the Nernst–Planck–

Poisson equation set is solved in full.

The utility of the zero-field approximation has been borne out by a number of experimental studies which have been analysed and accurately simulated using this approach.[4–9] One of these studies is reported later in the chapter. At this stage, it is instructive to consider the theory of the zero-field approximation in more detail.

9.2 Validity of decoupling the double layer and diffusion layer

9.2.1 Formal understanding of the zero-field approximation

The zero-field approximation represents an ideal, maximal decoupling of the double layer from the diffusion layer. For less than infinite support, there will exist an electric field due to the charge on the electrode, as well as an electric field due to charge generated in solution by electrolysis, which can be interpreted as an ohmic drop. The excess charge on the electrode leads to a double layer localised at its surface, as discussed in Chapters 5–6. Given the strength of the electroneutrality approximation, as discussed in the previous chapter, separated charge is screened outside the extent of the double layer, and therefore uncompensated charge arising from electrolysis can also be expected to be contained within the double layer.

In the limits of a large electrode or high support ratio, mass transport gradients associated with electrolysis are vanishing on the scale of the Debye length. By contrast, mass transport gradients associated with the diffuse double layer are vanishing beyond a few Debye lengths away from the electrode surface. The zero-field approximation assumes that because of the disparity between the diffusional and Debye length scales,

these effects may be decoupled. The potential in solution is treated as the sum of a double layer (DL) term and a zero field (ZF) term, the former being only associated with excess electrode charge and the latter being only associated with charge separation due to electrolysis:

$$\theta = \theta_{\mathrm{DL}} + \theta_{\mathrm{ZF}} \tag{9.2}$$

Defining the position of zero field as r_{ZF}, the double layer is contained within $r < r_{\mathrm{ZF}}$. Then, in the above decoupling, $\theta_{\mathrm{DL}} = 0$ for the domain outside the double layer ($r \geq r_{\mathrm{ZF}}$), and $\theta_{\mathrm{ZF}} = \Delta\theta_{\mathrm{OD}}$ for the domain of the double layer ($r_{\mathrm{e}} \leq r \leq r_{\mathrm{ZF}}$). Here, $\Delta\theta_{\mathrm{OD}}$ is the ohmic drop through the predominantly electroneutral solution from r_{ZF} to bulk solution, which is due to electrolytically generated charge. In fact, *both* components of potential must vary continuously from r_{e} to bulk, but in the zero-field limit, they can be treated as separable without significant error.

9.2.2 Mathematical analysis

In the original exposition of the zero-field approximation, it was described as accurate when the size of the diffusion layer greatly exceeds that of the electrical double layer,[1] but this is a slight oversimplification. It is necessary to define carefully what is meant by "the size of the diffusion layer". For a hemispherical system at steady state, both the double layer and diffusion layer formally extend to bulk solution, which is typically treated as being infinitely distant – what matters is the extent to which the concentration gradients and electric field differ from their bulk values.

We may consider two exemplar functions, both of which are representative at steady state. We can imagine a 'typical' potential in the region of the double layer to be

described by the low potential limit of the Gouy–Chapman equation (Equation 5.18), and a 'typical' concentration profile to be described by the steady-state concentration profile of an uncharged species being generated electrolytically at the electrode surface. Respectively, these are:

$$\phi = \phi_0 \exp\left(-\frac{r - r_\mathrm{e}}{x_\mathrm{D}}\right) \tag{9.3}$$

and

$$c_i = \frac{J_i}{D_i}\frac{r_\mathrm{e}^2}{r} \tag{9.4}$$

Of course, this latter concentration profile is atypical of the concentration profile when migration of an ionic species becomes significant, such as for weakly supported voltammetry, but such bulk migration gradients are generally of similar order to diffusional gradients, since they arise in response to the developing diffusion layer. The low potential Gouy–Chapman equation also sets an upper bound on double layer extent, since a more charged diffuse double layer is comparatively contracted (Equation 5.14).

If the interior boundary for a Nernst–Planck–Poisson problem is set at a zero-field boundary at $r = r_\mathrm{e} \approx r_\mathrm{e} + \delta$, this will be accurate if both the double layer potential is approximately zero at this point, and the gradient of the diffusion profile is approximately zero. In consideration of the former condition, we can define δ as the point by which $\phi = \phi_0 \cdot 10^{-n}$, with some appropriate tolerance n.

The requirement that dc_i/dr at $r = r_\mathrm{e} + \delta$ exceeds $(1 - 10^{-n})$ times its value at at $r = r_\mathrm{e}$ – that is, negligible variation in the concentration gradient over this scale – places a lower limit on the ratio $r_\mathrm{e}/x_\mathrm{D}$, namely:

$$\frac{r_\mathrm{e}}{x_\mathrm{D}} > n10^n\left(2\ln 10 + 1\right) \tag{9.5}$$

This expression is approximate, for the sake of simplicity, but can be used establish the order of r_e where the zero-field boundary position significantly perturbs the solution to the NPP equations. For $n = 2$, implying a less-than-1% deviation in the concentration gradient due to electrolysis across 99% of the double layer, this gives:

$$\frac{r_e}{x_D} = R_e > 1000 \tag{9.6}$$

In real units this would correspond to $r_e > 1$ μm for a moderately supported case, or $r_e > 10$ μm for unsupported 1 mM A^+ ($x_D \approx 10$ nm).

9.2.3 Graphical demonstration

Simulating electrolysis processes with an explicit description of the diffuse double layer can be difficult, because the length scales associated with the double layer varies markedly from the length scales over which diffusion and migration to bulk take place. Simulation processes in conventional radial space, or the y-transform presented by Streeter et al.[1] and applied in the previous chapter (Section 8.3), can often fail if insufficient grid density is allowed in the diffuse double layer range*. At the same time, it is important to admit sufficient grid density in the domain from $r = r_e + x_D$ to infinity, in which the diffusion and migration processes associated with electrolysis take place.

A novel transformation was developed by the author in order to ensure that both the double layer and diffusion layer occur over a similar range of the transform space, with similar gradients, in order to assist visualisation of the coupling of the double

*Since this work was performed, work involving the diffuse double layer and multiple length scales has successfully been performed using a simple radial transformation, as reported in Chapter 10. This success is due to the refinement of numerical techniques, particularly in terms of the quality of the initial guess for the concentration and potential profiles. Nonetheless, the transformation in this chapter is optimal for clear visualisation of multiple length scales.

layer to the diffusion layer:

$$y = 1 - \left(\frac{r_\mathrm{e}}{r_\mathrm{e} + \gamma_1 (r - r_\mathrm{e})} + \frac{x_\mathrm{D}}{x_\mathrm{D} + \gamma_2 (r - r_\mathrm{e})} \right) \tag{9.7}$$

where $\gamma_1 = 10$ and $0.1 \leq \gamma_2 \leq 0.2$ give optimal solution smoothness and allow convergent simulations for a wide range of conditions and electrode sizes. The electrode then occurs at $y = -1$ and bulk solution is $y = +1$. The example functions above are depicted in Figure 9.2 for a range of values of R_e.

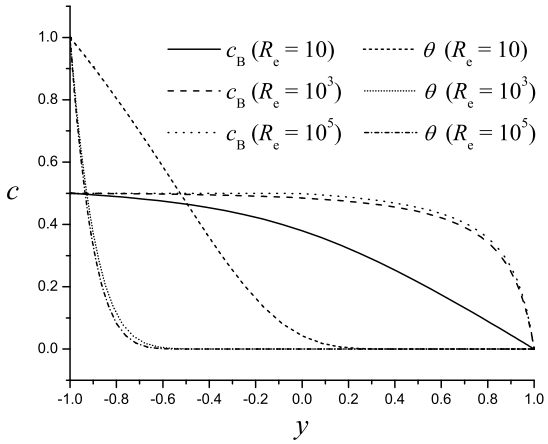

Figure 9.2: A comparison of exemplar concentration and potential profiles at varying R_e, in a novel transform space.

The zero-field decoupling condition is clearly expressed in terms of the requirement that $\partial c_i / \partial y \approx 0$ for all species in the same range that $\partial \theta / \partial y \approx 0$. Considering the region of $-0.5 < y < 0$ in Figure 9.2, this criterion is generally satisfied for $R_\mathrm{e} \geq 10^3$.

9.3 Relation between the zero-field approximation and electroneutrality

As illustrated in the previous chapter, simulations using the zero-field approximation give very similar results to those using electroneutrality, so long as the electrode is

large with respect to the Debye length ($R_\mathrm{e} \gg 1$). However, the zero-field formulation is consistent with Gauss's Law, within the approximation of ignoring the double layer, and does not introduce a potential difference without a corresponding charge separation in the solution. Simulations demonstrate that in a zero-field formulation the charge corresponding to the ohmic drop, and hence to bulk migration, is confined to a thin but finite layer adjacent to the zero-field boundary[8] – correctly, we should assume this charge to be intrinsic to the double layer and so the zero-field description remains strictly approximate.

The zero-field solution relates to the electroneutral solution as follows. First, let us suppose that the two solutions are distinct only in a boundary layer within a few Debye lengths of the zero-field boundary, since the outer boundaries are unaltered and electroneutrality will hold elsewhere. We now make the assumption that $r \approx r_\mathrm{e}$ in this range and introduce a Debye scale $X' = (\sqrt{\sigma}/x_\mathrm{D}) \cdot (r - r_\mathrm{e})$ where σ' is the normalised conductivity of the solution at $y = 0$:

$$\sigma' = \sum_i z_i^2 c_{i,0} \tag{9.8}$$

Hence the Poisson equation takes the form:

$$\frac{d^2\theta}{dX'^2} + \frac{1}{\sigma}\sum_i z_i c_i = 0 \tag{9.9}$$

in this range. Further, let us assume that the potential can be written in the form $\theta = \theta^{(0)} + \theta^{(1)}$ where $\theta^{(0)}$ is the electroneutral solution and $\theta^{(1)}$ is the zero-field perturbation.

On the relevant scale close to the electrode, $\theta^{(0)}$ is approximately linear so long as R_e is large. Therefore $d^2\theta^{(0)}/dX'^2 \approx 0$, and $\theta^{(1)} \to 0$ as $X' \to \infty$. At $X' = 0$, the

electrode surface:

$$\frac{d\theta^{(0)}}{dX'} + \frac{d\theta^{(1)}}{dX'} = 0 \tag{9.10}$$

to satisfy the zero-field condition.

If the flux is not limited by the change of boundary condition, the limiting flux is controlled by diffusion and migration outside the position of zero-field. Assuming, then, that the flux is unaltered by the presence of the zero-field condition:

$$j_i = \frac{dc_i}{dX'} + z_i c_i \frac{d\theta}{dX'} = j_i^{(0)} \tag{9.11}$$

so

$$\frac{dc_i}{dX'} - \frac{dc_i^{(0)}}{dX'} + z_i c_i \frac{d\theta^{(1)}}{dX'} = 0 \tag{9.12}$$

If the zero-field condition is negligibly perturbing then we can take $c_i \approx c_i^{(0)}$ and hence

$$c_i \approx c_i^{(0)} \exp(-z_i \theta^{(1)}) \tag{9.13}$$

where $\theta^{(1)}$ then becomes the solution to a corresponding Poisson–Boltzmann equation

$$\frac{d^2\theta^{(1)}}{dX'^2} + \frac{1}{\sigma} \sum_i z_i c_i^{(0)} \exp(-z_i \theta^{(1)}) = 0 \tag{9.14}$$

subject to the inner boundary condition of Equation 9.10 and the outer boundary condition $\theta^{(1)} = 0$.

It is clear that the above approximations are well justified if $\theta^{(1)} \ll 1$. For typical electric fields arising from the passage of Faradaic current in the electroneutrality solutions, this is certainly the case, and therefore the zero-field approximation simply imposes a weak Gouy–Chapman diffuse layer perturbation on the electroneutrality result, which does not significantly alter the flux. If, however, $\theta^{(1)} \gg 1$, then the above analysis will fail, and so it is not appropriate for a double layer with a considerable

excess charge.

9.4 Electrochemical boundary conditions

9.4.1 The implied approximation in the zero-field model

Having determined the range of electrode size for which the zero-field approximation does not significantly affect predicted concentration profiles due to misplacement of the electrode boundary, and having also determined the manner in which the zero-field condition perturbs the electric field from the electroneutrality solution, it is necessary to consider whether equations such as the Nernst equation or Butler–Volmer equation may be correctly applied at the point of zero field. Of course, if the point of zero field is close enough to the electrode that electron tunnelling is rapid here, then we may freely assume that the zero field boundary is indeed the site of electron transfer, and so overpotential and concentration may be related by one of the above equations at this boundary.

At low support in particular, however, the exponential decay distance of the electric field in the double layer, as defined by the Debye length, is at least 0.3 nm, whereas the exponential decay distance of the tunnelling process is typically shorter: a value of at most 1 Å is suggested by Edwards et al. for aqueous solution.[10] In a real system, electron transfer is then likely to take place inside the double layer. A more detailed theory, including tunnelling, will be discussed in the next chapter, but for the moment it is useful to consider how to relate diffuse double layer potential to the electron transfer equations.

9.4.2 Relation of excess charge to overpotential

First, the surface potential, ϕ_{w}, as defined in Chapter 5, must be determined as a function of the applied overpotential.

The applied Faradaic overpotential for a cyclic voltammogram is defined by reference to the formal reduction potential of the system.

$$E_{\mathrm{far}} \equiv E - E_{\mathrm{f}}^{\ominus} \tag{9.15}$$

From the definition of the potential difference across the electrochemical cell in Equations 5.2 and 5.3:

$$\begin{aligned} E &= \phi_{\mathrm{w}} - \phi_{\mathrm{ref}} \\ &= \phi_{\mathrm{w}} + E_{\mathrm{pzc}} \end{aligned} \tag{9.16}$$

Equating the two expressions for E:

$$E = E_{\mathrm{far}} + E_{\mathrm{f}}^{\ominus} = \phi_{\mathrm{w}} + E_{\mathrm{pzc}} \tag{9.17}$$

and so

$$\phi_{\mathrm{w}} = E_{\mathrm{far}} - (E_{\mathrm{pzc}} - E_{\mathrm{f}}^{\ominus}) \tag{9.18}$$

which places the definition for the surface potential at the outer Helmholtz plane in terms of a potential scale centred at $E_{\mathrm{f}}^{\ominus}$. A normalised potential of zero charge on this scale can then be defined as:

$$\theta_{\mathrm{pzc}} = \frac{F}{RT}\,(E_{\mathrm{pzc}} - E_{\mathrm{f}}^{\ominus}) \tag{9.19}$$

and then if the electrode surface potential is defined with respect to bulk solution as

$$\theta_0 = \frac{F}{RT}\,\phi_{\mathrm{w}} \tag{9.20}$$

the appropriate boundary condition for a diffuse double layer at the electrode surface is:

$$\begin{aligned}\theta_0 &= \frac{F}{RT}\left(E_{\text{far}} - E_{\text{pzc}}\right) \\ &= \frac{\eta}{n} - \theta_{\text{pzc}}\end{aligned} \tag{9.21}$$

The apparent overpotential, taking into account the potential difference to bulk solution, is $\eta_{\text{app}} = \eta - n\theta_0$ from Equation 7.49. Then, at the outer Helmholtz plane:

$$\eta_{\text{app},0} = n\theta_{\text{PZC}} \tag{9.22}$$

which makes clear that, interestingly, the perceived overpotential for electron transfer to or from a solution-phase species at the outer Helmholtz plane is independent of the applied overpotential with respect to a reference electrode in bulk solution. This relation can now be applied in the context of the potential and concentration profiles derived for the decoupled limit above.

9.4.3 Fully reversible electron transfer

Let us define a position $y = y_{\text{ZF}}$ as the zero-field boundary outside the double layer, where $c_i = c_{i,\text{ZF}}$ and $\theta = \Delta\theta_{\text{OD}}$, denoting the ohmic drop from the zero-field boundary to bulk solution. If the double layer is at equilibrium, then the concentration at the outer Helmholtz plane can be expressed in terms of the potential difference across the double layer according to the Boltzmann equation (Equation 1.33):

$$c_{i,0} = c_{i,\text{ZF}} \exp\left(-z_i\left(\frac{\eta}{n} - \theta_{\text{pzc}} - \Delta\theta_{\text{OD}}\right)\right) \tag{9.23}$$

If electron transfer is reversible, the Nernst equation is obeyed at the site of electron transfer, which we take to be the outer Helmholtz plane, where $\eta - n\theta_0 = n\theta_{\mathrm{pzc}}$:

$$c_{\mathrm{A},0} - c_{\mathrm{B},0}\,\mathrm{e}^{-n\theta_{\mathrm{pzc}}} = 0 \tag{9.24}$$

Substituting in Equation 9.23:

$$c_{\mathrm{A,ZF}}\,\mathrm{e}^{-z_{\mathrm{A}}(\frac{\eta}{n}-\theta_{\mathrm{pzc}}-\Delta\theta_{\mathrm{OD}})} - c_{\mathrm{B,ZF}}\,\mathrm{e}^{-z_{\mathrm{B}}(\frac{\eta}{n}-\theta_{\mathrm{pzc}}-\Delta\theta_{\mathrm{OD}})}\,\mathrm{e}^{-n\theta_{\mathrm{pzc}}} = 0 \tag{9.25}$$

and re-arranging, recalling that $n = z_{\mathrm{B}} - z_{\mathrm{A}}$:

$$c_{\mathrm{A,ZF}} - c_{\mathrm{B,ZF}}\,\mathrm{e}^{-(\eta - n\Delta\theta_{\mathrm{OD}})} = 0 \tag{9.26}$$

which is the Nernst equation as set for the conditions at $y = y_{\mathrm{ZF}}$.

This relation can be understood as demonstrating that in an equilibrated diffuse double layer, the altered apparent overpotential due to the electric field in the diffuse double layer is exactly offset by the corresponding accumulation or depletion of the species A and B, which are accumulated or depleted to a different extent due to their different charge.

Although striking, this result is not surprising, and is easily justified: since the double layer is equilibrated with respect to $y = 0$ and A and B are equilibrated at this point by the Nernst equation, they must necessarily be at equilibrium at all points through the double layer, $0 \leq y \leq y_{\mathrm{ZF}}$ in accordance with the laws of thermodynamics. The implication is significant, nonetheless – if electrochemical kinetics are sufficiently fast, steady-state voltammetry is blind to the actual position of electron transfer. Therefore, for fast electron transfer, the zero-field approximation can be applied with confidence.

9.4.4 Finite electrode kinetics

The above analysis does not hold so precisely if kinetics are finite. Following the same approach as above, we substitute in the expressions for c_i within the double layer to the Butler-Volmer equation as constructed at $y = 0$, with the result that a 'Frumkin correction'[11] arises between the 'real' k^0, if electron transfer is at $y = 0$, and the apparent k^0 assuming electron transfer at the zero field boundary.

From the assumption that the Butler-Volmer equation does apply at $y = 0$:

$$c_{\mathrm{A},0} - c_{\mathrm{B},0}\,\mathrm{e}^{-n\theta_{\mathrm{pzc}}} - \frac{J'_{\mathrm{A}}}{K^0}\,\mathrm{e}^{-n\alpha'\theta_{\mathrm{pzc}}} = 0 \tag{9.27}$$

As before, substituting Equation 9.23 gives:

$$c_{\mathrm{A,ZF}}\,\mathrm{e}^{-z_{\mathrm{A}}(\frac{\eta}{n}-\theta_{\mathrm{pzc}}-\Delta\theta_{\mathrm{OD}})} - c_{\mathrm{B,ZF}}\,\mathrm{e}^{-z_{\mathrm{B}}(\frac{\eta}{n}-\theta_{\mathrm{pzc}}-\Delta\theta_{\mathrm{OD}})}\,\mathrm{e}^{-n\theta_{\mathrm{pzc}}} - \frac{J'_{\mathrm{A}}}{K^0}\,\mathrm{e}^{-n\alpha'\theta_{\mathrm{pzc}}} = 0 \tag{9.28}$$

and multiplying through as before

$$c_{\mathrm{A,ZF}} - c_{\mathrm{B,ZF}}\,\mathrm{e}^{-(\eta-n\Delta\theta_{\mathrm{OD}})} - \frac{J'_{\mathrm{A}}}{K^0}\,\mathrm{e}^{-n\alpha'\theta_{\mathrm{pzc}}+z_{\mathrm{A}}(\frac{\eta}{n}-\theta_{\mathrm{pzc}}-\Delta\theta_{\mathrm{OD}})} = 0 \tag{9.29}$$

Rearranging

$$c_{\mathrm{A,ZF}} - c_{\mathrm{B,ZF}}\,\mathrm{e}^{-(\eta-n\Delta\theta_{\mathrm{OD}})} - \frac{J'_{\mathrm{A}}}{K^0}\,\mathrm{e}^{-\alpha'(\eta-n\Delta\theta_{\mathrm{OD}})}\,\mathrm{e}^{(\frac{z_{\mathrm{A}}}{n}+\alpha')(\eta-n\theta_{\mathrm{pzc}}-n\Delta\theta_{\mathrm{OD}})} = 0 \tag{9.30}$$

Therefore the Butler–Volmer equation holds at $y = y_{\mathrm{ZF}}$, but subject to an altered apparent heterogeneous rate constant:

$$c_{\mathrm{A,ZF}} - c_{\mathrm{B,ZF}}\,\mathrm{e}^{-(\eta-n\Delta\theta_{\mathrm{OD}})} - \frac{J'_{\mathrm{A}}}{K^0_{\mathrm{app}}}\,\mathrm{e}^{-\alpha'(\eta-n\Delta\theta_{\mathrm{OD}})} = 0 \tag{9.31}$$

with

$$K^0_{\mathrm{app}} = K^0\,\mathrm{e}^{-(\frac{z_{\mathrm{A}}}{n}+\alpha')(\eta-n\theta_{\mathrm{pzc}}-n\Delta\theta_{\mathrm{OD}})} \tag{9.32}$$

This is then a Frumkin correction[11] across the double layer, since the overpotential

where the electron transfer in fact takes place – at the outer Helmholtz plane, in the discussion above – is not the same as the overpotential at the outer edge of the double layer where electron transfer is *expected* to take place in the zero-field approximation. This has the troubling implication that k^0 is effectively indeterminable without prior knowledge of the position of electron transfer. The Frumkin correction is explored in more detail in the next chapter.

This effect did not cause significant problems in fitting the experimental weakly supported voltammetry of known 'fast' electron transfers, including that reported later in this chapter, as well as other examples reported in the literature: thallium(I),[5,9] ferrocene,[6] hexaammineruthenium(III)[4,8] (also below), cadmium(II),[7] cobaltocenium[8] and hexacyanoferrate(III).[8] These are mostly near-Nernstian systems with $k^0 > 0.5$ cm s^{-1} in general, as discussed in the respective publications, but k^0 possibly as low as 0.07 cm s^{-1} for thallium(I).

9.5 Conclusion on the validity of the approximation

A lower limit of $R_e \approx 1000$ has been placed on the radius of electrode for which the double layer and the diffusion layer are effectively decoupled. The success of the zero-field approximation has been shown to be dependent on the site where electron transfer takes place, and the correctness of extending the Butler-Volmer equation to the plane of zero field has been questioned. Only if electrochemical kinetics are infinitely fast is the voltammetry independent of the site of electron transfer, as then a reduced apparent overpotential at the outer Helmholtz plane is modulated by a corresponding excess of the electroactive reactant with respect to product, and *vice versa*.

The detailed theory of steady-state voltammetry involving the diffuse double layer will be introduced in the next chapter. First, weakly supported macroelectrode cyclic voltammetry will be analysed by solving the Nernst–Planck–Poisson equations subject to the zero-field approximation. Since in the macroelectrode limit, the electrode size greatly exceeds the size of the diffusion layer, a time-dependent theory is required.

9.6 Theoretical model for dynamic voltammetry

9.6.1 Introduction

A theory for dynamic cyclic voltammetry subject to the zero-field approximation, across a wide range of normalised scan rate (σ) and electrolytic ratio (c_{sup}), can now be developed by numerical solution of the time-dependent Nernst–Planck–Poisson equation set. The normalised hemispherical electrode system introduced in Section 7.5 will be used.

The study of weakly supported cyclic voltammetry is of general interest, since the introduction of excess supporting electrolyte may introduce problems to voltammetric analysis. Supporting electrolyte increases capacitive currents which do not contribute to the analytical signal, and especially if either supporting ion adsorbs specifically to the electrode, these currents may be considerable and difficult to predict theoretically. The introduction of large quantities of salt is often inappropriate for analytical measurements concerning biological compounds, and in some otherwise analytically useful solvents, it is impossible to dissolve sufficient supporting electrolyte to use diffusion-only theory.

Consequently it is important to establish theoretically, and to demonstrate by exper-

iment, the minimum quantity of supporting electrolyte required for voltammetry to be indistinguishable from the predictions of diffusion-only theory. Additionally, to be able to accurately model and interpret voltammetry under non-diffusion-only conditions considerably widens the scope of voltammetric investigation. Since the publication of this work, this has already yielded striking results, such as the use of weakly supported voltammetry to infer homogeneous reaction kinetics in an anthraquinone system which would have been impossible to determine by conventional voltammetric methods.[12]

Past treatments of weakly supported macroelectrode cyclic voltammetry have used electroneutrality. These include the studies of diffusion coefficient effects by Stojek and co-workers.[13,14] The mathematical description of migration and the role of supporting electrolyte was discussed in detail by Oldham and Zoski in the context of general electrochemical mass transport,[15] in which a minimum support ratio of $c_{\mathrm{sup}} = 26$ was suggested for steady-state voltammetry. This will be shown below to be a substantial underestimate under transient conditions. The problem of ohmic drop has also been considered at microelectrodes in a recent theoretical discussion by Amatore et al.[16]

To the author's knowledge, the detailed theoretical treatment of weakly supported cyclic voltammetry at macroelectrodes was neglected until the publication of this work, perhaps due to the implicit practical problems of high ohmic drop associated with any experimental exploitation. The only experimental examples encountered in the literature involve self-support for highly charged species at high concentrations, where convective effects cannot be ruled out.[17–19]

This work therefore represents the first application of the full time-dependent Nernst–Planck–Poisson equation set with the zero-field approximation to cyclic voltammetry. Theoretical results are presented and discussed, and then the theory is

compared with experimental voltammetry to establish the validity of the model.

9.6.2 Detail of theoretical model

The theoretical system described in Section 7.5 is employed, with the Poisson equation being applied to describe the electrodynamics. In the hemispherical geometry, this is:

$$\nabla^2\theta + \frac{1}{2} R_\mathrm{e}^2 \sum_i z_i c_i = 0 \tag{9.33}$$

and the zero-field approximation (Equation 9.1) is applied at the electrode surface. The Butler–Volmer equation is applied, since Nernstian kinetics can be considered within the same model by artificially setting $K^0 \gg \sigma$:

$$c_{\mathrm{A},0} - c_{\mathrm{B},0}\,\mathrm{e}^{-(\eta - n\theta_0)} - \frac{\mathrm{e}^{-\alpha'(\eta - n\theta_0)}}{K^0} \left.\frac{\partial c_\mathrm{A}}{\partial R}\right|_{R=1} = 0 \tag{9.34}$$

Because the electric field is zero at the electrode surface, the current can be recorded as simply:

$$j = \left.\frac{\partial c_\mathrm{A}}{\partial R}\right|_{R=1} \tag{9.35}$$

For computational convenience, the $R \to \infty$ boundary is set at a finite position $R = R_\mathrm{max}$ and is set to the maximum extent of the diffusion layer for a diffusion-only system, in the same manner as for the liquid junction simulations (Section 4.4.2):

$$R_\mathrm{max} = 1 + 6\sqrt{D'_\mathrm{max}\tau_\mathrm{max}} \tag{9.36}$$

Due to the requirement of electroneutrality in bulk solution, this is an appropriate outer boundary position even for a weakly supported solution. Following Limon-Petersen et al.,[6] integration of the hemispherical Laplace equation (the electroneutral Poisson

equation) outside $R = R_{\max}$ gives:

$$\theta(R_{\max}) + R_{\max} \left.\frac{\partial\theta}{\partial R}\right|_{R=R_{\max}} = 0 \tag{9.37}$$

which is set as the outer boundary condition for the variable θ.

9.6.3 Gridding and computation

The simulation space is discretised across the domain $1 \leq R \leq R_{\max}$, with the grid expanding outwards from the electrode surface, where concentration gradients are most extreme and where the most charge separation is expected. The definitions in Section 3.2 are used. Because the initial conditions are not significantly perturbed after the start of the simulation, since $\eta_{\mathrm{i}} \ll 0$, a regular time grid is employed, with a constant number of time steps τ_{PT} per unit η.

A convergence study was performed, using j_{pf}, j_{pb} and $\Delta\eta_{\mathrm{pp}}$ as diagnostic variables. The optimal parameters, giving $< 0.2\%$ error with respect to a fully converged parameter set, were: $\gamma_{\mathrm{R}} = 5 \times 10^{-3}$, $R_{\mathrm{s}} = 2 \times 10^{-3}$, $\tau_{\mathrm{PT}} = 100$ or 200.

The first and second derivatives are centrally differenced and the time derivative is differenced according to the fully implicit method[†]. In the discretised equations, the Poisson equation is substituted for $\nabla^2\theta$ in the Nernst–Planck equations to improve convergence, since the system is very nearly electroneutral over the majority of the simulation space. The iterative Newton–Raphson method is applied at each timestep as normal, with unconditional convergence using the above gridding parameters. The Jacobian matrix is 15-diagonal; typical runtimes were 90 s – 10 min per voltammogram.

[†]The data reported in the original publication used the alternative Crank-Nicolson method,[20] but the fully implicit method has since been found to be more accurate in some situations and is preferable. The data reported here are unaffected by choice of time differencing.

9.7 Theoretical results and discussion

9.7.1 Qualitative effects of incomplete support

For dynamic cyclic voltammetry, just as for steady-state voltammetry as discussed in the previous chapter, the passage of Faradaic current introduces charge to solution in the vicinity of the electrode. Because the solution conductivity is finite, this charge can only be compensated at a finite rate, and therefore an electric field arises in solution. The lower the conductivity of the solution relative to the quantity of reactant, the greater this electric field, and therefore the more significant ohmic drop and migration effects will become.

For weakly supported cyclic voltammetry, we expect the characteristic observables j_{pf} and $\Delta\eta_{\mathrm{pp}}$ to become functions of of c_{sup} and R_{e}, as well as σ and D'_{B} as for diffusion-only voltammetry.

Microelectrode voltammetry is expected to be substantially less sensitive to changes in c_{sup}, as the passed current is very small and so ohmic drop becomes increasingly insignificant; consequently, microelectrode voltammetry in weakly supported media is already a well established technique.[21]

9.7.2 Exemplar voltammetry and ohmic drop

Simulations of three exemplar macroelectrode voltammograms are shown at Figure 9.3.

The limiting effect on current and the marked effect of ohmic drop on peak-to-peak separation are clear. The perceptible broadening of the peak-to-peak separation is notable even in the $c_{\mathrm{sup}} = 100$ case, by contrast to the determination that at steady-state, $c_{\mathrm{sup}} = 26$ is sufficient to limit ohmic drop to < 1 mV.[15] Because of the significantly

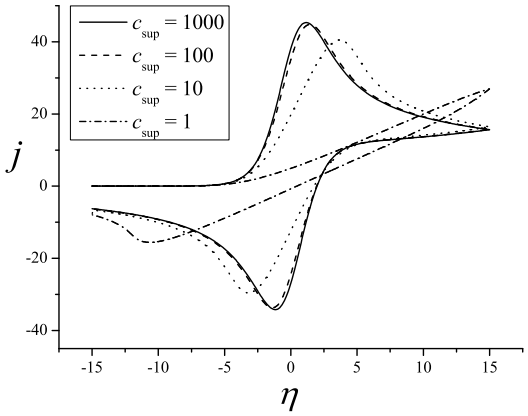

Figure 9.3: Exemplar voltammetry for the reversible one-electron oxidation of neutral A to B^+ at a macroscale hemispherical electrode ($\sigma = 10^4$, $R_e > 10^5$, $K^0 = 10^5$) at electrolytic support ratios varying from excess support ($c_{sup} = 1000$) to weak support ($c_{sup} = 1$).

increased current passed at a macroelectrode, the ohmic drop is much larger than for steady-state voltammetry a microelectrode (Figure 8.2); this is consistent with the traditional interpretation[22] of the ohmic drop as an ohmic voltage equal to the product of current and solution resistance (iR_s).

In the most weakly supported case, the forward peak is not encountered within the scan range. A 'ramping' effect is observed, where the current increase with potential becomes approximately linear, rather than exponential, due to the dominating contribution of uncompensated solution resistance. A concentration profile in the pre-peak region (Figure 9.4) shows clearly that migration of M^+ and X^- accompanies the flux of A towards the electrode. To maintain electroneutrality in the diffusion layer as positive B^+ is generated, depletion of M^+ and accumulation of X^- is required. Since $c_{A,0} \approx c_{B,0}$ in the figure, it can be inferred that $\eta_{app} \approx 0$ and so $n\theta_0 \approx \eta = 10$.

To examine the concept of solution resistance in more detail, a plot of the simulated variation of current, ohmic drop and inferred solution resistance during a scan with c_{sup} is shown at Figure 9.5.

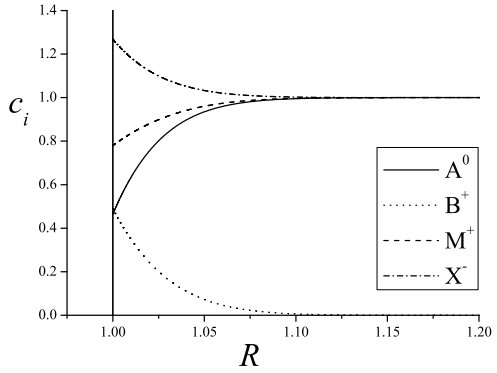

Figure 9.4: Concentration profiles at $\theta = 10$ for the weakly supported reversible one-electron oxidation of neutral A to B^+ at a macroscale hemispherical electrode ($\sigma = 10^4$, $R_e > 10^5$, $K^0 = 10^5$, $c_{sup} = 1$).

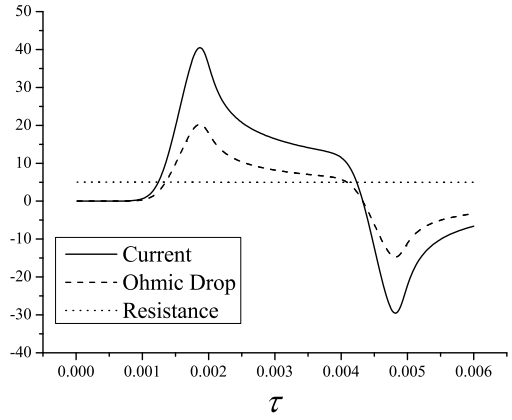

Figure 9.5: Simulated current, ohmic drop, and resistance during a cyclic voltammetry experiment performed for the one-electron oxidation of neutral A. to B^+ ($\sigma = 10^4$, $R_e > 10^5$, $K^0 = 10^5$, $c_{sup} = 10$). In order to plot all three observables on a single ordinate scale, normalised ohmic drop has been multiplied by 10 and normalised resistance by 100.

The dimensionless resistance $P_s = 0.05$ is exactly as expected given the expression:

$$P_s = \frac{1}{\sum_i z_i^2 c_i} \tag{9.38}$$

which is suggested by the electroneutral analysis in Section 1.6.

Therefore, dimensional analysis of the Nernst–Planck equations correctly reveals the resistance of the macroelectrode system, considering that the timescale of the voltammetry experiment is very slow with respect to the Debye time, and electroneutrality is maintained closely throughout solution.

The approximation of time-independent uncompensated solution resistance, R_s, throughout the scan is accurate for a macroelectrode system. For the high σ regime there are no charging or migration effects which suggest strong deviation from electroneutrality. Hence, the ohmic drop does obey Ohm's law with constant R_s in this system. There is no reason to assume inadequacy in compensating ohmic drop by simple arithmetic correction with a constant R_s, as reviewed by Britz.[22]

9.7.3 Dependence of j_{pf} and $\Delta\eta_{pp}$ on c_{sup}

The quantitative variation of the normalised observables j_{pf} and $\Delta\eta_{pp}$ with c_{sup} was studied by producing surface plots in which the change in the observable is plotted in the z-axis against variation in the support ratio and normalised scan rate. By considering a full range of normalised scan rates, both the macro- and microelectrode limits are included. Figures 9.6 and 9.7 show the variation of these observables with c_{sup} for the one-electron oxidation of a neutral species ($z_A = 0$, $n = +1$, e.g. ferrocene to ferrocenium).

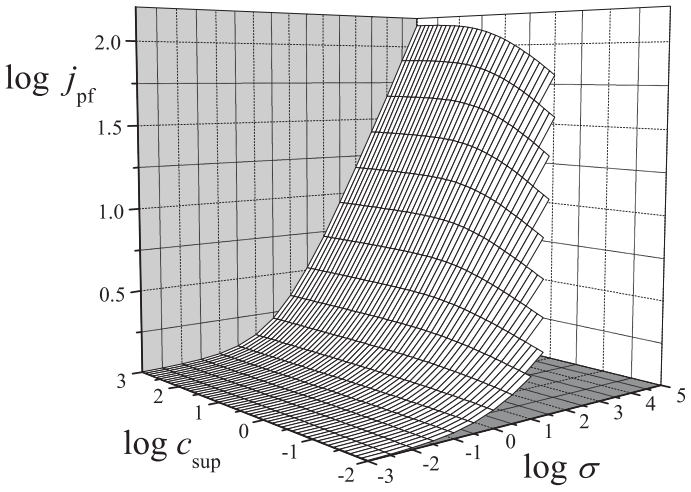

Figure 9.6: $\log j_{pf}$ *vs.* $\log\sigma$ and $\log c_{sup}$ for $z_A = 0$, with $R_e > 10^5$.

In Figure 9.6, the recognisable transition with increasing σ from steady-state (low

σ) behaviour to Randles-Ševčík (high σ) behaviour is observed at high c_{sup}. As c_{sup} decreases, peak currents in the Randles-Ševčík region are reduced from the ideal diffusion-only value, since the rate of migration of supporting electrolyte becomes rate-limiting as the ratio of electrolytic support is reduced. By comparison, peak current is not significantly affected in the low σ regime.

The variation of the normalised scan rate, σ, does not strictly correspond to a variation in r_{e}, as R_{e} has been held constant at $\sqrt{2} \times 10^5$ (macroelectrode). So long as R_{e} is large enough to exceed a nanoelectrode scale, however, varying R_{e} has no observable effect on the voltammetry since the double layer and diffusion layer are accurately decoupled. Therefore, the low σ regime is equivalent to a microelectrode regime, and in this case, voltammetry is not strongly affected by c_{sup} at low σ, as expected because the negligible current drawn leads to negligible ohmic drop.

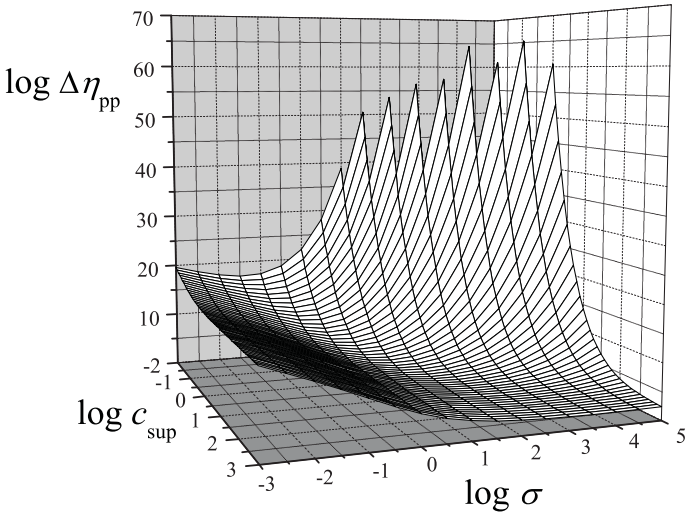

Figure 9.7: $\Delta\eta_{\text{pp}}$ *vs.* $\log\sigma$ and $\log c_{\text{sup}}$ for $z_{\text{A}} = 0$, with $R_{\text{e}} > 10^5$. The switching potential is $\eta_{\text{f}} = 40$.

Figure 9.7 demonstrates the increased peak-to-peak separation, $\Delta\eta_{\text{pp}}$, resulting from increased ohmic drop at macroelectrodes as the support ratio is decreased. Under typical macroelectrode voltammetry conditions of $\sigma > 10^3$, a significant positive deviation from the expected diffusion-only value of $\Delta\eta_{\text{pp}} \approx 2.3$ is noted as the support

ratio is reduced. Distinguishable ohmic drop effects are observed even under relatively high support ratios in the range $10 < c_{\text{sup}} < 100$.

The extent of the ohmic drop at the lowest support ratios is such that no diffusion-limited peak occurs within the range of the scan, for which the simulated switching potential was $\approx E_{\text{f}}^{\ominus} + 1.5$ V; consequently, some j_{pf} and $\Delta\eta_{\text{pp}}$ data points in Figures 9.6 and 9.7 cannot be reported. For all scan rates the limit of infinite resistance is achieved for a non-conducting solution with $c_{\text{sup}} \to 0$, and hence no electrolyte: infinite peak-to-peak separation would be observed.

9.7.4 Effect of z_{A} and the concept of self-support

Where $z_{\text{A}} \neq 0$, the electroactive species and its counter-ion are charged and so can act themselves as supporting electrolyte, contributing to the compensation of solution charge by migration. Additionally, if $z_{\text{A}}n < 0$, the electroactive species can compensate the change in solution charge resulting from its own oxidation or reduction by migrating towards the electrode surface, leading to the attractive migration regime where transport-limited current is elevated. Where $z_{\text{A}} \neq 0$ and $c_{\text{sup}} \to 0$, the migration of the electroactive species and its counter-ion dominate charge transport and are crucial to allowing electron transfer by migrating in order to maintain electroneutrality outside the diffuse double layer. Consequently a minimum 'intrinsic' degree of electrolytic support exists for the case $z_{\text{A}} \neq 0$, even at $c_{\text{sup}} = 0$.

Figure 9.8 shows the variation with c_{sup} for the one-electron reduction of a singly-charged species ($z_{\text{A}} = +1$, $n = -1$, e.g. cobaltocenium to cobaltocene).

Figure 9.9 shows the variation of the observables with c_{sup} for the one-electron reduction of an ion with $z_{\text{A}} = +3$ (e.g. hexaammineruthenium(III) to hexaammineruthe-

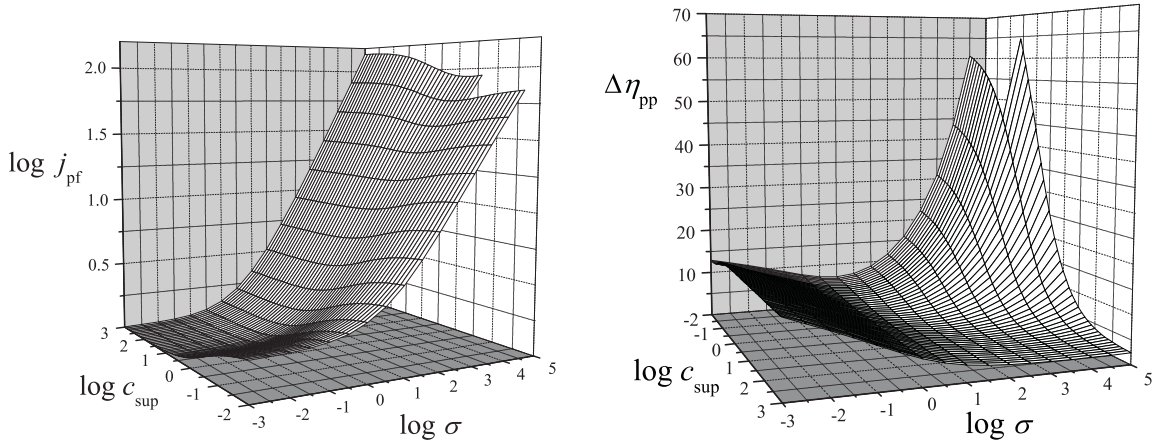

Figure 9.8: log j_{pf} and $\Delta\eta_{pp}$ *vs.* $\log\sigma$ and $\log c_{sup}$ for $z_A = +1$ and $n = -1$, with $R_e = 10^5$. The switching potential is $\eta_f = -40$.

nium(II)).

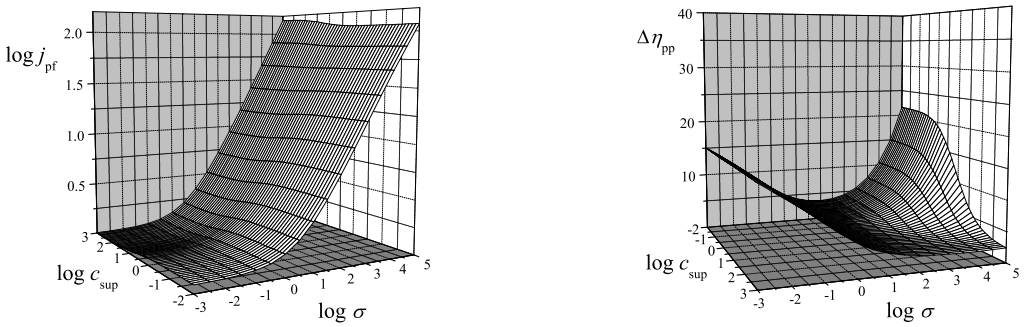

Figure 9.9: log j_{pf} and $\Delta\eta_{pp}$ *vs.* $\log\sigma$ and $\log c_{sup}$ for $z_A = +3$ and $n = -1$ at a hemispherical electrode with $R_e = 10^5$, switching potential $\eta_f = -40$.

Both these plots clearly indicate elevated current at low support due to the influence of attractive migration, since $z_A n < 0$ in both cases. For the macroelectrode limit, the peak current initially decreases with support ratio, due to the influence of ohmic drop, before the current increases at even lower support where attractive migration of the electroactive species dominates the charge transport required to maintain electroneutrality close to the electrode surface. Equally, the peak-to-peak separation does not become infinite at zero support, but rather tends to a limiting value due to the intrinsic solution conductivity supplied by the electroactive species and its counter-ion.

Rooney et al. reported "approximately reversible" self-supported macroelectrode voltammetry for the $[Fe(CN)_6]^{3-/4-}$ couple at glassy carbon, Au and Pt electrodes.[17] Examination of the published voltammograms suggests $\Delta E_{pp} \gg 60$ mV is in fact observed, and at the high concentrations of the electroactive species and low scan rates employed, convection is likely to significantly influence mass transport. On the basis of time-dependent theory using the Nernst–Planck–Poisson equations, in a self-supported regime, the ohmic drop observed in cyclic voltammetry is not a function of the electroactive species concentration since in the absence of deliberately added support, both the conductivity of the solution and the Faradaic current scale linearly with the concentration of the electrolytic species. A large concentration of electroactive species cannot be used to recover reversible voltammetry under self-supported conditions. This conclusion holds provided that there is sufficient ionic strength in solution to render the Debye length much smaller than the diffusion layer, so that the zero-field model is accurate.

9.7.5 Effect of R_e

The dimensionless parameter R_e in the normalised Poisson equation is the ratio of the electrode radius to the Debye length, and hence of the relative scale of the diffusion layer to the diffuse double layer. The effect of R_e on observed cyclic voltammetry as a function of σ was studied for a one-electron oxidation of a neutral species with $c_{sup} = 5$ and 0.2. In both cases, R_e was found to have no significant effect on the voltammetry, so long as it is large enough for the zero-field approximation to be accurate: if the intrinsic conductivity of the solution is sufficient to make the Debye length negligible on the electrode scale, electroneutrality holds until a distance very close to the electrode

surface. Therefore, ohmic drop dominates the effect of c_{sup} on the voltammetry.

9.7.6 Effect of D_{B}

The effect of the ratio of diffusion coefficients, $D'_{\mathrm{B}} = D_{\mathrm{B}} \,/\, D_{\mathrm{A}}$, on the observable $\Delta\eta_{\mathrm{pp}}$ was considered. Although for diffusion-only voltammetry, the position of the voltammetric wave is a function of D'_{B}, the peak-to-peak separation is independent of D'_{B}. It was found that D'_{B} influences the peak-to-peak separation only to a small extent, and only where c_{sup} is very low, such that the migration of the product species becomes significant to maintaining charge balance.

9.7.7 Effect of D_{M} and D_{X}

If one or both of the supporting electrolyte ions has a high diffusion coefficient compared to the electroactive species, and so can migrate rapidly with respect to the rate of diffusion of the electroactive species to the surface, solution resistance is compensated more rapidly and hence the ohmic drop is correspondingly less. A plot of $\Delta\eta_{\mathrm{pp}}$ *vs.* D_{M} and D_{X} is shown at Figure 9.10.

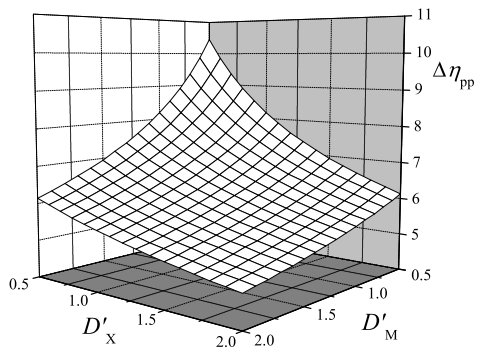

Figure 9.10: $\Delta\eta_{\mathrm{pp}}$ as a function of D'_{M} and D'_{X} for the one-electron oxidation of A^0 with $c_{\mathrm{sup}} = 10$ (weak support), $\sigma = 10^4$, $R_{\mathrm{e}} > 10^5$. The switching potential is $\eta_{\mathrm{f}} = 20$.

The symmetry of Figure 9.10 demonstrates that charge introduced to the solution by the passage of Faradaic current is equally well compensated by the migration of like charges away from the surface as for opposite charges towards it. A relatively high supporting electrolyte diffusion coefficient is clearly helpful to minimisation of ohmic drop effects by accelerating the compensation of electric fields in solution.

9.8 Experimental results and discussion

9.8.1 Experimental setup

Aqueous solutions of 5 mM hexaammineruthenium(III) chloride (HexRu(III), Aldrich, 98%) and different quantities of potassium chloride (Aldrich, > 99%) as supporting electrolyte were prepared with ultra pure water with resistivity > 18.2 MΩ cm^{-1} (at 298 K). The solutions were degassed for 30 min with N_2 (BOC, High Purity Oxygen Free) before starting each experiment.

A platinum disc with radius 1 mm was used as a working electrode, a platinum foil was used as a counter electrode and a saturated calomel electrode (SCE) was used as the reference electrode. The working electrode surface was polished prior to the experiment using diamond spray (0.3 and 0.1 μm, Kemet International, UK) on soft lapping pads (Buehler, USA). The solution temperature was maintained at a constant 298 K during the experiments using a water bath (W14, Grant).

The range of potassium chloride concentrations investigated was 2000, 500, 150 and 50 mM KCl, corresponding to c_{sup} = 400, 100, 30, and 10. For each solution, voltammetry was performed across a range of scan rates (50, 100, 200, 500 and 1000 mV s^{-1}) using an analogue potentiostat (built in-house) which was connected to an

oscilloscope (TDS 3034B, Tektronix, USA) to record the data.

The analogue potentiostat was used in place of a digital equivalent to prevent artefacts introduced by the digital staircase voltage waveform, especially the broadening of peak-to-peak separation which is an essential observable in the study of weakly supported voltammetry. Bilewicz et al.[23] noted these effects in diffusion-only cyclic voltammetry in which the triangular voltage waveform was approximated by a digital staircase, and these effects have been investigated theoretically for disc-shaped electrode systems.[24]

Since double layer charging is not considered by the theoretical model, the capacitive current was estimated using blank voltammetry recorded in solutions containing the same degree of electrolytic support, but without the electroactive species. The excess of chloride ions introduced by the hexaammineruthenium(III) chloride into the experimental solutions was emulated by augmenting the concentration of potassium chloride in the blank solutions by 15 mM in each case. This allowed the background non-Faradaic current to be subtracted from the experimental voltammograms, so that the Faradaic current could be accurately compared to a simulation ignoring capacitive current.

The diffusion coefficients for the hexaammineruthenium(III) and hexaammineruthenium(II) cations in the aqueous KCl system were determined via fully supported double potential step chronoamperometry using a 25 μm radius platinum disk, according to the procedure established by Klymenko et al.[25] The measured values were $D_{\mathrm{HexRu(III)}} = 9.0 \times 10^{-6}$ cm^2 s^{-1} and $D_{\mathrm{HexRu(II)}} = 1.0 \times 10^{-5}$ cm^2 s^{-1}. These compare well to literature values for the diffusion coefficient of HexRu(III),[26–28] which range from 8.5–9.1 $\times 10^{-6}$ cm^2 s^{-1}, all measured in 0.1 M KCl in aqueous solution at 298 K.

9.8.2 Experimental voltammetry

The resulting experimental voltammetry is presented at Figures 9.11–9.15, below, for the five scan rates investigated. In each case, the four support ratios are indicated in voltammograms A–D: respectively, c_{sup} = (A) 400, (B) 100, (C) 30 and (D) 10. The zero-field simulation procedure set out above was used to determine a best fit to the experimental voltammetry, and is indicated by the closed circles.

The following parameters were used in the simulation:

- $r_{\text{e}} = 0.71$ mm to correspond area-to-area with a disc electrode with $r_{\text{e}} = 1$mm.
- $C^{*}_{\text{A}} = 5$ mM.
- $D_{\text{HexRu(III)}} = 9 \times 10^{-6}$ cm^2 s^{-1}, as characterised by microelectrode double potential step chronoamperometry.
- $D_{\text{HexRu(II)}} = 10^{-5}$ cm^2 s^{-1}, as characterised by microelectrode double potential step chronoamperometry.
- $D_{\text{K+}} = 1.8 \times 10^{-5}$ cm^2 s^{-1}, from the literature.[29]
- $D_{\text{Cl-}} = 1.95 \times 10^{-5}$ cm^2 s^{-1}, from the literature.[29]
- $k^0 = 1$ cm s^{-1} and $\alpha = 0.5$, to render the system effectively reversible, as expected for the hexaammineruthenium(III/II) couple.[30]
- $\epsilon_{\text{s}} = 78.54$.[31]
- $T = 298$ K, thermostatically controlled.

The formal potential in the simulation, $E^{\ominus}_{\text{f}}$, was different for each support ratio and was treated as a simulation parameter. Since the diffusion coefficients of the two species

are characterised to within a close tolerance, the shift in both forward and back peaks, which is consistent at all scan rates for a given support ratio, must be attributed to variation in $E_f^{\ominus}$. This support ratio dependence is justified since the formal potential varies with the activity coefficients of the electroactive species and hence also with ionic strength (Equation 7.14).

C_{sup} / mM	$E_f^{\ominus}$ *vs.* SCE / mV
2000	-213
500	-190
150	-175
50	-170

Table 9.1: Observed shift in formal potential of the HexRu(III/II) couple as a function of ionic strength.

The formal potential varied consistently with ionic strength, as indicated in Table 9.1.

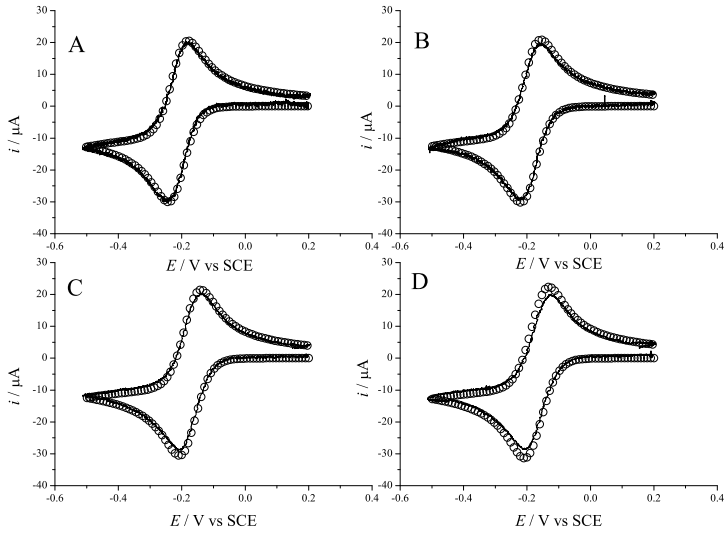

Figure 9.11: Comparison of experiment and simulation for $[Ru(NH_3)_6]^{3+} + e^- \rightleftarrows [Ru(NH_3)_6]^{2+}$, $v = 50$ mV s^{-1}. A: $C_{sup} = 2$M; B: $C_{sup} = 500$ mM; C: $C_{sup} = 150$ mM; D: $C_{sup} = 50$ mM.

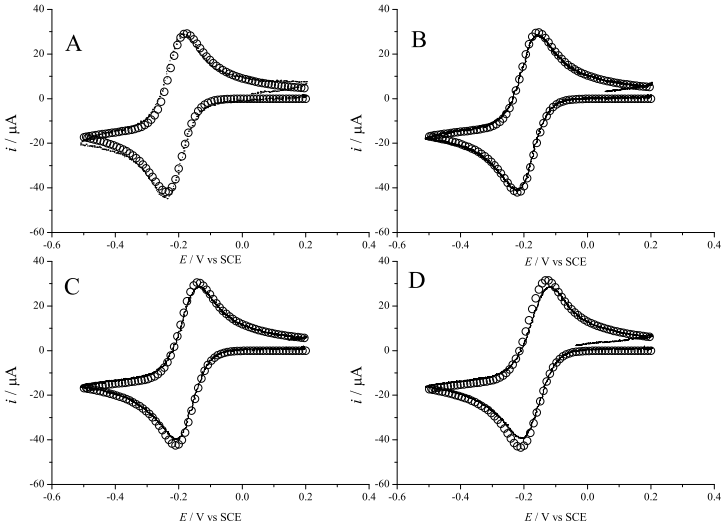

Figure 9.12: Comparison of experiment and simulation for $[Ru(NH_3)_6]^{3+} + e^- \rightleftarrows [Ru(NH_3)_6]^{2+}$, $v = 100$ mV s^{-1}. A: $C_{sup} = 2$M; B: $C_{sup} = 500$ mM; C: $C_{sup} = 150$ mM; D: $C_{sup} = 50$ mM.

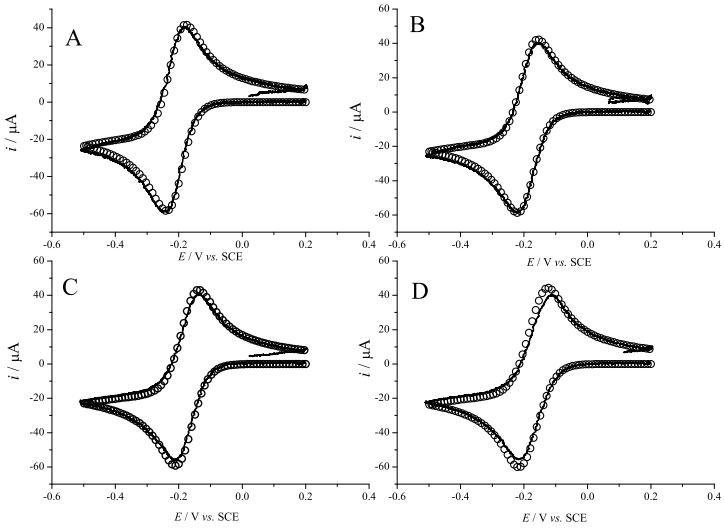

Figure 9.13: Comparison of experiment and simulation for $[Ru(NH_3)_6]^{3+} + e^- \rightleftarrows [Ru(NH_3)_6]^{2+}$, $v = 200$ mV s^{-1}. A: $C_{sup} = 2$M; B: $C_{sup} = 500$ mM; C: $C_{sup} = 150$ mM; D: $C_{sup} = 50$ mM.

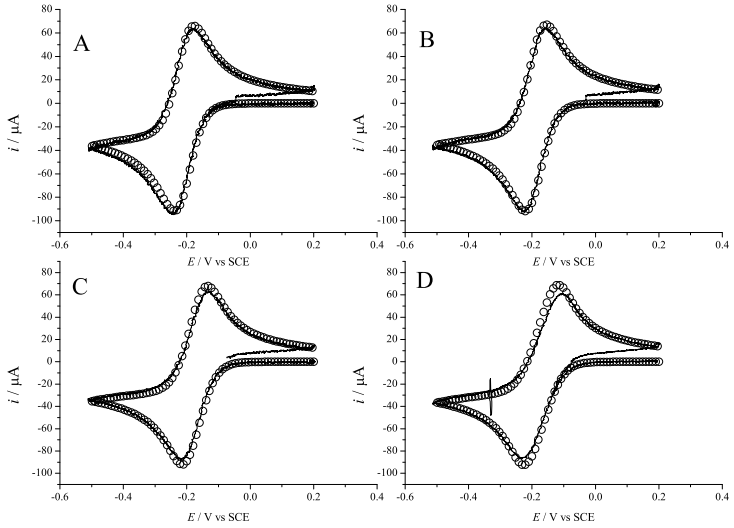

Figure 9.14: Comparison of experiment and simulation for $[Ru(NH_3)_6]^{3+} + e^- \rightleftarrows [Ru(NH_3)_6]^{2+}$, $v = 500$ mV s^{-1}. A: $C_{sup} = 2$M; B: $C_{sup} = 500$ mM; C: $C_{sup} = 150$ mM; D: $C_{sup} = 50$ mM.

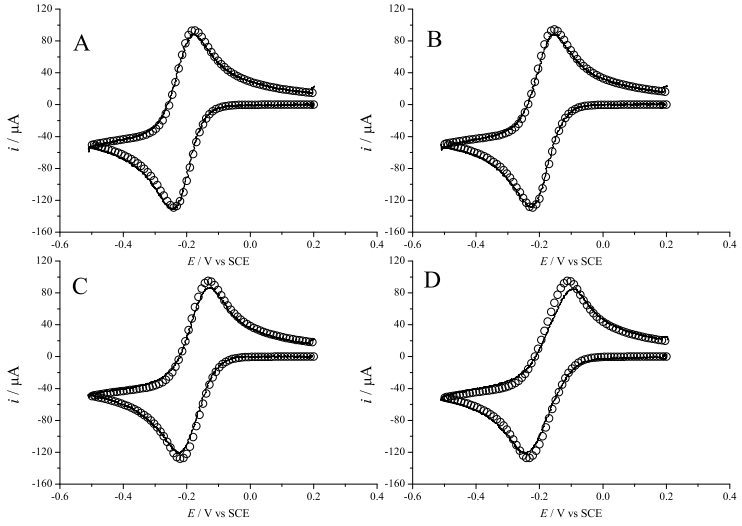

Figure 9.15: Comparison of experiment and simulation for $[Ru(NH_3)_6]^{3+} + e^- \rightleftarrows [Ru(NH_3)_6]^{2+}$, $v = 1$ V s^{-1}. A: $C_{sup} = 2$M; B: $C_{sup} = 500$ mM; C: $C_{sup} = 150$ mM; D: $C_{sup} = 50$ mM.

In general, Figures 9.11–9.15 illustrate a very close fit between the theoretical and experimental data for Cases A–C, but an underestimation of peak-to-peak separation the theoretical model in Case D, to beyond experimental error. In Case D, the trends in i_{pf} and ΔE_{pp} are still predicted qualitatively, but not quantitatively. These results are summarised by a plot of ΔE_{pp} against $\log v$ for the theoretical and experimental data at Figure 9.16.

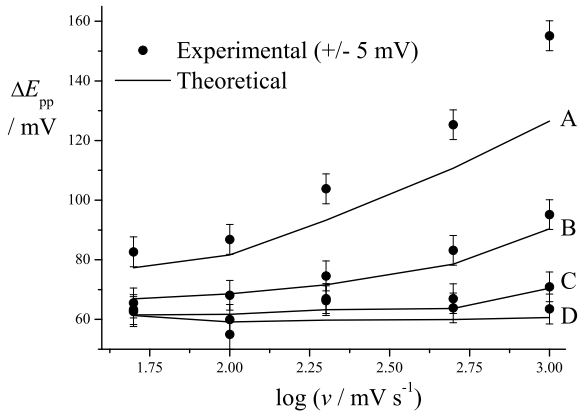

Figure 9.16: Comparison of experimentally observed and theoretically predicted ΔE_{pp} for macroelectrode cyclic voltammetry of HexRu(III) with support ratios: (A) 400, (B) 100, (C) 30, and (D) 10.

A variety of the approximations in this model are likely insufficient under weakly supported conditions, but under typical experimental conditions of $c_{\mathrm{sup}} \geq 30$, the theoretical model accurately predicts the extent of broadening of peak-to-peak separation caused by uncompensated solution resistance.

9.8.3 How much supporting electrolyte is required?

At this stage it is possible to quantitatively consider the following question: how much supporting electrolyte is required to achieve 'diffusional' cyclic voltammetry? In the diffusion-only limit, the observables i_{pf} and ΔE_{pp} can be used analytically without

inaccuracy due to the presence of an electric field in solution.

If 'experimental distinguishability' is defined to a given tolerance in terms of the relative change in either i_{pf} or ΔE_{pp}, it is possible to derive the minimum value of c_{sup} required to render the voltammetry indistinguishable from the diffusion-only case, for any given combination of r_{e}, v, D_{A}, D_{B}, D_{M} and D_{X}. According to the comparison of the hemispherical zero-field model with experimental voltammetry, this theory is accurate when $c_{\mathrm{sup}} \geq 30$, and for disc electrodes as well as hemispherical electrodes in the region where a disc-shaped electrode may be approximated by a hemisphere of the same area, which is roughly $\sigma > 10^3$. Our conclusions will therefore be quantitatively accurate in this range.

As an example, three model systems can be considered. In these model systems, $D_{\mathrm{A}} = D_{\mathrm{B}}$ and $D_{\mathrm{M}} = D_{\mathrm{X}}$, and $\epsilon_{\mathrm{s}} = 78.54$ (as for water). Three cases were studied, where D'_{M} takes values of 1, 2 and 3. In each case, voltammetry was simulated for the hemispherical electrode for a range of σ and c_{sup}. Each of the resulting voltammograms was classified by comparison of the recorded ΔE_{pp} to that predicted for the diffusion-only case, with $c_{\mathrm{sup}} \to \infty$ but the same parameters otherwise. The 'diffusion-only' voltammetry was calculated using the same numerical simulation method, but with the artificially high support ratio $c_{\mathrm{sup}} = 10^6$. Each data set is presented as a contour plot (Figures 9.17–9.19) to show the value of the deviation as a function of σ and c_{sup}:

$$\Delta\Delta E_{\mathrm{pp}} = \Delta E_{\mathrm{pp}} - \Delta E_{\mathrm{pp,diff}} \tag{9.39}$$

The possible regimes of $\Delta\Delta E_{\mathrm{pp}}$ compared to experimental error are: less than 1 mV (indistinguishable); 1–3 mV (well supported, i.e. indistinguishable within likely experimental error for a digital potentiostat); 3–5 mV (distinguishable within experimental

error); 5–10 mV (insufficiently supported), and greater than 10 mV (acutely unsupported).

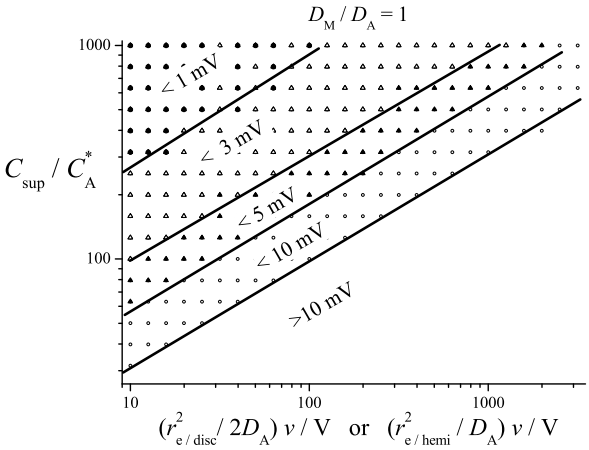

Figure 9.17: Contour plot showing the deviation $\Delta\Delta E_{pp}$ of theoretically observed ΔE_{pp} from the diffusion-only value at a hemispherical electrode for varying $c_{sup} = C_{sup}/C_A^*$ and $(r_e^2/D_A)v$, where $D_M/D_A = 1$, $A^0 \rightleftarrows B^+ + e^-$. $K^0 = 10^5$; $R_e > 10^5$.

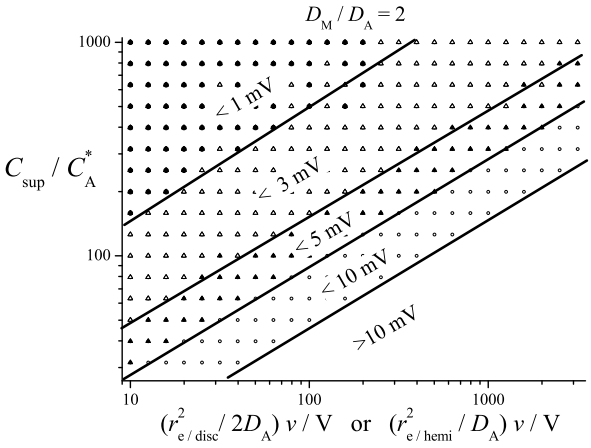

Figure 9.18: Contour plot showing the deviation $\Delta\Delta E_{pp}$ of theoretically observed ΔE_{pp} from the diffusion-only value at a hemispherical electrode for varying $c_{sup} = C_{sup}/C_A^*$ and $(r_e^2/D_A)v$, where $D_M/D_A = 2$, $A^0 \rightleftarrows B^+ + e^-$. $K^0 = 10^5$; $R_e > 10^5$.

The data are simulated here for a hemispherical electrode for which it is assumed that the voltammetry is largely indistinguishable from a disc macroelectrode. The correspondence, for equal area, that $r^2_{e,disc} = 2r^2_{e,hemi}$, and hence the horizontal scale of the plots varies by a factor of two, depending on the geometry in which r_e is measured.

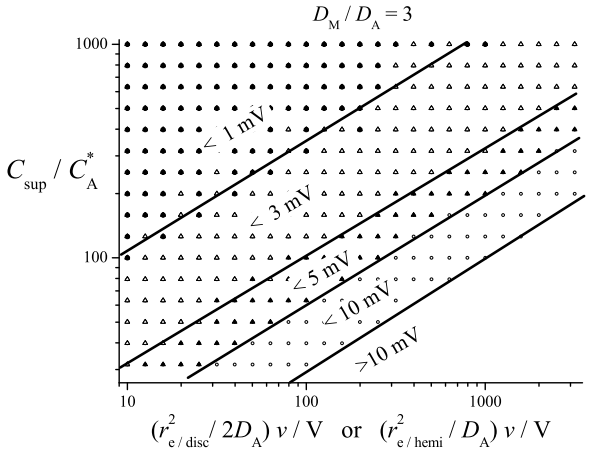

Figure 9.19: Contour plot showing the deviation $\Delta\Delta E_{pp}$ of theoretically observed ΔE_{pp} from the diffusion-only value for cyclic voltammetry at a hemispherical electrode for varying $c_{sup} = C_{sup}/C^*_A$ and $(r^2_e/D_A)v$, where $D_M/D_A = 3$, $A^0 \rightleftarrows B^+ + e^-$. $K^0 = 10^5$; $R_e > 10^5$.

The approximation of a disc to a hemisphere is justified provided the reference electrode is situated sufficiently far from the working electrode, as then the electric field can be treated using a hemispherical geometry in solution in either case. The approximation limited by electrode size to where both a hemisphere and a disc electrode yield a predominantly planar diffusion layer, which can be defined as the range of normalised scan rates where $\sigma > 10^3$.

Note that the choice of switching potential will affect ΔE_{pp}. The data set above uses a potential window of ≈ 1 V, from $\eta_i = -20$ to $\eta_f = +20$. In a narrower switching window, the same support regions are expected to remain appropriate.

These data are simulated for the one-electron oxidation of a neutral species, and so do not necessarily apply directly to other reactant charges. Since at support ratios $c_{sup} \geq 30$, the contribution of counter-ions to the total ionic strength is negligible and migrational currents are also negligible, these plots are also expected to be valid for other values of z_A.

9.9 Conclusions

In this chapter, the zero-field approximation has been rigorously justified subject to the electrode being larger than nanoscale, and the Nernst or Butler–Volmer equation being applicable at the outer edge of the double layer. The theory of macroelectrode cyclic voltammetry in weakly supported solution has then been described subject to this approximation, with special consideration given to the conventional observables of forward peak current and peak-to-peak separation.

Comparison was then drawn with experimental cyclic voltammetry for the aqueous $[Ru(NH_3)_6]^{3+/2+}$ system at a Pt macroelectrode: the theoretical model based on the zero-field approximation was shown to be quantitatively accurate, within experimental error for our system, for at least the region $c_{\text{sup}} \geq 30$, across a range of typical experimental scan rates.

The contour plots presented at Figures 9.17–9.19 are designed to be instructive to the experimentalist; for any macroelectrode system, the required c_{sup} to limit deviations from the diffusion-only case to within a certain tolerance may be inferred. The range of applicability of these plots is confined, however, to macroelectrode voltammetry and, at this stage, to electrochemically reversible systems. Of additional interest is the practical observation of the thermodynamic effect of varying ionic strength in such a system, such that $E_{\text{f}}^{\ominus}$ becomes a function of c_{sup}.

These contour plots clearly demonstrated that the minimum support ratio of 26 proposed for the steady-state system[15] is not equally useful for transient cyclic voltammetry, but rather is broadly inappropriate. The majority of macroelectrode systems require support ratios greater than 100 to prevent detectable ohmic drop effects which

corrupt kinetic or mechanistic measurements using cyclic voltammetry. Additionally, this work affords further understanding of the microscopic and macroscopic effects associated with extended electric fields in solution.

Both the electroneutrality and zero-field approximations ignore the diffuse double layer, however. As indicated by the analysis beginning this chapter, to extend the theory of weakly supported cyclic voltammetry to finite electrode kinetics or to nano-electrode voltammetry, it is necessary to incorporate the diffuse double layer into the theory. This problem is considered in the next chapter.

Bibliography

[1] I. Streeter and R. G. Compton, *J. Phys. Chem. C*, 2008, **112**, 13716–13728.

[2] E. J. F. Dickinson and R. G. Compton, *Chem. Phys. Lett.*, 2010, **497**, 178–183.

[3] E. J. F. Dickinson and R. G. Compton, *J. Electroanal. Chem.*, 2011, **661**, 198–212.

[4] E. J. F. Dickinson, J. G. Limon-Petersen, N. V. Rees and R. G. Compton, *J. Phys. Chem. C*, 2009, **113**, 11157–11171.

[5] J. G. Limon-Petersen, I. Streeter, N. V. Rees and R. G. Compton, *J. Phys. Chem. C*, 2008, **112**, 17175–17182.

[6] J. G. Limon-Petersen, I. Streeter, N. V. Rees and R. G. Compton, *J. Phys. Chem. C*, 2009, **113**, 333–337.

[7] J. G. Limon-Petersen, E. J. F. Dickinson, N. V. Rees and R. G. Compton, *J. Phys. Chem. C*, 2009, **113**, 15320–15325.

[8] J. G. Limon-Petersen, J. T. Han, N. V. Rees, E. J. F. Dickinson, I. Streeter and R. G. Compton, *J. Phys. Chem. C*, 2010, **114**, 2227–2236.

[9] J. G. Limon-Petersen, E. J. F. Dickinson, T. Doneux, N. V. Rees and R. G. Compton, *J. Phys. Chem. C*, 2010, **114**, 7120–7127.

[10] P. P. Edwards, H. B. Gray, M. T. J. Lodge and R. J. P. Williams, *Angew. Chem., Int. Ed.*, 2008, **47**, 6758–6765.

[11] A. Frumkin, *Z. Physik. Chem.*, 1933, **164A**, 121–133.

[12] S. R. Belding, J. G. Limon-Petersen, E. J. F. Dickinson and R. G. Compton, *Angew. Chem., Int. Ed.*, 2010, **49**, 9242–9245.

[13] M. J. Palys and Z. Stojek, *J. Electroanal. Chem.*, 2002, **534**, 65–73.

[14] W. Hyk and Z. Stojek, *Anal. Chem.*, 2005, **77**, 6481–6486.

[15] K. B. Oldham and C. G. Zoski, in *Comprehensive Chemical Kinetics*, ed. C. H. Bamford and R. G. Compton, Elsevier, Amsterdam, 1986, vol. 26, ch. 2.

[16] C. Amatore, A. Oleinick and I. Svir, *Anal. Chem.*, 2008, **80**, 7947–7956.

[17] M. B. Rooney, D. C. Coomber and A. M. Bond, *Anal. Chem.*, 2000, **72**, 3486–3491.

[18] N. P. C. Stevens, M. B. Rooney, A. M. Bond and S. W. Feldberg, *J. Phys. Chem. A*, 2001, **105**, 9085–9093.

[19] A. M. Bond, D. C. Coomber, S. W. Feldberg, K. B. Oldham and T. Vu, *Anal. Chem.*, 2001, **73**, 352–359.

[20] J. Crank and P. Nicolson, *Math. Proc. Cambridge Phil. Soc.*, 1947, **43**, 50–67.

[21] A. M. Bond, *Analyst (Cambridge, U.K.)*, 1994, **119**, R1–R21.

[22] D. Britz, *J. Electroanal. Chem.*, 1978, **88**, 309–352.

[23] R. Bilewicz, R. A. Osteryoung and J. Osteryoung, *Anal. Chem.*, 1986, **58**, 2761–2765.

[24] A. S. Barnes, E. I. Rogers, I. Streeter, L. Aldous, C. Hardacre and R. G. Compton, *J. Phys. Chem. B*, 2008, **112**, 7560–7565.

[25] O. V. Klymenko, R. G. Evans, C. Hardacre, I. B. Svir and R. G. Compton, *J. Electroanal. Chem.*, 2004, **571**, 211–221.

[26] C. E. Banks, R. G. Compton, A. C. Fisher and I. E. Henley, *Phys. Chem. Chem. Phys.*, 2004, **6**, 3147–3152.

[27] C. E. Banks, N. V. Rees and R. G. Compton, *J. Electroanal. Chem.*, 2002, **535**, 41–47.

[28] F. Marken, J. C. Eklund and R. G. Compton, *J. Electroanal. Chem.*, 1995, **395**, 335–338.

[29] V. M. M. Lobo, A. C. F. Ribeiro and L. M. P. Verissimo, *J. Mol. Liq.*, 1998, **78**, 139–149.

[30] C. Beriet and D. Pletcher, *J. Electroanal. Chem.*, 1994, **375**, 213–218.

[31] *CRC Handbook of Chemistry and Physics*, ed. D. R. Lide, CRC Press, London, 89th edn., 2008.

Chapter 10

Cyclic voltammetry: effect of the diffuse double layer

Thus far, the theory of charge transport in cyclic voltammetry has been considered subject to simplifying approximations which neglect the diffuse double layer. In this chapter, the influence of the diffuse double layer on the passage of Faradaic current is investigated for steady-state voltammetry, according to the Nernst–Planck–Poisson model. The effects of reactant charge, electrode charge, electrode size and quantity of supporting electrolyte are all considered, and both infinite and finite electrode kinetics will be investigated, as well as distance-dependent electron transfer (tunnelling) and activity effects.

Certain combinations of reactant charge and electrode excess charge can be shown to profoundly alter the predicted current by exclusion of the reactant (Levich effect) or deceleration of apparent kinetics (Frumkin effect), although tunnelling can overcome both effects by moving the plane of electron transfer. The structurally altered double layer at nanoelectrodes is also discussed, for which the partially unscreened electric field can increase or decrease the predicted current, depending on the electrode charge.

The results reported in this chapter have been published by the Journal of Electroanalytical Chemistry.[1] Relevant work is also incorporated from prior publications in the Journal of Physical Chemistry C,[2] the Journal of Solid State Electrochemistry,[3] and Chemical Physics Letters.[4]

10.1 Introduction

The traditional (Gouy–Chapman–Stern) theory of the electrical double layer, as introduced in Chapter 5, supposes that a part of the potential difference between the electrode and bulk solution is contained within a compact layer within the plane of closest approach of solvated ions. This plane is termed the outer Helmholtz plane, outside of which the remaining electric field is screened by unequal concentrations of cations and anions in a diffuse double layer close to the electrode surface.[5–7] The size of the double layer is parameterised by the Debye length which at typical ionic strengths is of the order of nanometres, as introduced in Section 1.3.3.

The development of practical nanoelectrochemical systems in the last decade[8,9] has led to renewed interest in the fundamental theories of electrode kinetics and charge transport dynamics, particularly at the nanoscale. The nanoscale is especially interesting because in this limit the size of a normal depletion layer approaches the Debye length, and so the charged double layer and the depletion layer become interlinked. Therefore, the electroneutrality and zero-field approximations are inapplicable in this limit. Non-classical charge transport effects for nanoelectrodes have already been predicted for the capacitive charging problems discussed in Chapters 5–6.

A number of theoretical works have introduced different models for the double layer, of varying sophistication.[10–14] In many of these works, numerical simulation is required

in order to approach the Nernst–Planck–Poisson equation set without approximation for the study of systems with complex boundary conditions or under transient conditions. This work will explore theoretical aspects of the effect of the *diffuse* double layer on the passage of Faradaic current, using a very simple, classical model of the double layer in order to avoid convoluting important trends.

Three possible descriptions of the electron transfer kinetics will be considered: the Nernst equation applied at the outer Helmholtz plane, the Butler–Volmer equation applied at the outer Helmholtz plane, and distance-dependent electron transfer (tunnelling). In this way, both mass transport effects and electron transfer kinetic effects associated with the double layer can be inferred. Activity effects arising from the variation in ionic strength across the double layer will also be discussed. In particular, the theory will consider a wide range of possible potentials of zero charge for the electrochemical system, as well as a range of reactant charges, allowing for a fuller and more consistent treatment of diffuse double layer effects than in recent, otherwise detailed studies.[14,15]

While highlighting the significance of the results to nanoscale voltammetry and voltammetry with low concentrations of supporting electrolyte, it is also necessary address implications for 'conventional' fully supported voltammetry at larger electrodes, which were excluded from early studies of the topic.[16–18] In this manner, unusual voltammetric behaviour attributable to double layer effects can be identified, as well as identifying discrepancies between common experimental observation and the predictions of the Nernst–Planck–Poisson theory.

10.2 Theoretical model

The basis of the theoretical model is the description of cyclic voltammetry using the Nernst–Planck–Poisson equations, as set out in Section 7.5. The current-potential relationship for the n-electron reaction of A^{z_A} to B^{z_B} is to be determined at steady state, in the presence of a certain quantity of a supporting electrolyte M^+X^-. The current can be limited either by the transport of A to the electrode or by the rate of its reaction at the electrode, and will be controlled by both the positions of equilibrium of these processes as well as their absolute rate due to the finite rates of diffusion, migration, electron transfer, etc.

The assumption of steady state is only relevant for a practical cyclic voltammetry experiment if the timescales associated with capacitive charging and mass transport of the reactant from bulk solution are very fast compared to the timescale of the experiment. In Chapter 7, the diffusion length on an experimental timescale was established as $\sqrt{\frac{DRT}{vF}}$, and so both the Debye length x_D and the electrode radius r_e must be much smaller than this distance if steady state can be used to describe a transient system. These inequalities hold for small microelectrodes and nanoelectrodes. In these cases, both double layer charging (as discussed in Chapter 6) and mass transport are much faster than the rate at which the applied potential is varied, and so there will be negligible voltammetric hysteresis. The steady state solution is therefore representative of the likely outcome of a real dynamic experiment.

10.2.1 Geometry and normalisation

As in the analysis in Section 8.3, a transformed length scale will be used for simulation:

$$y = 1 - \frac{r_\mathrm{e}}{r} \tag{10.1}$$

where $y = 0$ is the electrode surface and $y = 1$ is bulk solution. This transformation was also employed in the work by Streeter et al. on potential step chronoamperometry subject to a complex description of the diffuse double layer.[19] It was found that by a suitable choice of gridding, this simple transformation allowed acceptable numerical convergence, and so the complicated y-transformations introduced previously (Equations 6.17 and 9.7) were probably superfluous.

Note that a steady-state concentration profile or potential profile scales as r^{-1} in hemispherical space, and so appears as a straight line across the domain $0 \leq y \leq 1$ in the radial transform above. Also, as $r \to r_\mathrm{e}$, $dy \to dr$, so for short Debye lengths, the y-space approximates to linear space: for $R_\mathrm{e} \gg 1$, the diffuse double layer is contained within this pseudo-linear domain.

In this geometry, the time-independent Nernst–Planck–Poisson equation set is:

$$\frac{dc_\mathrm{A}}{dy} + z_\mathrm{A} c_\mathrm{A} \frac{d\theta}{dy} - j_\mathrm{A} = 0 \tag{10.2}$$

$$\frac{dc_\mathrm{B}}{dy} + z_\mathrm{B} c_\mathrm{B} \frac{d\theta}{dy} + \frac{j_\mathrm{A}}{D'_\mathrm{B}} = 0 \tag{10.3}$$

$$(1-y)^4 \frac{d^2\theta}{dy^2} + \frac{1}{2} R_\mathrm{e}^2 \sum_i z_i c_i = 0 \tag{10.4}$$

$$\frac{dj_\mathrm{A}}{dy} = 0 \tag{10.5}$$

subject to the bulk conditions detailed in Table 7.2, as well as the reference potential $\theta = 0$ in bulk solution.

Because the ion concentrations are at steady state, the inert ions M^+ and X^- obey the Boltzmann equation, since if their flux is zero at the electrode surface, it must be zero over all solution. Hence, for all y:

$$c_{\mathrm{M}} = c^*_{\mathrm{M}}\, \mathrm{e}^{-\theta} \tag{10.6}$$

$$c_{\mathrm{X}} = c^*_{\mathrm{X}}\, \mathrm{e}^{+\theta} \tag{10.7}$$

10.2.2 Diffuse double layer

The diffuse double layer is included by imposition of a fixed surface potential, θ_0, at $y = 0$:

$$\theta = \theta_0 = \frac{\eta}{n} - \theta_{\mathrm{pzc}} \tag{10.8}$$

The excess charge on the electrode is a function of both the applied overpotential, η, and the potential of zero charge, θ_{pzc}, as derived previously (Section 9.4.2). Note that the excess charge of the electrode varies across a voltammetric scan, since changing η also changes θ_0.

The potential of zero charge is an important system parameter which can be freely varied in the context of the simulation in order to alter the excess charge on the electrode – from definition, a positive θ_{pzc} implies that the electrode has negative excess charge in the range close to the formal potential at $\eta = 0$, and *vice versa*.

Note that this description of the double layer considers only the diffuse (Gouy–Chapman) component, and therefore excludes the effects of the compact (Stern) component, or of any specifically adsorbed ions. This is therefore a limiting case, in which only those effects due to the diffuse double layer are considered. The extension to a

more detailed description of the double layer will necessarily encompass diffuse double layer effects and therefore the work reported in this chapter constitutes a hopefully useful first step.

10.2.3 Electron transfer kinetics

A boundary condition is also applied at $y = 0$ to describe the kinetics of the electron transfer. We will initially address two such boundary conditions – one is the Nernst equation:

$$f_{\mathrm{NE}} = c_{\mathrm{A}} - c_{\mathrm{B}} \exp\Big(- (\eta - n\theta_0)\Big) = 0 \tag{10.9}$$

The Nernst equation implies thermodynamic equilibrium at $y = 0$ and so the electron transfer *cannot* be rate-limiting if it holds.

Our alternative is the Butler–Volmer equation which admits finite electrode kinetics:

$$f_{\mathrm{BV}} = f_{\mathrm{NE}} - \frac{j_{\mathrm{A}}}{K^0} \exp\Big(- \alpha'(\eta - n\theta_0)\Big) = 0 \tag{10.10}$$

As discussed in Section 7.3, as $K^0 \to \infty$, so $f_{\mathrm{BV}} \to f_{\mathrm{NE}}$.

10.2.4 Transformation of the dependent variables

The use of logarithmic concentration variables, as introduced in Section 6.2.3 for the simulation of capacitive charging, improves numerical convergence when there are natural exponential relationships in the equation set to be solved, as is the case for the Nernst–Planck–Poisson equations for a diffuse double layer. However, because $c_{\mathrm{B}} = 0$ at $y = 1$, $\ln c_{\mathrm{B}}$ is not an appropriate variable. Therefore, the following transformed

variables were chosen:

$$u_{\mathrm{A}} = \ln c_{\mathrm{A}} \tag{10.11}$$

$$u_{\sigma} = \ln(c_{\mathrm{A}} + c_{\mathrm{B}}) \tag{10.12}$$

The Nernst–Planck–Poisson equations then become:

$$\frac{du_{\mathrm{A}}}{dy} + z_{\mathrm{A}} \frac{d\theta}{dy} - j_{\mathrm{A}} \, \mathrm{e}^{-u_{\mathrm{A}}} = 0 \tag{10.13}$$

$$\frac{du_{\sigma}}{dy} + \left(z_{\mathrm{B}} - n \, \mathrm{e}^{u_{\mathrm{A}} - u_{\sigma}}\right) \frac{d\theta}{dy} - j_{\mathrm{A}} \delta \, \mathrm{e}^{-u_{\sigma}} = 0 \tag{10.14}$$

$$(1-y)^4 \frac{d^2\theta}{dy^2} + \frac{1}{2} R_{\mathrm{e}}^2 \left(c_{\mathrm{M}}^* \, \mathrm{e}^{-\theta} - c_{\mathrm{X}}^* \, \mathrm{e}^{+\theta} - n \, \mathrm{e}^{u_{\mathrm{A}}} + z_{\mathrm{B}} \, \mathrm{e}^{u_{\sigma}}\right) = 0 \tag{10.15}$$

$$\frac{dj_{\mathrm{A}}}{dy} = 0 \tag{10.16}$$

The Nernst equation can be written as:

$$1 + \frac{\mathrm{e}^{-n\theta_0}}{\mathrm{e}^{-\eta}} - \mathrm{e}^{u_{\sigma,0} - u_{\mathrm{A},0}} = 0 \tag{10.17}$$

and the Butler–Volmer equation as:

$$\left(1 + \frac{\mathrm{e}^{-n\theta_0}}{\mathrm{e}^{-\eta}} - \mathrm{e}^{u_{\sigma,0} - u_{\mathrm{A},0}}\right) - \frac{j_{\mathrm{A}} \mathrm{e}^{-\alpha'(\eta - n\theta_0)}}{K^0} \, \mathrm{e}^{-u_{\mathrm{A},0}} = 0 \tag{10.18}$$

10.2.5 Gridding and computation

The time-independent Nernst–Planck–Poisson equations are solved with forward differencing using the iterative Newton–Raphson method. A grid is chosen which maximises grid point density at the boundaries $y = 0$ and $y = 1$, according to the definitions in Section 3.2. This ensures a minimum density of points in the range $0 \leq y \leq y_{\mathrm{EN}}$, corresponding to the double layer. A maximum density of points is also set at the boundary $y = 1$, to avoid problems with $\Delta y \to 0$ in this limit when larger grid density was re-

quired at the electrode boundary. Optimal simulation parameters were determined by a convergence study using j_{A} as the diagnostic variable. These varied depending on the particular boundary conditions, but in the worst case, $\gamma_{\mathrm{R}} = 10^{-4}$ and $R_{\mathrm{s}} = 10^{-6}$ were found to be appropriate, with $R_{\mathrm{s},y=1}$ correspondingly reduced to ensure that $\Delta y > 10^{-6}$ at this boundary.

By contrast to the time-dependent problems considered previously, the steady-state diffuse double layer with Faradaic current is a complicated time-independent problem in multiple variables, and so numerical convergence of the iterative Newton–Raphson method cannot be guaranteed, as discussed in Section 3.5. Therefore, a strong initial guess for the concentration and potential functions is required. The Nernst–Planck–Poisson equations with a diffuse double layer and $|\theta_0| \gg 1$ are a particularly difficult equation set to solve, due to the contribution of multiple length scales to the unknown functions, and the likelihood of extreme behaviour at high surface potentials given the exponential relationships involved. Consequently, for many unsuitable initial guesses, the Newton–Raphson method is not able to converge to a solution.

For this reason, a method of successive elaboration of the boundary conditions was used to minimise failure in the numerical process. The following approach was taken:

1. Determine the electroneutral solution by the appropriate method from Section 8.3.

2. Solve the Poisson–Boltzmann equation given the surface concentrations and potential under electroneutrality, as discussed in the previous chapter (Equation 9.14), and apply this is a perturbation to the electroneutral solution. This is an initial guess which obeys the full double layer boundary condition of arbitrary sur-

face potential (Equation 10.8), but which neglects the possible effect of Faradaic current on the structure of the double layer, and does not admit that steady-state flux may be other than predicted by electroneutrality, due to rate-limiting mass transport or electrode kinetics within the double layer. Nonetheless, it is a superior initial guess to the unperturbed electroneutral solution.

3. If the Newton–Raphson method fails to converge with this initial guess, hold the surface potential constant but reduce the overpotential η by one unit, and repeat steps 1–2. Repeat until the Newton–Raphson method converges. Then use the result as an initial guess for the solution with overpotential η one unit higher, and repeat until the solution for the original parameter set is determined. This approach is effective when incorporating the diffuse double layer causes a significantly different steady-state current.

4. If tunnelling is required, use the normal double layer result as an initial guess to the tunnelling solution. Backtrack the applied overpotential as necessary. If this fails, use the Poisson–Boltzmann perturbation on the electroneutral result and try this as an initial guess. On failure, backtrack the surface potential θ_0 as required. Again, this recovers a limit where the diffuse double layer perturbs the electroneutral steady-state current less profoundly.

Taken together, these techniques ensured convergence of the numerical method without further intervention from the user for the vast majority ($> 99.9\%$) of simulations attempted, and enabled the construction of complete data sets for j_A across a wide range of η and θ_pzc for the various boundary conditions. The runtime to solve for a single data point (one set of η, θ_pzc, etc.) varied from one or two seconds to up to a

minute if considerable backtracking was required.

Runge–Kutta integration techniques were used as a trial, but were found to be unsuitable due to the difficulty of convergence of the integrals in the presence of decaying exponential terms in the functions, which necessarily arise in the presence of a double layer.

Having solved the equation set, the result of interest is steady-state voltammetry, i.e. the function $j_{\mathrm{A}}(\eta, \ldots)$ where $(\ldots)$ represents the relevant system parameters, other than applied potential.

10.3 Double layer: mass transport effects

First, diffuse double layer effects on steady-state mass transport towards the electrode will be studied, by simulating Nernstian voltammetry in the presence of a significantly charged double layer. Since the Nernst equation implies thermodynamic equilibrium, the electron transfer kinetics cannot be rate-limiting, and so deviations from the predictions of electroneutral theory must be due to rate-limiting mass transport within the diffuse double layer.

10.3.1 Simulation results: Nernstian kinetics

An ultramicroelectrode system with $R_{\mathrm{e}} = 100$ was studied: this corresponds to $r_{\mathrm{e}} = 0.96\ \mu$m for a 1 mM concentration of the electroactive species in water, at room temperature. The three migrational categories from electroneutral theory – attractive migration, zero migration and repulsive migration – were considered using the one-electron oxidations ($n = +1$) of electroactive species with $z_{\mathrm{A}} = -1$, 0 and +1 respectively. Each

voltammogram was simulated from $\eta = -10$ to $\eta = +10$, for potentials of zero charge in the range $-10 \leq \theta_{\text{pzc}} \leq +10$ and for support ratios varying from negligible support ($c_{\text{sup}} = 10^{-2}$) to full support ($c_{\text{sup}} = 10^{3}$). The largest excess charge considered was therefore $|\theta_0| = 20$, which is approximately 0.5 V.

With 378 voltammograms arising from the comprehensive study of a single electrode size under ideal Nernstian electron transfer, it is clear that it will not be feasible to present or discuss the full extent of the data set. Rather, here and later in the chapter, the data will be used selectively to highlight and provide evidence for key trends, which in all cases are borne out by the full data set available.

10.3.2 Migration effects at low support

When the potential of zero charge was set such that the excess charge on the electrode is minimised at overpotentials where the oxidation of A is thermodynamically driven, a conventional migrational influence on the transport-limited current was observed with varying support ratio. This is shown in Figures 10.1 and 10.2 for examples of attractive migration ($z_{\text{A}} = -1$) and repulsive migration ($z_{\text{A}} = +1$) respectively. In each case, decreased electrolytic support increases the strength of the migrational effect.

The effect of θ_{pzc} was then considered. The cases where $z_{\text{A}} = -1$ and $z_{\text{A}} = 0$ showed negligible double layer dependence. Where currents were dependent on the double layer for these cases, this occurred only at negligible support ratio, where the Debye length is longest. In this case, the approximation $r_{\text{e}} \gg x_{\text{D}}$ is less exact and so small discrepancies from the electroneutral solution are expected.

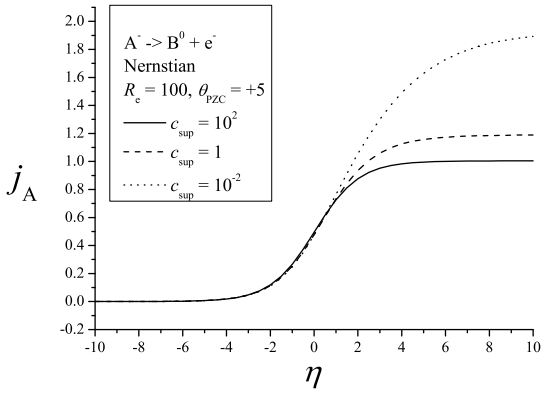

Figure 10.1: Simulated steady-state voltammetry for a microelectrode with different electrolytic support ratios c_{sup}, obeying the Nernst equation, with $z_{\mathrm{A}} = -1$ and $\theta_{\mathrm{pzc}} = +5$. Attractive migration is observed as the support ratio is reduced.

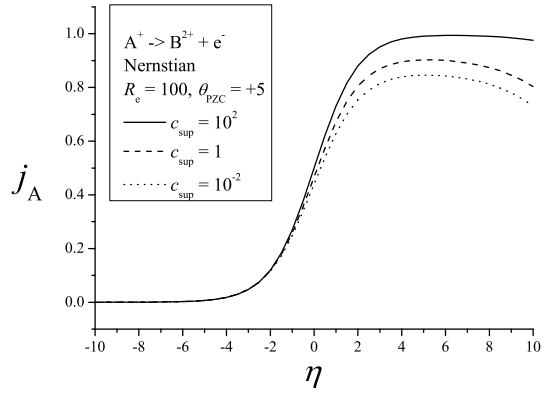

Figure 10.2: Simulated steady-state voltammetry for a microelectrode with different electrolytic support ratios c_{sup}, obeying the Nernst equation, with $z_{\mathrm{A}} = +1$ and $\theta_{\mathrm{pzc}} = +5$. Repulsive migration is observed as the electrolytic support ratio is reduced.

10.3.3 Electrode size effects

The availability of a full diffuse double layer solution enabled a comparison of steady-state currents, as a function of support ratio, between the zero-field approximation and the full treatment with $\theta_{\mathrm{pzc}} = -5, 0, +5$, for reversible electrochemical kinetics. Results at an applied overpotential of $\eta = +5$ for the case $z_{\mathrm{A}} = -1$ are shown for four electrode sizes, from $R_{\mathrm{e}} = 10$ to $R_{\mathrm{e}} = 10^4$, at Figures 10.3–10.6.

It is clear that deviations from zero-field are negligible in the previously determined

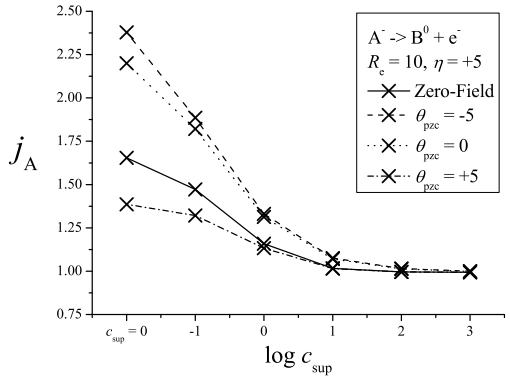

Figure 10.3: Steady-state currents, j_{A}, for $z_{\mathrm{A}} = -1$ as a function of c_{sup}, comparing the zero-field model with the full diffuse double layer model for $\theta_{\mathrm{pzc}} = -5$, 0 and +5. $R_{\mathrm{e}} = 10$; $\eta = +5$.

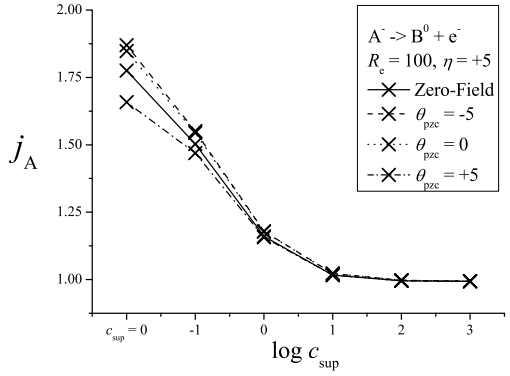

Figure 10.4: Steady-state currents, j_{A}, for $z_{\mathrm{A}} = -1$ as a function of c_{sup}, comparing the zero-field model with the full diffuse double layer model for $\theta_{\mathrm{pzc}} = -5$, 0 and +5. $R_{\mathrm{e}} = 100$; $\eta = +5$.

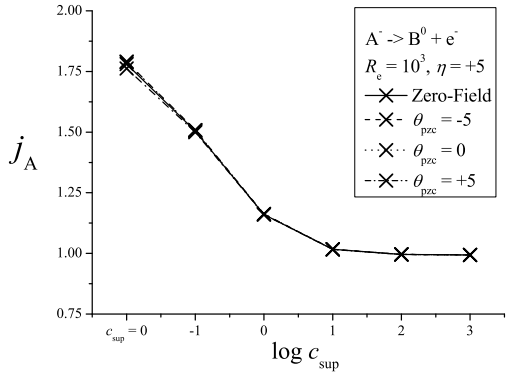

Figure 10.5: Steady-state currents, j_{A}, for $z_{\mathrm{A}} = -1$ as a function of c_{sup}, comparing the zero-field model with the full diffuse double layer model for $\theta_{\mathrm{pzc}} = -5$, 0 and +5. $R_{\mathrm{e}} = 1000$; $\eta = +5$.

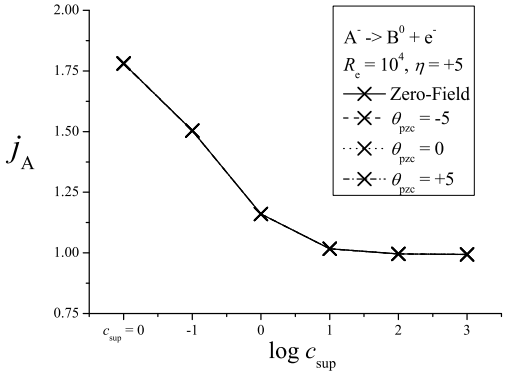

Figure 10.6: Steady-state currents, j_{A}, for $z_{\mathrm{A}} = -1$ as a function of c_{sup}, comparing the zero-field model with the full diffuse double layer model for $\theta_{\mathrm{pzc}} = -5$, 0 and +5. $R_{\mathrm{e}} = 10^4$; $\eta = +5$.

range $R_{\mathrm{e}} \geq 1000$, irrespective of the internal structure of the double layer. For nanoelectrode voltammetry, however, the inextricability of the double layer from the electric field associated with electrolysis causes a wide range of behaviour; the steady-state current is a strong function of θ_{pzc} and the zero-field approximation is, as expected, unsuitable. This confirms a lower limit of $R_{\mathrm{e}} = 1000$ for the zero-field approximation, as determined in the previous chapter.

Potential profiles are compared for zero-field and the full simulation (with $\theta_0 = +10$) at Figure 10.7.

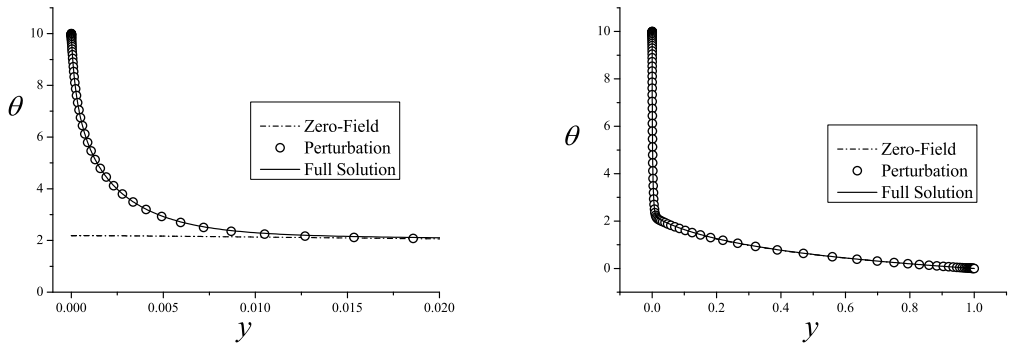

Figure 10.7: Steady-state potential profiles for the one-electron oxidation of A^- to B^0 at $\eta = +5$, with zero support. $\theta_{\mathrm{pzc}} = -5$; $R_{\mathrm{e}} = 10^3$. The diffuse double layer is magnified on the left; the figure on the right shows ohmic drop through the depletion layer.

Even at zero support, for $R_e = 1000$ it is clear that the potential profile for the full simulation is well represented by a decoupled sum of an inner double layer contribution, and an outer potential profile which is associated with the zero-field or electroneutral solution and accounts for the ohmic drop (Equation 9.2). This outer potential profile ($\theta^{(0)}$ or θ_{ZF} in the previous chapter) is approximately constant through the diffuse double layer range.

As a consequence, for modest values of θ_0 and for $R_e \geq 1000$, the potential and concentration profiles determined by the perturbation procedure described above match those from the full simulation almost exactly. This is shown in Figure 10.7 and the corresponding concentration profiles are displayed in Figure 10.8.

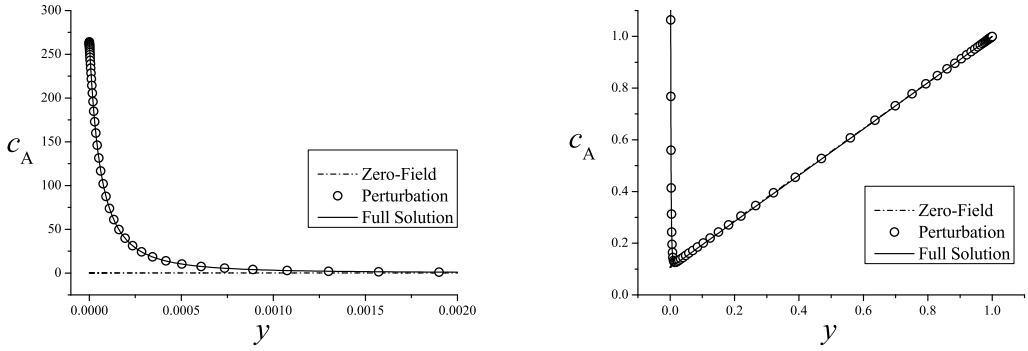

Figure 10.8: Steady-state concentration profiles of the electroactive species A^- for the one-electron oxidation at $\eta = +5$, with zero support. $\theta_{pzc} = -5$; $R_e = 10^3$. The diffuse double layer is magnified on the left; the figure on the right shows the depletion layer.

It is particularly significant that although the concentration of A at the site of electron transfer differs between the full diffuse double layer and zero-field treatments by a factor of over 2000 (Figure 10.8), the steady-state currents are respectively $j_A = 1.791$ and $j_A = 1.781$, a difference of only 0.55%. This underlines the dramatic independence of current from double layer structure revealed for thermodynamic electron transfer in Section 9.4.3. The evidence from simulation including the diffuse double layer confirms

the suitability of the zero-field approximation in such a case. The detailed behaviour of steady-state voltammetry for low R_e will be explored further in Section 10.6.

10.3.4 Double layer charge dependence

By contrast to the other two cases, extreme double layer dependence was observed for the repulsive migration case where $z_A = +1$. Specifically, currents were highly suppressed, at all support ratios, wherever the excess charge of the electrode was highly positive. This corresponds to potentials for which the reactant and the product are both strongly repelled. These results are exemplified by the fully supported voltammetry at Figures 10.9 and 10.10, in which the disparate behaviour between $z_A = 0$ and $z_A = +1$ is illustrated.

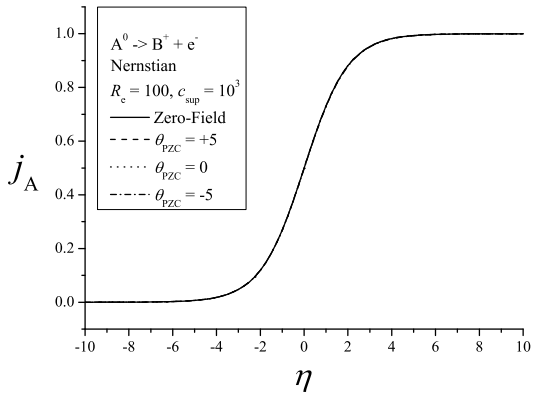

Figure 10.9: Simulated steady-state voltammetry for a microelectrode with high support, obeying the Nernst equation, with $z_A = 0$. All four lines overlap and no Levich exclusion effect is observed.

As set out in Section 9.4.3, thermodynamics require that if the Nernst equation holds at the outer Helmholtz plane, it equally holds at the outer edge of the double layer, so long as the double layer is internally equilibrated. Hence, the electroneutral solution with the Nernst equation will give an unaltered current in the presence of a

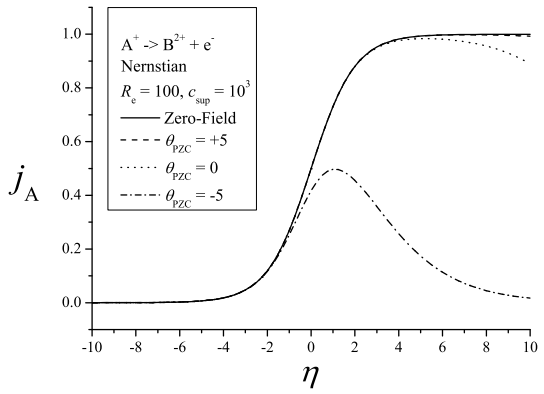

Figure 10.10: Simulated steady-state voltammetry for a microelectrode with high support, obeying the Nernst equation, with $z_A = +1$. A marked Levich exclusion effect is observed when the surface charge is highly positive.

double layer. This is observed in the full simulation study in some cases (e.g. Figure 10.6), but not in others (e.g. Figure 10.10).

Since the Nernst equation guarantees infinitely fast electron kinetics, the additional loss of current with a strongly repulsive excess charge on the electrode implies the presence of rate-limiting mass transport. Specifically this must be the mass transport across the diffuse double layer, and therefore we need to consider whether a charged layer limits the current that can be driven through it. This latter point was not considered in the analysis in the previous chapter.

10.3.5 Levich exclusion effect

Is there a maximum flux that can be driven through a double layer? The evidence of Figures 10.9 and 10.10 is that this will depend on the charge of the reacting species. The question was posed in the Russian literature by Levich as early as 1949.[20] He

integrated the Nernst–Planck equation using an integrating factor, as follows:

$$\begin{aligned} j_i &= \frac{dc_i}{dy} + z_i c_i \frac{d\theta}{dy} \\ j_i \exp(z_i\theta) &= \frac{d}{dy}\left(\exp(z_i\theta)\, c_i\right) \\ j_i \int_y^1 \exp(z_i\theta)\, dy &= c_i^* - \exp(z_i\theta)\, c_i \end{aligned} \tag{10.19}$$

Hence

$$c_i = \exp(-z_i\theta)\left(c_i^* - j_i \int_y^1 \exp(z_i\theta)\, dy\right) \tag{10.20}$$

If $j_i = 0$, this expression equals the normalised Boltzmann equation (Equation 1.33), as required. Otherwise the passage of flux will cause a perturbation of the concentration. If $j_i < 0$, i.e. flux away from the electrode, this deviation is positive and need not concern us further – this is the case for the product species. For the reacting species where $j_i > 0$, the concentration is negatively perturbed. The perturbation is negligible if the species A is attracted to the electrode and so $z_\mathrm{A}\theta < 0$, since the integral vanishes in this case. However, if the species A is repelled by the electrode, $\exp(z_\mathrm{A}\theta)$ may be large.

Levich considered that since $c_\mathrm{A} \geq 0$, we can define the maximum flux across the double layer as being that where $c_\mathrm{A} = 0$ at $y = 0$, i.e. complete depletion. The integral of $\exp(z_\mathrm{A}\theta)$ from $y = 0$ to $y = 1$ is not trivially evaluated, however, since θ becomes a function of c_A if A is charged.

If the support ratio is high, we can approximate that θ is dictated by the conductivity supplied by the supporting species alone, and so is independent of c_A. In this case, Levich used the Gouy–Chapman expression for the potential profile (Equation 5.15) to derive an expression for $j_{\mathrm{A,max}}$. This expression does not agree well with simulation,

however, because it fails to consider that the limit $c_\mathrm{A} = 0$ is not necessarily consistent with the Nernst equation.

Substitution of the integrated expressions for $c_{\mathrm{A},0}$ and $c_{\mathrm{B},0}$ into the Nernst equation *does* accurately reproduce the simulation results for Levich exclusion at high support, as will be demonstrated. From Equation 5.15, the Gouy–Chapman equation gives:

$$\exp(z_i\theta) = \left(\coth\left(\frac{X + X_0}{2}\right)\right)^{2|z_i|} \tag{10.21}$$

for the exclusion case $z_i n > 0$. So, to determine $c_{i,0}$ from Equation 10.20, the following integral must be evaluated:

$$\int_0^1 \left(\coth\left(\frac{X + X_0}{2}\right)\right)^{2m} dy \tag{10.22}$$

Ignoring spherical effects we can take

$$y \approx \frac{r - r_\mathrm{e}}{r_\mathrm{e}} = \frac{1}{R_\mathrm{e}\sqrt{I}} X \tag{10.23}$$

where I is the ionic strength, so the integral may be expressed as

$$\frac{2}{R_\mathrm{e}\sqrt{I}} \int_{\frac{y_0}{2}}^{\frac{(1+y_0)}{2}} (\coth u)^{2m}\, du \tag{10.24}$$

where

$$u = \frac{X + X_0}{2} \tag{10.25}$$

The integral

$$I_m = \int_a^b (\coth u)^{2m}\, du \tag{10.26}$$

evaluates to

$$I_m = b - a - \sum_{k=1}^{m} \frac{1}{2k-1} \left(\coth^{2k-1} b - \coth^{2k-1} a\right) \tag{10.27}$$

for $m \geq 0$. For the integration at hand, then, when $z_i n > 0$:

$$\int_0^1 \left(\coth\left(\frac{X+X_0}{2}\right)\right)^{2|z_i|} dy = \frac{2}{R_\mathrm{e}\sqrt{I}} \quad \times \\ \left(\frac{R_\mathrm{e}\sqrt{I}}{2} + \sum_{k=1}^{|z_i|} \frac{1}{2k-1}\left(\coth^{2k-1}\left(\frac{1+y_0}{2}\right) - \coth^{2k-1}\left(\frac{y_0}{2}\right)\right)\right) \tag{10.28}$$

Noting that:

$$\coth\left(\frac{1+y_0}{2}\right) = \mathrm{e}^{\frac{|\theta(y)|}{2}} \tag{10.29}$$

it follows that

$$\int_0^1 \left(\coth\left(\frac{X+X_0}{2}\right)\right)^{2z_i} dy = 1 + \frac{2}{R_\mathrm{e}\sqrt{I}} \sum_{k=1}^{|z_i|} \frac{1}{2k-1}\left(1 - \exp\left((2k-1)\frac{|\theta_0|}{2}\right)\right) \tag{10.30}$$

and so, substituting into Equation 10.20:

$$c_{i,0} = \exp(-z_i\theta_0)\ (c_i^* - j_i\,\Theta_i) \tag{10.31}$$

where

$$\Theta_i = \frac{2}{R_\mathrm{e}\sqrt{I}} \sum_{k=1}^{|z_i|} \frac{1}{2k-1}\left(1 - \exp\left((2k-1)\frac{|\theta_0|}{2}\right)\right) \tag{10.32}$$

Then, substituting Equation 10.31 into the Nernst equation gives:

$$j_\mathrm{A} = \frac{1}{1 + \Theta_\mathrm{A} + \mathrm{e}^{-n\eta}\ (1 + \Theta_\mathrm{B})} \tag{10.33}$$

This expression is compared to simulated steady-state voltammetry in Figure 10.11: it evidently reproduces simulation to much greater accuracy than the prediction by Levich based on a depletion condition.[20]

If the reactive species A and B contribute strongly to the ionic composition of the double layer, a simple Gouy–Chapman expression with respect to the supporting electrolyte concentration cannot be used to describe the potential profile, so this analysis is

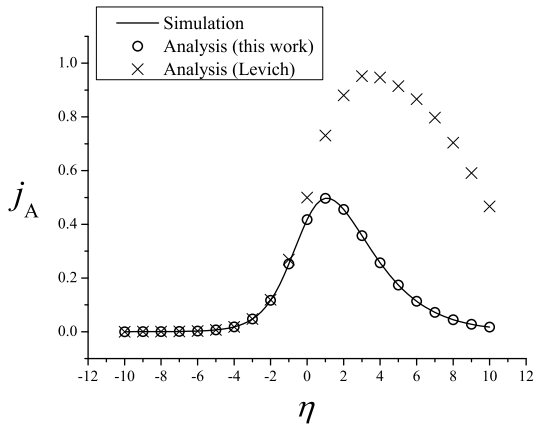

Figure 10.11: Simulated steady-state voltammetry for a microelectrode with high support, obeying the Nernst equation; $z_A = +1$ and $\theta_{pzc} = -5$. The magnitude of Levich exclusion effect is correctly predicted by substitution into the Nernst equation but not by a depletion condition.

less accurate. In the limit of high overpotential, however, the exclusion effect nonetheless dominates voltammetry in the repulsive migration case of $z_A n > 0$, to the extent that the flux is negligible.

The physical effect behind Levich exclusion is the difficulty of driving flux of a species that is present at low concentration due to Coulombic repulsion from the electrode. A flux can be driven by a small perturbation of the concentration gradient (diffusion) or electric field (migration) away from their zero flux values, as for an equilibrated diffuse double layer in which diffusion and migration are exactly balanced. To drive significant flux through the double layer then requires a sufficiently large concentration of the electroactive species, since in this case considerable diffusional flux can be driven by a negligible perturbation of the concentration, or considerable migrational flux can be driven by a negligible perturbation of the electric field. If the concentration c_A is small, however, the perturbation required to concentration or electric field makes driving a large flux impossible, within the constraints of solution electrodynamics.

In the attractive migration case ($z_A n < 0$), the Levich exclusion effect does not

occur under normal conditions of electrolysis, since if $z_{\mathrm{A}}n < 0$, then $z_{\mathrm{A}}((\eta/n) - \theta_0)$ becomes more negative at larger η, and so the attraction of A to the surface is increased according to the Boltzmann equation. Therefore, Levich exclusion, which is due to repulsion of A, becomes less significant with increasing overpotential.

By contrast, in the repulsive migration case, elevating the overpotential alters the excess charge of the electrode and so increases the repulsion of A, thereby limiting the flux due to Levich exclusion. Levich exclusion therefore occurs for any charged reactive species, but it will only be significant for the repulsive migration case, because otherwise it is likely to occur only at overpotentials where Faradaic current is otherwise negligible and therefore Levich exclusion is not itself rate-limiting.

10.4 Double layer: kinetic effects

The influence of the diffuse double layer on the kinetics of electron transfer at the electrode surface will now be considered.

10.4.1 Computational setup

Having used the Nernst equation to consider diffuse double layer effects exclusively associated with mass transport, an equivalent study across a range of support ratios and electrode charges can now be performed using the Butler–Volmer equation (Equation 10.10) in order to consider diffuse double layer effects due to the finite kinetics of electron transfer at the electrode surface. In addition to R_{e}, c_{sup}, η and θ_{pzc} as above, then, steady-state voltammetry with finite kinetics also depends on K^0 and α which describe the absolute rate and potential dependence of the heterogeneous electron

transfer, respectively.

A study was performed using $R_e = 100$, as before, with $\alpha' = 0.5$ and $K^0 = 10$, corresponding to a conventionally 'fast' $k^0 = 1.36$ cm s^{-1} for the electrode size in question. Note that because we are considering an ultramicroelectrode, this value of k^0 will not in fact give perfectly Nernstian behaviour. The simulated steady-state voltammetry is compared to the result using the Nernst equation, in order to identify effects which are exclusively due to the finite electron transfer kinetics.

For the attractive migration case ($z_A = -1$), a negligible difference is observed between infinite and finite electrode kinetics as a function of diffuse double layer charge. Only for an extremely negatively charged electrode is any difference observed, and it amounts to only a small shift of the voltammetric wave to higher overpotential.

For the zero migration case ($z_A = 0$), the waveforms remain sigmoidal, but the limiting current at high overpotential is lowered for highly positive electrode excess charge, as illustrated in Figure 10.12.

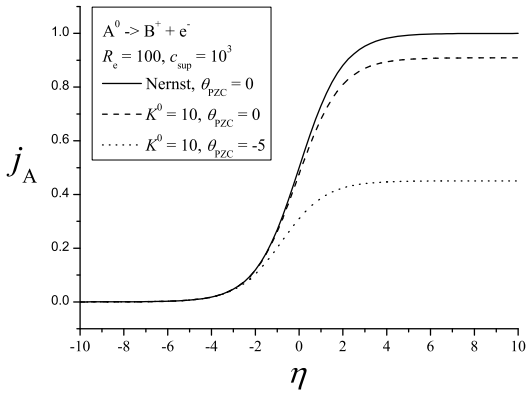

Figure 10.12: Simulated steady-state voltammetry for a microelectrode with high support, comparing the Nernst equation to the Butler–Volmer equation for different charges of electrode; $z_A = 0$. If the electrode kinetics are finite, the limiting current is reduced for an increasingly positive electrode.

The more positive the electrode, the greater the magnitude of this effect. Note

that no Levich exclusion effect was predicted for this case above (Figure 10.9), but the introduction of finite electrode kinetics introduces a double layer effect even in the absence of migration of the reacting species.

For the repulsive migration case ($z_A = +1$), the waveform is peaked and an enhanced suppression of the steady-state current is observed at large overpotential, especially for highly positive electrode surface charge (see Figures 10.13 and 10.14). This effect occurs additionally to the Levich exclusion effect described previously. Even for electrode charges where a Levich exclusion effect was not observed, there is some suppression of current at high overpotential, where the electrode becomes positively charged.

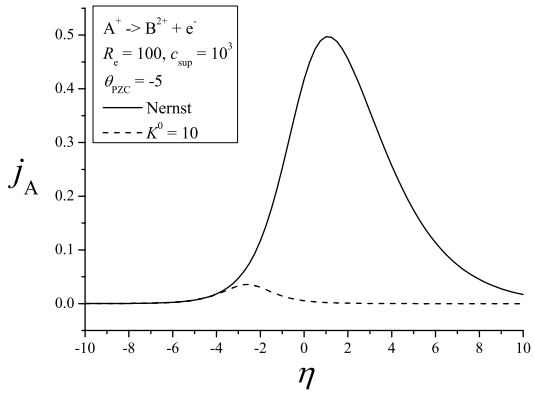

Figure 10.13: Simulated steady-state voltammetry for a microelectrode with high support, comparing the Nernst equation to the Butler–Volmer equation; $z_A = +1$, $\theta_{pzc} = -5$. The electrode is highly positive over most of the potential range and a strong Frumkin effect is observed in addition to the Levich exclusion acting on the Nernstian voltammetry.

Similar trends were observed at low support. In the repulsive migration case the effect is in fact less extreme at lower support, because the ohmic drop in bulk solution offsets the amount of excess charge at the electrode surface, and so the potential difference across the double layer is reduced.

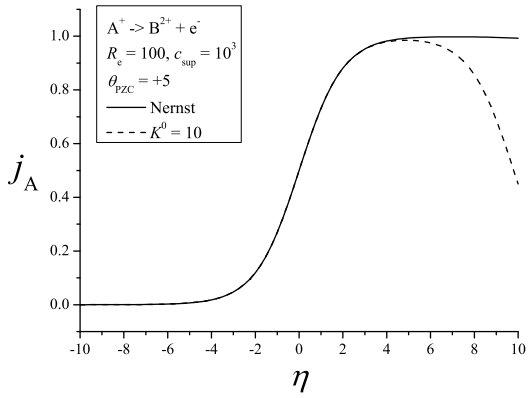

Figure 10.14: Simulated steady-state voltammetry for a microelectrode with high support, comparing the Nernst equation to the Butler–Volmer equation; $z_{\mathrm{A}} = +1$, $\theta_{\mathrm{pzc}} = +5$. The electrode is negative over most of the potential range but becomes positive at high overpotential, where a Frumkin effect is observed.

10.4.2 Frumkin correction

The effects reported above may be understood on the basis of the classical 'Frumkin correction'.[21] The introduction of Butler–Volmer kinetics introduces the possibility that the current may be limited because electron transfer is slower at the outer Helmholtz plane (inside the double layer) than outside the double layer. This idea was originally discussed by Frumkin who proposed a correction to the apparent k^0 inferred from diffusion-only theory in order to determine the 'real' k^0.

The theory of the Frumkin correction was set out in the previous chapter. Following the same derivation as used with respect to the zero-field approximation, if there exists a point outside which electroneutrality holds, and where the ohmic drop to bulk solution is θ_{EN}, then from Equation 9.32, the Frumkin correction is:

$$K^0_{\mathrm{app}} = K^0 \exp\left(-\left(\frac{z_{\mathrm{A}}}{n} + \alpha'\right)(\eta - n\theta_{\mathrm{pzc}} - n\theta_{\mathrm{EN}})\right) \tag{10.34}$$

The physical cause of the change in apparent K^0 is that the potential dependence of the transition state Gibbs energy is not equivalent to that of either reactant or product,

and therefore the rates of the anodic and cathodic reactions change as a function of potential through the double layer in a manner that is not exactly compensated by the relative change in concentration of the reactant and product, by Coulombic attraction or repulsion. For thermodynamic equilibrium, this compensation *is* exact, and so the Nernst equation is unperturbed by an applied potential, as was discussed above.

10.4.3 Analysis at full support

If the supporting electrolyte concentration is high, there is negligible resistance outside the double layer and so $\theta_{\mathrm{EN}} \to 0$ irrespective of the current being passed. Hence:

$$K^0_{\mathrm{app}} \approx K^0 \exp\left(-\left(\frac{z_{\mathrm{A}}}{n} + \alpha'\right)(\eta - n\theta_{\mathrm{pzc}})\right) \tag{10.35}$$

Given that mass transport outside the double layer will be diffusion-only if c_{sup} is large, it is suitable to substitute the Frumkin-corrected K^0 into the expression for steady-state current subject to the Butler–Volmer equation under diffusion-only conditions (Equation 7.76), such that:

$$j_{\mathrm{A,FC}} \approx \frac{1}{1 + \frac{\exp(-\eta)}{D'_{\mathrm{B}}} + \frac{1}{k'}} \tag{10.36}$$

where

$$\begin{aligned} k' &= K^0 \exp(+\alpha'\eta) \exp\left(-\left(\frac{z_{\mathrm{A}}}{n} + \alpha'\right)(\eta - n\theta_{\mathrm{pzc}})\right) \\ &= K^0 \exp(-z_{\mathrm{A}} n\eta) \exp((z_{\mathrm{A}} + n\alpha')\,\theta_{\mathrm{pzc}}) \end{aligned} \tag{10.37}$$

Using 0.5 as a typical value of α', the predicted behaviour for the three values of z_{A} can now be considered.

Where $z_{\mathrm{A}} n < 0$, a positive θ_{pzc} reduces k'. However, as with the Levich exclusion effect, increasing the overpotential η will elevate k'. In the attractive migration regime,

then, the Frumkin correction effect disappears at high overpotential, with Nernstian behaviour being recovered. Therefore, the Frumkin correction is difficult to observe where $z_{\mathrm{A}}n < 0$ because, as with Levich exclusion, the thermodynamics of electron transfer are typically rate-limiting at overpotentials where Frumkin correction might otherwise be significant.

Where $z_{\mathrm{A}} = 0$, k' is independent of η, and therefore as $\eta \to \infty$, j_{A} approaches a constant limiting value not necessarily equal to unity, which is entirely consistent with the the simulation data (Figure 10.12). In this case, the Frumkin correction reducing the rate of reaction exactly balances the elevation of that rate due to increased thermodynamic driving force, as η increases. For greater $n\theta_{\mathrm{pzc}}$, the Frumkin correction becomes more considerable.

Where $z_{\mathrm{A}}n > 0$, a negative θ_{pzc} strongly reduces k', and this effect increases with overpotential. Therefore, an extreme Frumkin correction is expected in this case. The consequently peaked voltammogram has been predicted previously.[16]

For all three examples, these results are consistent with the simulation data. At full support, the exact current in the full diffuse double layer simulation model can be predicted based on the electroneutral solution (Section 8.3) with the Butler–Volmer equation and a heterogeneous rate constant K^0_{app}.

10.4.4 Analysis at low support

At low support, it is still possible to analyse the data on the basis of a Frumkin correction. The situation is complicated by the dependence of the Frumkin correction on θ_{EN}, which corresponds to the ohmic drop arising from the electroneutral solution: at low support, this will be non-zero. Therefore a K^0_{app} cannot be directly determined

but rather arises as a self-consistent solution for K^0_{app} to the equation:

$$K^0_{\mathrm{app}} = K^0 \exp\Big(- (z_{\mathrm{A}} n + \alpha')(\eta - n\theta_0 - n\theta_{\mathrm{EN}}(K^0_{\mathrm{EN}} = K^0_{\mathrm{app}}))\Big) \tag{10.38}$$

The concordance between electroneutral solutions obeying this equation and the full simulation is good in extreme limits of θ_0 but has an inaccuracy of up to 20% in some ranges of θ_0, for $R_{\mathrm{e}} = 100$. In this case, the additional influence of Levich exclusion may lead to a more complex interaction than predicted by the simple Frumkin correction.

10.5 Influence of tunnelling

10.5.1 Distance-dependent electron transfer

Up to this point, electron transfer has been considered to occur classically, at a plane of electron transfer coincident with the outer Helmholtz plane, inside the diffuse double layer. This theoretical model predicts unusual effects concerning both mass transport and apparent electrode kinetics, in which both 'Levich exclusion' and the Frumkin effect may contribute strongly to the observed voltammetry, depending on the excess charge on the working electrode.

In fact, electron transfer is understood to take place via tunnelling, a process of instantaneous transfer of the electron between two classically separate points. The rate of tunnelling has a distance dependence of the form $\exp(-\beta' x)$, where the tunnelling decay constant β' is of the order of 1 $\mathrm{\AA}^{-1}$ in aqueous solution.[22] Therefore, electron transfer may in fact take place some distance away from the outer Helmholtz plane, at which point the potential may be such that the Levich exclusion or Frumkin effects are less significant. We will consider the effects of tunnelling to determine whether more

'conventional' sigmoidal voltammetry is predicted if the plane of electron transfer is allowed to move away from the outer Helmholtz plane.

Feldberg considered the potential step chronoamperometry experiment subject to distance-dependent electron transfer, but only under diffusion-only conditions.[23] He found that deviations from classical behaviour occur only where the dimensionless parameter $k^0/\beta' D$ is greater than unity, which is not the case for normal values of these parameters. In this paper, the steady-state solution in a spherical geometry was said to have been reported by Marcus and Siders,[24] but while this work implicitly contains the required calculations, the context is that of homogeneous electron transfer and the voltammetric result is not considered. Nonetheless, these calculations are quite feasible for diffusion-only conditions, and the steady-state current is given:

$$j_{\mathrm{A,TL}} = j_{\mathrm{A,NE}} \cdot \left(1 + \frac{2}{\beta' r_{\mathrm{e}}} f\left(\eta, \left(\frac{k^0}{\beta' D}\right)\right)\right) \tag{10.39}$$

where the function $f(\eta, (k^0/\beta' D))$ is given in Appendix C, together with the derivation. The above equation tends to the Butler–Volmer limit for $k^0 \ll \beta' D$. Again, only for large values of the dimensionless parameter $k^0/\beta' D$ does tunnelling become significant.

Distance-dependent electron transfer in the presence of migration has been considered more recently. Gavaghan and Feldberg used analytical techniques to consider its relevance to the Frumkin correction.[25] This work defined the range of Debye lengths where the standard Frumkin correction is expected to apply, and a range where it is perturbed by the distance-dependent electron transfer, including the range in which the plane of electron transfer moves fully outside the diffuse double layer. Also, the recent works of White[26] and of Chen and co-workers[14] have incorporated distance-dependent electron transfer according to a similar formalism to our own, although without direct

comparison to the case where $\beta' \to \infty$, in which electron transfer is confined to the outer Helmholtz plane.

10.5.2 Theoretical model

Following previous works in the field, the Butler–Volmer equation can be assumed to dictate the relative rate of electron transfer at any point in solution. Therefore, a source or sink applies to the concentration of species A, such that its rate of change at a given position is:

$$\frac{\partial c_{\mathrm{A}}}{\partial \tau} = (1-y)^4 \frac{\partial j_{\mathrm{A}}}{\partial y} - k' f_{\mathrm{BV}}(y) \tag{10.40}$$

where the Butler–Volmer expression is

$$f_{\mathrm{BV}} = \exp\Big(+ \alpha'(\eta - n\theta)\Big) \Big(c_{\mathrm{A}} - c_{\mathrm{B}} \exp(-(\eta - n\theta))\Big) \tag{10.41}$$

and

$$k' = v \cdot \exp\left(-\frac{\beta y}{1-y}\right) \tag{10.42}$$

where v is a constant and β is a dimensionless parameter equal to $\beta' r_{\mathrm{e}}$.

At steady state, $\partial c_{\mathrm{A}}/\partial \tau = 0$, and so:

$$(1-y)^4 \frac{\partial j_{\mathrm{A}}}{\partial y} = v \cdot \exp\left(-\frac{\beta y}{1-y}\right) \cdot f_{\mathrm{BV}} \tag{10.43}$$

As $\beta \to \infty$, electron transfer is confined to a plane close to $y = 0$ where f_{BV} becomes effectively constant, such that:

$$\begin{aligned} \frac{\partial j_{\mathrm{A}}}{\partial y} &\approx v \cdot f_{\mathrm{BV}} \exp(-\beta y) \\ j_{\mathrm{A}} &\approx v \cdot f_{\mathrm{BV}} \int_0^\infty \exp(-\beta y)\, dy \\ &= \frac{v f_{\mathrm{BV}}}{\beta} \end{aligned} \tag{10.44}$$

Since the Butler–Volmer equation for electron transfer confined to the outer Helmholtz plane is:

$$j_{\mathrm{A}} = K^0 \, f_{\mathrm{BV}} \tag{10.45}$$

then for continuity of theory in this limit, we require

$$v = K^0 \beta \tag{10.46}$$

such that

$$(1-y)^4 \, \frac{dj_{\mathrm{A}}}{dy} - K^0 \cdot \beta \exp\left(-\frac{\beta y}{1-y}\right) \cdot f_{\mathrm{BV}} = 0 \tag{10.47}$$

Together with the Nernst–Planck–Poisson equations, this condition is used in place of the condition of constant j_{A} (Equation 10.16) to simulate steady-state voltammetry in the presence of distance-dependent electron transfer. At the electrode surface ($y = 0$), the electrode is impermeable to the species A:

$$j_{\mathrm{A}}(0) = 0 \tag{10.48}$$

since the reaction of A is now described by the tunnelling condition.

10.5.3 Results from simulation

A comprehensive simulation study was carried out, using the tunnelling description of electron transfer kinetics across the three cases for z_{A}, and the full range of η and θ_{pzc} used in the previous studies. The parameters $K^0 = 10$ and $\alpha = 0.5$ were used as before, and β was set to 10^4, which corresponds to $\beta' = 1.04$ Å^{-1}. The resulting voltammetry was compared with the results from the Nernst and Butler–Volmer studies to analyse the extent to which Levich exclusion or Frumkin effects can be mitigated by distance-dependent electron transfer.

For the case where $z_A = +1$, sigmoidal voltammetry was recovered for a highly positively charged electrode at high support, where both the Levich exclusion and Frumkin effects were observed if electron transfer was confined to the outer Helmholtz plane. This is exemplified by the voltammetry in Figure 10.15. Note that an apparent kinetic shift is still observed compared to the result if the Butler–Volmer equation is used in conjunction with electroneutrality.

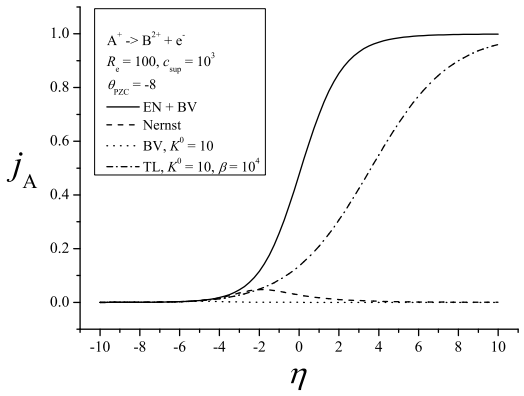

Figure 10.15: Simulated steady-state voltammetry for a microelectrode with high support, comparing different kinetic regimes. $z_A = +1$, $\theta_{pzc} = -8$. The Levich and Frumkin effects are largely avoided by the inclusion of tunnelling.

In order to confirm that this dramatic effect can be attributed to a change in the plane of electron transfer, the mean position of electron transfer was calculated from the simulated concentration profiles according to the formula:

$$y_{ET,mean} = \frac{\int_0^{j_{A,max}} y \, dj_A}{j_{A,max}} \tag{10.49}$$

which is straightforwardly determined numerically from the simulation data. The position of maximum electron transfer was also determined, being the position where $(1-y)^4 \, dj_A/dy$ takes its maximum value. The data are presented in Figure 10.16.

It is clear that at overpotentials where a marked double layer effect is encountered for the conventional kinetic models, the predicted $y_{ET,mean}$ and $y_{ET,max}$ deviate

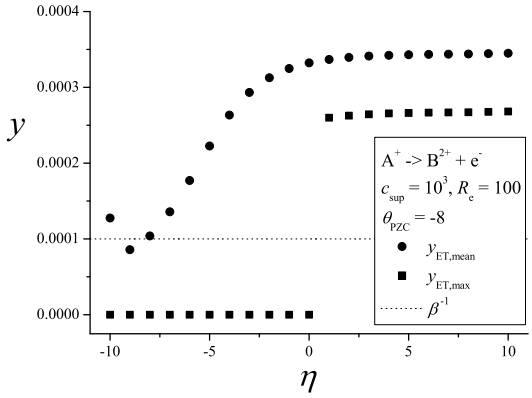

Figure 10.16: Effect of applied potential and electrode excess charge on the mean and maximum positions of electron transfer by tunnelling (y_{ET}) for oxidation with $z_{\mathrm{A}} = +1$. In the region where the Frumkin effect is significant in the absence of tunnelling, the plane of electron transfer with tunnelling changes to maximise flux.

markedly from $y = 0$ if distance-dependent electron transfer is allowed. By moving the plane of electron transfer away from the electrode, the Frumkin effect is mitigated by maximising $\eta - n\theta$ at the point of electron transfer. Equally, the Levich exclusion effect is minimised since the species A does not need to be transported across a considerable portion of the potential difference lying between $y = 0$ and $y = y_{\mathrm{EN}}$. This is particularly significant where $|\theta_0| > 10$, in which case the Gouy–Chapman theory predicts that the vast majority of the additional potential difference is confined to a range much less than the tunnelling distance away from the electrode surface.

The case of $z_{\mathrm{A}} = 0$ was also considered, for a potential where a Frumkin effect was expected, but not a Levich exclusion effect. Again, a normal (electroneutral) limiting current was recovered by permitting distance-dependent electron transfer, although an alteration of the apparent kinetics attributable to the tunnelling process is also observed in the voltammetry, as shown in Figure 10.17.

This kinetic effect was examined by applying a constant $\eta = +5$ and considering a wide range of positive surface potentials, as shown in Figure 10.18.

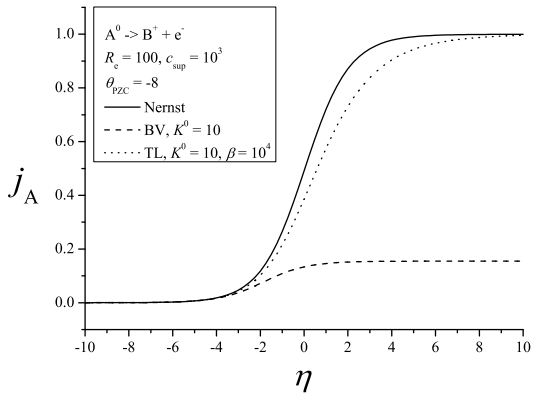

Figure 10.17: Simulated steady-state voltammetry for a microelectrode with high support, comparing different kinetic regimes. $z_{\mathrm{A}} = 0$, $\theta_{\mathrm{pzc}} = -8$. The Frumkin effect is largely avoided by the inclusion of tunnelling.

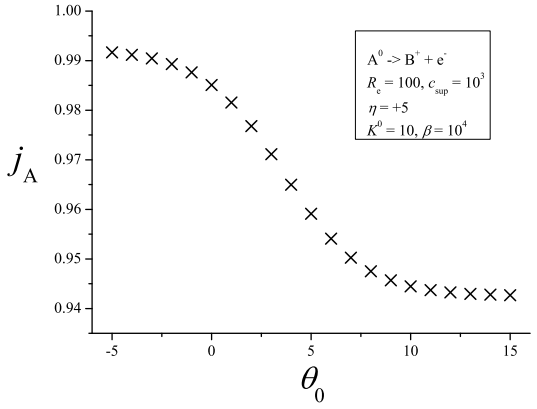

Figure 10.18: Dependence of voltammetric current on electrode excess charge for $z_{\mathrm{A}} = +0$ and $\eta = +5$. Two limits are observed.

Figure 10.19 illustrates the altered plane of electron transfer corresponding to these steady-state currents with tunnelling.

Two distinct limits are observed. The first is where the excess charge is negligible, and so the Frumkin effect is also negligible. Therefore, $y_{\mathrm{ET,mean}} \to 0$ since mass transport across the double layer to the electrode, where the tunnelling rate is maximum, occurs on a rapid timescale compared to the rate-limiting diffusion outside the double layer. This corresponds to the determination that under diffusion-only conditions, ignoring the double layer, the theoretical inclusion of tunnelling does not alter the plane

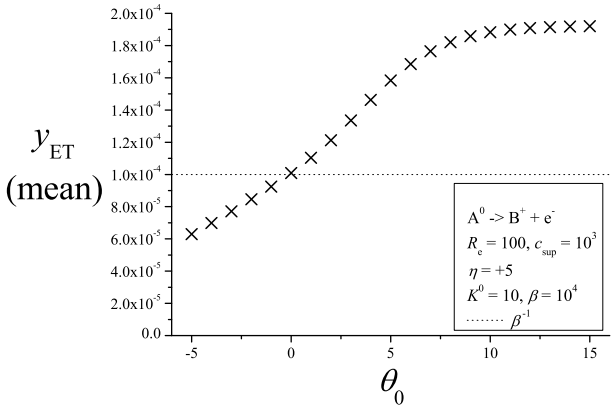

Figure 10.19: Effect of electrode excess charge on the mean position of electron transfer by tunnelling (y_{ET}) for oxidation with $z_A = 0$, indicating a change of the plane of electron transfer.

of electron transfer for normal values of k^0, β' and D.[23]

In the limit of high excess charge and a considerable Frumkin effect, a 'tunnelling limit' is noted, in which the plane of electron transfer achieves a maximum value. A different limiting current is observed in this regime, due to the impossibility of overcoming the full Frumkin effect with a finite β. A plot of the flux of A as it varies through space is presented at Figure 10.20 for different surface charges, demonstrating the shift of the plane of electron transfer away from the electrode in the region where the Frumkin effect applies.

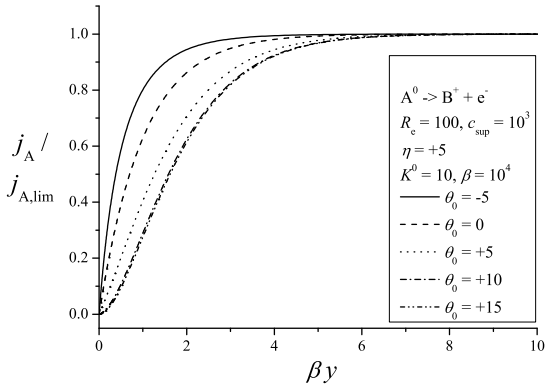

Figure 10.20: Flux profiles across the tunnelling region for oxidation with $z_A = 0$ and $\eta = +5$, as a function of excess charge.

In the case of low support, the mitigation of Levich or Frumkin effects by incorporation of distance-dependent electron transfer is less straightforward. Since the Debye length is longer in a weakly supported solution, proportionally less of the diffuse double layer effect can be avoided by electron transfer at a fixed tunnelling distance. Significantly, 'normal' currents can be driven at low support in the presence of tunnelling regardless of the potential of zero charge, but extreme overpotentials may be required to achieve this in the Frumkin-limited regime. This is demonstrated in Figure 10.21, which compares Butler–Volmer and distance-dependent electron transfer kinetics for a weakly supported case, with $z_{\mathrm{A}} = +1$. In the latter case, a normal sigmoidal waveform is observed, but only at extreme overpotential by comparison to the prediction of electroneutral theory.

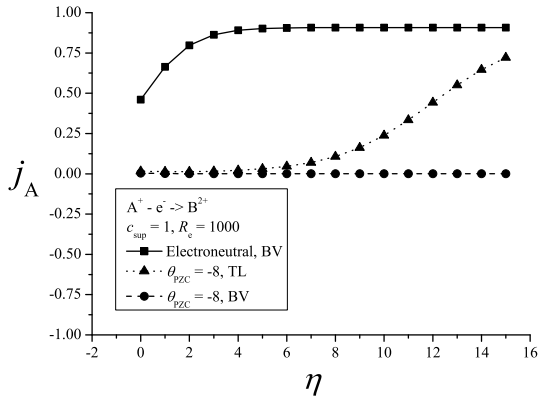

Figure 10.21: Simulated steady-state voltammetry for a microelectrode with low support, comparing different kinetic regimes. $z_{\mathrm{A}} = +1$, $\theta_{\mathrm{pzc}} = -8$. The Frumkin effect is avoided by the inclusion of tunnelling, but only at extreme overpotential.

This behaviour arises since the electron transfer rate k' has exponential dependence upon η and so can always be driven to a large enough value to drive appreciable flux in an outer region of the double layer where the Frumkin correction is not rate-limiting. However, due to the exponentially decaying spatial dependence of the electron transfer rate, the required overpotential increases with the Debye length, since the region of

bulk solution potential is more distant from the electrode. This behaviour is not possible for electron transfer confined to the outer Helmholtz plane, where increasing the overpotential will simply add to the double layer charge and hence to the extent of Frumkin correction to the rate constant. The unbounded exponential dependence of the electron transfer rate upon applied potential difference cannot be viewed as physically exact, however.

10.6 Nanoelectrode voltammetry

We have considered a range of double layer effects for an electrode radius-to-Debye length ratio characteristic of an ultramicroelectrode ($R_\mathrm{e} = 100$), which is not quite large enough for the zero-field approximation to be exact, but nonetheless sufficient for nanoelectrode effects on the double layer structure, such as those introduced in Chapter 5, to be insignificant. Here, electrode size effects due to the reduced size of the double layer are introduced.

10.6.1 'Coulombic' voltammetry

For systems with low conductivity or with a very small nanoelectrode, $r_\mathrm{e} \to x_\mathrm{D}$ and so $R_\mathrm{e} \to 1$. It has already been shown that the diffuse double layer deviates from the classical (planar) Gouy–Chapman description in this limit, due to the effects of curvature upon the double layer (Equation 5.37 and Section 5.7). The extreme theoretical limit of nanoelectrode voltammetry is that where $R_\mathrm{e} \to 0$, i.e. where the Debye length is much larger than the diffuse double layer. In this case, electric fields are effectively unscreened across the entire depletion layer, which completely changes the charac-

teristics of the voltammetry, since concepts such as electroneutrality or the zero-field approximation are no longer relevant or meaningful.

As a limiting case, the steady-state voltammetric current is derived for $R_\mathrm{e} = 0$. Even at low support, this is not a practically achievable limit, since it implies sub-atomic electrode sizes, but nonetheless it predicts relevant results for for describing the transitional region ($R_\mathrm{e} \approx 1$) where unscreened charge in the depletion layer contributes to voltammetry.

As $R_\mathrm{e} \to 0$, the electric field ceases to depend on the solution conductivity and is unscreened to well beyond the depletion layer. It therefore obeys the Laplace equation in the region of interest, and takes the form:

$$\theta = \theta_0(1 - y) \tag{10.50}$$

Substituting this expression into the Nernst–Planck equation:

$$\frac{dc_i}{dy} - z_i\theta_0 c_i = j_i \tag{10.51}$$

so

$$\frac{d}{dy}(\mathrm{e}^{-z_i\theta_0 y}\, c_i) = j_i\, \mathrm{e}^{-z_i\theta_0 y} \tag{10.52}$$

and integrating

$$\int_{y=0}^{y=1} d(\mathrm{e}^{-z_i\theta_0 y}\, c_i) = j_i \int_0^1 \mathrm{e}^{-z_i\theta_0 y}\, dy \tag{10.53}$$

$$\mathrm{e}^{-z_i\theta_0}\, c_i^* - c_{i,0} = -\frac{j_i}{z_i\theta_0}\left(\mathrm{e}^{-z_i\theta_0} - 1\right)$$

Therefore

$$c_{i,0} = c_i^*\, \mathrm{e}^{-z_i\theta_0} + j_i\, \frac{\mathrm{e}^{-z_i\theta_0} - 1}{z_i\theta_0} \tag{10.54}$$

Applying the Nernst equation and the outer boundary conditions:

$$\mathrm{e}^{-z_\mathrm{A}\theta_0} + j_\mathrm{A}\,\frac{\mathrm{e}^{-z_\mathrm{A}\theta_0}-1}{z_\mathrm{A}\theta_0} + \frac{j_\mathrm{A}}{D'_\mathrm{B}}\,\frac{\mathrm{e}^{-z_\mathrm{B}\theta_0}-1}{z_\mathrm{B}\theta_0}\,\mathrm{e}^{-(\eta-n\theta_0)} = 0 \tag{10.55}$$

Multiplying through by $\mathrm{e}^{-z_\mathrm{A}\theta_0}$

$$1 + j_\mathrm{A}\left(\frac{1-\mathrm{e}^{z_\mathrm{A}\theta_0}}{z_\mathrm{A}\theta_0} + \frac{\mathrm{e}^{-\eta}}{D'_\mathrm{B}}\frac{1-\mathrm{e}^{z_\mathrm{B}\theta_0}}{z_\mathrm{B}\theta_0}\right) = 0 \tag{10.56}$$

and hence

$$j_\mathrm{A} = \frac{1}{a + \frac{b}{D'_\mathrm{B}}\mathrm{e}^{-\eta}} \tag{10.57}$$

where

$$a = \frac{\mathrm{e}^{z_\mathrm{A}\theta_0}-1}{z_\mathrm{A}\theta_0} \tag{10.58}$$

$$b = \frac{\mathrm{e}^{z_\mathrm{B}\theta_0}-1}{z_\mathrm{B}\theta_0} \tag{10.59}$$

The derivation of this equation was alluded to in the work of Norton et al.,[16] who considered a slightly more complex system and do not appear to have reported this particular result.

The three electroneutral cases again all exhibit distinct voltammetric behaviour according to this equation, and these cases have been recognised previously by both analysis and simulation.[16,17] Where $z_\mathrm{A} = 0$, there is a strong apparent catalytic effect where a positive electrode limits the rate of oxidation, whereas a negative electrode accelerates the rate. The maximum achievable rate remains $j_\mathrm{A} = 1$ since the transport of A is diffusion-only.

Where $z_\mathrm{A}n < 0$, extremely large currents are achievable for an electrode of opposite charge to the reactive species, since it is strongly attracted towards the electrode surface. At high overpotential, the steady-state current tends towards infinity rather

than towards a limiting value.

Where $z_A n > 0$, peaked voltammetry is typically seen, due to the interplay of the relative attraction and repulsion of the species A and B. At appropriate surface charges, $j_A > 1$ is possible; equally, high overpotential tends to limit current due to repulsion of the reacting species.

10.6.2 Effect of unscreened charge separation

Although the predictions here are based on the unrealistic assumption that $R_e = 0$, the same trends can be observed in simulation results for feasibly small R_e. A comprehensive study was performed with $R_e = 1$, corresponding to $r_e = 9.6$ nm for a 1 mM concentration of electroactive species in water at room temperature. At low support, where the Debye length is longer, trends corresponding to 'Coulombic' voltammetry are observed, as exemplified by Figures 10.22 and 10.23, which compare voltammetry for the three z_A cases at $\theta_{pzc} = 0$ and +5 respectively. The effect of tunnelling (using $\beta = 10^4$) has been retained for consistency with the previous section; it does not substantially alter the results.

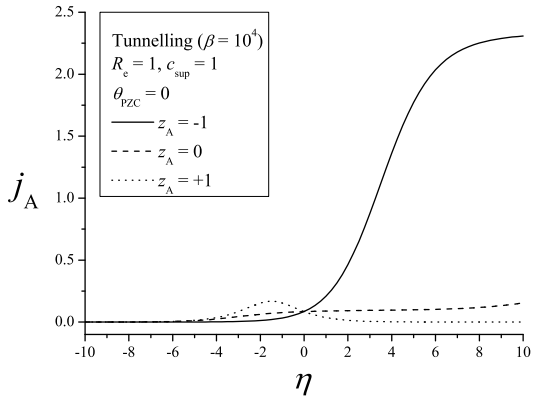

Figure 10.22: Simulated steady-state voltammetry for a nanoelectrode with low support, showing the effect of the reactant charge where $\theta_{pzc} = 0$.

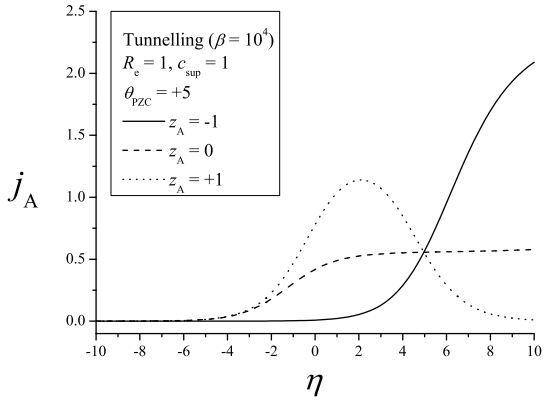

Figure 10.23: Simulated steady-state voltammetry for a nanoelectrode with low support, showing the effect of the reactant charge where $\theta_{\mathrm{pzc}} = +5$.

As discussed above, the current drawn for the attractive migration case greatly exceeds that predicted for low support according to electroneutral theory. For the $z_{\mathrm{A}} = 0$ case, a partial Frumkin effect is observed such that $j_{\mathrm{A}} < 1$, but the voltammetry is generally sigmoidal. For the repulsive migration case, $j_{\mathrm{A}} > 1$ is observed for certain values of θ_{pzc}, in contrast to the predictions of electroneutral theory, and the voltammetry is also characteristically peaked, showing a collapse of voltammetric current even for a θ_{pzc} where no strong Frumkin correction is expected.

The unscreened nature of the depletion layer for this example is clearly illustrated by comparing two typical concentration profiles for the attractive migration case, with $R_{\mathrm{e}} = 1$, shown for high support and low support at Figures 10.24 and 10.25 respectively.

In the highly supported case, the Debye length is sufficiently short with respect to the electrode that a conventional Gouy–Chapman diffuse double layer is observed, with negligible ohmic drop outside this layer. By contrast, at zero added support, the conductivity is low and the Debye length is comparable to the electrode size. Hence, the electric field is unscreened across a wide portion of the depletion layer. This leads to significant additional current due to the unscreened Coulombic attraction of A^- to the

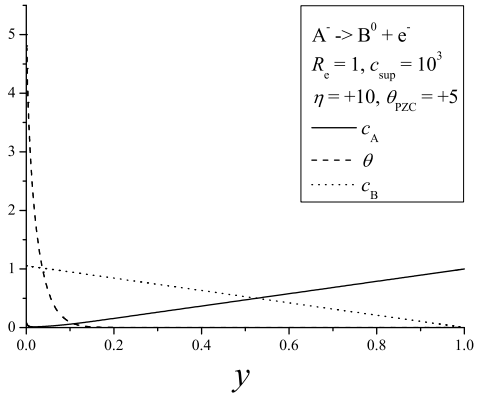

Figure 10.24: Concentration and potential profiles for the oxidation of A^- to B^0 at a nanoelectrode, with full electrolytic support.

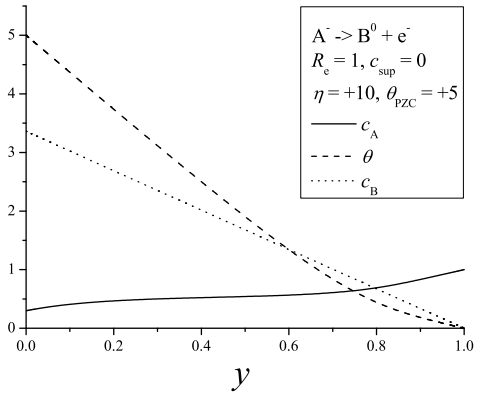

Figure 10.25: Concentration and potential profiles for the oxidation of A^- to B^0 at a nanoelectrode, with zero added electrolytic support.

electrode. The negligible concentration gradient of species A for $y < 0.7$ shows that the transport of A is predicted to be almost entirely due to migration in the range of about 30 nm from the electrode surface where charge separation is largely unconstrained.

The effects of electrode size upon Faradaic current are complex and particularly difficult to relate to the double layer structure as predicted in the absence of electrolysis. For example, on the basis of the elevated charge density on a nanoelectrode due to the curvature of the double layer, discussed in Section 5.7, the overpotential at a given distance is increased for a nanoelectrode compared to a larger electrode. An exemplar potential profile for the equilibrium diffuse double layer in the absence of electrolysis

is shown at Figure 10.26, for $\theta_0 = +5$ at two different nanoelectrode sizes and with an electrolyte concentration of $C^* = 1$ mM. A size-dependent difference is observed, implying a more powerful driving force for electrolysis for the smaller electrode, because the potential drop from the electrode to solution in the outer tunnelling region is greater.

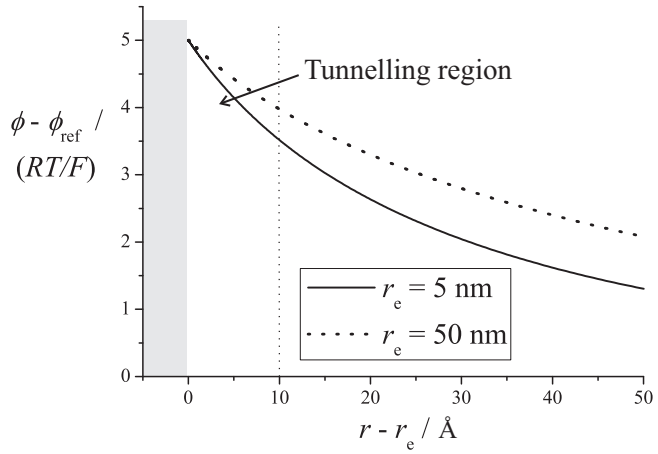

Figure 10.26: Simulated potential profile in the diffuse double layer for $\theta_0 = +5$ and $C^* = 1$ mM, comparing $r_e = 5$ and 50 nm.

This might suggest that for quasi-reversible cases, the Frumkin correction is more easily mitigated for smaller electrodes, and the steady-state current subject to distance-dependent electron transfer is larger for smaller electrodes. However, this trend does not arise clearly in simulation: rather, the relative normalised steady-state current as a function of electrode size depends on the charge of the reacting species and the excess charge on the electrode, in a complex manner.

This inadmissability of arguments based on diffuse double layer structure in the absence of electrolysis arises specifically in the case of nanoelectrode voltammetry because the diffuse double layer and depletion layer cannot be decoupled. Therefore, the distribution of the additional charge introduced into solution due to the passage of Faradaic current is fundamental to controlling charge transport in the depletion

layer, and hence the limiting current drawn at a nanoelectrode. This uncompensated charge is predicted to either elevate or reduce steady-state currents depending on the interaction of electrode excess charge and the solution charge generated by electrolysis.

10.7 Activity effects

The results presented above predict significant deviations from sigmoidal steady-state voltammetry for a range of systems. The Faradaic current may be limited either by a Levich exclusion effect where depletion of the reactant in the double layer limits the flux, or by a Frumkin effect where the potential dependence of the transition state slows the apparent kinetics of the reaction. Both effects are mitigated to some extent by distance-dependent electron transfer, and with nanoelectrodes, entirely different behaviour may be observed.

These theories are based on the assumption of unit activity coefficients, however. The concentrations of ions are unconstrained in the theoretical model, and due to the exponential dependence of the Boltzmann equation, the predicted concentration of the support species may reach unrealistic values. For instance, if 1 M support is assumed ($c_{\mathrm{sup}} = 1000$), then for $\eta = 10$ and $\theta_{\mathrm{pzc}} = -10$, the predicted surface concentration of X^- is approximately 5×10^8 M, which is altogether unreasonable due to finite ion size and electrostriction of solvent.

10.7.1 Theoretical model

To account for this inaccuracy and to determine whether the various double layer effects may still be observed under conditions where extreme concentrations are not permitted,

activity will be treated empirically using the Robinson–Stokes equation,[27] in which the stabilisation of ions by the Debye-Hückel ionic atmosphere effect and the destabilisation of all solution species by electrostriction and related effects are accounted for by an activity coefficient (γ_i) of the following form:

$$\ln \gamma_i = \frac{-Az_i^2\sqrt{I}}{1 + B_i\sqrt{I}} + m_i I \tag{10.60}$$

where the ionic strength I has been taken in dimensionless units as:

$$I = \frac{1}{2}\sum_k z_k^2 c_k \tag{10.61}$$

and so the constants A, B_i and m_i are normalised appropriately.

Recalling Equation 1.29 the Nernst–Planck equation can be framed in the general normalised form:

$$j_i = c_i \nabla \frac{\mu_i}{RT} \tag{10.62}$$

where μ_i is the chemical potential, and so:

$$j_i = D_i' \left(\nabla c_i + z_i c_i \nabla\theta + \frac{\partial \ln \gamma_i}{\partial I} c_i \nabla I \right) \tag{10.63}$$

where I is normalised ionic strength:

$$I = \frac{1}{2}\sum_i z_i^2 c_i \tag{10.64}$$

This accounts for the influence of ionic strength gradients on mass transport, due to differential stablilisation at different ionic strengths.

10.7.2 Double layer structure

The effect of activity upon the structure of the diffuse double layer can be considered by solving for above equation at zero flux for a monovalent inert salt M^+X^-, by analogy for

the work using the ideal solution approximation reported in Chapter 5. The following representative parameters were used for both M^+ and X^-, assuming 1 M concentration in bulk: $A = 1.17$, $B = 0.95$, $m = 0.25$. As expected, the surface charge density in the diffuse double layer is limited by the electrostriction effect, such that both the double layer charge and the differential capacitance are found to be much less than predicted from the Gouy–Chapman theory, in which the charge density is unconstrained.

Figure 10.27 illustrates the difference in the potential profile in the double layer when the Robinson–Stokes equation is incorporated into the Poisson–Boltzmann equation. The simulation here assumed $C^* = 1$ M and $R_e = 100$, with $\theta_0 = +10$. Note that the Debye length is unchanged, and so the distance over which the surface charge is compensated is similar. However, the total charge in the double layer is greatly reduced, and the electric field is much less extreme within one Debye length of the electrode surface.

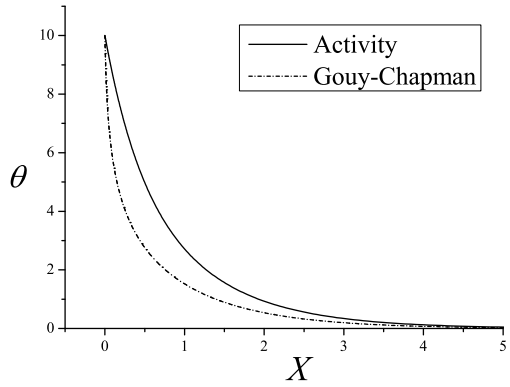

Figure 10.27: Simulated potential profiles for the diffuse double layer with $R_e = 100$ and $\theta_0 = 10$, comparing the normal Gouy–Chapman result with a simulation invoking activity effects according to the Robinson–Stokes equation.

10.7.3 Voltammetry

Having established that the double layer structure differs markedly when activity effects are considered, a comprehensive study was performed as above. The three cases of $z_{\mathrm{A}} = -1$, 0, and +1 were considered for $-5 \leq \theta_{\mathrm{pzc}} \leq +5$ and $-10 \leq \eta \leq +10$, subject to both the Nernst and Butler–Volmer equations. All species were assumed to obey the Robinson–Stokes equation with the same parameters given above, with respect to a reference concentration of 1 M.

The necessary re-formulation of the Nernst equation to take into account non-ideality is given below:

$$c_{\mathrm{A}} - c_{\mathrm{B}}\, \mathrm{e}^{\Delta\mu} = 0 \tag{10.65}$$

where

$$\Delta\mu = -(\eta - n\theta) + \ln \gamma_{\mathrm{B}} - \ln \gamma_{\mathrm{A}} \tag{10.66}$$

at the point in solution where the equation is applied.

On the assumption that the ionic strength dependence of the transition state energy follows the same linear relationship with α' as the potential dependence, a non-ideal Butler–Volmer equation can also be constructed:

$$c_{\mathrm{A}} - c_{\mathrm{B}}\mathrm{e}^{\Delta\mu} - \frac{j_{\mathrm{A}}}{K^0}\, \mathrm{e}^{-\alpha'\Delta\mu} = 0 \tag{10.67}$$

The Nernst–Planck equation with activity can be solved using the same Newton–Raphson method with finite differencing as described above, in Section 10.2.5.

The results showed that Levich and Frumkin effects are observed in steady-state voltammetry even where the effects of activity were considered, although the effects were qualitatively altered in some cases. For example, the Levich exclusion effect for

Nernstian voltammetry with $z_A = +1$ occurs to a different extent depending on the support ratio, as shown in Figure 10.28.

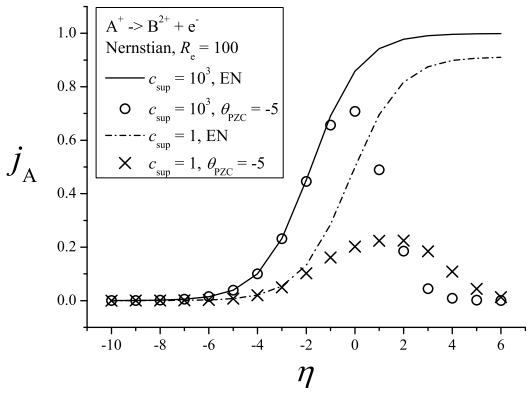

Figure 10.28: Simulated steady-state voltammetry for a microelectrode using the Robinson–Stokes equation; $R_e = 100$, $z_A = 1$. The extent of the Levich exclusion effect resulting from a double layer with $\theta_{pzc} = -5$ alters as a function of the support ratio.

The shift of the half-wave potential as a function of support ratio results from the dependence of the formal potential $E_f^{\ominus}$ upon ionic strength, whereas the difference in limiting current under the electroneutrality approximation occurs because of the well understood repulsive migration effect discussed in Section 10.3.2. Further, the change of ionic strength between the high and low support regimes alters the degree of exclusion of A, since both Coulombic repulsion and electrostriction of the solvent by the support species contribute to the exclusion of A^+ from the diffuse double layer. Note that the positive shift of the weakly supported voltammetry means that the current is significantly lower at the potential where Levich exclusion affects the limiting current, which is quite similar in both cases.

Additionally, a Levich exclusion effect is observed at high overpotential even when $z_A = 0$, because A^0 is excluded from the double layer by the destabilising effect of high ionic strength caused by a non-zero m_A in Equation 10.60. This is illustrated in Figure 10.29.

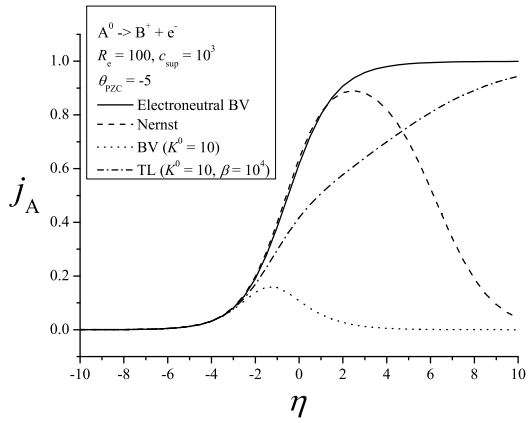

Figure 10.29: Simulated steady-state voltammetry for a microelectrode using the Robinson–Stokes equation with full support and hence high ionic strength; $R_\mathrm{e} = 100$, $z_\mathrm{A} = 0$, and $c_\mathrm{sup} = 10^3$. By comparing the electroneutral solution with a double layer with $\theta_\mathrm{pzc} = -5$ under different kinetic regimes, we see that both Levich exclusion and Frumkin effects are observed.

This effect is necessarily less marked at low ionic strength. Hence, a Frumkin effect with a constant limiting current, as expected in all cases for $z_\mathrm{A} = 0$ in the extreme of a highly positively charged electrode with an ideal solution, was not observed when the Robinson–Stokes equation was applied, even at low support where the ionic strength effects are less extreme (Figure 10.30).

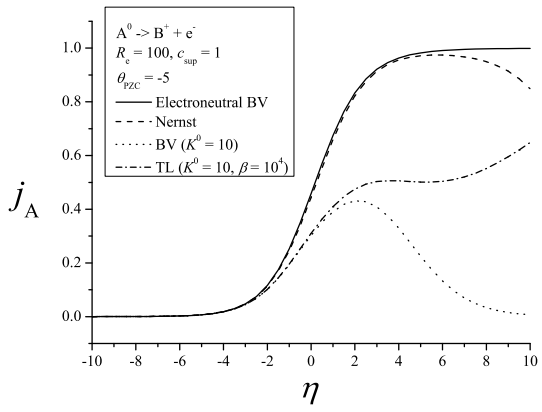

Figure 10.30: Simulated steady-state voltammetry for a microelectrode using the Robinson–Stokes equation with low support and hence low ionic strength; $R_\mathrm{e} = 100$, $z_\mathrm{A} = 0$, $c_\mathrm{sup} = 1$, and $\theta_\mathrm{pzc} = -5$. Compared to the fully supported case, the Levich and Frumkin effects are weaker, since the ionic strength is less extreme.

By substitution of the Boltzmann equation for an equilibrated diffuse double layer

into the Butler–Volmer equation, a Frumkin correction including activity can be derived. It takes the general form:

$$K^0_{\text{app}} = K^0 \frac{c_{\text{A,0}}}{c_{\text{A,EN}}} \exp\left(-\alpha'(n\theta_0 + \ln\frac{\gamma_{\text{B,0}}}{\gamma_{\text{A,0}}} - \ln\frac{\gamma_{\text{B,EN}}}{\gamma_{\text{A,EN}}})\right) \tag{10.68}$$

This indicates the increased complexity of the Frumkin effect when activity is considered.

The incorporation of tunnelling is able to overcome the Levich and Frumkin effects, just as for the case of an ideal solution (Figure 10.29). As before, the plane of electron transfer moves away from the electrode wherever the current was altered by the distance-dependent electron transfer. Strikingly non-sigmoidal voltammetry is also observed, due to the interplay of the different effects noted (Figure 10.30).

The extent to which the Levich and Frumkin effects can be mitigated by tunnelling is in fact less than the ideal solution case. This can be understood because tunnelling is only helpful in overcoming the Frumkin or Levich effects where either the depletion of c_{A} or the relative chemical potentials of A and B are markedly altered within the tunnelling distance of the electrode surface. Since the electric field in the double layer is damped by the electrostriction effect, the potential and double layer composition differ less between the outer Helmholtz plane and the outermost plane of electron transfer with tunnelling than would be the case for a model involving an 'ideal solution'.

10.8 Correlation to experimental data

Given the range of deviations from normal sigmoidal steady-state voltammetry predicted by theories based on the Nernst–Planck equations, it is relevant to consider whether any of these deviations have been observed in reported voltammetry. The

literature on the topic contains a diverse set of experiments that unfortunately lack clear trends.

In general, the extreme suppression of Faradaic current at high overpotential and the consequently peak-shaped voltammetry suggested for certain systems by Sections 10.3 and 10.4 have not been observed. This suggests that the role of the compact double layer, which is ignored in the theoretical model of this chapter, must then be significant in mitigating the influence of the diffuse component of the double layer upon the overall current, as has previously been suggested by He et al.[12] and as is indicated by the results of Norton et al.[16] The theoretical study by He et al. and later related works[12,14] report exclusively sigmoidal voltammetry even for the repulsive migration case, suggesting that the involvement of the compact layer at high excess charge is particularly important. Therefore, the results reported in this work represent an outer limit on behaviour due to the possibly reduced significance of the diffuse double layer under normal voltammetric conditions.

A loss of current at low support for nanoelectrodes has been reported by Chen et al.[28] for the reduction of hexaammineruthenium(III), which could arguably be attributed, at least in part, to the effect of the unscreened Coulomb potential, which would be markedly more significant at zero support than at high support due to the change in the Debye length. A similar effect has been reported for the reduction of hexachloroiridate(IV)[29] as well as the reverse reaction of this couple.[30] The effect was also noted for the ferri/ferrocyanide couple, but was exhibited in the microelectrode size range also, implying possible follow-up kinetics or the involvement of a surface reaction. A positive deviation from the expected current has been observed for the oxidation of the modified ferrocene species $FcTMA^+$ at nanoelectrodes.[30,31] This is consistent with

some predictions above concerning the case $z_A n > 0$, but the characteristically peaked voltammetry predicted by simulation is not observed in the experimental voltammetry.

Our simulation results suggest that the current with weak electrolytic support at a nanoelectrode can deviate either positively or negatively from the current expected at full support, depending on the value of θ_{pzc}, and, more generally, upon the distribution of charge in the double layer. It is perhaps not surprising in this case that both elevated and reduced limiting currents for low support at nanoelectrodes have been observed in the literature. The quantitative prediction of these results on a case-by-case basis is not yet feasible, however.

10.9 Conclusions

The full range of effects by which the diffuse double layer may influence steady-state Faradaic current have been discussed. The current at a given overpotential may depend upon the charge of the reactant, the direction of oxidation or reduction, the excess charge on the electrode which must be compensated by the diffuse double layer, the quantity of supporting electrolyte, and the electrode size.

Distinct behaviour is observed for the three cases where $z_A n < 0$, $z_A = 0$ and $z_A n > 0$. These three cases arise because increasing the thermodynamic overpotential to promote the passage of Faradaic current may cause the excess charge on the electrode to change in such a manner as to either attract or repel the electroactive species A, or neither, if it is uncharged.

An electrode excess charge which repels the reactant from the electrode may cause rate-limiting mass transport through the diffuse double layer, according to the the-

ory pioneered by Levich. Additionally, the apparent kinetics are altered according to the Frumkin correction. The alteration of the diffuse double layer arising from the non-ideality of the solution was considered by simulation, and is not predicted to significantly affect these conclusions. For $z_{\mathrm{A}}n < 0$, apparent electrode kinetics are accelerated with increasing overpotential and therefore the effect is not noticeable. By contrast, for $z_{\mathrm{A}} = 0$ or $z_{\mathrm{A}}n > 0$, the apparent electrode kinetics are decelerated with increasing overpotential, leading to decreased or near-zero limiting current.

For nanoelectrodes at low support where the diffuse double layer is of comparable size to the depletion layer, the theory based on the Nernst–Planck–Poisson equations predicts a complete change the waveshapes and magnitude of the observed voltammetry, due to the influence of unscreened charge. Limiting currents may be either increased or decreased depending on the particular excess charge on the electrode. The inclusion of distance-dependent electron transfer into the theoretical model is able to mitigate both the Frumkin and Levich effects, especially at higher support ratio where the Debye length is short. This is because both of these effects arise due to the presence of the diffuse double layer, and specifically with respect to limitations on charge transport through the double layer. Therefore, if it is possible for electron transfer to occur outside the double layer, or at least a substantial part of it, these effects do not constrain Faradaic current. So, it is reasonable to hypothesise that tunnelling is significant to the observation of normal sigmoidal steady-state voltammetry at microelectrodes.

The compact double layer is likely to play an additional, significant role in alleviating diffuse double layer effects, by reducing the excess potential at the outer Helmholtz plane, as has been indicated by previous studies.[12,16] Such an effect is implied by the absence of peak-shaped steady-state voltammetry in the experimental literature.

The work reported in this chapter was not intended to construct an exact model to describe the passage of Faradaic current between an electrode and the neighbouring solution. Rather, certain idealisations of the double layer structure and the kinetics of electron transfer were assumed, in order to determine the perturbation of voltammetric behaviour that is specifically due to the diffuse double layer, under diverse conditions and subject to different assumptions. This should provide a guide to future experimentation in terms of behaviour attributable to the diffuse double layer, as well as identifying situations where voltammetry is influenced by other structural features of the electrode-solution interface.

In particular, this work reveals that charge transport on the local Debye scale is able to affect the observable behaviour of macroscopic, predominantly electroneutral systems by limiting the rate of charge transport and electron transfer. This is exemplified by the Levich and Frumkin effects in steady-state voltammetry. The requirement of bulk electroneutrality certainly constrains the dynamic behaviour of systems involving charge separation, such as a developing liquid junction (Chapter 4), a charging diffuse double layer (Chapter 6), or macroelectrode cyclic voltammetry (Chapter 9). Equally, the thermodynamics and kinetics of local regions of charge separation can themselves control the rate of charge transport through the electrolytic solution in an electrochemical cell.

Bibliography

[1] E. J. F. Dickinson and R. G. Compton, *J. Electroanal. Chem.*, 2011, **661**, 198–212.

[2] E. J. F. Dickinson and R. G. Compton, *J. Phys. Chem. C*, 2009, **113**, 17585–17589.

[3] E. J. F. Dickinson, J. G. Limon-Petersen and R. G. Compton, *J. Solid State Electrochem.*, 2011, **15**, 1335–1345.

[4] E. J. F. Dickinson and R. G. Compton, *Chem. Phys. Lett.*, 2010, **497**, 178–183.

[5] L. G. Gouy, *C. R. Hebd. Séances Acad. Sci.*, 1909, **149**, 654–657.

[6] D. L. Chapman, *Philos. Mag.*, 1913, **25**, 475–481.

[7] O. Stern, *Z. Elektrochem.*, 1924, **30**, 508–516.

[8] R. W. Murray, *Chem. Rev.*, 2008, **108**, 2688–2720.

[9] S. R. Belding, F. W. Campbell, E. J. F. Dickinson and R. G. Compton, *Phys. Chem. Chem. Phys.*, 2010, **12**, 11208–11221.

[10] W. Hyk, M. Palys and Z. Stojek, *J. Electroanal. Chem.*, 1996, **415**, 13–22.

[11] A. Bonnefont, F. Argoul and M. Z. Bazant, *J. Electroanal. Chem.*, 2001, **500**, 52–61.

[12] R. He, S. Chen, F. Yang and B. Wu, *J. Phys. Chem. B*, 2006, **110**, 3262–3270.

[13] X. Yang and G. Zhang, *Nanotechnology*, 2007, **18**, 335201/1–335201/9.

[14] Y. Liu, R. He, Q. Zhang and S. Chen, *J. Phys. Chem. C*, 2010, **114**, 10812–10822.

[15] Y. Liu, Q. Zhang and S. Chen, *Electrochim. Acta*, 2010, **55**, 8280–8286.

[16] J. D. Norton, H. S. White and S. W. Feldberg, *J. Phys. Chem.*, 1990, **94**, 6772–6780.

[17] C. P. Smith and H. S. White, *Anal. Chem.*, 1993, **65**, 3343–3353.

[18] K. B. Oldham and A. M. Bond, *J. Electroanal. Chem.*, 2001, **508**, 28–40.

[19] I. Streeter and R. G. Compton, *J. Phys. Chem. C*, 2008, **112**, 13716–13728.

[20] V. Levich, *Dokl. Akad. Nauk SSSR*, 1949, **67**, 309–312.

[21] A. Frumkin, *Z. Physik. Chem.*, 1933, **164A**, 121–133.

[22] P. P. Edwards, H. B. Gray, M. T. J. Lodge and R. J. P. Williams, *Angew. Chem., Int. Ed.*, 2008, **47**, 6758–6765.

[23] S. W. Feldberg, *J. Electroanal. Chem.*, 1986, **198**, 1–18.

[24] R. A. Marcus and P. Siders, *J. Phys. Chem.*, 1982, **86**, 622–630.

[25] D. J. Gavaghan and S. W. Feldberg, *J. Electroanal. Chem.*, 2000, **491**, 103–110.

[26] R. J. White and H. S. White, *Langmuir*, 2008, **24**, 2850–2855.

[27] R. A. Robinson and R. H. Stokes, *Electrolyte Solutions*, Butterworths Publications Ltd., London, 1955.

[28] S. Chen and A. Kucernak, *Electrochem. Commun.*, 2002, **4**, 80–85.

[29] S. Chen and A. Kucernak, *J. Phys. Chem. B*, 2002, **106**, 9396–9404.

[30] J. Watkins and H. White, *Langmuir*, 2004, **20**, 5474–5483.

[31] J. L. Conyers and H. S. White, *Anal. Chem.*, 2000, **72**, 4441–4446.

Conclusion

Mathematical and numerical solutions to the Nernst–Planck–Poisson equation set have been used to study solution-phase charge transport in three types of electrochemical system.

In a liquid junction, a concentration gradient causes charge separation, which engenders a potential difference in the solution. The charge separation decays with continuing diffusion as electroneutrality is restored following the Debye time, but the dynamics of the system cause the potential difference to remain constant.

For an ideally polarisable electrode, a potential difference is applied across the cell to force an equilibrium condition with charge separation, which is contained in a diffuse double layer with a spatial extent parameterised by the Debye length. The dynamics of the contraction of the electric field to this region, and hence double layer formation, depend on the conductivity of the solution and become non-linear if the applied potential is large.

For cyclic voltammetry at a charged working electrode, the diffuse double layer can be ignored and electroneutrality is a good approximation wherever the electrode is large and double layer effects are not rate-limiting. However, uncompensated charge separation within a few Debye lengths of the working electrode may still radically alter

the maximum rate of charge transport and the kinetics of electron transfer. For nanoelectrodes, unscreened charge pervades the depletion layer and so the diffuse double layer is intrinsic to mass transport.

These observations suggest some general features of charge transport in electrolytic solutions. It is clear that the equilibrium condition of an electrolytic solution is electroneutral, with equal concentrations of positive and negative ions, unless there is some boundary where the application of an electric field induces charge separation. In this case, the charge separation is confined to a diffuse double layer which screens the electric field within a distance of a few Debye lengths, which is a distance of tens of nanometres for a typical system. Where an electrode is of comparable size to the Debye length, the equilibrium structure of the double layer is altered.

Both the liquid junction and capacitive charging experiments involve a rapid perturbation away from equilibrium. In both cases, electroneutrality dictates dynamics after a Debye time scale, which is the time scale of diffusion or migration across the diffuse double layer. Because the liquid junction system contains an infinite quantity of bulk solution, equilibrium cannot be achieved in finite time, and therefore exact electroneutrality is never recovered. By contrast, the capacitive charging experiment can attain its equilibrium since it involves a finite double layer at a fixed boundary, and therefore capacitive charging current decays exponentially, whereas ionic current in a liquid junction decays proportionally to the rate of diffusion.

The cyclic voltammetry experiment involves a slow perturbation of electrode kinetics with respect to the Debye time. Therefore charge transport can be described using the electroneutrality or zero-field approximtion, and the diffuse double layer can be ignored, unless it limits the rate of mass transport or electron transfer. In the latter

case, it is generally accurate to treat the double layer as internally equilibrated, such that the Levich and Frumkin effects can be parameterised: the diffuse double layer acts as an infinitesimal boundary to an electroneutral system. Again, an important exception arises if the electrode scale becomes comparable to the Debye length, for which novel nanoelectrode effects are predicted.

These ideas can be summarised as follows:

1. The equilibrium of an electrolytic solution is electroneutral except on a Debye length scale away from a boundary where charge separation is induced.

2. A perturbation away from equilibrium which is rapid compared to the Debye time tolerates non-equilibrium charge separation at times less than the Debye time.

3. Once a depletion layer has extended a long distance from a point of perturbation, compared to the Debye length, electroneutrality dictates charge transport. Equally, electroneutrality dictates charge transport outside regions of equilibrium charge separation, after a Debye time scale following perturbation.

4. Equilibrium can be recovered in finite time only if the the system has been perturbed only across a finite domain. This requires at least one fixed boundary.

5. A perturbation away from equilibrium which is slow compared to the Debye time allows the approximation of a boundary layer across a Debye length scale. The boundary layer is at equilibrium and tolerates charge separation; outside the boundary layer, charge transport is controlled by electroneutrality.

6. A system in which a fixed scale is comparable to the Debye length, such as a na-

noelectrode, has a complex interaction of charge transport with other properties and does not obey the generalisations above.

It is hoped that the trends discussed here can act as a guide for the future experimental and theoretical investigation of charge transport.

The versatility of the combination of the numerical finite difference method with the Nernst–Planck–Poisson equation set has been demonstrated. In certain cases the difficulty of solving these equations numerically has required the refinement of the numerical approach with guidance from physical intuition. Numerical solution allows the avoidance of approximations that may be inappropriate, and provides data from which system trends can be readily inferred. Therefore, this methodology is a practical approach for the theoretical investigation of charge transport dynamics in electrochemistry. Since the theories presented here have been inferred from particular electrochemical systems, their extension to other more elaborate systems is a logical direction for future research.

Glossary

Roman symbols

Symbol	Definition	Unit
A	area	m^2
A	Debye-Hückel constant = 0.509 $\mathrm{mol}^{-\frac{1}{2}}$ $\mathrm{kg}^{\frac{1}{2}}$	
a_i	activity of species i	
C_d	capacitance	F
C'_d	capacitance per unit area	F m^{-2}
C_i	concentration of species i	mol dm^{-3}
$C_{i,0}$	surface concentration of species i	mol dm^{-3}
C^*	bulk concentration	mol dm^{-3}
c_i	normalised concentration	
c_i^*	normalised bulk concentration	
c_sup	support ratio	
D	diffusion coefficient	(c)m^2 s^{-1}
D'	normalised diffusion coefficient	
E	applied cell potential	V
$E^\ominus$	standard reduction potential	V
$E_\mathrm{f}^\ominus$	formal reduction potential	V
E_pzc	potential of zero charge	V
ΔE_pp	peak-to-peak separation	V
e	the charge on an electron = 1.602×10^{-19} C	
F	the Faraday constant = 96485.3 C mol^{-1}	
G	Gibbs energy	J
$\Delta G^\ominus$	change in Gibbs energy under standard conditions	J mol^{-1}

$\Delta G^{\ddagger}$	activation energy	J mol^{-1}
H	enthalphy	J mol^{-1}
i	current	A
i_{pf}	forward peak current	A
I	ionic strength	mol m^{-3}
$\mathbf{J}$	flux vector	mol m^{-2} s^{-1}
j	normalised current	
j_{cap}	normalised capacitive current	
K^0	normalised heterogeneous rate constant	
K'_{d}	normalised capacitance per unit area	
k^0	Butler–Volmer heterogeneous rate constant	(c)m s^{-1}
k	the Boltzmann constant = 1.381×10^{-23} J K^{-1}	
n	number of electrons transferred in the oxidative direction	
n	number of moles (Chapter 1)	
P_{s}	normalised solution resistance	
p	pressure	bar
$p^{\ominus}$	standard pressure = 1 bar	
Q'	charge per unit area	C m^{-2}
q	charge	C
q	radial transform of normalised conductivity	
R	the gas constant = 8.31447 J K^{-1} mol^{-1}	
R_{e}	ratio of electrode radius to Debye length, = $r_{\mathrm{e}}/x_{\mathrm{D}}$	
R_{s}	computational: switching point of an expanding grid	
R_{s}	physical: solution resistance	Ω
r	radial space coordinate	m
r_{e}	electrode radius	m
S	entropy	J K^{-1} mol^{-1}
T	temperature	K
t	time	s
t_{D}	Debye time	s
u	inverse normalised time (Chapter 4)	
u	radial transform of normalised charge separation (Chapter 6)	
V	volume	m^3

v	voltammetric scan rate	V s^{-1}
X	normalised linear space coordinate	
X_s	switching point of an expanding grid	
x	linear space coordinate	m
x_D	Debye length	m
Z	normalised complex impedance	
z	Boltzmann transform coordinate	
z_i	charge number of species i	

Greek symbols

Symbol	Definition	Unit
α	Butler-Volmer transfer coefficient for reduction	
α'	transfer coefficient in direction of reaction	
β	normalised tunnelling decay constant	
β'	tunnelling decay constant	m^{-1}
γ_i	activity coefficient of species i	m^3 mol^{-1}
γ_R	grid expansion coefficient (radial space)	
γ_X	grid expansion coefficient (linear space)	
γ_τ	grid expansion coefficient (time)	
δ	composite diffusion coefficient	
ϵ_0	the permittivity of free space = 8.854×10^{-12} F m−1	
ϵ_s	relative permittivity or dielectric constant of a solvent	
η	normalised electric field on the Boltzmann scale (Chapter 4)	
η	normalised overpotential (Chapters 7–10)	
$\Delta\eta_{pp}$	normalised peak-to-peak separation	
θ	normalised potential	
θ_0	normalised electrode surface potential	
θ_{EN}	potential at the outer edge of the double layer	
θ_{PZC}	normalised potential of zero charge	
$\Delta\theta_{LJP}$	normalised liquid junction potential	
$\Delta\theta_{OD}$	normalised ohmic drop	
κ_e	$\equiv \sqrt{R_e}$	

Λ	the Matsuda-Ayabe parameter	
μ_i	chemical potential of species i	J mol^{-1}
Π	osmotic pressure	N m^{-2}
ρ	charge density	C m^{-3}
σ	normalised conductivity	
σ	normalised voltammetric scan rate	
τ	normalised time	
τ_{PT}	time grid points per unit η	
τ_{s}	switching point of an expanding time grid	
ϕ	potential	V
ϕ_{m}	potential of an electrode	V
ϕ_{ref}	potential of the reference electrode	V
ϕ_{s}	potential of the solution phase	V
ϕ_{w}	potential of the working electrode	V
$\Delta\phi_{\mathrm{OD}}$	ohmic drop	V
χ	radial transform of normalised potential	

Abbreviations

erf(x)	the error function
NPP	Nernst–Planck–Poisson
sgn(x)	the sign function
$\ominus$	standard state
*	standard quantity for normalisation
‡	transition state
$^-$	Laplace transform
$'$	per unit area
$'$	variable of integration

Unusual or foreign journal abbreviations

Ann. Phys.	Annalen der Physik (1900–)

Ber. Kgl. Pr. Akad. Wiss.	Sitzungsberichte der Königlich Preußischen Akademie der Wissenschaften zu Berlin
Coll. Czech. Chem. Commun.	Collection of Czechoslovak Chemistry Communications
C. R. Hebd. Séances Acad. Sci.	Comptes Rendus Hebdomadaires des Séances de l'Académie des Sciences
Dokl. Akad. Nauk SSSR	Doklady Akademii Nauk SSSR (Proceedings of the USSR Academy of Sciences)
J. ACM	Journal of the ACM (Association for Computing Machinery)
J. Gen. Physiol.	Journal of General Physiology
Physik. Z.	Physikalische Zeitschrift
Pogg. Ann.	Annalen der Physik und Chemie (1824–1876, ed. Poggendorff)
Wied. Ann.	Annalen der Physik und Chemie (1877–1899, ed. Wiedemann)
Z. Elektrochem	Zeitschrift für Elektrochemie
Z. Physik. Chem.	Zeitschrift für Physikalische Chemie

Appendix A

Diagonal matrix equations

A set of n coupled simultaneous linear equations can be expressed in matrix form as

$$\mathbf{A}\mathbf{x} = \mathbf{z} \tag{A.1}$$

where the matrix of coefficients $\mathbf{A}$ is a square matrix of size n, and $\mathbf{x}$ and $\mathbf{z}$ are vectors of size n, where $\mathbf{x}$ contains unknowns and $\mathbf{z}$ contains known coefficients.

The matrix element in the ith row and jth column of $\mathbf{A}$ is conventionally denoted a_{ij}.

The process of LU decomposition writes the matrix $\mathbf{A}$ as the product of lower and upper triangular matrices, $\mathbf{L}$ and $\mathbf{U}$:

$$\mathbf{A} = \mathbf{L}\,\mathbf{U} \tag{A.2}$$

where $l_{ij} = 0$ for $i < j$, $l_{ij} = 1$ for $i = j$, and $u_{ij} = 0$ for $i > j$.

Hence

$$\mathbf{A}\mathbf{x} = \mathbf{L}(\mathbf{U}\mathbf{x}) = \mathbf{L}\mathbf{y} = \mathbf{z} \tag{A.3}$$

because matrix multiplication is associative.

From the rules of matrix multiplication:

$$a_{ij} = \sum_{k=0}^{n-1} l_{ik} u_{kj} \tag{A.4}$$

Given the distribution of zeroes in **L** and **U**, $l_{ik} \neq 0$ only where $k \leq i$, and $u_{kj} \neq 0$ only where $k \leq j$. Therefore:

$$\begin{aligned} j < i \qquad & a_{ij} = \sum_{k=0}^{j} l_{ik} u_{kj} \\ j \geq i \qquad & a_{ij} = \sum_{k=0}^{i} l_{ik} u_{kj} \end{aligned} \tag{A.5}$$

Now, let us assume that the matrix **A** is diagonal. Hence, the matrices **L** and **U** are also diagonal. If the matrix has $2q + 1$ diagonals, these can be enumerated from 0 to $2q$ with q denoting the central diagonal. Therefore, $l_{ik} \neq 0$ only if $k - i + q \geq 0$, i.e. if $k \geq i - q$. Equally, $u_{kj} \neq 0$ only if $j - k + q \leq 2q$, i.e. if $k \geq j - q$.

If $i, j \geq q$:

$$\begin{aligned} j < i \qquad & a_{ij} = \sum_{k=i-q}^{j} l_{ik} u_{kj} \\ j \geq i \qquad & a_{ij} = \sum_{k=j-q}^{i} l_{ik} u_{kj} \end{aligned} \tag{A.6}$$

and otherwise

$$\begin{aligned} j < i, \quad i < q \qquad & a_{ij} = \sum_{k=0}^{j} l_{ik} u_{kj} \\ j \geq i, \quad j < q \qquad & a_{ij} = \sum_{k=0}^{i} l_{ik} u_{kj} \end{aligned} \tag{A.7}$$

Now, in order to consider the diagonal matrix, we introduce a notation $a_{f,g}$ to denote the element in the f-th diagonal and g-th row. Hence:

$$f = (j - i) + q \tag{A.8}$$

$$g = i \tag{A.9}$$

In this notation, it follows that for $g \geq q$ and $f + g \geq 2q$:

$$\begin{aligned} f < q \qquad a_{fg} &= \sum_{k=g-q}^{f+g-q} l_{g,k-g+q} u_{k,f+g-k} \\ f \geq q \qquad a_{fg} &= \sum_{k=f+g-2q}^{g} l_{g,k-g+q} u_{k,f+g-k} \end{aligned} \tag{A.10}$$

and otherwise

$$\begin{aligned} f < q, \quad g < q \qquad a_{ij} &= \sum_{k=0}^{f+g-q} l_{g,k-g+q} u_{k,f+g-k} \\ f \geq q, \quad f + g < 2q \qquad a_{ij} &= \sum_{k=0}^{g} l_{g,k-g+q} u_{k,f+g-k} \end{aligned} \tag{A.11}$$

Introducing the substitution:

$$k' = k - g + q \tag{A.12}$$

it then follows that

$$\begin{aligned} f < q \qquad a_{fg} &= \sum_{k'=0}^{f} l_{k',g} u_{f+q-k',k'+g-q} \\ f \geq q \qquad a_{fg} &= \sum_{k'=f-q}^{q} l_{k',g} u_{f+q-k',k'+g-q} \end{aligned} \tag{A.13}$$

and otherwise

$$\begin{aligned} f < q, \quad g < q \qquad a_{fg} &= \sum_{k'=q-g}^{f} l_{k',g} u_{f+q-k',k'+g-q} \\ f \geq q, \quad f + g < 2q \qquad a_{fg} &= \sum_{k'=q-g}^{q} l_{k',g} u_{f+q-k',k'+g-q} \end{aligned} \tag{A.14}$$

These equations have the property that the equation for the outermost diagonals $f = 0$ and $f = 2q$ have only one term. Then the equations in $f = 1$ and $f = 2q - 1$ have two terms, and so on to $f = q$ which has $q + 1$ terms. Excluding the term containing l_{fg} or

u_{fg} as appropriate, the equations have $q - |f - q|$ terms.

The interdependency of the equations can also be considered. From analysis of the above equations, it is found that the equation a_{fg} contains no terms containing elements of $\mathbf{L}$ or $\mathbf{U}$ with *both* the diagonal greater than f and the row greater than g. Also, for $f < q$, the equations do not depend on upper matrix elements for $g \geq f+g-q$. Now, $f + g - q = i$, which is the column number, so the g-th row only is required to solve for the g-th column.

Considering that the last term in each equation contains an unknown value at the point fg, it can be removed from the sums, as:

$$\sum_{k'}^{f} l_{k',g} u_{f+q-k',k'+g-q} = l_{f,g} u_{q,g+f-q} + \sum_{k'}^{f-1} l_{k',g} u_{f+q-k',k'+g-q} \tag{A.15}$$
$$\sum_{k'}^{q} l_{k',g} u_{f+q-k',k'+g-q} = u_{f,g} + \sum_{k'}^{q-1} l_{k',g} u_{f+q-k',k'+g-q}$$

since $l_{q,g} = 1$ from definition. Then:

$$f < q \qquad l_{fg} = \left(a_{fg} - \sum_{k'=0}^{f-1} l_{k',g} u_{f+q-k',k'+g-q} \right) / u_{q,g+f-q} \tag{A.16}$$
$$f \geq q \qquad u_{fg} = a_{fg} - \sum_{k'=f-q}^{q-1} l_{k',g} u_{f+q-k',k'+g-q}$$

and otherwise

$$f < q, \quad g < q \qquad l_{fg} = \left(a_{fg} - \sum_{k'=q-g}^{f-1} l_{k',g} u_{f+q-k',k'+g-q} \right) / u_{q,g+f-q} \tag{A.17}$$
$$f \geq q, \quad f + g < 2q \qquad u_{fg} = a_{fg} - \sum_{k'=q-g}^{q-1} l_{k',g} u_{f+q-k',k'+g-q}$$

Note that $g + f - q$ is not a function of k' and is kept constant for constant i, i.e. progression down a column.

Therefore, an appropriate order in which to solve the equations for the $\mathbf{L}$ and $\mathbf{U}$

matrices is from top-left to bottom right. First, the top-row is solved, then the left-hand column, and so on. Each row-column solution is termed a 'chevron' and n chevrons are solved down the matrix from top-left to bottom-right. The first $q-1$ chevrons have constraints since these contain elements where $i < q$ or $j < q$; the last $q-1$ chevrons exceed the matrix bounds and therefore also have special constraints.

Iterative solution methods for the equations $\mathbf{Ly} = \mathbf{z}$ and $\mathbf{Ux} = \mathbf{y}$ are found easily by inspection. In the former case, iteration begins at the top-left of the matrix $\mathbf{L}$ and proceeds downwards; in the latter case, iteration begins at bottom-right and proceeds upwards.

The relevant calculations to determine $\mathbf{y}$ are, for $g < q$:

$$y_g = z_g - \sum_{k'=q-g}^{q-1} l_{k',g} y_{k'+g-q} \tag{A.18}$$

and otherwise

$$y_g = z_g - \sum_{k'=0}^{q-1} l_{k',g} y_{k'+g-q} \tag{A.19}$$

which are iterated from $g = 1$ to $g = (n-1)$.

The relevant calculations to determine $\mathbf{x}$ are, for $g \geq (n-q)$:

$$x_g = \left(y_g - \sum_{k'=q+1}^{n-1-g+q} l_{k',g} x_{k'+g-q} \right) / u_{q,g} \tag{A.20}$$

and otherwise

$$x_g = \left(y_g - \sum_{k'=q+1}^{2q} l_{k',g} x_{k'+g-q} \right) / u_{q,g} \tag{A.21}$$

which are iterated from $g = n-1$ to $g = 0$.

The overall LU decomposition is $O(m^2 n)$ and the determination of the solution once the matrix is decomposed is $O(mn)$.

Appendix B

Debye–Falkenhagen equation: unequal diffusion coefficients

The solution of the hemispherical Debye–Falkenhagen equation will be presented here for unequal diffusion coefficients, following the terminology and notation used in Chapter 6.

In the case of unequal diffusion coefficients, it is helpful to normalise time as:

$$t^* = \frac{2x^{*2}}{D_\mathrm{A} + D_\mathrm{X}} \tag{B.1}$$

such that

$$\tau = \frac{(D_\mathrm{A} + D_\mathrm{X})t}{2r_\mathrm{e}x_\mathrm{D}} \tag{B.2}$$

Then by defining

$$\delta_i = \frac{2D_i}{(D_\mathrm{A} + D_\mathrm{X})} \tag{B.3}$$

the full Nernst–Planck–Poisson equations are:

$$\frac{\partial c_\mathrm{A}}{\partial \tau} = \delta_\mathrm{A}\left(\frac{1}{R^2}\frac{\partial}{\partial R}\left(R^2\left(\frac{\partial c_\mathrm{A}}{\partial R} + c_\mathrm{A}\frac{\partial \theta}{\partial R}\right)\right)\right) \tag{B.4}$$

$$\frac{\partial c_\mathrm{X}}{\partial \tau} = \delta_\mathrm{X}\left(\frac{1}{R^2}\frac{\partial}{\partial R}\left(R^2\left(\frac{\partial c_\mathrm{X}}{\partial R} - c_\mathrm{X}\frac{\partial \theta}{\partial R}\right)\right)\right) \tag{B.5}$$

$$\frac{1}{R^2}\frac{\partial}{\partial R}\left(R^2\frac{\partial\theta}{\partial R}\right)+\frac{1}{2}\kappa_{\mathrm{e}}^2(c_{\mathrm{A}}-c_{\mathrm{X}})=0 \tag{B.6}$$

with initial conditions for the potential step at $\tau = 0$:

$$c_{\mathrm{A}}=c_{\mathrm{X}}=1 \tag{B.7}$$

$$\theta=\frac{\theta_0\kappa_{\mathrm{e}}}{R} \tag{B.8}$$

and conditions as $R \to \infty$:

$$c_{\mathrm{A}}\to 1, \qquad c_{\mathrm{X}}\to 1 \tag{B.9}$$

$$\theta\to 0 \tag{B.10}$$

and conditions at $R = \kappa_{\mathrm{e}}$:

$$\frac{\partial c_{\mathrm{A}}}{\partial R}+c_{\mathrm{A}}\frac{\partial\theta}{\partial R}=0 \tag{B.11}$$

$$\frac{\partial c_{\mathrm{X}}}{\partial R}-c_{\mathrm{X}}\frac{\partial\theta}{\partial R}=0 \tag{B.12}$$

$$\theta=\theta_0 \tag{B.13}$$

As before we shall take the Debye–Falkenhagen limit and therefore make the linearising approximation:

$$c_{\mathrm{A}}\frac{\partial\theta}{\partial R}\approx c_{\mathrm{X}}\frac{\partial\theta}{\partial R}\approx\frac{\partial\theta}{\partial R} \tag{B.14}$$

Taking $\rho = c_{\mathrm{A}} - c_{\mathrm{X}}$ as before, and additionally defining $\sigma = c_{\mathrm{A}} + c_{\mathrm{X}}$:

$$\frac{\partial\sigma}{\partial\tau}=\frac{1}{R^2}\frac{\partial}{\partial R}\left(R^2\left(\frac{(\delta_{\mathrm{A}}+\delta_{\mathrm{X}})}{2}\frac{\partial\sigma}{\partial R}+\frac{(\delta_{\mathrm{A}}-\delta_{\mathrm{X}})}{2}\frac{\partial\rho}{\partial R}+(\delta_{\mathrm{A}}-\delta_{\mathrm{X}})\frac{\partial\theta}{\partial R}\right)\right) \tag{B.15}$$

$$\frac{\partial\rho}{\partial\tau}=\frac{1}{R^2}\frac{\partial}{\partial R}\left(R^2\left(\frac{(\delta_{\mathrm{A}}-\delta_{\mathrm{X}})}{2}\frac{\partial\sigma}{\partial R}+\frac{(\delta_{\mathrm{A}}+\delta_{\mathrm{X}})}{2}\frac{\partial\rho}{\partial R}+(\delta_{\mathrm{A}}+\delta_{\mathrm{X}})\frac{\partial\theta}{\partial R}\right)\right) \tag{B.16}$$

Noting that $\delta_{\mathrm{A}} + \delta_{\mathrm{X}} = 2$ and defining $\delta = (D_{\mathrm{A}} - D_{\mathrm{X}})/(D_{\mathrm{A}} + D_{\mathrm{X}})$:

$$\frac{\partial\sigma}{\partial\tau}=\frac{1}{R^2}\frac{\partial}{\partial R}\left(R^2\left(\frac{\partial\sigma}{\partial R}+\delta\frac{\partial\rho}{\partial R}\right)\right)-\delta\kappa_{\mathrm{e}}^2\rho \tag{B.17}$$

$$\frac{\partial \rho}{\partial \tau} = \frac{1}{R^2}\frac{\partial}{\partial R}\left(R^2\left(\frac{\partial \rho}{\partial R} + \delta\frac{\partial \sigma}{\partial R}\right)\right) - \kappa_{\mathrm{e}}^2\rho \tag{B.18}$$

$$\frac{1}{R^2}\frac{\partial}{\partial R}\left(R^2\frac{\partial \theta}{\partial R}\right) = -\frac{1}{2}\kappa_{\mathrm{e}}^2\rho \tag{B.19}$$

with $\sigma = 2$ and $\rho = 0$ at $\tau = 0$ and $R \to \infty$, and the following conditions at $R = \kappa_{\mathrm{e}}$:

$$\frac{\partial \sigma}{\partial R} = 0 \tag{B.20}$$

$$\frac{\partial \rho}{\partial R} + 2\frac{\partial \theta}{\partial R} = 0 \tag{B.21}$$

The spherical dependence of these linear equations can be removed as before by taking $q = R \cdot \sigma$, $u = R \cdot \rho$, and $\chi = R \cdot \theta$, such that:

$$\frac{\partial q}{\partial \tau} = \frac{\partial^2 q}{\partial R^2} + \delta\left(\frac{\partial^2 u}{\partial R^2} - \kappa_{\mathrm{e}}^2 u\right) \tag{B.22}$$

$$\frac{\partial u}{\partial \tau} = \delta\frac{\partial^2 q}{\partial R^2} + \frac{\partial^2 u}{\partial R^2} - \kappa_{\mathrm{e}}^2 u \tag{B.23}$$

$$\frac{\partial^2 \chi}{\partial R^2} + \frac{1}{2}\kappa_{\mathrm{e}}^2 u = 0 \tag{B.24}$$

subject to the following conditions at $\tau = 0$:

$$u = 0 \tag{B.25}$$

$$q = 2R \tag{B.26}$$

$$\chi = \theta_0\kappa_{\mathrm{e}} \tag{B.27}$$

and the following as $R \to \infty$:

$$\frac{u}{R} \to 0 \tag{B.28}$$

$$\frac{q}{R} \to 2 \tag{B.29}$$

$$\frac{\chi}{R} \to 0 \tag{B.30}$$

and the following at $R = \kappa_e$:

$$\frac{\partial q}{\partial R} - \frac{q}{R} = 0 \tag{B.31}$$

$$\frac{\partial u}{\partial R} - \frac{u}{R} + 2\left(\frac{\partial \chi}{\partial R} - \frac{\chi}{R}\right) = 0 \tag{B.32}$$

$$\frac{\chi}{R} = \theta_0 \tag{B.33}$$

On Laplace transformation of Equations B.22 and B.23, we find on rearrangement:

$$\frac{\partial^2 \bar{q}}{\partial R^2} + \delta\left(\frac{\partial^2 \bar{u}}{\partial R^2} - \kappa_e^2 \bar{u}\right) - s\bar{q} = -2R \tag{B.34}$$

$$\frac{\partial^2 \bar{u}}{\partial R^2} - (s + \kappa_e^2)\bar{u} + \delta\frac{\partial^2 \bar{q}}{\partial R^2} = 0 \tag{B.35}$$

These are now ordinary differential equations in R which can be solved to give solutions with unknown coefficients in s only. Let us suppose, in accordance with the theory of linear differential equations, that we can assume solutions of the form:

$$\bar{q} = \frac{2R}{s} + \sum_{i=1}^{4} A_i \exp(-\lambda_i R) \tag{B.36}$$

$$\bar{u} = \sum_{i=1}^{4} B_i \exp(-\lambda_i R) \tag{B.37}$$

where A_i, B_i and λ_i may be functions of s but not R. Hence:

$$\frac{\partial^2 \bar{q}}{\partial R^2} = \sum_{i=1}^{4} A_i \lambda_i^2 \exp(-\lambda_i R) \tag{B.38}$$

$$\frac{\partial^2 \bar{u}}{\partial R^2} = \sum_{i=1}^{4} B_i \lambda_i^2 \exp(-\lambda_i R) \tag{B.39}$$

On substitution into Equations B.34 and B.35, we find:

$$\sum_{i=1}^{4} \left(A_i (\lambda_i^2 - s) + B_i \delta(\lambda_i^2 - \kappa_e^2)\right) \exp(-\lambda_i R) = 0 \tag{B.40}$$

$$\sum_{i=1}^{4} \left(A_i \delta \lambda_i^2 + B_i (\lambda_i^2 - (s + \kappa_e^2))\right) \exp(-\lambda_i R) = 0 \tag{B.41}$$

which must hold at all R, so each term in the sum must be equal to zero. From Equation B.41:

$$\delta\,\lambda_i^2\,A_i = (s + \kappa_\mathrm{e}^2 - \lambda_i^2)\,B_i \tag{B.42}$$

Note that either coefficient may be zero and so we shall not cancel terms directly. Rather if we multiply Equation B.40 through by δ and substitute:

$$(s + \kappa_\mathrm{e}^2 - \lambda_i^2)\,B_i - \delta s A_i + \delta^2(\lambda_i^2 - \kappa_\mathrm{e}^2)\,B_i = 0 \tag{B.43}$$

Multiplying by λ_i^2 again, we can substitute further:

$$\left(\lambda_i^2\,(s + \kappa_\mathrm{e}^2 - \lambda_i^2 + \delta^2(\lambda_i^2 - \kappa_\mathrm{e}^2)) - s(s + \kappa_\mathrm{e}^2 - \lambda_i^2)\right)\,B_i = 0 \tag{B.44}$$

which must require that for non-zero B_i (a non-trivial solution), λ_i must obey a quartic characteristic equation expressed as:

$$(1-\delta^2)\lambda_i^4 - (2s + (1-\delta^2)\kappa_\mathrm{e}^2)\,\lambda_i^2 + s(s + \kappa_\mathrm{e}^2) = 0 \tag{B.45}$$

Since $(1-\delta^2)$ only equals zero for an infinite difference in diffusion coefficients, we will exclude this case and hence divide through by $(1-\delta^2)$. Defining $s' = s/(1-\delta^2)$, the characteristic equation for λ_i becomes:

$$\lambda_i^4 - (2s' + \kappa_\mathrm{e}^2)\,\lambda_i^2 + s'(s + \kappa_\mathrm{e}^2) = 0 \tag{B.46}$$

which has solutions:

$$\lambda_i = \pm\sqrt{s' + \frac{\kappa_\mathrm{e}^2}{2} \pm \sqrt{\delta^2 s'^2 + \frac{R_\mathrm{e}^4}{4}}} \tag{B.47}$$

The requirement that $\bar{q}/R \to 2/s$ and $\bar{u}/R \to 0$ as $R \to \infty$ allows us to determine that $A_i(s) = B_i(s) = 0$ for positive λ_i. Only the negative roots need to be considered, such

that if we define:

$$\lambda_1 = +\sqrt{s' + \frac{\kappa_\mathrm{e}^2}{2} + \sqrt{s'^2\delta^2 + \frac{R_\mathrm{e}^4}{4}}} \tag{B.48}$$

$$\lambda_2 = +\sqrt{s' + \frac{\kappa_\mathrm{e}^2}{2} - \sqrt{s'^2\delta^2 + \frac{R_\mathrm{e}^4}{4}}} \tag{B.49}$$

with all square roots in the positive sense, then we may express $\bar{q}$ and $\bar{u}$ as:

$$\bar{q} = A_1 \exp(-\lambda_1 R) + A_2 \exp(-\lambda_2 R) + \frac{2R}{s} \tag{B.50}$$

$$\bar{u} = B_1 \exp(-\lambda_1 R) + B_2 \exp(-\lambda_2 R) \tag{B.51}$$

where A_1, A_2, B_1 and B_2 are related by Equation B.42 and are unknown functions of s. Note that by definition:

$$\lambda_1 > \lambda_2 \geq 0 \tag{B.52}$$

for $\kappa_\mathrm{e} > 0$ and $|\delta| < 1$. We now consider the boundary condition at Equation B.31. Taking the Laplace transform of this expression and substituting the expression for $\bar{q}$ yields:

$$-A_1\,\lambda_1 \exp(-\lambda_1\kappa_\mathrm{e}) - A_2\,\lambda_2 \exp(-\lambda_2\kappa_\mathrm{e}) + \frac{2}{s} - \frac{A_1}{\kappa_\mathrm{e}} \exp(-\lambda_1\kappa_\mathrm{e}) - \frac{A_2}{\kappa_\mathrm{e}} \exp(-\lambda_2\kappa_\mathrm{e}) - \frac{2}{s} = 0 \tag{B.53}$$

and therefore

$$(1 + \lambda_1\kappa_\mathrm{e})\,A_1 \exp(-\lambda_1\kappa_\mathrm{e}) + (1 + \lambda_2\kappa_\mathrm{e})\,A_2 \exp(-\lambda_2\kappa_\mathrm{e}) = 0 \tag{B.54}$$

and hence

$$A_2 = -\frac{(1 + \lambda_1\kappa_\mathrm{e})}{(1 + \lambda_2\kappa_\mathrm{e})} \exp((\lambda_2 - \lambda_1)\kappa_\mathrm{e})\,A_1 \tag{B.55}$$

It then follows from Equation B.42 that:

$$B_2 = -\frac{(1 + \lambda_1\kappa_\mathrm{e})}{(1 + \lambda_2\kappa_\mathrm{e})} \frac{\lambda_2^2(s + \kappa_\mathrm{e}^2 - \lambda_1^2)}{\lambda_1^2(s + \kappa_\mathrm{e}^2 - \lambda_2^2)} \exp((\lambda_2 - \lambda_1)\kappa_\mathrm{e})\,B_1 \tag{B.56}$$

Via cumbersome but elementary algebra it can be demonstrated from the definitions of λ_1 and λ_2 that

$$\frac{\lambda_2^2(s+\kappa_\mathrm{e}^2-\lambda_1^2)}{\lambda_1^2(s+\kappa_\mathrm{e}^2-\lambda_2^2)} = \frac{\kappa_\mathrm{e}^2-2\alpha}{\kappa_\mathrm{e}^2+2\alpha} \equiv b_1 \tag{B.57}$$

where

$$\alpha = +\sqrt{s'^2\delta^2 + \frac{R_\mathrm{e}^4}{4}} \tag{B.58}$$

and hence

$$B_2 = -\frac{(1+\lambda_1\kappa_\mathrm{e})}{(1+\lambda_2\kappa_\mathrm{e})}\, b_1\, \exp((\lambda_2-\lambda_1)\kappa_\mathrm{e})\, B_1 \tag{B.59}$$

and

$$\bar{u} = B_1\left(\exp(-\lambda_1 R) - \frac{(1+\lambda_1\kappa_\mathrm{e})}{(1+\lambda_2\kappa_\mathrm{e})}\, b_1\, \exp((\lambda_2-\lambda_1)\kappa_\mathrm{e})\, \exp(-\lambda_2 R)\right) \tag{B.60}$$

From the Poisson equation:

$$\frac{\partial^2\bar{\chi}}{\partial R^2} = -\frac{1}{2}\kappa_\mathrm{e}^2\bar{u} \tag{B.61}$$

so

$$\int_R^\infty \frac{\partial^2\bar{\chi}}{\partial R'^2}\,\mathrm{d}R' = -\frac{1}{2}\kappa_\mathrm{e}^2\int_R^\infty \bar{u}\,\mathrm{d}R' \tag{B.62}$$

which on performing the integration yields:

$$\frac{\partial\bar{\chi}}{\partial R} = \left.\frac{\partial\bar{\chi}}{\partial R}\right|_{R\to\infty} + \frac{1}{2}\kappa_\mathrm{e}^2\, B_1\left(\frac{\exp(-\lambda_1 R)}{\lambda_1} - \frac{(1+\lambda_1\kappa_\mathrm{e})}{(1+\lambda_2\kappa_\mathrm{e})}\,\frac{b_1}{\lambda_2}\,\exp((\lambda_2-\lambda_1)\kappa_\mathrm{e})\,\exp(-\lambda_2 R)\right) \tag{B.63}$$

On a further integration, it is clear that the requirement that $\bar{\chi}/R \to 0$ as $R \to \infty$ also requires that $\partial\bar{\chi}/\partial R = 0$ in the same limit. We therefore have expressions for $\bar{u}$ and $\partial\bar{\chi}/\partial R$, which we can substitute into the Laplace transform of Equation B.32:

$$\frac{\partial\bar{u}}{\partial R} - \frac{\bar{u}}{R} + 2\left(\frac{\partial\bar{\chi}}{\partial R} - \frac{\theta_0}{s}\right) = 0 \tag{B.64}$$

Again, following some cumbersome but elementary algebra, we can derive:

$$B_1 = \frac{-2\theta_0}{s}\,\exp(\lambda_1\kappa_\mathrm{e})\frac{\lambda_1\lambda_2}{\left(\left(\lambda_1^2+\frac{\lambda_1}{\kappa_\mathrm{e}}-\kappa_\mathrm{e}^2\right)\,\lambda_2-\left(\frac{1+\lambda_1\kappa_\mathrm{e}}{1+\lambda_2\kappa_\mathrm{e}}\,b_1\,\left(\lambda_2^2+\frac{\lambda_2}{\kappa_\mathrm{e}}-\kappa_\mathrm{e}^2\right)\right)\,\lambda_1\right)} \tag{B.65}$$

Defining the denominator of the above as $\phi(s)$, on resubstitution to Equation B.63:

$$\frac{\partial\bar{\chi}}{\partial R} = -\frac{\theta_0}{s}\frac{\kappa_\mathrm{e}^2}{\phi(s)}\left(\lambda_2\,\exp(-\lambda_1(R-\kappa_\mathrm{e}))-\frac{(1+\lambda_1\kappa_\mathrm{e})}{(1+\lambda_2\kappa_\mathrm{e})}\,b_1\lambda_1\exp(-\lambda_2(R-\kappa_\mathrm{e}))\right) \tag{B.66}$$

Since

$$\bar{i}(s) = \mathcal{L}(j_\mathrm{cap}(\tau)) = -\frac{(1+\frac{D_\mathrm{X}}{D_\mathrm{A}})}{\kappa_\mathrm{e}^2}\,s\,\left.\frac{\partial\bar{\chi}}{\partial R}\right|_{R=\kappa_\mathrm{e}} \tag{B.67}$$

we can determine that

$$j_\mathrm{cap}(\tau) = \left(1+\frac{D_\mathrm{X}}{D_\mathrm{A}}\right)\,\theta_0\,\mathcal{L}^{-1}(f(s)) \tag{B.68}$$

where

$$f(s) = \left(\frac{\lambda_2(1+\lambda_2\kappa_\mathrm{e})-\lambda_1(1+\lambda_1\kappa_\mathrm{e})\,b_1}{(1+\lambda_2\kappa_\mathrm{e})\,\phi(s)}\right) \tag{B.69}$$

To determine the capacitive transient it suffices to perform the above inversion.

It is possible to rewrite this function to be inverted, $f(s)$, as:

$$f(s) = \frac{1}{\Phi(s)-\kappa_\mathrm{e}^2} \tag{B.70}$$

where

$$\Phi(s) = \frac{\lambda_1(1+\lambda_1\kappa_\mathrm{e})}{\kappa_\mathrm{e}}\,\frac{(1-b_1)}{1-\frac{\lambda_1(1+\lambda_1\kappa_\mathrm{e})}{\lambda_2(1+\lambda_2\kappa_\mathrm{e})}\,b_1} \tag{B.71}$$

provided that $s>0$.

Note that

$$b_1 = \frac{1-\frac{2\alpha}{\kappa_\mathrm{e}^2}}{1+\frac{2\alpha}{\kappa_\mathrm{e}^2}} \tag{B.72}$$

where

$$\frac{2\alpha}{\kappa_\mathrm{e}^2} = \sqrt{1 + \frac{4\delta^2 s'^2}{R_\mathrm{e}^4}} \approx 1 + \frac{2\delta^2 s'^2}{R_\mathrm{e}^4} \tag{B.73}$$

so long as s' is small. This is a "long time" approximation, although not a very stringent one as κ_e is typically ≥ 10 and so $R_\mathrm{e}^4/2\delta^2$ will greatly exceed a wide range of s'^2. Hence for small s':

$$b_1 \to \frac{\frac{-2\delta^2 s'^2}{R_\mathrm{e}^4}}{2} = \frac{-\delta^2 s'^2}{R_\mathrm{e}^4} \tag{B.74}$$

Hence $(1 - b_1) \approx 1$ and this term can be neglected. When s' is small, $\lambda_2(1 + \lambda_2\kappa_\mathrm{e})$ is also vanishing, however, so the other term involving b_1 must be treated more carefully. Here by making the same first order approximation of the square root (or zeroth order if it is a small term in a sum):

$$\frac{\lambda_1(1 + \lambda_1\kappa_\mathrm{e})}{\lambda_2(1 + \lambda_2\kappa_\mathrm{e})} \approx \frac{s' + \kappa_\mathrm{e}^2 + 1}{s' + \sqrt{\frac{s'}{\kappa_\mathrm{e}^2}}} \tag{B.75}$$

and on substitution

$$\frac{\lambda_1(1 + \lambda_1\kappa_\mathrm{e})}{\lambda_2(1 + \lambda_2\kappa_\mathrm{e})}\, b_1 \approx \frac{-\delta^2 s'}{\kappa_\mathrm{e}} \frac{\sqrt{s'}}{(1 + \kappa_\mathrm{e}\sqrt{s'})} \tag{B.76}$$

such that

$$\frac{(1 - b_1)}{1 - \frac{\lambda_1(1+\lambda_1\kappa_\mathrm{e})}{\lambda_2(1+\lambda_2\kappa_\mathrm{e})}\, b_1} \approx \frac{1 + \kappa_\mathrm{e}\sqrt{s'}}{1 + \kappa_\mathrm{e}\sqrt{s'} + \frac{\delta^2 s'\sqrt{s'}}{\kappa_\mathrm{e}}} \tag{B.77}$$

Continuing the same approximation, we can elaborate $\Phi(s)$ in full as:

$$\Phi(s) \approx \frac{(s' + \kappa_\mathrm{e}^2 + 1)(1 + \kappa_\mathrm{e}\sqrt{s'})}{(1 + \kappa_\mathrm{e}\sqrt{s'}) + \frac{\delta^2 s'\sqrt{s'}}{\kappa_\mathrm{e}}} \tag{B.78}$$

and so

$$f(s) \approx \frac{1}{s' + 1 - \frac{\kappa_\mathrm{e}\sqrt{s'}}{1+\kappa_\mathrm{e}\sqrt{s'}}\, \delta^2 s'} \tag{B.79}$$

in the limit that

$$s \ll \kappa_\mathrm{e}^2 \frac{1 - \delta^2}{2\delta} \tag{B.80}$$

Two further limits arise within this expression. One is the conventional long time:

$$s \gg \frac{(1-\delta^2)}{\kappa_\mathrm{e}^2} \tag{B.81}$$

since κ_e^2 is typically large. The other is a "very long time" limit:

$$s \ll \frac{(1-\delta^2)}{\kappa_\mathrm{e}^2} \tag{B.82}$$

which is typically some time long after the capacitive current has decayed to zero, unless κ_e is small.

The former limit corresponds to $\kappa_\mathrm{e}\sqrt{s'} \gg 1$, and hence:

$$f(s) \to \frac{1}{1+(1-\delta^2)s'} = \frac{1}{1+s} \tag{B.83}$$

giving a transient of $\exp(-\tau)$, which corresponds mathematically to two single-ion resistors in series.

In the "very long time" limit, $\kappa_\mathrm{e}\sqrt{s'} \ll 1$, so:

$$f(s) \to \frac{1}{1+s'} \tag{B.84}$$

giving a transient of $(1-\delta^2)\exp(-(1-\delta^2)\tau)$. This corresponds mathematically to two single-ion resistors in parallel.

Appendix C

Steady-state voltammetry: diffusion-only tunnelling

The solution of the problem of steady-state voltammetry under diffusion-only conditions ($\theta = 0$) and subject to distance-dependent electron transfer will be presented here, using the terminology and notation of Chapter 10.

The equation set required is:

$$j_{\mathrm{A}} = \frac{dc_{\mathrm{A}}}{dy} \tag{C.1}$$

$$c_{\mathrm{B}} = \frac{1 - c_{\mathrm{A}}}{D'_{\mathrm{B}}} \tag{C.2}$$

$$(1-y)^4 \frac{dj_{\mathrm{A}}}{dy} = K^0 \cdot \beta \exp\left(-\frac{\beta y}{1-y}\right) \cdot f_{\mathrm{BV}} \tag{C.3}$$

where

$$f_{\mathrm{BV}} = \mathrm{e}^{+\alpha'\eta}\left(c_{\mathrm{A}} - c_{\mathrm{B}}\,\mathrm{e}^{-\eta}\right) \tag{C.4}$$

Hence if we let $c = c_{\mathrm{A}}$, then

$$\begin{aligned} f_{\mathrm{BV}} &= \mathrm{e}^{+\alpha'\eta} + \left(c - (1-c)\,\frac{\mathrm{e}^{-\eta}}{D'_{\mathrm{B}}}\right) \\ &= \mathrm{e}^{+\alpha'\eta}\left(\left(1 + \frac{\mathrm{e}^{-\eta}}{D'_{\mathrm{B}}}\right)\,c - \frac{\mathrm{e}^{-\eta}}{D'_{\mathrm{B}}}\right) \end{aligned}$$

Hence

$$f_{\mathrm{BV}} = \left(1 + \frac{\mathrm{e}^{-\eta}}{D'_{\mathrm{B}}}\right) \mathrm{e}^{+\alpha'\eta} \left(c - c_{\mathrm{N}}\right) \tag{C.5}$$

where c_{N} is the Nernstian (equilibrated) concentration of A and is given

$$c_{\mathrm{N}} = \frac{1}{1 + D'_{\mathrm{B}}\,\mathrm{e}^{\eta}} \tag{C.6}$$

Note that when $\alpha' = 0.5$ and $D'_{\mathrm{B}} = 1$, this reduces to

$$f_{\mathrm{BV}} = \cosh\left(\frac{\eta}{2}\right) \left(c - c_{\mathrm{N}}\right)$$

implying a 'restoring force' such that the rate of the reaction to recover equilibrium increases exponentially for large overpotentials either side of $E_{\mathrm{f}}^{\ominus}$.

Substituting the various relations as required, we find that we must solve:

$$\frac{d^2c}{dy^2} - k \cdot \beta \mathrm{e}^{-\frac{\beta y}{1-y}} \cdot (c - c_{\mathrm{N}}) = 0 \tag{C.7}$$

subject to

$$\left.\frac{dc}{dy}\right|_{y=0} = 0 \tag{C.8}$$

$$c(1) = 1 \tag{C.9}$$

where the collection of constants k is given:

$$k = K^0 \left(1 + \frac{\mathrm{e}^{-\eta}}{D'_{\mathrm{B}}}\right) \mathrm{e}^{+\alpha'\eta} \tag{C.10}$$

C.1 Outer Solution

Where

$$\frac{y}{1-y} \gg \frac{1}{\beta}$$

then the reaction term becomes negligible and so a simple diffusive steady state applies

$$\frac{d^2c}{dy^2} \to 0$$

Solving such that the outer boundary condition applies, and ignoring the inner boundary condition as applying to a boundary layer that is perturbed by the reaction, we determine that

$$c \to 1 - j_{\mathrm{A}}(1-y) = 1 - \frac{j_{\mathrm{A}}}{R} \tag{C.11}$$

where $R = r/r_{\mathrm{e}}$.

C.2 General Inner Solution (Tunnelling)

We are now concerned with solving the full equation C.7 in the boundary layer close to $y = 0$ where the reaction term is non-zero. We will solve in terms of the spherical coordinate R, rather than y. As $R \to \infty$ we require that the inner solution approaches the outer solution (Equation C.11) asymptotically.

First we will introduce the following substitution of the dependent variable:

$$u = (c - c_{\mathrm{N}}) \cdot R \tag{C.12}$$

such that

$$\frac{dc}{dR} = \frac{1}{R}\frac{du}{dR} - \frac{u}{R^2} \tag{C.13}$$

and hence

$$\frac{d^2c}{dy^2} = \frac{1}{R^2}\frac{d}{dR}\left(R^2\frac{dc}{dR}\right) = \frac{1}{R}\frac{d^2u}{dR^2} \tag{C.14}$$

such that Equation C.7 becomes

$$\frac{d^2u}{dR^2} - k\beta\,\mathrm{e}^{-\beta(R-1)}\cdot u = 0 \tag{C.15}$$

Now we substitute the independent variable:

$$q = a\cdot\mathrm{e}^{-\frac{\beta(R-1)}{2}} \tag{C.16}$$

where a is a constant.

Therefore

$$\begin{aligned}\frac{du}{dR} &= -\frac{\beta}{2}\,q\,\frac{du}{dq}\\ \frac{d^2u}{dR^2} &= \frac{\beta^2}{4}\,q\,\frac{d}{dq}\left(q\,\frac{du}{dq}\right)\\ &= \frac{\beta^2}{4}\left(q^2\,\frac{d^2u}{dq^2} + q\,\frac{du}{dq}\right)\end{aligned}$$

so

$$q^2\,\frac{d^2u}{dq^2} + q\,\frac{du}{dq} - \frac{4k}{\beta}\frac{q^2}{a^2}\,u = 0$$

If we let

$$\begin{aligned}a &= \sqrt{\frac{4k}{\beta}}\\ &= \sqrt{\frac{4K^0}{\beta}\left(1+\frac{\mathrm{e}^{-n\eta}}{D'_{\mathrm{B}}}\right)\mathrm{e}^{-\alpha_{\mathrm{A}}\eta}}\end{aligned} \tag{C.17}$$

then the equation we must solve is simply

$$q^2\,\frac{d^2u}{dq^2} + q\,\frac{du}{dq} - q^2\,u = 0 \tag{C.18}$$

which is the modified Bessel equation of zeroth order.

Note that this equation is to be solved over the range from $q = 0$, corresponding to

$R \to \infty$, to $q = a$, corresponding to $R = 1$. The constant a contains the ratio K^0/β which is equivalent to:

$$\kappa = \frac{K^0}{\beta} = \frac{k^0}{\beta' D} \tag{C.19}$$

where D is the diffusion coefficient of A. Typically, $\kappa \ll 1$: it represents the ratio of the rate of electron transfer to the rate of diffusion across the distance $1/\beta'$ in which electron transfer by tunnelling proceeds at a perceptible rate. Typically diffusion across this distance occurs on a very short timescale with respect to electron transfer. This parameter was identified by Feldberg,[1] who found that deviations from classical theory in dynamic diffusion-only chronoamperometry arise only when $\kappa > 1$.

The general solution of Equation C.18 is:

$$u = A \cdot I_0(q) + B \cdot K_0(q) \tag{C.20}$$

where I_0 and K_0 are the zeroth order modified Bessel functions of the first and second kinds respectively, and A and B are constants. Hence:

$$c = c_{\mathrm{N}} + \frac{1}{R}\left(A \cdot I_0(q) + B \cdot K_0(q)\right) \tag{C.21}$$

We must determine A, B and j_{A} such that Equation C.21 satisfies the boundary condition at Equation C.8, and such that Equation C.21 approaches Equation C.11 as $R \to \infty$ ($q \to 0$).

C.3 Determination of coefficients

We must relate A and B such that

$$\left.\frac{dc}{dR}\right|_{R=1} = 0$$

Differentiating Equation C.21, we find

$$\begin{aligned}\frac{dc}{dR} &= \frac{1}{R}\cdot\frac{d}{dR}\left(A\cdot I_0(q)+B\cdot K_0(q)\right)-\frac{1}{R^2}\left(A\cdot I_0(q)+B\cdot K_0(q)\right)\\ &= \frac{1}{R}\left(-\frac{\beta}{2}\,q\,\frac{d}{dq}\left(A\cdot I_0(q)+B\cdot K_0(q)\right)-\frac{1}{R}\left(A\cdot I_0(q)+B\cdot K_0(q)\right)\right)\\ &= -\frac{1}{R}\left(\frac{\beta}{2}\,q\left(A\cdot I_1(q)-B\cdot K_1(q)\right)+\frac{1}{R}\left(A\cdot I_0(q)+B\cdot K_0(q)\right)\right)\end{aligned}$$

where I_1 and K_1 are the first order modified Bessel functions of the first and second kinds respectively.

Substituting $R = 1$ ($q = a$):

$$-\left(\frac{\beta}{2}\,a\left(A\cdot I_1(a)-B\cdot K_1(a)\right)-\left(A\cdot I_0(a)+B\cdot K_0(a)\right)\right)=0$$

and so rearranging

$$\frac{A}{B}=\frac{aK_1(a)-\frac{2}{\beta}K_0(a)}{aI_1(a)+\frac{2}{\beta}I_0(a)}\equiv\Phi \tag{C.22}$$

This ratio is then a function of a and β. Hence

$$c = c_{\mathrm{N}}+\frac{B}{R}\left(\Phi I_0(q)+K_0(q)\right) \tag{C.23}$$

To assess the asymptotic approach of this equation to the outer solution, it is useful to know the asymptotic forms of the modified Bessel functions when $q \to 0$. These are:

$$I_0(0)\approx 1 \tag{C.24}$$

$$K_0(q\to 0)\approx -\ln\left(\frac{q}{2}\right)-\gamma \tag{C.25}$$

where the Euler–Mascheroni constant $\gamma = 0.5772....$

Expanding the logarithm:

$$\begin{aligned} K_0(q \to 0) &\to -\ln\left(\frac{a}{2} \cdot \mathrm{e}^{-\frac{\beta(R-1)}{2}}\right) - \gamma \\ &= -\ln\left(\frac{a}{2}\right) + \frac{\beta R}{2} - \frac{\beta}{2} - \gamma \\ &= \frac{\beta}{2}\left(R - \left(1 + \frac{2}{\beta}\left(\gamma + \ln\left(\frac{a}{2}\right)\right)\right)\right) \end{aligned}$$

Substituting into Equation C.21 with the asymptotic expressions:

$$\begin{aligned} c &\to c_{\mathrm{N}} + \frac{B}{R}\left(\Phi + \frac{\beta}{2}\left(R - \left(1 + \frac{2}{\beta}\left(\gamma + \ln\left(\frac{a}{2}\right)\right)\right)\right)\right) \\ &= \left(c_{\mathrm{N}} + \frac{B\beta}{2}\right) - \frac{B\beta}{2}\frac{1}{R}\left(1 + \frac{2}{\beta}\left(\gamma + \ln\left(\frac{a}{2}\right) - \Phi\right)\right) \end{aligned}$$

Equating the constant term with Equation C.11:

$$\frac{B\beta}{2} = 1 - c_{\mathrm{N}}$$

and hence

$$c = 1 - \frac{1}{R}\left(1 - c_{\mathrm{N}}\right)\left(1 + \frac{2}{\beta}\left(\gamma + \ln\left(\frac{a}{2}\right) - \Phi\right)\right) \tag{C.26}$$

such that from equating the term in $(1/R)$ with that in Equation C.11

$$j_{\mathrm{A}} = \left(1 - c_{\mathrm{N}}\right)\left(1 + \frac{2}{\beta}\left(\gamma + \ln\left(\frac{a}{2}\right) - \Phi\right)\right) \tag{C.27}$$

which indicates a deviation from Nernstian behaviour as for the Butler–Volmer expression (reported in the main text).

C.4 Limiting behaviour

Let us consider the classical limit in which $\kappa \ll 1$ and so $\beta \gg K^0$. In this limit, $a \to 0$ and so we should evaluate Φ in this limit. The asymptotic limits required are:

$$I_0(0) \approx 1 \tag{C.28}$$

$$K_0(a \to 0) \approx -\ln\left(\frac{a}{2}\right) - \gamma \tag{C.29}$$

$$I_1(a \to 0) \approx \frac{a}{2} \tag{C.30}$$

$$K_1(a \to 0) \approx \frac{1}{a} \tag{C.31}$$

so

$$\begin{aligned}\Phi &\to \frac{1 - \frac{2}{\beta}K_0(a)}{\frac{a^2}{2} + \frac{2}{\beta}} \\ &= \frac{\frac{\beta}{2} - K_0(a)}{1+k}\end{aligned}$$

Now

$$\begin{aligned}\frac{j_\mathrm{A}}{j_\mathrm{A,N}} &= 1 + \frac{2}{\beta}\left(-K_0(a) - \Phi\right) \\ &= 1 + \frac{2}{\beta}\left(\frac{-K_0(a)(1+k) - \frac{\beta}{2} + K_0(a)}{1+k}\right) \\ &= 1 + \frac{2}{\beta}\left(\frac{-kK_0(a) - \frac{\beta}{2}}{1+k}\right) \\ &= 1 + \left(\frac{-\frac{a^2}{2}K_0(a) - 1}{1+k}\right)\end{aligned}$$

$K_0(a)$ scales in $\ln a$, and therefore as $a \to 0$

$$\frac{j_\mathrm{A}}{j_\mathrm{A,N}} \to 1 - \frac{1}{1+k} = \frac{1}{1+\frac{1}{k}} \tag{C.32}$$

thus reproducing the Butler-Volmer result in the classical limit.

C.5 Plane of electron transfer

The maximum rate of electron transfer occurs when the source-sink term is largest, i.e. on maximisation of

$$f(q) = \frac{q^2}{R}\left(\Phi I_0(q) + K_0(q)\right) \tag{C.33}$$

It can be demonstrated by graphical investigation for a range of β and a values that this maximum occurs at $q = a$ for almost all values of $k < \beta$. Only when $k \geq \beta$ does the plane of electron transfer move away from the electrode surface. This is an extreme condition which requires very slow diffusion compared to the rate of electron transfer. Tunnelling effects are hence only observed in terms of altered currents for large κ.

Bibliography

[1] S. W. Feldberg, *J. Electroanal. Chem.*, 1986, **198**, 1–18.